EFFECT OF SECOND PHASE PARTICLES ON THE THERMO-MECHANICAL PROCESSING OF ALLOYS

A thesis submitted for the degree of
Doctor of Philosophy

By

MUHAMMAD ALMAS

Department of Materials,
Imperial College of Science,
Technology and Medicine,
London SW7 2BP.

September, 1989.

ABSTRACT

The high and low temperature deformation and recrystallization behaviour of a commercial purity aluminium (2S) and a 2014 aluminium alloy matrix composite containing large (up to 0.2) volume fractions of about 10 μm size SiC particles were investigated. The composites were rolled at low and high temperatures as well as deformed in tension and compression in a temperature range between ambient and 500°C at strain rates between $5x\ 10^{-4}$ and $5\ x\ 10^{-2}\ S^{-1}$. Similar tensile tests were also carried out on their unreinforced matrix alloys for comparative purposes.

The effect of the particles on the mechanical behaviour and the microstructure in low and high temperature regions showed that the reinforcement of SiC particles produced a marked increase in the strength of the composites at low temperatures, but at elevated temperatures, the strength of the composites was found to be similar to that of the matrix materials. It was observed that above a critical temperature, depending on the strain rate, the work hardening rates are much reduced as a consequence of a change in the nature of the dislocation-particle interactions, which can be accounted for quantitatively using the models developed to explain the behaviour of more dilute two phase aluminium alloys. The experimental results for the composites are in agreement with the values predicted by the model. The application of this model to the forming operations of these composites is discussed.

An investigation was also undertaken to evaluate the elevated temperature deformation behaviour of an Al-0.2%Zr-0.2%Si alloy containing small Al_3Zr precipitates over a similar range of temperature and strain rate as for the composites 2S/SiC and 2014/SiC. The dependence on temperature and strain rate of yield stress, flow stress and work hardening

rate during elevated temperature deformation is discussed.

The development of the microstructure in the composites 2S/SiC and 2014/SiC and the Al-Zr-Si alloy after compressive deformation at elevated temperatures was studied using optical and transmission electron microscopy. The formation and size of the sub-grains in the composites and the Al-Zr-Si alloy was found to be dependent on temperature and strain rate. The sub-grains became coarser and more equiaxed on increasing temperature or decreasing strain rate as a result of dynamic recovery. TEM of the hot deformed composites 2S/SiC and 2014/SiC revealed a high dislocation density superimposed on the original dynamic structure. This is generated during cooling as a result of the large difference in thermal expansion co-efficients between Al and SiC. The inhomogeneous microstructure was observed in the hot deformed Al-Zr-Si alloy as elongated bands at the grain boundaries consisting of fine sub-grains smaller than those in the interior of the grains. The effect was seen to be more prominent at higher temperatures.

The fracture behaviour of the 2S/SiC and 2014/SiC composite specimens deformed in tension was studied using scanning electron microscopy. The composites showed dimples on the fracture surfaces indicating that fracture occurred by a ductile mechanism. The fracture process is suggested to be controlled by a combined effect of particle fracture and nucleation of voids adjacent to the particles.

The recrystallization behaviour and microstructural variations of the composites after cold and hot deformations on annealing have been investigated, and a comparison study of the recrystallization behaviour of the matrix alloys has been performed. The recrystallization of the composites is controlled by the SiC particles. These large particles promote recrystallization of the cold rolled composites via particle stimulated

recrystallization, producing a fine grain size. The recrystallization temperature and the particle stimulated recrystallized grain size of the composites is in accord with the values predicted by the models developed to explain the recrystallization behaviour of conventional two phase alloys.

CONTENTS

Title *Page*

Abstract. ii
List of Figures. ix
List of Tables. xix

CHAPTER 1
(Literature Survey)
1.1 Introduction. 1
1.2 Effect of Particles on the Initial Yield Stress. 3
1.3 Plastic Relaxation. 4
1.3.1 Primary Prismatic Loops. 4
1.3.2 Secondary Prismatic Loops. 5
1.3.3 Local lattice Rotation. 5
1.3.4 Cavity Formation and Failure of Materials. 7
1.3.5 Diffusional Relaxation. 7
1.4 Effect of Particles on Work Hardening at Low Temperatures. 9
1.5 Microstructure of Alloys Containing Second Phase Particles. 13
1.6 Effect of Particles on the Yield Stress at Elevated Temperatures. 15
1.7 Effect of Particles on the Work Hardening at Elevated Temperatures. 16
1.8 Hot Worked Microstructure of Particle Containing Alloys. 20
1.9 Effect of Particles on Recovery. 20
1.10 Effect of Particles on Recrystallization. 21
1.10.1 Effect of Small Particles. 21
1.10.2 Effect of Large Particles. 23
1.10.3 Effect of Bi-Modal Dispersion. 24
1.11 Effect of Particles on the Dynamic Recovery. 26
1.12 Effect of Particles on the Dynamic Recrystallization. 27
1.13 Aluminium Matrix / SiC Particulate Composites. 29

1.13.1 Mechanical Properties of Al/SiC Particulate Composites. ... 29
1.13.2 Fracture Characteristics of Al/SiC Composites. 32
1.14 Al-Zr alloy. 33

CHAPTER 2
(Experimental Methods)
2.1 Materials. 35
2.2 Rolling of the Composites and the Matrix Alloys. 37
2.3 Heat Treatments and Hardness Measurements. 38
2.4 Mechanical Testing. 38
2.4.1 Compression Tests. 39
2.4.2 Tensile Testing. 40
2.5 Optical Microscopy. 41
2.6 Particle Size Distribution Measurements. 42
2.7 Transmission Electron Microscopy. 42
2.8 Scanning Electron Microscopy. 43

CHAPTER 3
(Compression testing and Microstructure of the Composites)
3.1 Characterization of the Composites as Starting Material. ... 44
3.2 Stress Strain Behaviour of the Composites (2S/SiC and 2014/SiC). 50
3.2.1 Yield Stress as a Function of Temperature and Strain Rate. 54
3.2.2 Flow stress as a Function of Temperature and Strain Rate. .. 54
3.2.3 Work Hardening Rate as a Function of Temperature and Strain Rate. 59
3.3 Microstructural Studies of the Deformed Composites. 62
3.3.1 Optical Microscopy of 2S/SiC Composite Deformed in Compression. 62
3.3.2 T.E.M. of 2S/SiC composite Deformed in Compression. ... 67
3.3.3 Optical Microscopy of 2014/SiC Composite Deformed in Compression. 72
3.3.4 T.E.M. of 2014/SiC Composite Deformed in Compression. 72

CHAPTER 4
(Tensile Testing and Fractography)
4.1 Stress Strain Behaviour of the Composites and the Matrix alloys. 83

4.1.1 Yield Stress. 90
4.1.2 Elongation. 90
4.1.3 Work Hardening Rates. 95
4.2 Fractography. 102

CHAPTER 5
(Annealed Microstructure and Recrystallization of the Deformed Composites and their Matrix Alloys)
5.1 Introduction. 114
5.2 Hardness Measurements. 114
5.2.1 Isochronal Annealing of 2S (Composite and Matrix Alloy). 115
5.2.2 Isochronal Annealing of 2014 (Composite and Matrix Alloy). 115
5.2.3 Isothermal Annealing of the Composites. 120
5.3 Effect of Strain and Annealing Temperature on the Microstructure During Recrystallization. 120
5.3.1 Observations Using Optical Microscopy for 2S (Composite and Matrix Alloy). 122
5.3.2 Observations Using T.E.M. for 2S/SiC Composite. 135
5.3.3 Observations Using Optical Microscopy for 2014 (Composite and Matrix Alloy). 140
5.3.4 Observations Using T.E.M. for 2014/SiC Composite. 145
5.4 Effect of Heating Rate on the Recrystallization of the Composites. 149
5.5 Effect of the Deformation Temperature on the Recrystallization of the Composite. 149

CHAPTER 6
(Compression Testing and Microstructure of Al-Zr-Si Alloy)
6.1 Annealed Microstructure. 159
6.2 Hardness Testing. 160
6.3 Mechanical Testing. 160
6.4 Deformed Microstructure of the Al-Zr-Si alloy. 163
6.4.1 Optical Microscopy. 166
6.4.2 Transmission Electron Microscopy. 173

CHAPTER 7
(Discussion)
7.1 Strength of the Composites at Low Temperature. 181
7.1.1 Rule of Mixtures. 182
7.1.2 Internal and Residual Stresses. 183
7.1.3 Particle Strengthening. 185
7.1.4 Grain and Sub-Grain Strengthening. 186
7.1.5 Combination of the Strengthening Mechanisms. 187
7.2 Work Hardening of the Composites at Low Temperature. .. 190
7.3 Mechanical Properties of the Composites at Elevated Temperatures. 194
7.4 Work Hardening of the Composites at Elevated Temperatures. 196
7.5 Microstructural Developments during Elevated Temperature Deformation of the Composites. 199
7.6 Effect of Quenching on the Microstructure of the Composites. 203
7.7 Fractography of the Composites. 204
7.8 Recrystallization Behaviour of the Composites. 207
7.9 Effect of Amount of Cold Deformation on the Recrystallization of the Composites. 209
7.10 Effect of Deformation Temperature on the Subsequent Recrystallization of the Composites. 212
7.11 High Temperature Deformation of Al-Zr-Si Alloy. 213
7.12 Microstructure of the Deformed Al-Zr-Si alloy. 215
7.13 Heterogeneous Deformation at the Grain Boundaries During Elevated Temperature Deformation of the Al-Zr-Si Alloy. 217

CHAPTER 8
(Conclusions and Proposals for Further Work)
8.1 Conclusions. 219
8.2 Proposals for Further Work. 225

References. 227
Acknowledgement. 234

LIST OF FIGURES.

	Figure	*Page*
1.1	The Orowan process of dislocations.	6
1.2	Schematic representation of the cross-slip for a dislocation at a particle (14).	6
1.3	Critical particle size for the primary to secondary and local lattice rotation in the structure (8).	6
1.4	Orientation of the matrix in the vicinity of a particle in cold-rolled aluminium (93).	8
1.5	Void formation at a particle under tensile stress (19).	8
1.6	The growth (a) and (b), and coalescence of voids at particles during ductile failure (27).	8
1.7	Local climb of a dislocation over particles (10).	17
1.8	The temperature dependence of the parabolic work hardening rates of aluminium crystals containing 0.31 vol % Si particles (62).	17
1.9	The influence of particle size and spacing upon time of recrystallization of two-phase alloys (81).	25
1.10	The conditions of particle size and amount of deformation for which nucleation is observed to occur at particles (93).	25
3.1	Optical micrograph of the 2S/SiC composite, reduced 50 % by rolling.	45
3.2	Optical micrograph of the 2014/SiC composite, reduced 50 % by hot rolling.	45
3.3	Distribution of the SiC particle size in the 2S/SiC composite determined by Malvern particle size analyzer under different conditions of processing.	47
3.4	Optical microstructure of the 2S/SiC composite after 50 % hot rolling and annealing at 500°C for one hour.	45
3.5	Optical microstructure of the 2014/SiC composite after 50 % hot rolling and annealing at 450°C for one hour.	45
3.6	TEM of the 2S/SiC composite after 50 % hot rolling and annealing at 500°C for one hour.	48
3.7	TEM of the 2014/SiC composite after 50 % hot rolling and annealing at 500°C for one hour.	48

3.8 True stress-strain curves of the 2S/SiC composite deformed in compression at temperatures between room temperature and 500°C at strain rates of (a) 5 x 10^{-4}, (b) 5 x 10^{-3}, and (c) 5 x 10^{-2} S^{-1}. 52

3.9 True stress-strain curves of the 2014/SiC composite deformed in compression at temperatures between 200 and 500°C at strain rates of (a) 5 x 10^{-4}, (b) 5 x 10^{-3}, and (c) 5 x 10^{-2} S^{-1}. 53

3.10 Modulus corrected yield stress of the 2S/SiC composite as a function of temperature after compression testing at different strain rates. 55

3.11 Modulus corrected yield stress of the 2014/SiC composite as a function of temperature after compression testing at different strain rates. 55

3.12 Yield stress of the 2S/SiC composite as a function of strain rate after compression testing at different temperatures. 56

3.13 Yield stress of the 2014/SiC composite as a function of strain rate after compression testing at different temperatures. 56

3.14 Flow stress of the 2S/SiC composite as a function of reciprocal of temperature after compression testing at different strain rates. 57

3.15 Flow stress of the 2014/SiC composite as a function of reciprocal of temperature after compression testing at different strain rates. 57

3.16 Flow stress of the 2S/SiC composite as a function of strain rates after compression testing at different temperatures. 58

3.17 Flow stress of the 2014/SiC composite as a function of strain rates after compression testing at different temperatures. 58

3.18 Initial work hardening rates of the 2S/SiC composite as a function of temperature after compression testing at different strain rates. 60

3.19 Initial work hardening rates of the 2014/SiC composite as a function of temperature after compression testing at different strain rates. 60

3.20 Initial work hardening rates of the 2S/SiC composite as a function of strain rate after compression testing at different temperatures. 61

3.21 Initial work hardening rates of the 2014/SiC composite as a function of strain rate after compression testing at different temperatures. 61

3.22 Optical micrographs of the 2S/SiC composite after compression testing at room temperature at strain rates of (a) 5 x 10^{-4} and (b) 5 x 10^{-2} S^{-1}. 48
3.23 Optical micrographs of the 2S/SiC composite after compression testing at 200°C at strain rates of (a) 5 x 10^{-2} and (b) 5 x 10^{-4} S^{-1}. 63
3.24 Optical micrographs of the 2S/SiC composite after compression testing at 300°C at strain rates of (a) 5 x 10^{-2} and (b) 5 x 10^{-4} S^{-1}. 63
3.25 Optical micrographs of the 2S/SiC composite after compression testing at 400°C at strain rates of (a) 5 x 10^{-2} and (b) 5 x 10^{-4} S^{-1}. 63
3.26 Optical micrographs of the 2S/SiC composite after compression testing at 500°C at strain rates of (a) 5 x 10^{-2} and (b) 5 x 10^{-4} S^{-1}. 65
3.27 TEM of the 2S/SiC composite after compression testing at room temperature at strain rates of (a) 5 x 10^{-4} and (b) 5 x 10^{-2} S^{-1}. .. 68
3.28 TEM of the 2S/SiC composite after compression testing at 200°C at strain rates of (a) 5 x 10^{-4} and (b) 5 x 10^{-2} S^{-1}. 68
3.29 TEM of the 2S/SiC composite after compression testing at 300°C at strain rates of (a) 5 x 10^{-4} and (b) 5 x 10^{-2} S^{-1}. 70
3.30 TEM of the 2S/SiC composite after compression testing at 400°C at strain rates of (a) 5 x 10^{-4} and (b) 5 x 10^{-2} S^{-1}. 70
3.31 TEM of the 2S/SiC composite after compression testing at 500°C at strain rates of (a) 5 x 10^{-4} and (b) 5 x 10^{-2} S^{-1}. 73
3.32 Optical micrographs of the 2014/SiC composite after compression testing at 200°C at strain rates of (a) 5 x 10^{-4} and (b) 5 x 10^{-2} S^{-1}. 73
3.33 Optical micrographs of the 2014/SiC composite after compression testing at 300°C at strain rates of (a) 5 x 10^{-4} and (b) 5 x 10^{-2} S^{-1}. 73
3.34 Optical micrographs of the 2014/SiC composite after compression testing at 400°C at strain rates of (a) 5 x 10^{-4} and (b) 5 x 10^{-2} S^{-1}. 75
3.35 Optical micrographs of the 2014/SiC composite after compression testing at 500°C at strain rates of (a) 5 x 10^{-4} and (b) 5 x 10^{-2} S^{-1}. 75
3.36 TEM of the 2014/SiC composite after compression testing at 200°C at strain rates of (a) 5 x 10^{-4} and (b) 5 x 10^{-2} S^{-1}. 78

3.37 TEM of the 2014/SiC composite after compression testing at 300°C at strain rates of (a) 5 x 10^{-4} and (b) 5 x 10^{-2} S^{-1}. 78
3.38 TEM of the 2014/SiC composite after compression testing at 400°C at strain rates of (a) 5 x 10^{-4} and (b) 5 x 10^{-2} S^{-1}. 80
3.39 TEM of the 2014/SiC composite after compression testing at 500°C at strain rates of (a) 5 x 10^{-4} and (b) 5 x 10^{-2} S^{-1}. 80
4.1 True stress-strain curves of the 2S/SiC composite after tensile testing at temperatures between room temperature and 450°C at strain rates of (a) 5 x 10^{-4}, (b) 5 x 10^{-3}, and (c) 5 x 10^{-2} S^{-1}. ... 85
4.2 True stress-strain curves of the 2S aluminium after tensile testing at temperatures between room temperature and 450°C at strain rates of (a) 5 x 10^{-4}, (b) 5 x 10^{-3}, and (c) 5 x 10^{-2} S^{-1}. ... 86
4.3 True stress-strain curves of the 2014/SiC composite after tensile testing at temperatures between room temperature and 450°C at strain rates of (a) 5 x 10^{-4}, (b) 5 x 10^{-3}, and (c) 5 x 10^{-2} S^{-1}. ... 88
4.4 True stress-strain curves of the 2014 alloy after tensile testing at temperatures between room temperature and 450°C at strain rates of (a) 5 x 10^{-4}, (b) 5 x 10^{-3}, and (c) 5 x 10^{-2} S^{-1}. 89
4.5 Modulus corrected yield stress of the 2S/SiC composite as a function of temperature after tensile testing at different strain rates. 91
4.6 Modulus corrected yield stress of the 2014/SiC composite as a function of temperature after tensile testing at different strain rates. 91
4.7 Modulus corrected yield stress of the 2S aluminium as a function of temperature after tensile testing at different strain rates. ... 92
4.8 Modulus corrected yield stress of the 2014 alloy as a function of temperature after tensile testing at different strain rates. 92
4.9 Yield stress of the 2S/SiC composite as a function of strain rate after tensile testing at different temperatures. 93
4.10 Yield stress of the 2014/SiC composite as a function of strain rate after tensile testing at different temperatures. 93
4.11 Yield stress of the 2S aluminium as a function of strain rate after tensile testing at different temperatures. 94
4.12 Yield stress of the 2014 alloy as a function of strain rate after tensile testing at different temperatures. 94

4.13 Initial work hardening rates of the 2S/SiC composite as a function of temperature after tensile testing at different strain rates. 96
4.14 Initial work hardening rates of the 2014/SiC composite as a function of temperature after tensile testing at different strain rates. 96
4.15 Initial work hardening rates of the 2S aluminium as a function of temperature after tensile testing at different strain rates. 97
4.16 Initial work hardening rates of the 2014 alloy as a function of temperature after tensile testing at different strain rates. 97
4.17 Initial work hardening rates of the 2S/SiC composite as a function of strain rate after tensile testing at different temperatures. 98
4.18 Initial work hardening rates of the 2014/SiC composite as a function of strain rate after tensile at different temperatures. 98
4.19 Initial work hardening rates of the 2S aluminium as a function of strain rate after tensile testing at different temperatures. 99
4.20 Initial work hardening rates of the 2014 alloy as a function of strain rate after tensile testing at different temperatures. 99
4.21 SEM micrographs of the matching halves (a) and (b) of the 2S/SiC composite fracture surfaces after tensile testing at room temperature at a strain rate of 5×10^{-4} S^{-1}. 103
4.22 SEM micrograph of the 2S/SiC composite fracture surface after tensile testing at 250°C at a strain rate of 5×10^{-4} S^{-1}. 103
4.23 SEM micrograph of the 2S/SiC composite fracture surface after tensile testing at 350°C at a strain rate of 5×10^{-4} S^{-1}. 103
4.24 SEM micrographs of the matching halves (a) and (b) of the 2S/SiC fracture surfaces composite after tensile testing at 500°C at a strain rate of 5×10^{-4} S^{-1}. 105
4.25 SEM micrographs of the matching halves (a) and (b) of the 2S/SiC fracture surfaces composite after tensile testing at room temperature at a strain rate of 5×10^{-2} S^{-1}. 105
4.26 SEM micrograph of the 2S/SiC composite fracture surface after tensile testing at 200°C at a strain rate of 5×10^{-2} S^{-1}. 107
4.27 SEM micrograph of the 2S/SiC composite fracture surface after tensile testing at 300°C at a strain rate of 5×10^{-2} S^{-1}. 107

4.28 SEM micrograph of the 2S/SiC composite fracture surface after tensile testing at 400°C at a strain rate of 5 x 10^{-2} S^{-1}. 107
4.29 SEM micrograph of the 2S/SiC composite fracture surface after tensile testing at 500°C at a strain rate of 5 x 10^{-2} S^{-1}. 107
4.30 SEM micrograph of the 2014/SiC composite fracture surface after tensile testing at room temperature at a strain rate of 5 x 10^{-4} S^{-1}. 109
4.31 SEM micrograph of the 2S/SiC composite fracture surface after tensile testing at 250°C at a strain rate of 5 x 10^{-2} S^{-1}. 109
4.32 SEM micrograph of the 2S/SiC composite fracture surface after tensile testing at 350°C at a strain rate of 5 x 10^{-2} S^{-1}. 109
4.33 SEM micrograph of the 2S/SiC composite fracture surface after tensile testing at 500°C at a strain rate of 5 x 10^{-2} S^{-1}. 111
4.34 SEM micrographs of the matching halves (a) and (b) of the 2014/SiC composite fracture surfaces after tensile testing at room temperature at a strain rate of 5 x 10^{-2} S^{-1}. 111
4.35 SEM micrograph of the 2014/SiC composite fracture surface after tensile testing at 300°C at a strain rate of 5 x 10^{-2} S^{-1}. 111
4.36 SEM micrograph of the 2014/SiC composite fracture surface after tensile testing at 500°C at a strain rate of 5 x 10^{-2} S^{-1}. 111
5.1 Vickers hardness as a function of temperature for the 2S/SiC composite, cold rolled to (a) 20%, (b) 35%, (c) 50%, and (d) 70%. 116
5.2 Vickers hardness as a function of temperature for the 2S aluminium, cold rolled to (a) 20%, (b) 50%,and (c) 70%. 117
5.3 Vickers hardness as a function of temperature for the 2014/SiC composite, cold rolled to (a) 20%, (b) 35%, (c) 50%, and (d) 70%. 118
5.4 Vickers hardness as a function of temperature for the 2014 alloy, cold rolled to (a) 20%, (b) 50%,and (c) 70%. 119
5.5 Vickers hardness as a function of time for the 2S/SiC composite, cold rolled to (a) 50% and (b) 70%. 121
5.6 Vickers hardness as a function of time for the 2014/SiC composite, cold rolled to (a) 50% and (b) 70%. 121
5.7 Optical micrograph of the 2S/SiC composite after 50% hot rolling. 123
5.8 Optical micrograph of the 2014/SiC composite after 50% hot rolling. 123

5.9 Optical micrograph of the 2S/SiC composite after 50% cold rolling. 123
5.10 Optical micrographs of the 2S/SiC composite, 70 % cold rolled and annealed for one hour at a) 200°C, (b) 300°C, (c) 400°C, and (d) 500°C. 125
5.11 Optical micrographs of the 2S/SiC composite, 50 % cold rolled and annealed for one hour at (a) 200°C, (b) 300°C, (c) 400°C and (d) 500°C. 127
5.12 Optical micrographs of the 2S/SiC composite, 35 % cold rolled and annealed for one hour at (a) 200°C, (b) 300°C, and (c) 500°C. 129
5.13 Optical micrographs of the 2S/SiC composite, 20 % cold rolled and annealed for one hour at (a) 200°C, (b) 300°C, and (c) 500°C. 129
5.14 Optical micrographs of the 2S aluminium, 70 % cold rolled and annealed for one hour at (a) 200°C and (b) 500°C. 131
5.15 Optical micrographs of the 2S aluminium, 50 % cold rolled and annealed for one hour at (a) 200°C and (b) 500°C. 131
5.16 Optical micrographs of the 2S aluminium, 20 % cold rolled and annealed for one hour at (a) 200°C and (b) 500°C. 133
5.17 Optical micrographs of the 2S/SiC composite, 50 % cold rolled and annealed for 48 hours at 300°C. 133
5.18 TEM of the 2S/SiC composite after 50% cold rolling. 133
5.19 TEM of the 2S/SiC composite, 70 % cold rolled and annealed for one hour at (a) 200°C, (b) 300°C, (c) 400°C, and (d) 500°C. 136
5.20 TEM of the 2S/SiC composite, 50 % cold rolled and annealed for one hour at (a) 200°C, (b) 300°C, (c) 400°C, and (d) 500°C. 138
5.21 Optical micrograph of the 2014/SiC composite after 50% cold rolling. 141
5.22 Optical micrographs of the 2014/SiC composite, 50 % cold rolled and annealed for one hour at (a) 200°C, (b) 400°C, and (c) 500°C. 141
5.23 Optical micrographs of the 2014/SiC composite, 35 % cold rolled and annealed for one hour at (a) 200°C and (b) 500°C. .. 141
5.24 Optical micrographs of the 2014/SiC composite, 20 % cold rolled and annealed for one hour at (a) 200°C and (b) 500°C. 143

5.25 Optical micrographs of the 2014 alloy, 50 % cold rolled and annealed for one hour at (a) 300 and (b) 500°C. 143
5.26 Optical micrographs of the 2014 alloy, 35 % cold rolled and annealed for one hour at (a) 300 and (b) 500°C. 143
5.27 TEM of the 2014/SiC composite after 50% cold rolling. 147
5.28 TEM of the 2014/SiC composite, 50 % cold rolled and annealed for one hour at (a) 200, (b) 300, (c) (d) (e) 400 and (f) 500°C. 147
5.29 Optical micrographs of the 50% cold rolled composites (a) 2S/SiC and (b) 2014/SiC, annealed for one minute in the salt bath at 350 and 400°C respectively. 150
5.30 Optical micrographs of the composite 2S/SiC deformed in compression at room temperature at strain rates of (a) 5 x 10^{-4} and (b) 5 x 10^{-2} S^{-1} and subsequently annealed for one hour at 500°C. 153
5.31 Optical micrographs of the composite 2S/SiC deformed in compression at 200°C at strain rates of (a) 5 x 10^{-4} and (b) 5 x 10^{-2} S^{-1} and subsequently annealed for one hour at 500°C. 153
5.32 Optical micrographs of the composite 2S/SiC deformed in compression at 300°C at strain rates of (a) 5 x 10^{-4} and (b) 5 x 10^{-2} S^{-1} and subsequently annealed for one hour at 500°C. 153
5.33 Optical micrographs of the composite 2S/SiC deformed in compression at 350°C at strain rates of (a) 5 x 10^{-4} and (b) 5 x 10^{-2} S^{-1} and subsequently annealed for one hour at 500°C. 155
5.34 Optical micrographs of the composite 2S/SiC deformed in compression at 400°C at strain rates of (a) 5 x 10^{-4} and (b) 5 x 10^{-2} S^{-1} and subsequently annealed for one hour at 500°C. 155
5.35 Optical micrographs of the composite 2S/SiC deformed in compression at 500°C at strain rates of (a) 5 x 10^{-4} and (b) 5 x 10^{-2} S^{-1} and subsequently annealed for one hour at 500°C. 155

6.1 Vickers hardness of the Al-Zr, Al-Zr-Si and Al-Zr-Cu alloys as a function of temperature. 161
6.2 True stress-strain curves of the Al-Zr-Si alloy deformed in compression at temperatures between 200 and 500°C at strain rates of (a) 5 x 10^{-4}, (b) 5 x 10^{-3}, and (c) 5 x 10^{-2} S^{-1}. 162
6.3 Modulus corrected yield stress of the Al-Zr-Si alloy as a function of temperature after compression testing at different strain rates. 164
6.4 Yield stress of Al-Zr-Si alloy as a function of strain rate deformed in compression at different temperatures. 164
6.5 Flow stress of Al-Zr-Si alloy as a function of strain rate deformed in compression at different temperatures. 165
6.6 Flow stress of the Al-Zr-Si alloy as a function of reciprocal of temperature after compression testing at different strain rates. 165
6.7 Initial work hardening rates of the Al-Zr-Si alloy as a function of temperature after compression testing at different strain rates. 165
6.8 TEM micrographs showing the distribution of Al_3Zr precipitates in (a) (b) Al-Zr-Si, (c) Al -Zr, and (d) Al-Zr-Cu alloys. 167
6.9 Optical micrographs of the Al-Zr-Si alloy after compression testing at 200°C at strain rates of (a) 5 x 10^{-4} and (b) 5 x 10^{-2} S^{-1}. 167
6.10 Optical micrographs of the Al-Zr-Si alloy after compression testing at 300°C at strain rates of (a) 5 x 10^{-4} and (b) 5 x 10^{-2} S^{-1}. 169
6.11 Optical micrographs of the Al-Zr-Si alloy after compression testing at 400°C at strain rates of (a) 5 x 10^{-4} and (b) 5 x 10^{-2} S^{-1}. 169
6.12 Optical micrographs of the Al-Zr-Si alloy after compression testing at 500°C at strain rates of (a) 5 x 10^{-4} and (b) 5 x 10^{-2} S^{-1}. 169
6.13 Optical micrographs of the Al-Zr-Si alloy showing heterogeneous substructure developed adjacent to the grain boundaries after deformations at (a) 400°C at 5 x 10^{-4} S^{-1}, (b) 400°C at 5 x 10^{-4} S^{-1}, (c) 500°C at 5 x 10^{-3} S^{-1}, and (d) 400°C at 5 x 10^{-2} S^{-1}. 171
6.14 TEM of the Al-Zr-Si alloy after compression testing at 200°C at strain rates of (a) 5 x 10^{-4} and (b) 5 x 10^{-2} S^{-1}. 175

6.15 TEM of the Al-Zr-Si alloy after compression testing at 300°C at strain rates of (a) 5 x 10^{-4} and (b) 5 x 10^{-2} S^{-1}. 175
6.16 TEM of the Al-Zr-Si alloy after compression testing at 400°C at strain rates of (a) 5 x 10^{-4} and (b) 5 x 10^{-2} S^{-1}. 177
6.17 TEM of the Al-Zr-Si alloy after compression testing at 500°C at strain rates of (a) 5 x 10^{-4} and (b) 5 x 10^{-2} S^{-1}. 177
6.18 TEM of the Al-Zr-Si alloy showing heterogeneous substructure developed adjacent to the grain boundaries after deformation at (a) (b) 500°C at 5 x 10^{-4} S^{-1}, (c) (d) 400°C at 5 x 10^{-4} S^{-1}, (e) 300°C at 5 x 10^{-3} S^{-1}, and (f) 500°C at 5 x 10^{-2} S^{-1}. 179
7.1 Correlation between steady state flow stress and sub-grain size for a variety of sub-grain sizes and metals. 188
7.2 σ vs. $\varepsilon^{1/2}$ curves of the composites 2S/SiC deformed in compression at ambient temperature at different strain rates. .. 193
7.3 σ vs. $\varepsilon^{1/2}$ curves of the composites 2014/SiC deformed in compression at ambient temperature at different strain rates. .. 193
7.4 The critical temperature below which stresses will accumulate at the particles (128). 200

LIST OF TABLES

Table		*Page*
2.1	Composition of commercial purity aluminium (2S) and 2014 aluminium alloy.	36
3.1	Average sub-grain size of the 2S/SiC composite deformed in compression at different temperatures and strain rates.	82
3.2	Average sub-grain size of the 2014/SiC composite deformed in compression at different temperatures and strain rates.	82
4.1	Tensile data obtained from the true stress-strain curves of the 2S/SiC composites deformed in tension.	100
4.2	Tensile data obtained from the true stress-strain curves of the 2S aluminium deformed in tension.	100
4.3	Tensile data obtained from the true stress-strain curves of the 2014/SiC composites deformed in tension.	101
4.4	Tensile data obtained from the true stress-strain curves of the 2014 alloy deformed in tension.	101
4.5	Average dimple size observed on the fracture surface of the composite (a) 2S/SiC and 2014/SiC deformed in tension.	113
5.1	Average grain size of the 2S/SiC composite in unrecrystallized and completely recrystallized state.	157
5.2	Average grain size of the 2S aluminium in unrecrystallized and completely recrystallized state.	157
5.3	Average sub-grain size developed in the 50 and 70 % cold deformed 2S/SiC composite during annealing prior to recrystallization.	157
5.4	Average grain size of the 2014/SiC composite in unrecrystallized and completely recrystallized state.	158
5.5	Average grain size of the 2014 alloy in unrecrystallized and completely recrystallized state.	158
5.6	Grain size of the 2S/SiC composite deformed between room temperature and 500°C at different strain rates and subsequently annealed for one hour at 500°C.	158

6.1 Sub-grain size of the Al-Zr-Si alloy deformed in compression at different temperatures and strain rates. 174
7.1 Experimentally measured and theoretically predicted temperatures of the transition in the mechanical behaviour of the composites. 200

CHAPTER 1

LITERATURE SURVEY

1.1 Introduction.

The introduction of dispersed second phase particles into a metal often provides a significant improvement in the mechanical properties. The second phase particles can play an influential role in the microstructure evolved after thermo-mechanical processing since the particles may have a considerable contribution to the alteration of the defect structure generated by plastic deformation, and leads to striking changes in the mechanical properties of the solids. The formation of second phase particles may be either as a consequence of precipitation or phase separation or nonmetallic inclusions coming from an impure base metal or deliberately mixed ceramic particles.

The use of dispersed particles in metals and alloys has permitted the refinement and improvement of many properties such as yield strength, work hardening, etc. and the addition of particles has allowed modification of the recrystallization behaviour. Particles have also been commonly added to enhance the properties of a material for use at high temperature. Extensive quantitative investigations and explanations have been offered (1, 2, 3, 4, 5, 6) in recent years in an attempt to develop a theoretical and systematic understanding of the influence of the second phase particles on plastic flow during deformation at low temperature.

The micromechanisms during elevated temperature deformation may vary from those at low temperatures. The presence of stable second phase particles can markedly affect the elevated temperature deformation behaviour by interfering with the dislocation movement and influencing

the degree of recovery and progress of recrystallization. The effect of second phase particles at high temperature is a complex phenomenon and the principle of dispersion hardening has been applied for many years. Only a basic understanding of the mechanism has been established and the details of the process at high temperature are far from complete. Therefore, the effort to understand the elevated temperature mechanical behaviour of the alloys containing stable non-deformable particles is a very important area in the field of optimising the thermo-mechanical processing of alloys.

The present work, therefore, was started to broaden the knowledge concerning the effect of second phase particles on high temperature deformation and recrystallization with the aim of identifying the mechanisms operating under different conditions of variables such as temperature, strain and strain rate. The models developed to describe the mechanical behaviour of conventional two phase alloys at elevated temperature (7, 8) can be used as a basis to advance the understanding in this direction.

To achieve the objective in this type of investigation, a choice is made in favour of those alloys which can maintain the dispersion structure at elevated temperatures since a majority of Al alloys contain metastable precipitates which disappear under these conditions.

It was decided to use two phase aluminium alloy systems containing various types of stable particle dispersions. The materials adopted were the 2S/SiC and 2014/SiC and Al-Zr alloys with the objective of studying the influence of large and small particles on the mechanical properties during thermo-mechanical processing of alloys.

1.2 Effect of Particles on the Initial Yield Stress.

To predict the service behaviour of engineering materials containing dispersed particles often requires a good knowledge of the initial level of yield stress. This is a problem that can be addressed by finding the stress required to send a dislocation a large distance through the array of precipitates. The size and distribution of the obstructing particles is random and the yield stress resulting from the resistance of individual particles to the passage of dislocations is generally a function of both particle size and spacing (9, 10). Many dislocations have to cover a considerable distance along an easy path before they interact with a particle so we can consider yield strength as a sum of matrix and particle contributions.

For hard non-deformable particles, the yield stress increment is due to the force needed for dislocations to bypass the particles. They leave dislocation loops around them as a discontinuity between undeformed particles and the matrix (fig.1.1) in a manner first described by Orowan (11).

The spacing of the particle dispersion is a critical parameter. Dislocations would have to be bent to a diameter of the order of the interparticle spacing in order to bow between the particles .

The increase in the flow stress from bypassing a dislocation around a particle is of the order of

$$\tau = G b / \lambda$$

where G is the shear modulus, b is Burgers vector and λ is the effective interparticle spacing.

This equation gives an approximate value of the yield stress due to the presence of impenetrable particles of known average spacing.

Much effort has been devoted over the last few years to refine the

derivation of yield stress, taking into account the influence of parameters such as the effective interparticle spacing (12, 13), the dislocation character (edge or screw) (14) and the type and statistical distribution of various obstacles of different strengths encountered by the dislocations (10, 12).

1.3 Plastic Relaxation.

The second phase particles, which are introduced into the microstructure to improve the mechanical properties of a metal, become sites of stress concentration during early stages of plastic deformation which leads to very high internal stresses around the particles as more and more Orowan loops are left around the particles. At some level of straining the process of stress relief may be induced through various mechanisms.

1.3.1 Primary Prismatic Loops.

It was proposed by Hirsch (15) that a dislocation may not remain confined to its slip plane when facing an obstacle (fig. 1.2). It can avoid particles by a mechanism of cross-slip and transform into stacks of prismatic loops aligned with particles in the direction of Burgers vector. Formation of these prismatic loops can produce relaxation around small particles (d<100nm) and at small strains (16, 17).

1.3.2 Secondary Prismatic Loops.

The presence of particles during deformation leads to activation of slip on many systems so prismatic loops can also be generated in directions other than the primary Burgers vector direction by moving the material to or from the particle resulting in plastic relaxation (14, 18). The punching out of secondary dislocation loops is favoured at large particles at critical strains which decreases with increase in the particle diameter (fig. 1.3).

1.3.3 Local lattice Rotation.

Plastic relaxation may be achieved by local crystallographic rotation in the neighbourhood of large particles associated with plastic flow of dense tangles and loops of dislocations in secondary slip system (18, 19, 20, 21, 22). The network of dense dislocations in the deformation zones adjacent to the particles rearranges itself into the sub-boundaries (23). Each sub-grain is slightly rotated with respect to its neighbour and the progressive misorientation increases upto the maximum rotation at the particle matrix interface (fig. 1.4). The magnitude of lattice rotation in the vicinity of the particles, found in the deformed crystals, is a function of the alloy, particle size and strain (21). The local lattice rotation is dependent on the particle size upto a size of 2 to 3 μm, beyond which the local lattice rotation is independent of particle size and is a function of strain and increases linearly with strain (22).

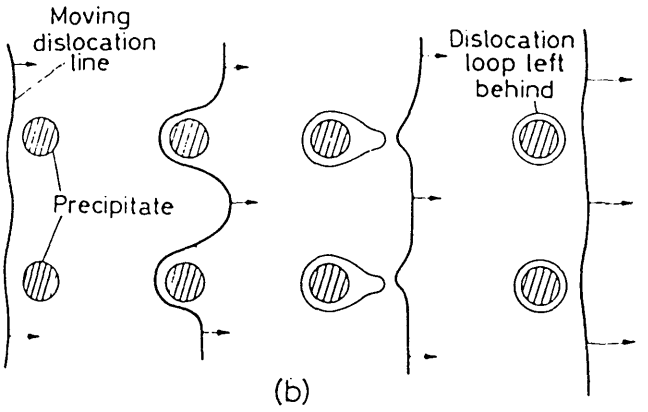


Fig. 1.1 The Orowan process of dislocations.



Fig. 1.2 Schematic representation of the cross-slip for a dislocation at a particle (14).

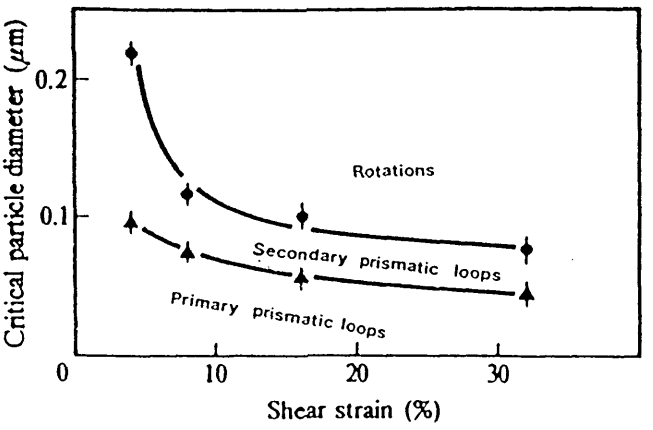


Fig. 1.3 Critical particle size for the primary to secondary and local lattice rotation in the structure (8).

1.3.4 Cavity Formation and Failure of Materials.

This type of stress relief operation occurs when the distribution of local stress exceeds the strength of the particle matrix interface and a cavity is formed at the particle (19). The stress distribution near the particle depends on the mode of deformation of particle and matrix. It has been shown that if the rate of stress relaxation is less than the rate of loading by producing fewer prismatic loops normal to the tensile axis then the particle matrix interface will tend to separate by the action of tensile stress on its axis (19, 24), (fig. 1.5). The nucleation of cavity depends on the shape and orientation of particles and the number of dislocations per pileup. The cavity is nucleated at a critical strain (25) which is greater for smaller particles (26).

Once nucleated, the cavities grow as the plastic deformation proceeds (25, 27). The area of matrix around non-deformable particles is under severe stress constraints. The spherical voids nucleated at the particles will elongate along the tensile axis. The growth rate of voids is determined by strain rate and stress state (28). It is assumed that the voids coalesce when the void length reaches some multiple of its distance from the neighbouring voids (29). Initially, the voids elongate at a rate about double compared to that of the specimen itself. As the voids grow to become ellipsoidal, the growth rate slows down and becomes similar to that of the specimen itself. When the length of the cavities is equal to their spacings, a plastic slip line field is localised (fig. 1.6) and coalescence occurs by final linking of these voids, leading to fracture.

1.3.5 Diffusional Relaxation.

Diffusion in the matrix around particle can relax elastic strain.

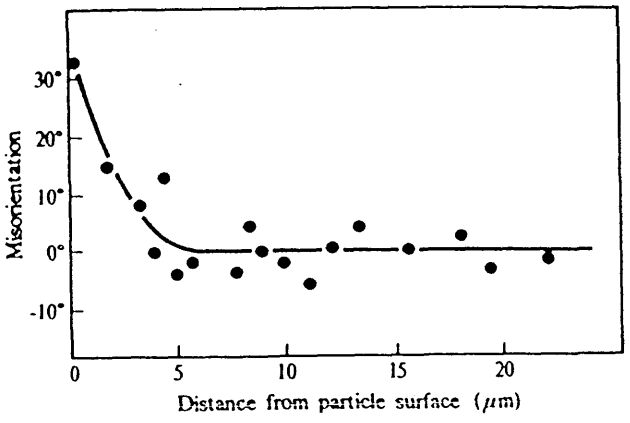


Fig. 1.4 Orientation of the matrix in the vicinity of a particle in cold-rolled aluminium (93).

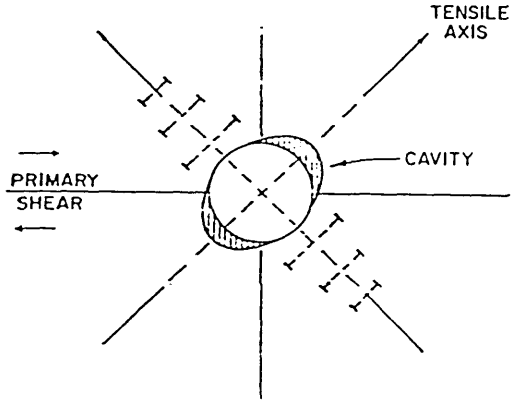


Fig. 1.5 Void formation at a particle under tensile stress (19).

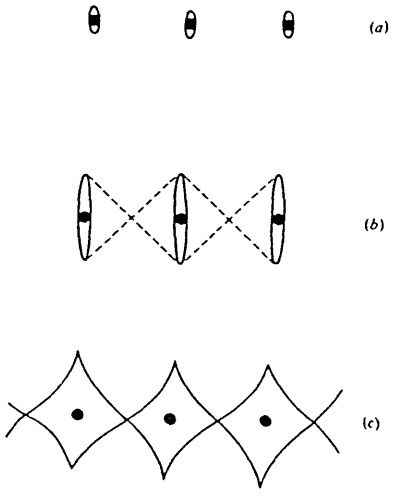


Fig. 1.6 The growth (a) and (b), and coalescence of voids at particles during ductile failure (27).

Hirsch and Humphreys (14, 30, 31) related this phenomenon to the removal of Orowan loops through climb, controlled by pipe diffusion which substantially decreases the strain hardening. Ashby (32) suggested that stress relief is caused by movement of flux of vacancies at the particle matrix interface producing climb of prismatic loops. It has been suggested (1, 33, 34) that diffusion relaxation is more important for small particles and strongly stress dependent. Koeller and Raj (24) argued that applied shear stress around the particles can provide relaxation by diffusional flow at the particle matrix interface or in the matrix. Humphreys and Kalu (7) suggested that the stress relaxation controlled by climb is due to bulk or interface diffusion or both at high temperature.

Diffusional climb has been reported (35, 36) to occur at a temperature lower than at which the bulk diffusion would occur. Shewfelt and Brown (37) reported this temperature as being about one fifth of the melting point depending upon the particle size. Atkinson and Brown (36) explained the removal of Orowan loops by thermally activated cross-slip of dislocation loops but Brown (33) considered this to be unlikely as it does not explain the dislocation structure variations with temperature observed by Humphreys and Hirsch (31). The process of diffusional relaxation is not well understood since all the evidence presented is indirect however, it can be imagined that the relaxation caused by diffusion is through bulk or interface diffusion or combination of both.

1.4 Effect of Particles on Work Hardening at Low Temperatures.

The mechanical behaviour of a particle containing system when

deformed beyond the yield stress not only depends on the stresses sustained in the matrix but also on the compatibility conditions and strain gradient enforced by the particles (10, 19). The presence of a non-deforming second phase is conducive to a much higher dislocation density in the initial stages of straining. This takes the form of tangles and loops around particles and throughout the matrix in contrast to the situation a single phase metal and leads to work hardening. At large strains, however, the stress strain curves of these two-phase alloys become parallel to those of single phase alloys and there is little increment in work hardening due to the particles. This is considered to be due to dynamic recovery (38, 39). The particles have their maximum effect on work hardening during the earliest stages of deformation.

For small deformations, the dislocations bypass the particles, leaving Orowan loops around them. The work hardening resulting from accumulation of Orowan loops around dispersed particles which gives rise to high local stress against the dislocation glide. There is an overall increase in elastic stress as the number of Orowan loops left at the particles increases with increasing plastic straining. The mean flow stress of the matrix arises from various contributions:

$$\tau = \tau_o + \tau_b + \tau_m + \tau_L$$

The first term is Orowan stress, given approximately by

$$\tau_o = G b / \lambda$$

The pile up of Orowan loops at the particles reduces the effective gap between them and repels bowing of the next gliding dislocations by a short range bowing stress, τ_b. Fisher et al. (40) proposed that the gliding dislocations bypass the particles by means of the Orowan mechanism and that the Orowan loops thus formed give rise to a shear stress on the slip plane which prevents the dislocation sources operating around Orowan

looped particles. The stress has linear relationship with strain and with $f^{3/2}$.

Hart (41) and Brown et al. (42, 43) modified the idea of the short range stresses of Orowan loops which oppose the bowing of gliding dislocations by assuming a uniform shear and considering an additional term of friction stress of the pure matrix in order to find the back stress.

The third term is the mean stress present in the matrix as a result of unrelaxed strain and is explained by Brown et al. (42, 43) on the basis of Eshelby's (44) theory. He shows that an inhomogeneous stress field arises out of the difference between the plastic deformation inside and outside the particles. This falls off as the cube of the distance from the particles when a material is subjected to deformation. This internal stress opposes dislocation motion and generates a uniform stress throughout the matrix. This gives rise to hardening in two phase alloys. Brown et al. (42, 43) calculated the value of the image stress as

$$\tau_m = \gamma G f \varepsilon$$

where γ is an accommodation factor which relates the elastic strain in the particles to the plastic strain in the matrix and is of the order of 0.5 for spherical particles, f is the volume fraction, G is the shear modulus and ε is the plastic shear strain.

τ_L is the long range stress introduced by Hazzledine et al. (45). They calculated it by considering the hardening effect derived from the pile up of the coplanar Orowan loops accumulated over a large area between the particles and assuming a constant slip line spacing. Hazzledine et al. (45) also recalculated τ_b and τ_m using a different approach, assuming a finite slip spacing to treat a pile up of Orowan loops.

At greater strains, the break down of linear hardening starts due to plastic relaxation at second phase particles. The Orowan loops disappear

by transforming into either primary or secondary loops. The loops parallel to the primary Burger's vector are formed by a process of cross-slip of gliding dislocations while bypassing the particles. The repeated occurrence of this event generates linear rows of prismatic loops (14). The number of primary loops in the stack increases with increasing strain. However, at larger strains and particle sizes, the arrangement of prismatic loops has been observed to be generated parallel to the secondary Burger's vector (22).

The multiplication of the dislocations enhanced by the operation of the stress relief mechanism around particles gives rise to a dense forest of dislocations in the matrix. These act as obstacles and oppose further slip. Ashby (18) determined the work hardening in terms of the number of dislocations generated as a result of incompatible deformation of the matrix and particles, recognizing them as geometrically necessary dislocations. He obtained a relationship giving the stress increment due to the dislocation density in the matrix, assuming homogeneous shear of the matrix, as

$$\tau = K G (f b / r)^{1/2} (\varepsilon)^{1/2}$$

where K is a constant, ε is the strain and f is the volume fraction of the particles of radius r. This equation gives a parabolic dependence of the strain hardening.

Brown et al. (43) modified the idea of a uniform dislocation density, as given by Ashby (18), by postulating the formation of local high dislocation density zones around the particles. This he described to be as a result of the concentration of secondary dislocation loops in this area and it gives rise to local lattice rotation around the particles. An expression was found similar to that due to Ashby (18) for forest hardening but combining the effects of local lattice rotations for the result.

Hirsch et al. (14) and Hazzledine et al. (45) adopted a different idea

to determine the work hardening, assuming that an increase in the length of the obstacles due to an increase on straining in the number of rows of prismatic loops in the slip planes leads to self hardening of the slip planes. The later coming dislocations when interact with neighboring gliding slip planes, cause work hardening, known as interaction hardening.

To interpret the hardening phenomena in order to estimate the total hardening, an expression can be made by supplementing the various hardening contributions such as mean stress and forest hardening from geometrically necessary dislocations in form of plastic zones. However as the linear additivity method to find hardening by plastically relaxed materials has been described (2) to be unjustifiable owing to the complex mutual interactions of the dislocations during deformation. Improvements are therefore required to be made in the presently available theories to predict hardening accurately as they currently ignore many important aspects of deformation such as initiation of dynamic recovery of geometrically necessary dislocations at larger strains.

1.5 Microstructure of Alloys Containing Second Phase Particles.

The size and shape of the deformed substructure can be significantly altered by the presence of particles. The substructure is dependent on the size and spacing of the particles. The dislocation structures resulting from the low temperature deformation in alloys containing strong, equiaxed particles under different conditions of particle size and deformation have been discussed by many authors (2, 3).

The effect of distribution of small, closely spaced particles after

higher deformations show that the formation of cell structure tends to be inhibited after straining. This is because the fine dispersion acts to promote uniform and fine scale distribution of slip (46, 47, 48). A large number of dislocation tangles of homogeneous density, which have less clear distinction between the walls and interiors of diffuse character cells, are observed in many small particle containing systems such as in Cu (47, 49, 50, 51) and Al (52, 53, 54) in which fine precipitates are pinning the dislocations and sub-boundaries. After a heavy deformation, dislocations tend to arrange themselves into cell walls and a distinct cell structure may appear in the particle containing materials which have a considerably finer sized structure than a comparable deformed single phase material and is of the same scale as the interparticle spacings (47, 52, 55).

The size of the cell decreases with increasing strain or decreasing interparticle spacing down to a certain level. Thereafter particles have little effect on sub-grain size (56, 57, 58). It has been reported that a smaller cell size (59, 60) and microbands (61) are present in the vicinity of grain boundaries as there is more dislocation activity in this region due to slip incompatibility and an inhibition of dislocation mobility by particles.

The magnitude of lattice misorientations between cells in the presence of small particles is observed, from the studies of Cu (61) and Al (59), to be similar to that in the particle free materials.

With large particles and / or at high strains, the magnitude of lattice rotation is a maximum at the particle matrix interface and decreases with increasing distance from the particles (21). A large dislocation density accumulates around the large particles during deformation and this gives rise to large local lattice rotations at the particles. The local lattice rotated zones extend in the matrix from the particles by a distance approximately

equal to the particle size. The deformed structure in these zones consists of sub-grains which are smaller than the sub-grains inside the matrix, away from the particles and are of mean size 0.1 μm. This size does not vary greatly with strain or particle size (21).

1.6 Effect of Particles on the Yield Stress at Elevated Temperatures.

The strengthening mechanisms in alloys dispersion hardened with oxide particles have been extensively investigated at low and high temperatures (2, 3, 10, 17, 37).

At low temperatures, the yield stress is found to be equal to the Orowan stress. On increasing the deformation temperature, the yield stress remains temperature insensitive until a particular temperature is reached where the yield stress is significantly decreased due to climb of dislocations around particles. The strong temperature dependence of the yield stress arises due to the freeing of dislocations from the particles and moving out of their original planes through climb. Various authors have discussed the reasons to account for variations in the high temperature strength of the particle hardened alloys. Brown and Ham (10) proposed that dislocations in their slip planes climb locally over the particles. The increase in the length of a dislocation during local climb (fig. 1.7) requires extra energy depending upon the extension in the length of a dislocation line . Dispersion hardened alloys for this reason, can retain reasonably good yield strength in contrast to single phase alloys even at a temperature close to melting point of the matrix. Brown and Ham (10) estimated the yield stress at high temperatures as being equal to one half of the Orowan stress measured at room temperature.

Gould et al. (35) suggested that the climb of dislocations is controlled by the motion of jogged screw dislocations with the help of thermally activated vacancy transfer. Dislocation climb by diffusion along a dislocation core i.e. pipe diffusion by nucleating jogs and enables the dislocations to advance.

Shewfelt and Brown (37) analyzed the movement of a dislocation and its velocity after climb while passing through a random array of obstacles. The dislocation velocity was found to be exponentially dependent on applied stress. Efforts have been made to calculate the yield stress as a function of temperature and by computer experiments, it was found that the yield stress at elevated temperatures drops to a limit of 3/8 of Orowan stress which reasonably agrees with the calculated results. The calculations are based on the effect of a single dislocation and do not include the effect of a dislocation network. It is therefore only applicable at relatively low stress levels.

1.7 Effect of Particles on the Work Hardening at Elevated Temperatures.

The rate of work hardening is very temperature dependent. Stewart and Martin (62) have illustrated the temperature dependence of parabolic work hardening in the form of shear stress-strain curves after studies on Al-0.5 wt.% Si-0.45 wt.% Cu (fig. 1.8) showing that there is a fall in the work hardening as the temperature of the specimens, deformed at various temperatures, is increased. Marked variations were observed to appear in the primary dislocation structure of the specimens deformed at high temperatures along with reduction in work hardening compared to

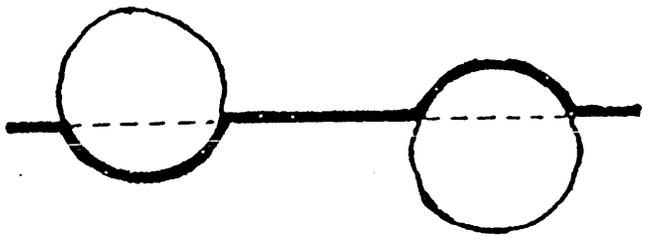


Fig. 1.7 Local climb of a dislocation over particles (10).

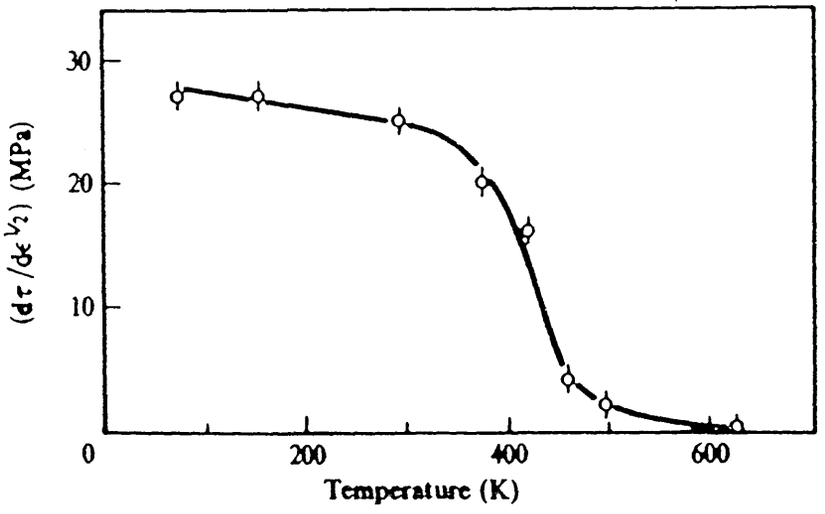


Fig. 1.8 The temperature dependence of the parabolic work hardening rates of aluminium crystals containing 0.31 vol % Si particles (62).

those deformed at room temperature. This pattern of behaviour is in consistent with the idea (35) that depending on particle size and strain rate, the Orowan loops shrink and are carried away from the particles by climb as the deformation temperature is raised from the room temperature, resulting in a marked decrease in the primary dislocation structure. The rate of escape overcomes the rate of dislocation accumulation around the particles.

In a number of studies, a drop in the work hardening and flow stress during high temperature deformation is considered to be as a consequence of various relaxation processes which act to allow the plastic deformation to occur at reduced stress levels. The principle relaxation mechanism which have been considered to produce the removal of stresses at the particles during deformation are climb assisted dislocation motion and diffusional relaxation.

Hirsch and Humphreys (30) discussed the conditions under which the Orowan loops escape from the particles by both cross-slip and climb as possible recovery mechanisms. The Orowan loops anneal out through climb by vacancy transfer along the dislocation pipe. They calculated the critical temperature at which the work hardening starts falling by this process. The theory accounts reasonably well for explaining the experimental observations made for lightly deformed single crystals containing small particles (16, 30). This theory assumes that the loops, while they climb out, do not get restricted by secondary dislocations, and is therefore only applicable to single crystals.

Increasing the temperature also demands an increase in the critical particle size required to generate dislocations on the secondary dislocation structure, so, if the large particles are present, they will significantly contribute to form the secondary dislocation structure. Several authors

have discussed the conditions under which elastic stresses will be relaxed by diffusion at the particle matrix interface. Stobbs (63) ascribed the decrease of work hardening to interface diffusion and has given a relaxation time proportional to the cube power of the particle size. Koeller et al. (24) and Mori et al. (64) also have a similar approach and calculated the strain rates at which the work hardening falls by relaxing the elastic stresses at the particles by diffusion at the particle-matrix interface. Apart from the difference in the numerical constants, the calculations agree well with each other, showing the dependence on the particle size and temperature and in all cases, the critical strain rate may be expressed in the form

$$\varepsilon^{\circ} = K \exp.(-Q_i / R T) / d^3 T$$

where Q_i is the activation energy for interface diffusion, d is the particle size and K is a constant whose value varies significantly for the different theories. This equation is true for low temperatures where surface diffusion occurs.

For high temperatures, the climb mechanism is through bulk diffusion which can be related to diffusion creep (2, 3). Humphreys and Kalu (7) have recently studied the effect of second phase particles on the high temperature behaviour of aluminium alloys. They analyzed the data and derived the critical strain rate at which the transition in the mechanical behaviour would occur, is given by

$$\varepsilon^{\circ} = K_1 \exp.(-Q_v / R T) / T d^2 + K_2 \exp.(-Q_i / R T) / T d^3$$

where Q_v and Q_i are the activation energies for volume and interface diffusion; K_1 and K_2 are derived constants. The first term is for volume diffusion and second for boundary diffusion. This model has been verified experimentally for low volume fraction aluminium alloys containing a range of particle sizes (7) and for SiC whisker reinforced aluminium matrix composites (65).

1.8 Hot Worked Microstructure of Particle Containing Alloys.

A dispersion of fine second phase particles tends to promote the formation of a dislocation substructure during hot deformation. The development of this network is governed by the stability of the particles. They generally stabilize an encapsulating finely meshed dislocation network and frequently determine its dimensions during high temperature deformation (66, 67). Also it is easier for a particle containing alloy to preserve hot worked structure during cooling since dispersions would inhibit static recrystallization (68). Dynamic sub-grain coalescence during hot deformation has been reported (69, 70) in some Al alloys containing small particles. This is attributed to strain induced particle reversion due to grain boundary migration (71, 72) and geometric particle coarsening (73). A rapid increase in the boundary misorientation in these alloys has been reported (73) during the initial stages of hot forming but the mechanism behind this aspect is not very clear.

1.9 Effect of Particles on Recovery.

Recovery proceeds by annihilation of the nearest redundant dislocations through cross-slip and climb and rearrangement into low energy configuration in the form of sharp and ordered walls of sub-grains.

The presence of second-phase particles in an alloy has the capability to modify the recovery process by acting as effective barriers to dislocation movement and can in turn influence the sub-grain formation.

The resistance to recovery from the distribution of the particles mainly comes as a result of pinning of migrating sub-boundaries (74). Therefore the dimensions and the formation of recovered substructure vary as a function of interparticle spacing (59). The inhibition of dislocation movement and sub-boundary transfer by particles stabilises the substructure, hindering the recovery process (75). In certain cases the particles inhibit the sub-grain formation altogether (47). A uniform dislocation distribution is observed in single crystals containing particles which contributes little to coarsening of the substructure on subsequent annealing and sluggish softening is reported to occur during recovery (16).

1.10 Effect of Particles on Recrystallization

If second phase particles are present in an alloy, the controlling factor in the recrystallization behaviour appears to be the size and spacing of the dispersed particles. Depending on these parameters, particles can either retard or accelerate recrystallization.

1.10.1 Effect of Small Particles.

It is well known (8, 76, 77, 78) that the presence of closely spaced fine particles homogenizes the dislocation distribution in the matrix after cold deformation, also producing intractable dislocations, in addition to which sub-grain formation is difficult. Fine particles pin the dislocations and boundaries and severely restrict their mobility. This inherently inhibits recrystallization. Sub-grain formation appears after heavy

deformation (47, 79) and the local misorientations are similar to those in single phase materials (51, 59). Mould and Cotteril (80) proposed that if the fine particles have spacings between them equal to twice the deformation cell size in the matrix after cold working, the recrystallization will be delayed. Jones and Hansen (74) found that below a critical particle interparticle spacing of 1 μm, the recrystallization is significantly retarded by particles in the size range of 0.005 to 0.1 μm. Hansen (81) showed that very fine particles retard recrystallization at all spacings (fig. 1.9).

It has been shown (82, 83, 84, 85, 86, 87) that the other effect to the retarded recrystallization from closely spaced particles apart from homogenizing the dislocation distribution comes from the ability of the particles to interfere with the migrating boundaries.The fine particles exert a drag force (88) on a migrating boundary. The retarding force per unit area of grain boundary is given by

$$P = 3 f \gamma / 2 r$$

where f is the volume fraction, γ is the grain boundary energy and r is the particle radius.This equation indicates that the small particles hinder grain boundaries more effectively than the large particles for a given volume fraction. This idea was originally due to Zener (88) and has been modified by several authors depending upon the grain boundary conditions, particle size, shape, distribution, etc.

Small changes in the dispersion parameter may result in an interchange between accelerated and retarded recrystallization (16, 78). The widely spaced fine particles can enhance the nucleation of recrystallization. Doherty and Martin (83) observed the recrystallization behaviour of Al-Cu alloys and showed that the rate of recrystallization was increased by widening the average interparticle distance of the same sized particles. Similarly Jones (76) showed that when aluminium

containing fine particles 13 μm apart was annealed at 300°C after 50 % rolling, it recrystallized in a few minutes. The transition between accelerated and retarded recrystallization is generally reported to be at a value of f/r ~ 0.2 - 0.4 μm^{-1} (83, 89, 90).

1.10.2 Effect of Large Particles.

It has been extensively observed (23, 77, 91, 92, 93) that large particles (> 1 μm) accelerate recrystallization by providing enhanced nucleation sites for recrystallization. Humphreys (93) studied the particule nucleation of recrystallization most systematically in cold rolled Al-Cu-Si single crystals containing widely spaced large particles. He showed that after cold working, the deformation zones form in the vicinity of particles due to the strain incompatibility of non-deforming particles. The size of the deformation zones from the surface of the particles is of the order of the particle diameter. The zones are comprised of small sub-grains whose misorientation is maximum at the particle matrix interface and gradually decreases with increase in the distance. The recrystallization may nucleate at one of these pre-existing localised sub-grains within the highly misoriented deformation zone, not necessarily at the particle matrix interface, on subsequent recrystallization. The nucleation occurs by a rapid poligonization process involving the sub-boundary migration which consumes the deformation zones. The growth from the deformation zones into the matrix is a critical step and the driving force for this arises from the heterogeneous distribution of dislocations. Nuclei for recrystallization requires the driving force for its growth, the nuclei grows until the grain

boundaries of the recrystallized grains impinge upon each other and the grain size develops according to the relation given by

$$D = 2d / 3f$$ (where d is the particle size & f is the volume fraction)

The combination of particle size and amount of strain determine the conditions for the nucleation of recrystallization at the particles (fig. 1.10). The greater the particle size, the lower the strain required to stimulate nuclei for recrystallization. The number of recrystallization nuclei formed at a particle is a function of particle size. For a particle size up to 5 μm, only one grain may nucleate but for larger particles, more than one grain may be nucleated at one particle (94).

If the particles exist, in the matrix, very closely spaced in the form of clusters, particles even smaller than the critical size to nucleate recrystallization can provide preferential nucleation sites by forming joint localised deformation zones (23, 92). In alloys containing closely spaced large particles, the recrystallization rapidly occurs due to particle stimulated nucleation and a fine grain size is obtained (8, 95, 96). The recrystallized grain in this case is expected to be of the order of interparticle spacing and further annealing will not produce grain growth.

1.10.3 Effect of Bi-Modal Dispersion.

In alloys containing bi-modal particle dispersions, both large and small particles will contribute their part to influence the recrystallization and the net result will depend on the size and spacing of the particles, grain size and degree and mode of deformation (8). The bi-modal dispersions may either retard or accelerate recrystallization, depending

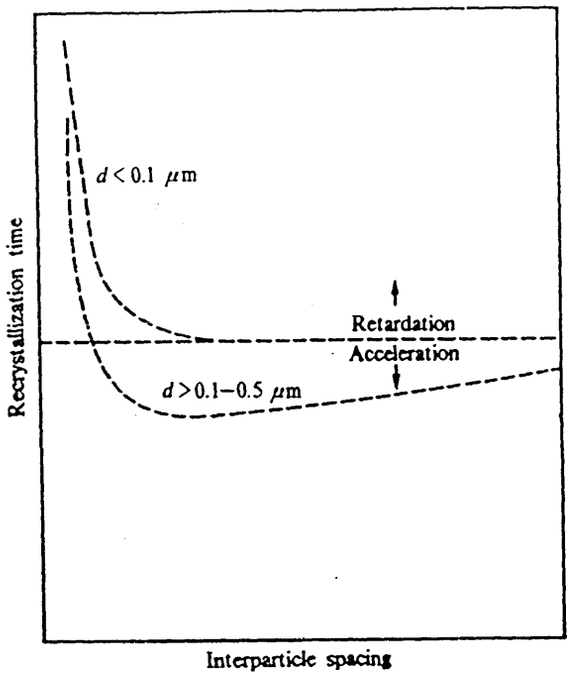


Fig. 1.9 The influence of particle size and spacing upon time of recrystallization of two-phase alloys (81).

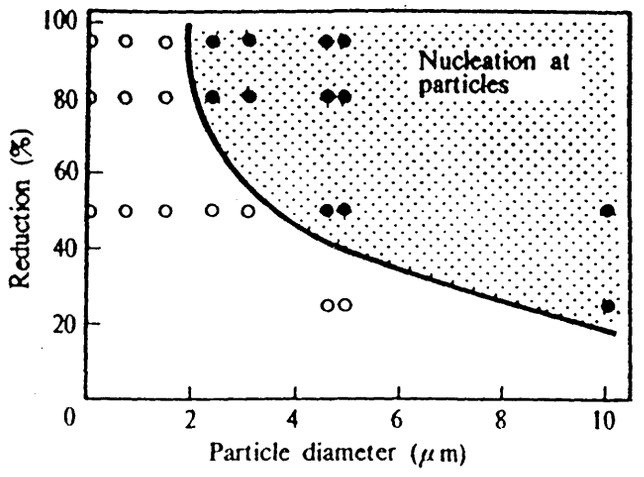


Fig. 1.10 The conditions of particle size and amount of deformation for which nucleation is observed to occur at particles (93).

on the distribution of the particles

Nes (97, 98, 99) studied the recrystallization behaviour of Al-Mn alloys with a bi-modal particle distribution and formulated the recrystallization kinetics, explaining that the nucleation sites are associated with large particles and fine dispersions inhibit nucleation, leading to a coarse final grain size. The recrystallization kinetics are discussed in terms of a parameter f/r. Nes assumed a random distribution of stable particles which exist prior to deformation. However, as in Al-Mn alloys, the fine particles may precipitate concurrently with recrystallization during the final stages of recrystallization and distribute randomly. Moreover, large particles may have precipitate free zones around them (100). These factors contradict the validity of the Nes' model.

Chan and Humphreys (101) investigated the recrystallization kinetics of Al-Si alloys containing a bi-modal particle distribution along with a comparison study of uni-modal alloys. It is shown that the large particles stimulate the recrystallization nuclei and growth rate is controlled by the retarding influence of fine particles, particularly in the early stages of recrystallization. The bi-modal particles display slower recrystallization kinetics than the uni-modal alloys which have no fine dispersions. The recrystallized grain size and shape is found to be dependent on the annealing temperature and the dispersion level of the fine particles.

1.11 Effect of Particles on the Dynamic Recovery.

Above a certain stress, initial linear hardening stops and the stress-strain curve deviates to a parabolic shape. This is attributed to the initiation of dynamic recovery process operating to balance the strain hardening

(1 0 2) .

The annihilation of dislocations of opposite sign starts multiplying to balance the generating dislocations caused by cross-slip. Adjacent pile-ups thus achieving an equilibrium value and resulting substructure whose walls are comprisedof edge remaining components of dislocations. Thus a stable structure persists with a steady state regime on further strain (102, 103, 104, 105).

At higher temperatures, the dynamic recovery is even more distinct due to the enhanced dislocation mobility and cell walls tend to be thinner and clearly defined with larger sub-grain size.

If the particles are present they will prevent cross-slip and reduce cell size to the order of interparticle spacings (66). The particles can restrain the formation of sub-grain substructure altogether if the spacing is very small and eventually keep down the dynamic recovery.

1.12 Effect of Particles on the Dynamic Recrystallization

Dynamic recrystallization is a well recognised deformation induced process in polycrystalline materials whereby the strain hardened grains are replaced by new unstrained grains predominantly nucleated at intergranular sites during high temperature deformation at low strains and strain rates. This process commonly occurs in metals with low stacking fault energy such as Cu (106) and Ni (107, 108).

The grains during deformation become distorted and an incomplete substructure is developed. This structure can be replaced wholly or partly by dynamic recrystallization. Dynamic recrystallization is initiated at a lower critical stress level than if the material was undergoing dynamic

recovery alone. The difference in stored energy of neighboring grains causes the high angle boundaries to migrate and leads to nucleation of recrystallization. The recrystalyzed grains again start deforming during their growth in deformation conditions and a substructure forms once more within them. When the substructure dislocation density builds up to a critical degree, another cycle of recrystallization is nucleated and is followed once more by substructure formation and a steady state regime of flow stress is achieved as a result of continuous distributed recrystallization (66, 107, 109, 110).

The presence of particles is reported to shift the initiation of dynamic recrystallization to higher strains in austenitic steel (67, 111). This is attributed (112) to the inhibiting effect of the particles on sub-grain formation, and therefore on the nucleation of new grains.

Softening in Al and Al alloys is generally only by dynamic recovery (66, 113) during deformation but it is speculated that the alloying additions such as Mg, Zn which may lower the stacking fault energy may induce dynamic recrystallization in which the dislocation motion is hindered by the solute content and dynamic recrystallization nucleates at the dislocation clusters (114). It is also reasoned that a dispersion of particles hampers the dislocation movement and results in an increase in the entangled dislocation density during high temperature deformation which facilitates the stress induced boundary migration uninhibited by the particles and nucleates dynamic recrystallization (69, 71, 115, 116, 117, 118). There is lack of evidence to show how the particles can circumscribe the kinetic dislocations without bothering the boundary migration. This has given rise to a controversy about the role of second phase particles in dynamic recrystallization. Kalu and Humphreys (118) have recently studied the recrystallization behaviour of aluminium alloys

containing second-phase particles deformed at high temperatures. They concluded that the large particles, by forming local lattice rotations, may provide the nuclei for dynamic recrystallization but the driving force for its growth is very low.

1.13 Aluminium Matrix / SiC Particulate Composites.

As a majority of the present investigations were carried out on the SiC particulate metal matrix composites therefore, a brief description of these materials as related to the present work is given in this section.

The aluminium matrix composites reinforced with ceramic particles such as SiC have recently received considerable attention due to a unique combination of improved mechanical properties, including high strength, modulus and creep resistance (119, 120, 121, 122), and workability using standard metallurgical processing (123). These attractive properties along with their low cost makes Al/SiC composites attractive for many structural applications for example in the aerospace and automobile industries.

1.13.1 Mechanical Properties of Al/SiC Particulate Composites.

The mechanical properties of Al/SiC composites are directly related to their microstructural features such as the SiC reinforcement, grain boundaries, sub-boundaries, precipitates, dislocations, etc. These microstructural constituents strongly influence the properties of the composites compared to the unreinforced matrix alloys. The SiC

reinforcement is especially an important microstructural feature. Apart from the morphology, size and distribution of the SiC particles, there is another characteristic associated with these particles that significantly modifies the mechanical properties of the composites. This characteristic is the large difference between the coefficients of thermal expansion (CTE) of SiC and Al. This results in the generation of a high dislocation density in the matrix during cooling (124, 125). This high dislocation density interacts with the mechanisms operating within the matrix during deformation of the composites. Several investigators (126, 127, 128) have discussed the strengthening mechanisms in Al/SiC composites in terms of high dislocation density due to CTE effect, small sub-grain size as a result of the generation of high dislocation density, internal stresses, elastic residual stresses, etc. due to the existence of SiC particles.

Although the increase in dislocation density provides strengthening, however, the difference in theoretical and measured data of quench strengthening shows that the high dislocation density due to CTE effect does not completely account for the strength of the composites (128).

Even though the most of the stresses are relieved by dislocation generation in composites during cooling, yet some of the stresses are stored within the matrix as unrelieved internal elastic stresses. Several authors found their existence and and magnitude in the composites based on Eshelbys's (44) theory. These stresses contribute in the strengthening of Al/SiC composites.

Al/SiC composites usually have a very fine grain and sub-grain structure (128, 129). A significant contribution to the strengthening of the composites may thus be expected from a fine grain and sub-grain structure.

The presence of large SiC particles may also contribute to the net

strengthening of the composites via Orowan mechanism but this contribution is expected to be very small.

The high dislocation density may accelerate the precipitation process as a consequence of the creation of short circuit paths for pipe diffusion of solute (121, 130) in case of Al alloy matrix/SiC composites. Hence increased precipitation may also contribute in the strengthening of the composites.

The low temperature mechanical properties of Al/SiC composites have been reported by several investigators (119, 120, 124, 131), but their mechanical properties at high temperatures have not been examined in much detail. It is reported (132, 133) that the Al/SiC particulate show a rapid decrease in flow stress around 300°C. The magnitude of flow stress of Al/SiC composites may fall to the order of that of the matrix alloy at or above 500°C (129). The properties of the matrix itself may then determine the strength of the composites (133).

Al/SiC composites due to their attractive combination of properties, show considerable promise as structural material but the only limitation is their poor formability (119, 134). However, by designing a route using a proper combination of temperature and strain rate, their performance can be improved (135). It is shown (134, 136, 137) that Al/SiC composites under certain circumstances behave superplastically. They can be processed to contain very small grain size. Superplasticity may then be achieved through grain boundary sliding of the fine grains at elevated temperatures. Large SiC particles may, however, inhibit grain boundary sliding and prevent significant ductilities being achieved.

1.13.2 Fracture Characteristics of Al/SiC Composites.

The SEM examinations of the fracture surfaces of Al/SiC composites reveal dimple morphology, characteristic of the materials that fail in a ductile manner.

It is generally accepted (25, 27, 138, 139, 140, 141) that a ductile fracture in the presence of second phase particles occurs by nucleation of voids at the particles which coalesce and interlink, resulting in a fracture. A considerable effort has been made to identify the mechanisms in the microstructure which may act as sources of weakness. Recent investigations (123, 142, 143, 144) have indicated that there are several variables affecting the origin of the fracture such as: applied stress, the bond strength, the stress concentration around the particles, the volume fraction of second phase particles, the strength of particles, the shape of particles, the microstructure inhomogeneities, etc.

The study of fracture processes in Al/SiC composites has been an area of continuing research along with the development of these materials. Attempts to study the details of the mechanisms leading to failure in these materials have indicated several reasons associated with the SiC reinforcement.

Interfacial bonding between particles and matrix is an important variable. The stronger the bond, the the greater the resistance to void nucleation. The bond strength between SiC and Al is suggested to be very strong (119, 144, 145). The bond strength is estimated to be ~ 1700 MPa which is comparable to the strength of the SiC and therefore, the SiC particle-aluminium interface decohesion is not evidenced on the fracture surface.

It is suggested (123, 131, 142, 146, 147) that the fracture coalesces,

close to the SiC particles within the matrix, in the form of microvoids whose growth leads to fracture. It is reported (119, 145, 148) that the fracture surfaces of the Al/SiC composites do not show the presence of the SiC particles or whiskers in the quantities corresponding to their volume fraction.

On the other hand, some authors (143, 149) by comparing both halves of the fracture surfaces, have shown that a significant amount of the fractured particles lie on on a fracture surface. This indicates the importance to the fracture of brittle fracture of the SiC particles (150).

The SiC particles are expected to fracture during deformation (149) as a result of either, increased stress concentration at the particles from the matrix due to a strong bond which allows the transfer of a high level of stresses, or due to the probability of the defects present in the SiC particles prior to deformation. The high dislocation density, due to the CTE effect, also adds to the localised stress concentration at the particles (151) which makes the particles more favourable for cracking. Also, the SiC particles may not be defect free and already have cracks existing in them before deformation. Such defects may consequently lead to the fracture of the composites.

It is hard to delineate the dominant reason for failure in the Al/SiC composites, whether the fracture occurs due to failure in the matrix adjacent to the particles or due to particle cracking due to complexity of contributions made by each mechanism (128, 149).

1.14 Al-Zr alloy.

Zr is used in many aluminium alloys to improve grain refinement,

toughness, and stress corrosion resistance. It is widely believed that these improvements are due to a high density of fine Al_3Zr precipitate dispersions. (152, 153). The applicability of finely dispersed Al_3Zr particles to some superplastic alloys has stimulated the interest in the Al-Zr system (69, 70, 71, 115, 154, 155) in which precipitates stabilise the structure by retarding recrystallization and controlling grain growth through pinning of the boundaries and dislocations.

Dilute Al-Zr is a peritectic system. This permits the amount of second phase produced to be controlled more accurately as the solute range is much longer and the sluggishness of the peritectic system enhances the formation of supersaturated solid solutions under very fast cooling during casting. This results in stable and finely dispersed particles during later thermal treatments. The particles so produced in a dilute Al-Zr are Al_3Zr metastable coherent particles having a lattice parameter a=0.4073 nm, close to that of the Al matrix, formed with a cube/cube orientation (87, 156, 157, 158, 159). Equilibrium phase particles appear after long annealing at high temperature (87, 160, 161). They have a body centered tetragonal crystal structure and lattice parameters a=0.4013 nm and c=1.732 nm.

The ability to form fine dispersions of Al_3Zr precipitates by the method of heat treatment makes Al-Zr alloy attractive for studies to understand further the influence of fine particles on hot worked structure because Al_3Zr precipitates are stable up to temperatures very close to the melting point of the matrix (162, 163). With any other finely dispersed particles unstable at high temperature, it would be difficult to assess their effect on the deformation behaviour of a metal matrix. This contrasts Al-Zr alloy with conventional heat treatable Al alloys.

CHAPTER 2

EXPERIMENTAL METHODS

2.1 Materials.

The materials under investigation were

(i) A 2S commercial purity aluminium matrix composite reinforced with 20 volume percent SiC particles and unreinforced 2S aluminium.

(ii) A 2014 aluminium alloy matrix composite reinforced with 12 volume percent SiC particles and unreinforced 2014 alloy.

(iii) Al-Zr, Al-Zr-Cu and Al-Zr-Si alloys.

The composite materials for investigation were produced by ALCAN using the Osprey spray process. The raw billets were in form of extruded bars with a cross section of 1.8 x 5.0 cm^2 and their matrix alloys were in the form of hot rolled bars with a cross section of 2.1 x 6.0 cm^2, supplied by ALCAN. The as received bars of 2S/SiC and 2014/SiC composites were initially hot rolled 50 percent at 500°C in the extrusion direction to provide the starting material. The composite materials have an average SiC particle size of about 13 μm with a volume fraction of 20 % in the 2S/SiC and 12 % in the 2014/SiC. The 2014 alloy matrix, apart from large SiC particles, is expected to form on ageing inter-metallic products such as $CuAl_2$ and $Cu_2Mg_8Si_6Al_5$ soluble phases along with $(Mn,Fe)_3SiAl_{12}$ and $Cu_2Mn_3Al_{20}$ (164).

The composition of 2S and 2014 matrix alloys is given in the table 2.1.

Al-Zr, Al-Zr-Cu and Al-Zr-Si alloys were prepared from super purity Al and Al-4.6%Zr, Al-5.0%Cu and Al-17.6%Si master alloys. The Al-4.6%Zr master alloy was prepared from another starting master alloy Zr-10%Al by diluting with pure Al in the arc melter under high purity Argon.

	Composition						
Alloy	Cu	Si	Mn	Fe	Mg	Zn	Al
2S	0.1 max.	0.5 max.	0.1 max.	0.7 max.	---	0.1 max.	99.0 min.
2014	4.4 max.	0.8 max.	0.8 max.	0.1 max.	0.5 max.	---	rem.

2.1 Composition of commercial purity aluminium (2S) and 2014 aluminium alloy.

Zr-10%Al was also prepared in the arc melter using high purity Al and Zr metals.

The composition of the alloys prepared for study were as follows

(i) Al-0.2%Zr,

(ii) Al-0.2%Zr-1.0%Cu,

(iii) Al-0.2%Zr-0.2%Si.

These alloys were melted in an alumina crucible and were chill cast in cylindrical copper moulds with a diameter of 9.5 mm and 100 mm length. Several rods of each alloy were cast in these moulds. Due to Al-Zr having a peritectic system with low solubility of Zr in Al, the final precipitate distribution will depend on the primary dendritic distribution. Therefore chill casting was required to retain high supersaturation and produce a uniform distribution of Al_3Zr precipitates.

One rod of each alloy was cold rolled to a thickness of 2 mm and (15 x 15) mm^2 slices were cut from the rolled strips. The rest of the cast rods were used to machine cylindrical compression specimens 1.6 cm long, with a diameter of 0.8 cm.

2.2 Rolling of the Composites and the Matrix Alloys.

The as received composites and their matrix alloy bars were hot rolled at 500°C by multipass rolling to reduce thickness by 50 % in a rolling mill having 25 cm diameter rolls, running at 100 rpm. The materials were then annealed at 500°C for one hour in a muffle furnace.

Both the composites and their matrix alloys were then cold rolled. The composites 2S/SiC and 2014/SiC were reduced to 20, 35, 50 and 70 % and the matrix alloys to 20, 50 and 70 % in total thickness.

2.3 Heat Treatments and Hardness Measurements.

The 2S/SiC and 2014/SiC composites were 20, 35, 50 and 70 percent cold rolled and their matrix alloys were 20, 50 and 70 percent cold rolled. Specimens were then annealed isochronally for one hour at temperature between 200 and 500°C and change in hardness was measured.

50 and 70 percent cold rolled 2S/SiC and 2014/SiC composites were annealed isothermally as well at 250°C, 400 minutes and 360°C, 300 minutes respectively.

Cold rolled sliced samples of Al-Zr, Al-Zr-Cu and Al-Zr-Si were solution treated at the highest possible temperature range, 630 to 635°C, followed by quenching. The specimens were then initially aged at 100°C for 24 hours then at 400°C for 24 hours. Some specimens were also aged for 168 hours in order to observe the precipitate distribution after long annealing. The change in the hardness of Al-Zr-Si alloy was measured after annealing at different temperatures.

The hardness measurements were recorded by Vickers hardness measurements using a 5 kg load at each temperature or time interval. Each hardness value taken was the representative of the average of at least six readings.

2.4 Mechanical Testing.

Both compression and tensile tests were conducted to study the high temperature mechanical behaviour of the composites, their matrix alloys and the Al-Zr-Si alloy.

2.4.1 Compression Tests.

Compression testing was performed on the 2S/SiC and 2014/SiC composites and on the Al-Zr-Si alloy. The composite compression specimens were circular cylinders 10 mm in diameter and 20 mm in length. Whereas Al-Zr-Si alloy specimens had a diameter of 8 mm and were 16 mm long. All the specimens were prepared and tested parallel to the rolling direction.

Compression tests were carried out on an Instron machine operating in a uniaxial compression direction, at a constant displacement rate and using a 500 kg load cell. The specimens were heated in a furnace attached to the testing rig. The temperature of the specimens and the piston head was continuously monitored during the tests by connected thermocouples. The specimens were maintained at test temperature for 20 minutes before the load was applied. The load displacement data recorded were processed by a microcomputer to provide true stress-strain curves on a plotter.

The tests were terminated by quenching with a water jet directed onto the specimen. This not only cooled the specimen very rapidly and retained the elevated dynamic structure, but also caused the specimen to shrink which prevented the compression rams from deforming further after the termination of the deformation. This was followed by immediately stopping and reversing the compression rams.

The 2S/SiC specimens were annealed at 500°C for one hour prior to testing. The mechanical properties of 2S/SiC composites in compression were evaluated at a temperature range between room temperature and 500°C at strain rates between 5×10^{-4} and 5×10^{-2} S^{-1} to a strain of 50 percent. The compression specimens of the composite 2014/SiC were annealed at 500°C for one hour before testing, to determine the mechanical

properties at temperatures between 200 and 500°C at a strain rate 5 x 10^{-4} and 5 x 10^{-2} S^{-1} to a strain of 50 percent.

The Al-Zr-Si alloy compression specimens were heat treated by homogenising first at 630°C. Then initially ageing at 100° C for 24 hour followed by ageing at 400°C for 24 hours. The tests on Al-Zr-Si alloy were executed in the temperature range between 200 and 500°C at a strain rate between 5 x 10^{-4} and 5 x 10^{-2} S^{-1}.

2.4.2 Tensile Testing.

Tensile tests were conducted on the composites 2S/SiC and 2014/SiC and on the 2S and 2014 matrix alloys. Flat tensile specimens with a gauge length of 23 mm and 5.77 mm x 1.0 mm cross section were fabricated from the hot rolled sheet with tensile axis parallel to the rolling direction. All the test samples prepared were annealed at 450°C prior to testing.

The specimens were stressed under constant load conditions in an Instron machine. The elevated temperature tests were conducted within a furnace. The specimens temperature was measured by two thermocouples, one connected to the top part of the specimen and the other in contact with the bottom part. The specimens were held at the test temperatures for 20 minutes prior to the commencement of testing.

The tensile properties of the composites and their matrix alloys were measured over the temperature range between room temperature and 450°C, and at strain rates between 5 x 10^{-4} and 5 x 10^{-2} S^{-1}. All the tensile specimens were pulled to fracture. As soon as the specimens fractured, they were rapidly quenched.

2.5 Optical Microscopy.

Optical microscopy was conducted on the specimens annealed and deformed in compression. To examine annealed samples, they were cut to a size of about one cm^3. The deformed compression specimens were sectioned by spark cutting parallel to the compression axis. The 2S/SiC and 2014/SiC composite annealed and deformed samples were mounted in Bakelite for easy handling during polishing under load. The composite specimens were ground through successively finer grades of 120, 220, 400, 800 and 1200 SiC papers, using water as lubricant and coolant. The composite specimens were then subsequently polished on Textmet cloth impregnated with 6 micron diamond spray under adequate loading to allow SiC particles and the matrix to be polished at similar rates and give a low relief polish. This was followed by a polish on Microcloth carrying colloidal silica with a constant stream of distilled water being sprayed during polishing. The composite specimens were then anodically etched to develop an oxide layer.

The unreinforced 2S and 2014 alloys and Al-Zr-Si alloy were ground through similar grade SiC papers. Diamond polishing was performed by polishing cloth impregnated with 3 μm, 1 μm and finally 1/4 μm diamond polishing compounds. These alloys were then finally polished electrochemically at a potential of 20 V in a solution of 10 % HNO_3 in methanol at a temperature of -30°C. The specimens were anodised and viewed under polarized light in a Nikon optical microscope to reveal the microstructure.

The grain size was measured by linear intercept method, using the number of grain-boundaries crossed in a known distance to calculate the average grain diameter. The average grain size was measured after counting between 100 and 500 grains, depending on different materials and conditions. Major difficulty in grain size measurements arose in the

composites in the cold rolled condition where it was difficult to reveal the grain-boundaries and in the recrystallized condition where the grain size was of about similar dimensions as that of SiC particles.

2.6 Particle Size Distribution Measurements.

The SiC particle size distribution analysis was conducted for the composite 2S/SiC under the different states of thermo-mechanical processing. The SiC particles were extracted from the composite by dissolving the matrix in a dilute NaOH solution followed by thoroughly washing the undissolved SiC particles with distilled water. The analysis was done on the Malvern 3600 particle size analyzer which consisted of a laser source, a lens system, sample cells and detectors to detect the diffracted light. The smaller the particle size, the greater the angle of diffraction. The diffracted light is collected and focussed by the lens system onto the detectors. The signals from the detectors are processed by a microcomputer to compare the angle of diffracted rays and their concentration in order to relate them to the proportion of the particles of different sizes. The processed data and its graph out put was provided on a printer.

2.7 Transmission Electron Microscopy.

Transmission electron microscopy of the composites, their matrix alloys and aluminium zirconium alloys, annealed and deformed in compression, was performed. The disc specimens 3 mm in diameter were

trepanned by spark machine 0.8 mm thick slices of the annealed and deformed composites and alloys. The discs were then ground to 0.3 mm thickness by lightly grinding on 1200 grit SiC paper.

The disc specimens were electrolytically polished in a PTFE holder using Struer Tenupol jet polishing system operating at 20 V with a current of 0.2 amperes, at a temperature of -30°C, using a polishing solution of 10 % HNO_3 in methanol for composites and 30 % HNO_3 in methanol for unreinforced alloys.

The regions near the hole in the TEM specimens were generally good for microscopy, however, the composite specimens revealed very little transparent regions. The microscopy of the composite for this reason required many samples to be prepared as compared to the unreinforced aluminium alloys.

The transmission electron microscopy was carried out using a Philips 301 and a Jeol 120 CX STEM operating at 100 KV and an HVEM operating at 500/1000 KV.

2.8 Scanning Electron Microscopy.

Observations for the tensile fracture surfaces of the composites 2S/SiC and 2014/SiC were carried out in a Jeol T-200 Scanning electron microscope in Secondary Electron Imaging (SEI), operating at 25 KV.

CHAPTER 3

(RESULTS)

Compression Testing and Microstructure of the Composites.

3.1 Characterization of the Composites as Starting Material.

Optical microstructure of the initially 50 % hot rolled composites is shown in the figs. 3.1 and 3.2. The SiC particle distribution in general was relatively homogeneous, however the SiC particles in many areas were aligned in the extrusion and rolling direction.The size of SiC particles measured in both of the composites was in the range of 5 to 20 μm although there were a few particles smaller or larger than this range. The average SiC particle size in the composites was measured to be 13 μm.

Particle size analysis of the composites was conducted by Malvern 3600 laser particle size analyzer and the SiC particle size histogram of fig. 3.3 shows the SiC particle size range in different conditions which are :

(a) SiC grit before spraying,

(b) SiC particles extracted from as sprayed form,

(c) SiC particles extracted from as extruded form,

(d) SiC particles extracted from hot rolled condition and

(e) SiC particles extracted from 70% cold rolled condition.

The particle size tended to shift to the smaller particle range as the further processing progressed which indicated the breaking of some particles in the matrix as a result of deformation.

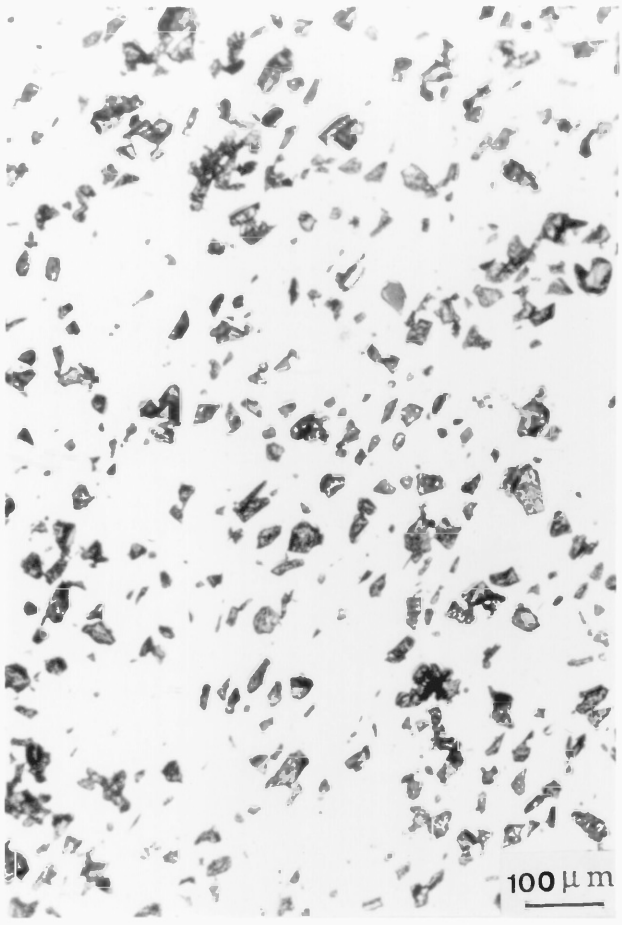
The 2S/SiC composite, in the hot rolled state and annealed at 500°C for one hour resulted in a large grain size of 180 μm as shown in the optical micrograph fig. 3.4. The microstructure of the initially hot rolled 2014/SiC illustrated in fig. 3.5 is

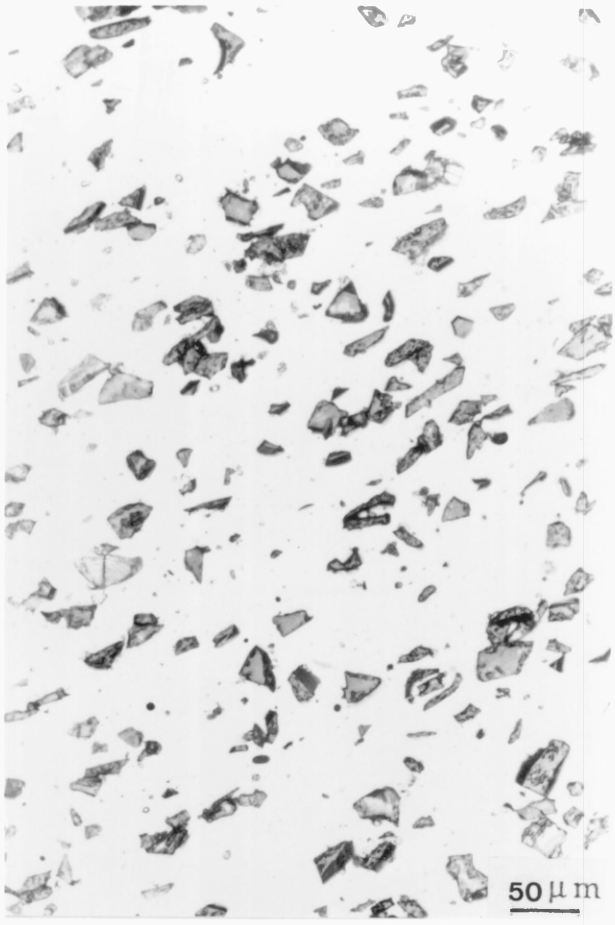
Fig. 3.1 Optical micrograph of the 2S/SiC composite, reduced 50 % by hot rolling.

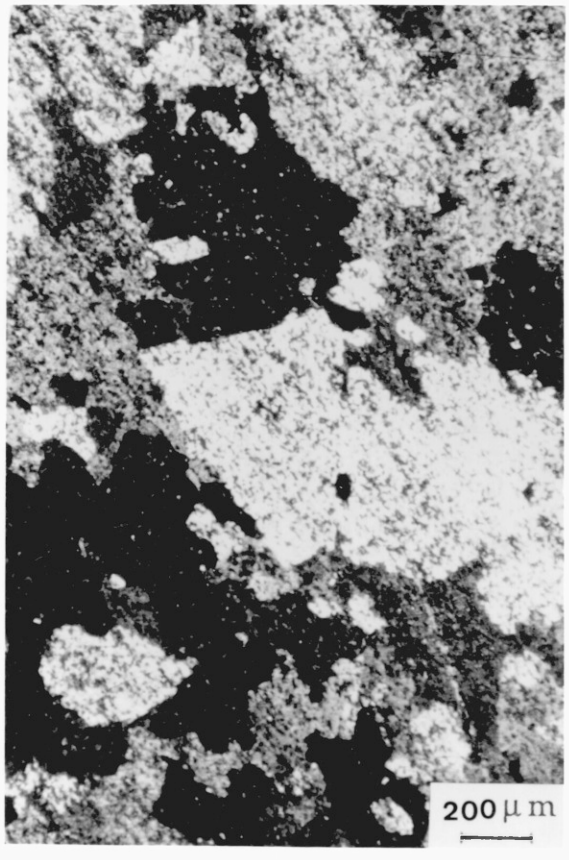
Fig. 3.2 Optical micrograph of the 2014/SiC composite, reduced 50 % by hot rolling.

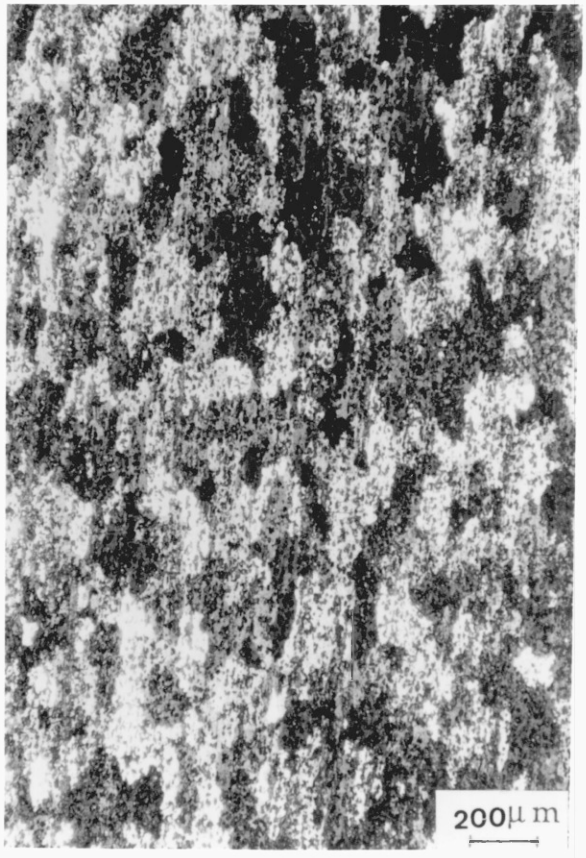
Fig. 3.4 Optical microstructure of the 2S/SiC composite after 50 % hot rolling and annealing at 500°C for one hour.

Fig. 3.5 Optical microstructure of the 2014/SiC composite after 50 % hot rolling and annealing at 450°C for one hour.


100 μ m


50 μ m


200 μ m


200μ m

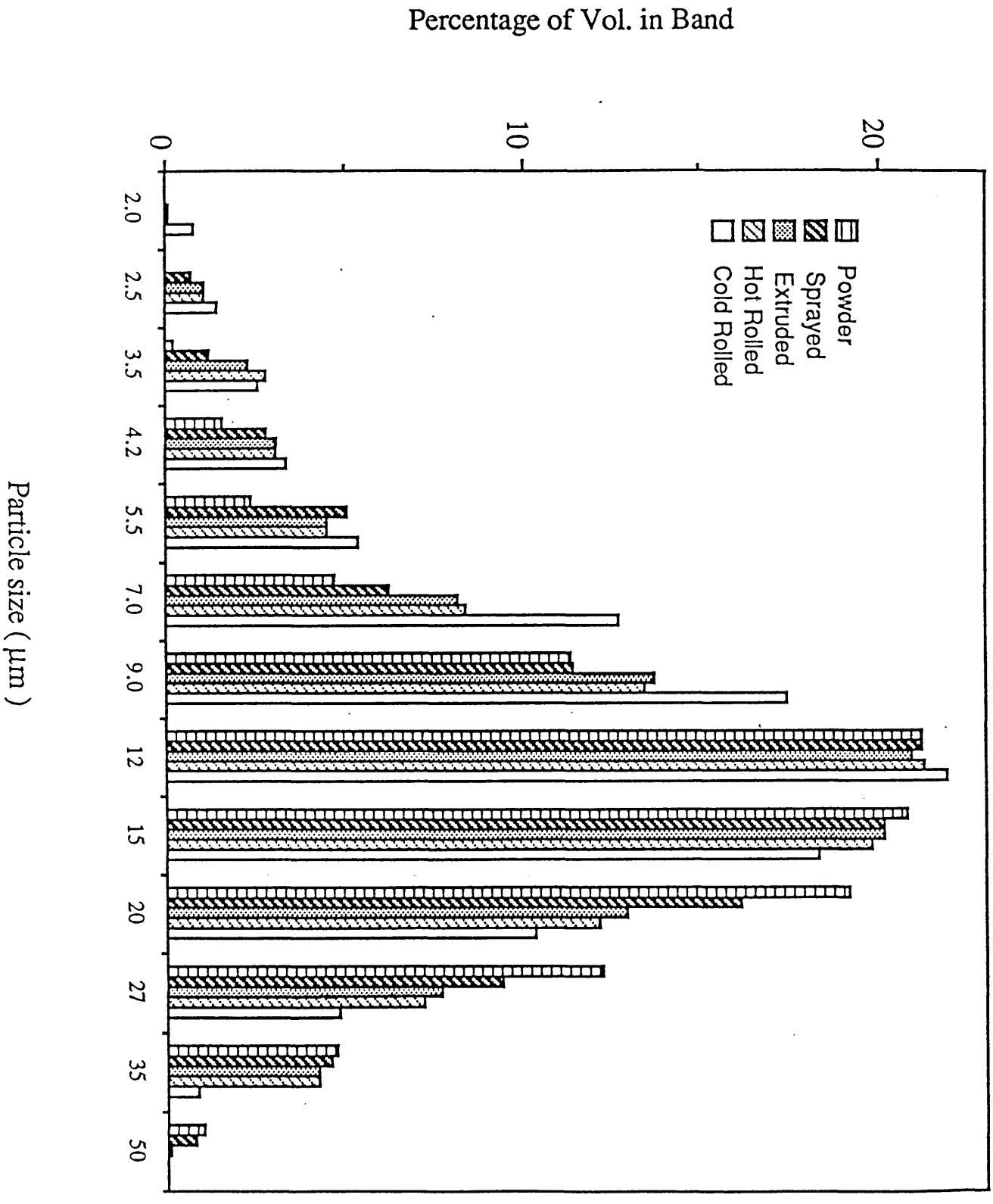


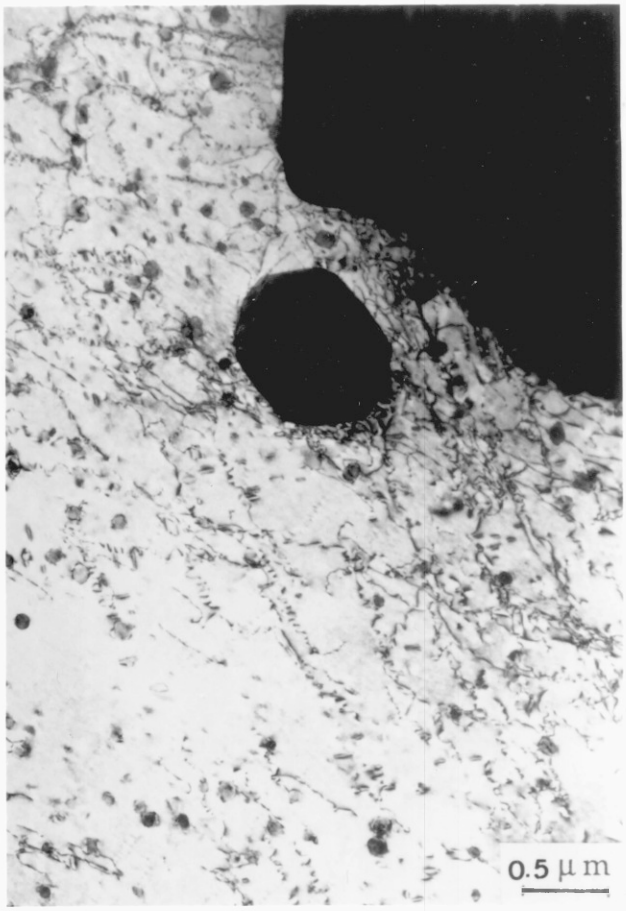
Fig 3.3 Distribution of the SiC particle size in the 2S/SiC composite determined by Malvern particle size analyzer under different conditions of processing.

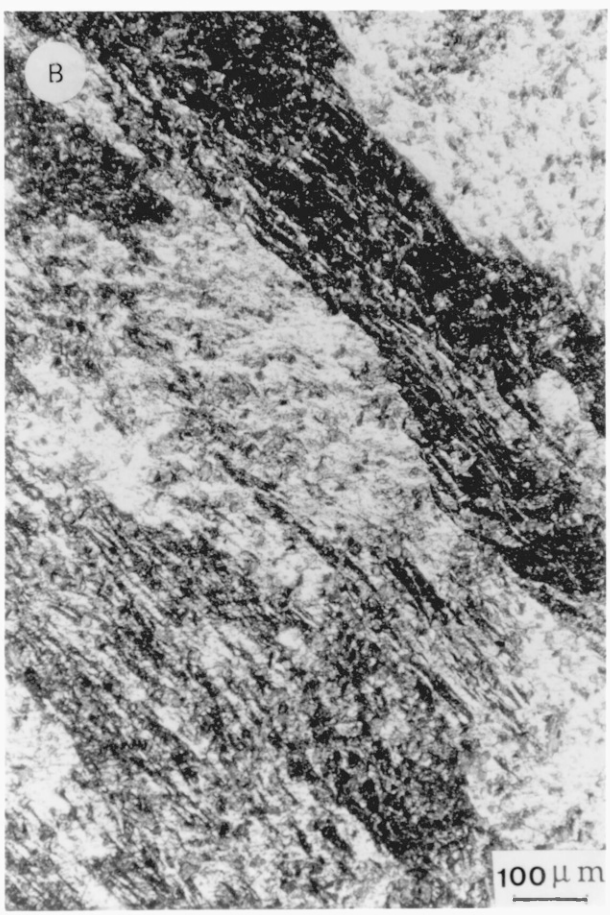
Fig. 3.6 TEM of the 2S/SiC composite after 50 % hot rolling and annealing at 500°C for one hour.

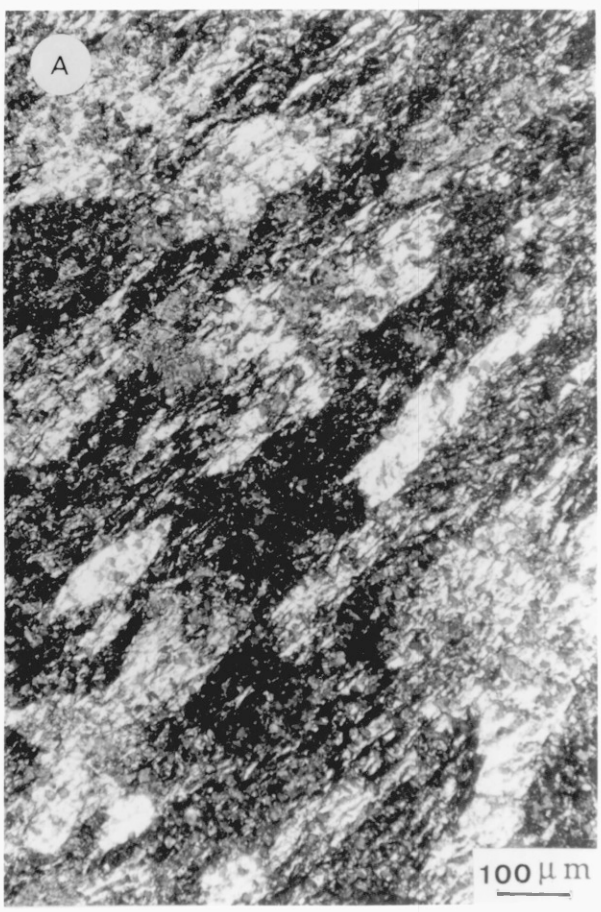
Fig. 3.7 TEM of the 2014/SiC composite after 50 % hot rolling and annealing at 500°C for one hour.

Fig. 3.22 Optical micrographs of the 2S/SiC composite after compression testing at room temperature at strain rates of (a) 5×10^{-4} and (b) 5×10^{-2} S^{-1}.


0.5 μm


0.5 μm


B
100 μm


A
100 μm

comprised of grains of about 120 μm size.

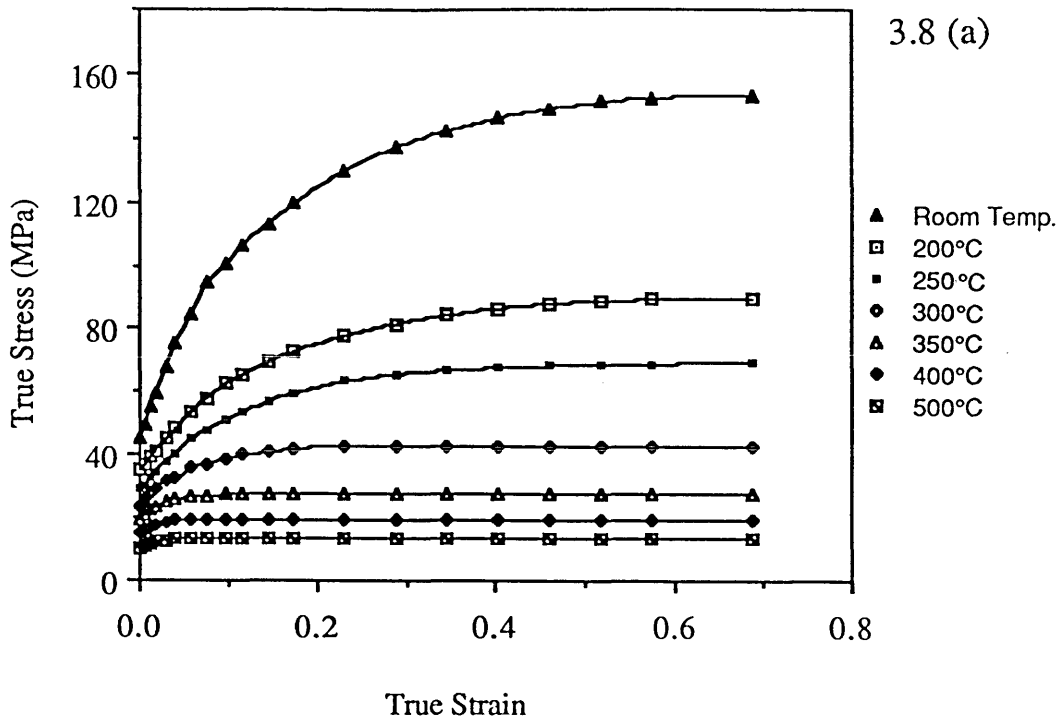
TEM observations of the 2S/SiC and 2014/SiC composites in the hot rolled and annealed state revealed a high dislocation density within the grain structure of the matrix (figs. 3.6 and 3.7). It showed a recrystallized grain structure with a superimposed quenched dislocation structure caused by the large mismatch in the thermal expansion coefficient between aluminium matrix and SiC particles during thermal processing. Quantitative measurements of dislocation density from the TEM micrographs was found to be of the order of 3×10^{14} m^{-2} and 7.5×10^{13} m^{-2} for the composites 2S/SiC and 2014/SiC respectively.

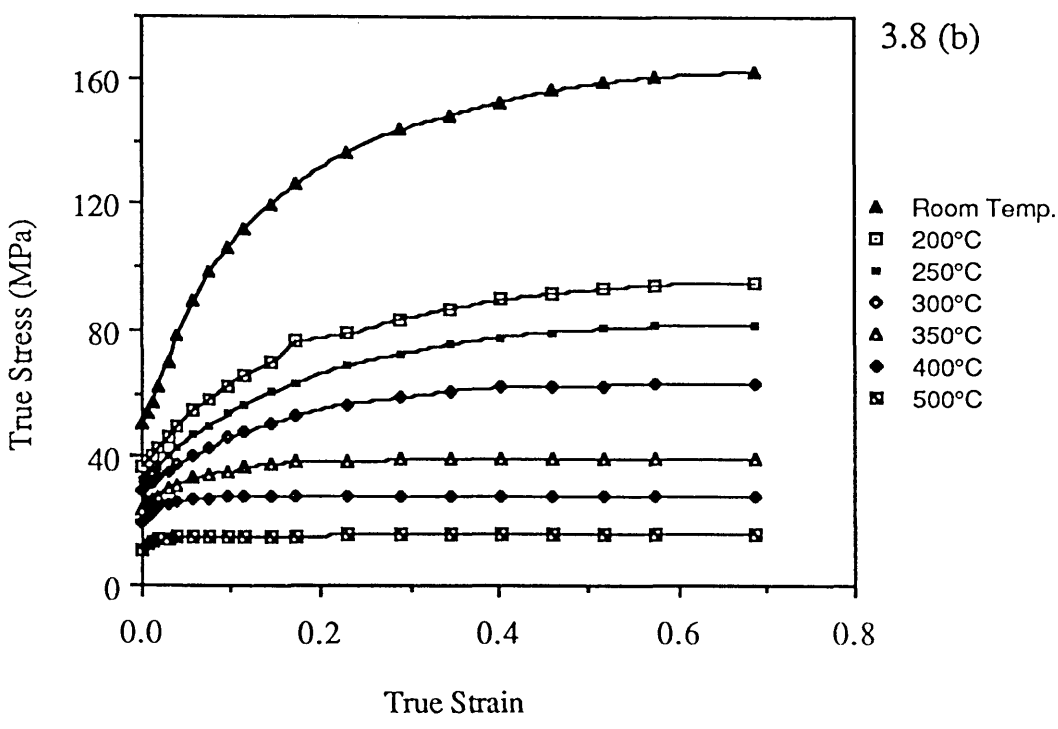
3.2 Stress Strain Behaviour of the Composites (2S/SiC and 2014/SiC).

True stress versus true strain curves for the compression tests which were conducted at nominal strain rates of 5×10^{-4} to 5×10^{-2} S^{-1} in a temperature range between room temperature and 500°C for the composite 2S/SiC and between 200 to 500°C for the composite 2014/SiC, are given in figs. 3.8 and 3.9 respectively. All the specimens were compressed to a strain of fifty percent (i.e. 0.7 true strain). The compression specimens were annealed at 500°C prior to testing.

At lower temperature, the curves are characterized by parabolic hardening but at higher temperatures, the curves exhibit work softening and a steady state is attained.

Variations in the yield stress, flow stress and work hardening rates of both materials as a function of temperature and strain rate are discussed in the following sections.


3.8 (a)
160
120
80
40
0
True Stress (MPa)
0.0
0.2
0.4
0.6
0.8
True Strain
Room Temp.
200°C
250°C
300°C
350°C
400°C
500°C


3.8 (b)
160
120
80
40
0
True Stress (MPa)
0.0
0.2
0.4
0.6
0.8
True Strain
Room Temp.
200°C
250°C
300°C
350°C
400°C
500°C

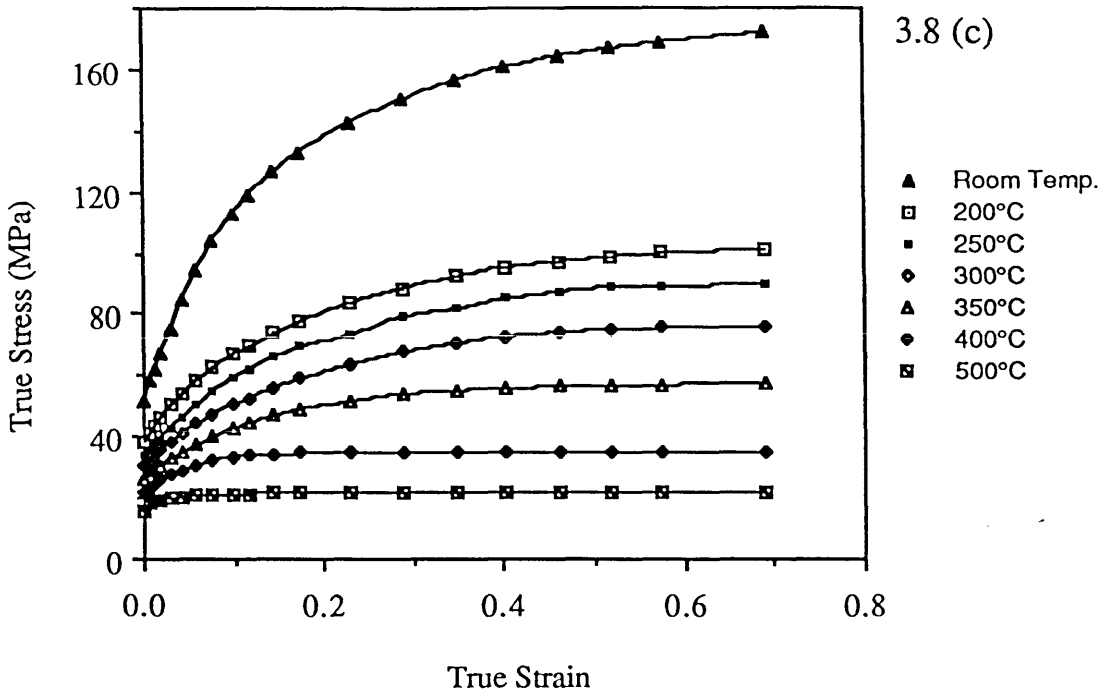
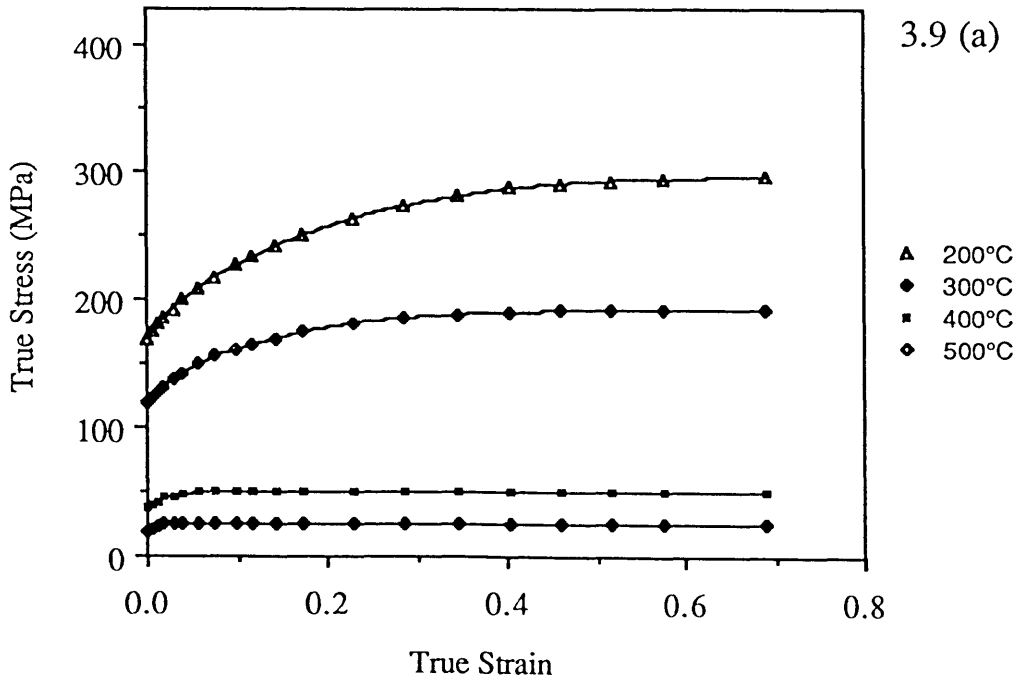
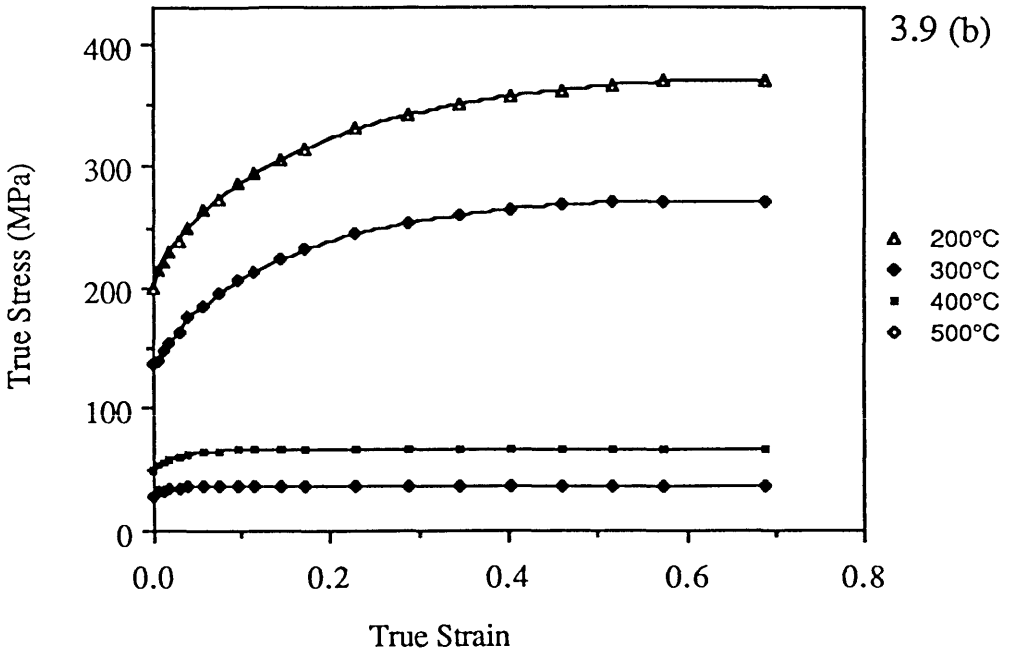


Fig. 3.8 True stress-strain curves of the 2S/SiC composite deformed in compression at temperatures between room temperature and 500°C at strain rates of (a) 5×10^{-4}, (b) 5×10^{-3}, and (c) 5×10^{-2} S^{-1}.





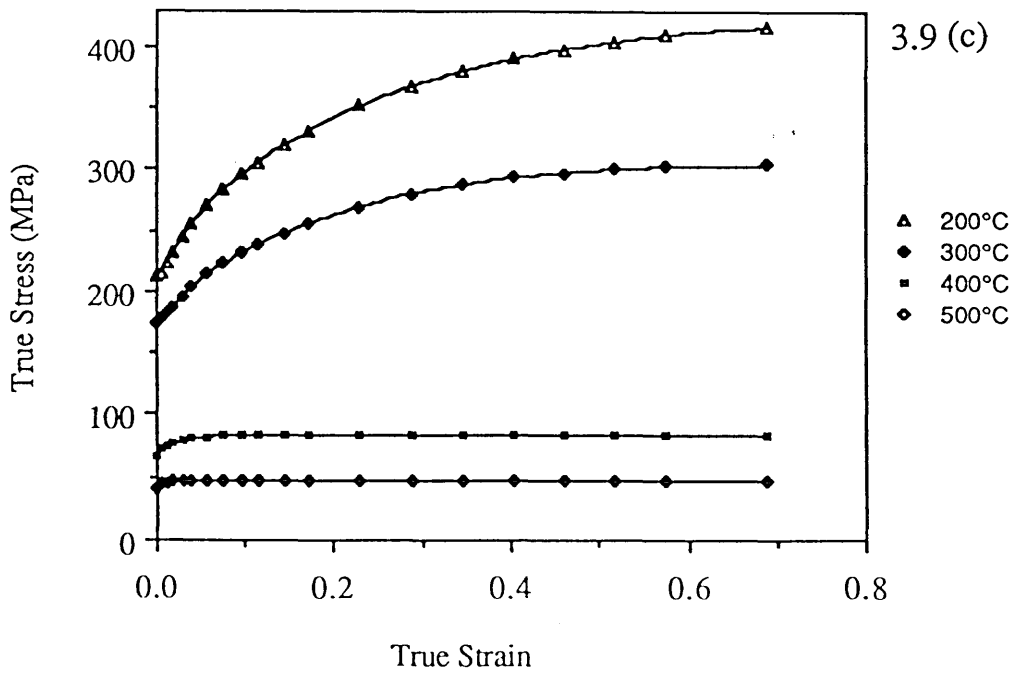


Fig. 3.9 True stress-strain curves of the 2014/SiC composite deformed in compression at temperatures between 200 and 500°C at strain rates of (a) 5×10^{-4}, (b) 5×10^{-3}, and (c) 5×10^{-2} S^{-1}.

3.2.1 Yield Stress as a Function of Temperature and Strain Rate.

Modulus corrected yield stress as a function of temperature is shown in fig. 3.10 and 3.11. For each strain rate, the modulus corrected yield stress remained relatively independent of temperature at lower temperatures but in the temperature range between 300 to 400°C for the composite 2S/SiC and also for 2014/SiC, depending on the strain rate, the yield stress of the composites exhibited strong temperature dependence. Following a rapid decline in the yield stress after this temperature range, there was again a steady linear decrease in the yield stress.

Variation in the yield stress as a function of strain rate is given in figs. 3.12 and 3.13 for the composites 2S/SiC and 2014/SiC. The yield stress of the composites decreased with decreasing strain rate at different temperature. The decrease in the yield stress was more significant at temperatures around 300°C.

3.2.2 Flow stress as a Function of Temperature and Strain Rate.

As illustrated in figs. 3.14 and 3.15, the log of flow stress values taken from the stress strain curves at fifty percent strain is given against the reciprocal of temperature. Figs. 3.14 and 3.15 illustrate the fall of flow stress on increasing temperature.

Figs. 3.16 and 3.17 show the log of flow stress as a function of strain rate. The values of stress exponent n, calculated from the fig. 3.16 for the composite 2S/SiC were calculated to be ≈ 14.5 at temperatures below 350°C, 6.5 above this temperature. Similarly the stress exponent calculated from fig. 3.17 for the composite 2014/SiC was ≈ 11.0 and 6.8 at

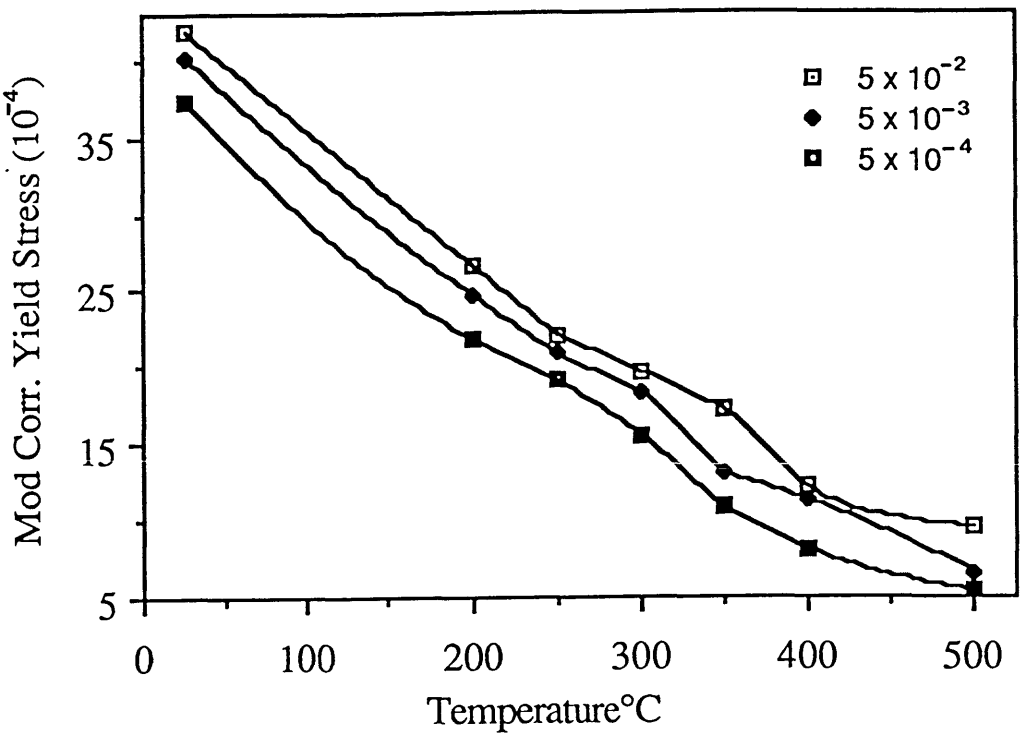


Fig. 3.10 Modulus corrected yield stress of the 2S/SiC composite as a function of temperature after compression testing at different strain rates.

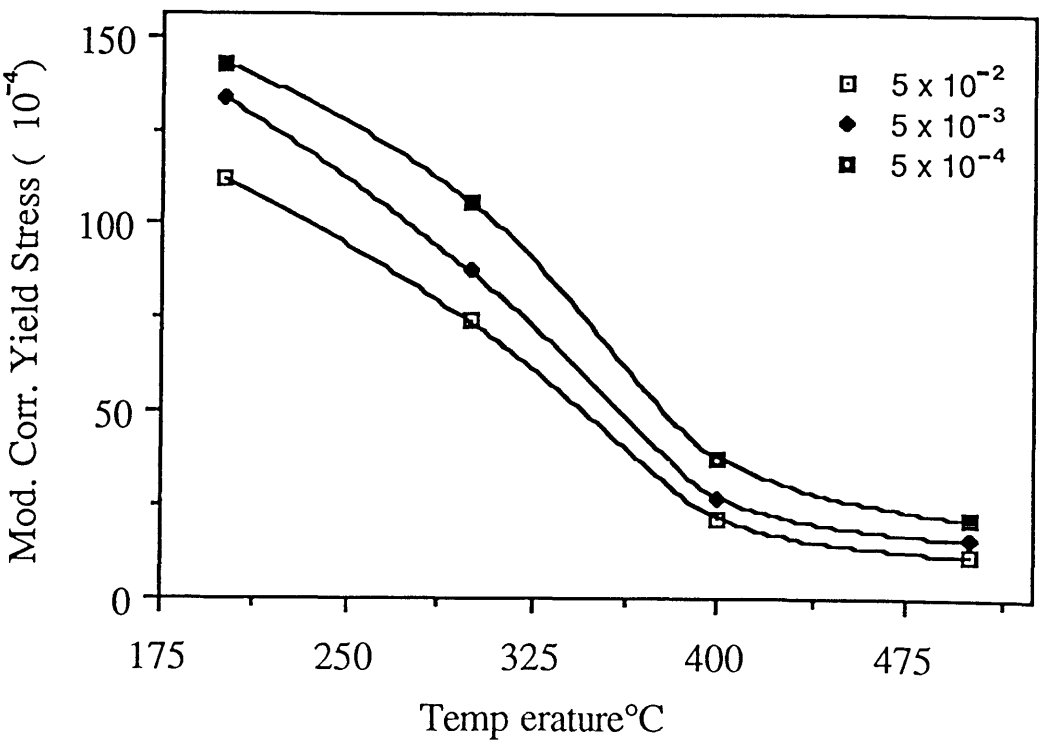


Fig. 3.11 Modulus corrected yield stress of the 2014/SiC composite as a function of temperature after compression testing at different strain rates.

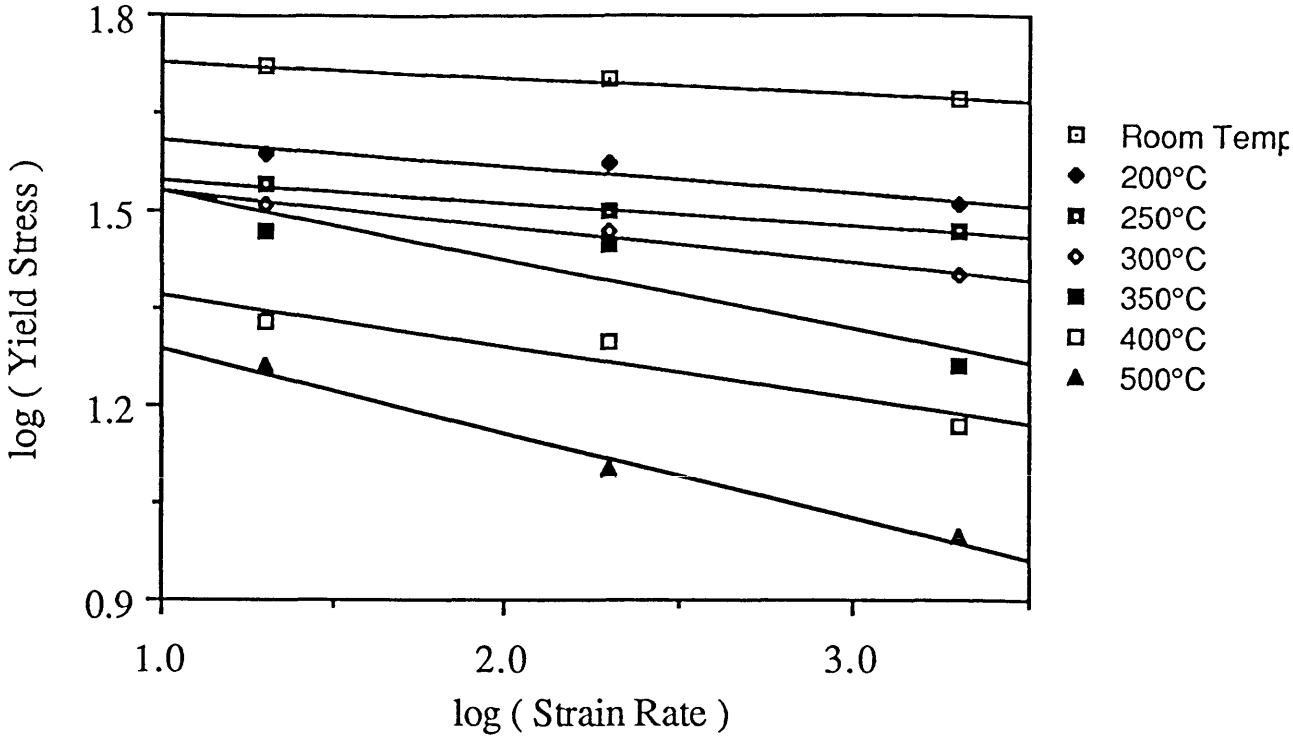


Fig. 3.12 Yield stress of the 2S/SiC composite as a function of strain rate after compression testing at different temperatures.

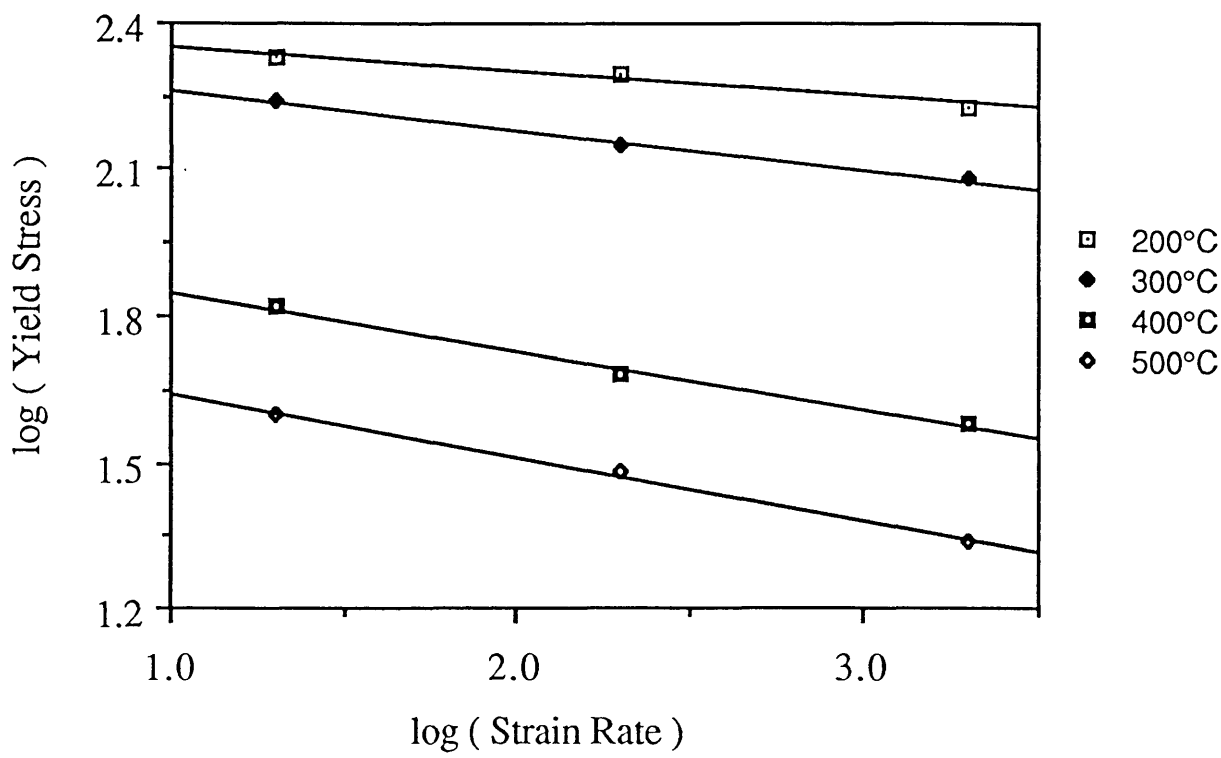


Fig. 3.13 Yield stress of the 2014/SiC composite as a function of strain rate after compression testing at different temperatures.

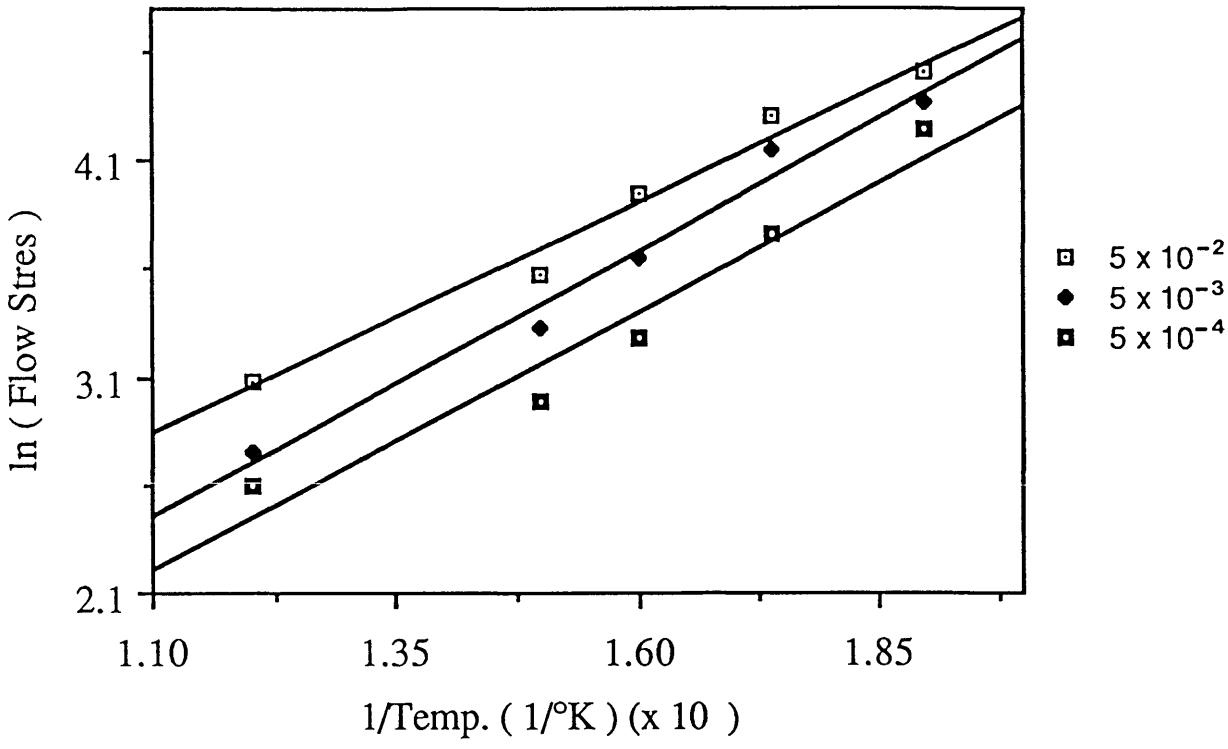


Fig. 3.14 Flow stress of the 2S/SiC composite as a function of reciprocal of temperature after compression testing at different strain rates.

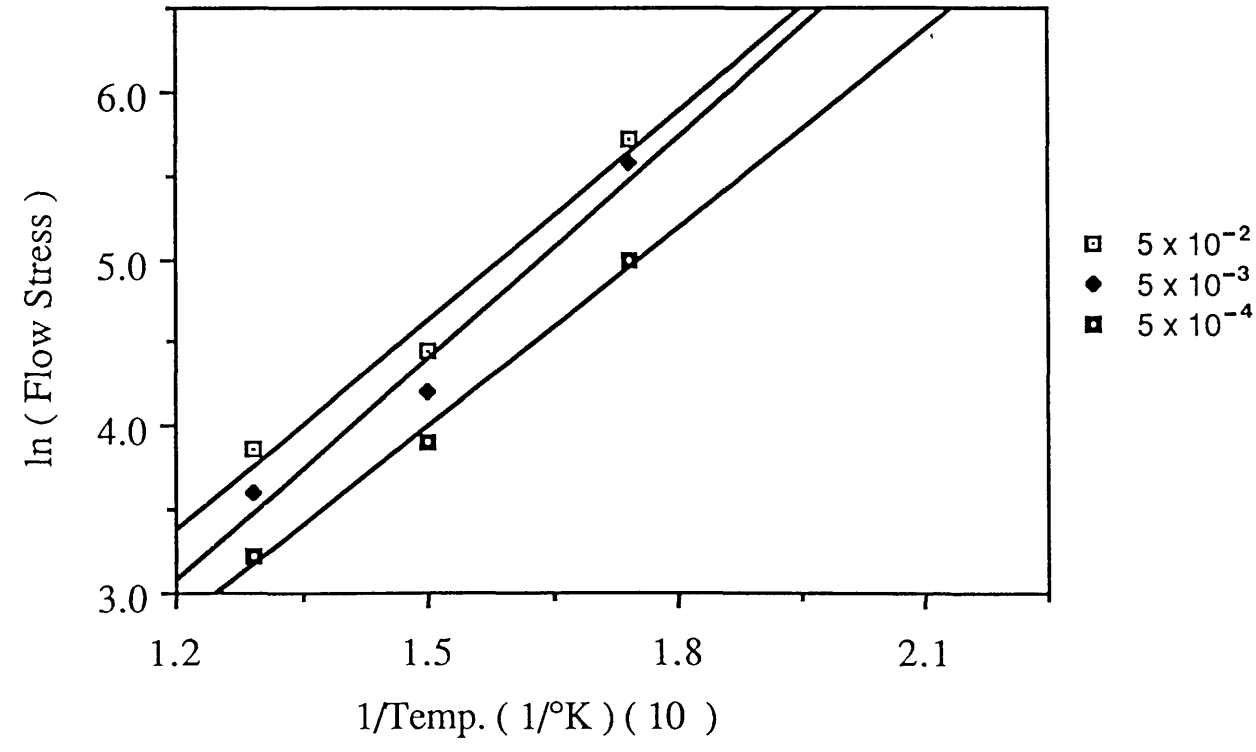


Fig. 3.15 Flow stress of the 2014/SiC composite as a function of reciprocal of temperature after compression testing at different strain rates.

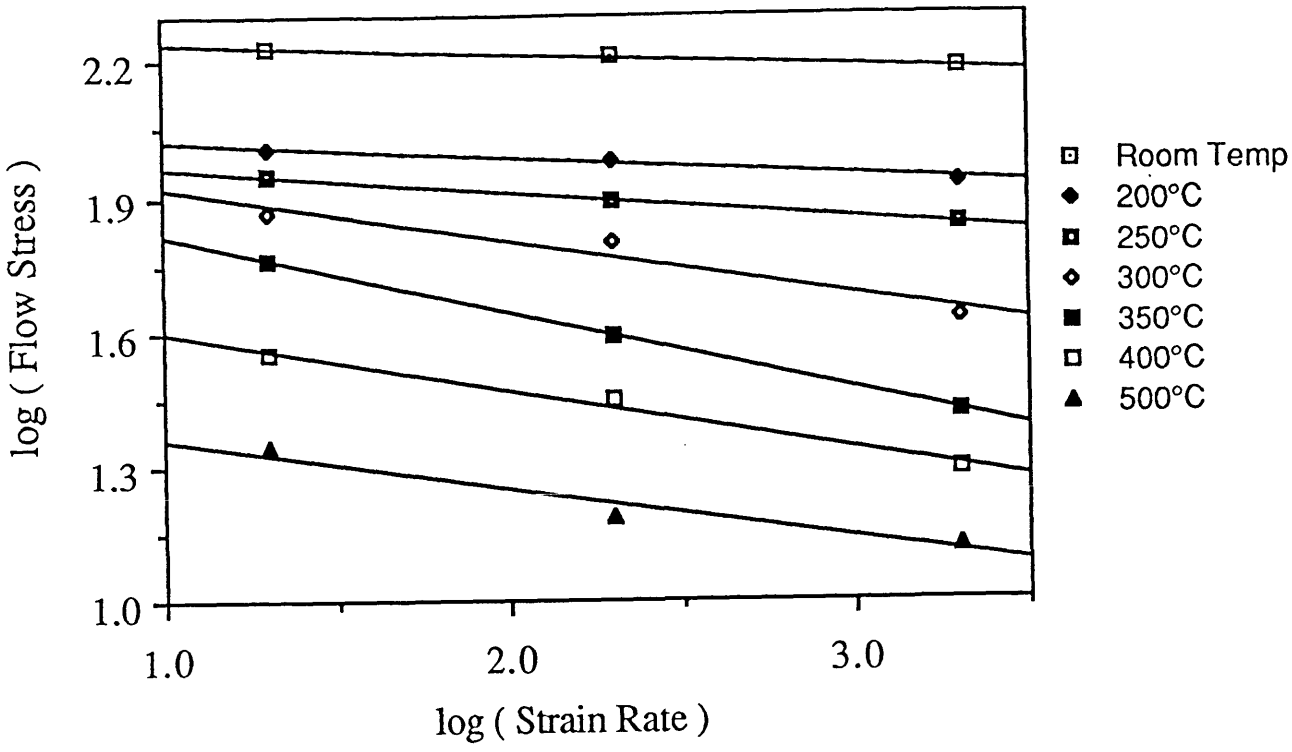


Fig. 3.16 Flow stress of the 2S/SiC composite as a function of strain rates after compression testing at different temperatures.

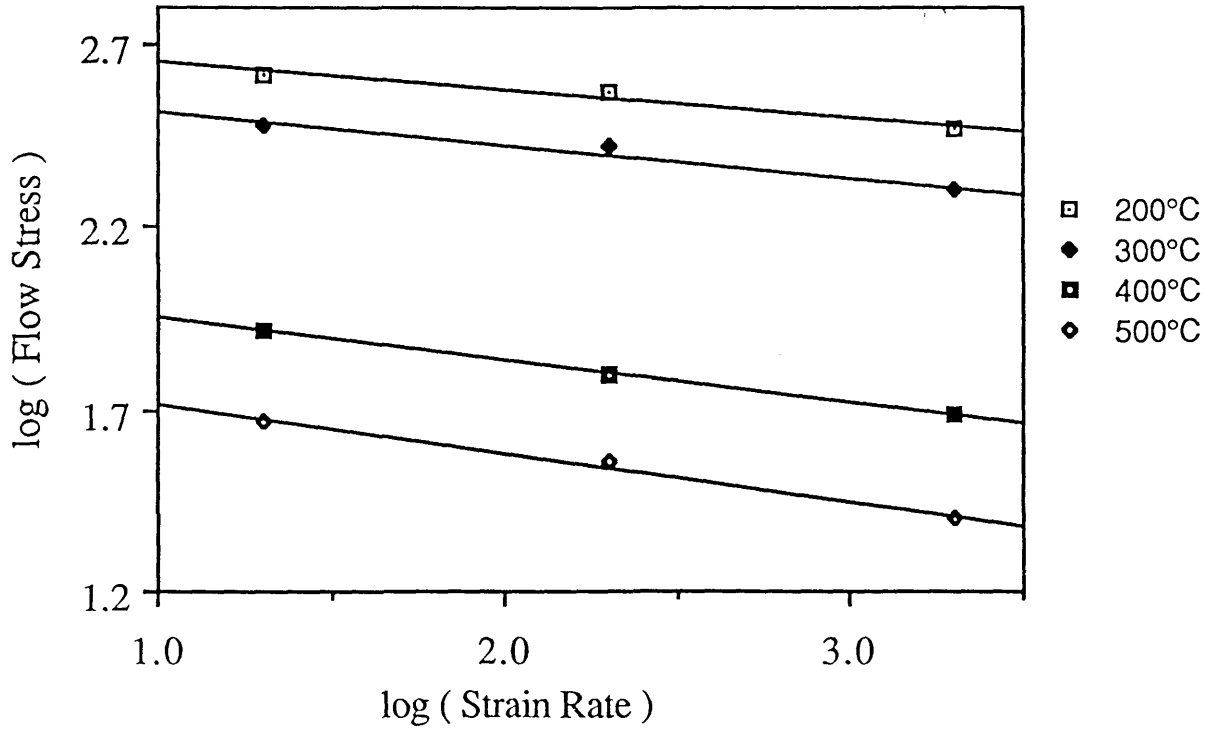


Fig. 3.17 Flow stress of the 2014/SiC composite as a function of strain rates after compression testing at different temperatures.

temperatures below and above 350°C. The flow stress-strain rate-temperature data calculated for each composite was fitted to the usual empirical relationship of the form to calculate the activation energy.

$$\varepsilon^{\circ} = A\,\sigma^{n} \exp(-Q / R T)$$

where A is a constant, Q is activation energy (k J $mole^{-1}$), and R, T have their usual meaning.

The values of activation energy, Q, was determined by using the higher temperature exponent values. The activation energy was calculated to be 148.4 kJ $mole^{-1}$ for the composite 2S/SiC and 154 kJ $mole^{-1}$ for the composite 2014/SiC.

3.2.3 Work Hardening Rate as a Function of Temperature and Strain Rate.

Figs. 3.18 and 3.19 show the work hardening rate as a function of temperature at initial strains ($0.02 \leq \varepsilon \leq 0.04$) in a rapid hardening region for the composites 2S/SiC and 2014/SiC. The curves were comprised of three portions. The first and third portion of the curves were less temperature sensitive whereas the second part displayed a significant drop in the curve and was the most temperature sensitive region. The fall was at a temperature approaching 300°C for the specimens deformed at a strain rate of 5×10^{-4} S^{-1}. The curve appearsshifted to higher temperatures as the strain rate was increased and hence for the highest strain rate of 5×10^{-2} S^{-1}, the drop was observed near 400°C.

Initial work hardening rate against strain rate is shown in figs. 3.20 and 3.21 for the composites 2S/SiC and 2014/SiC respectively. The curves indicated a greater rate of hardening at the same temperatures for the higher strain rates. The curves at higher and lower temperatures were

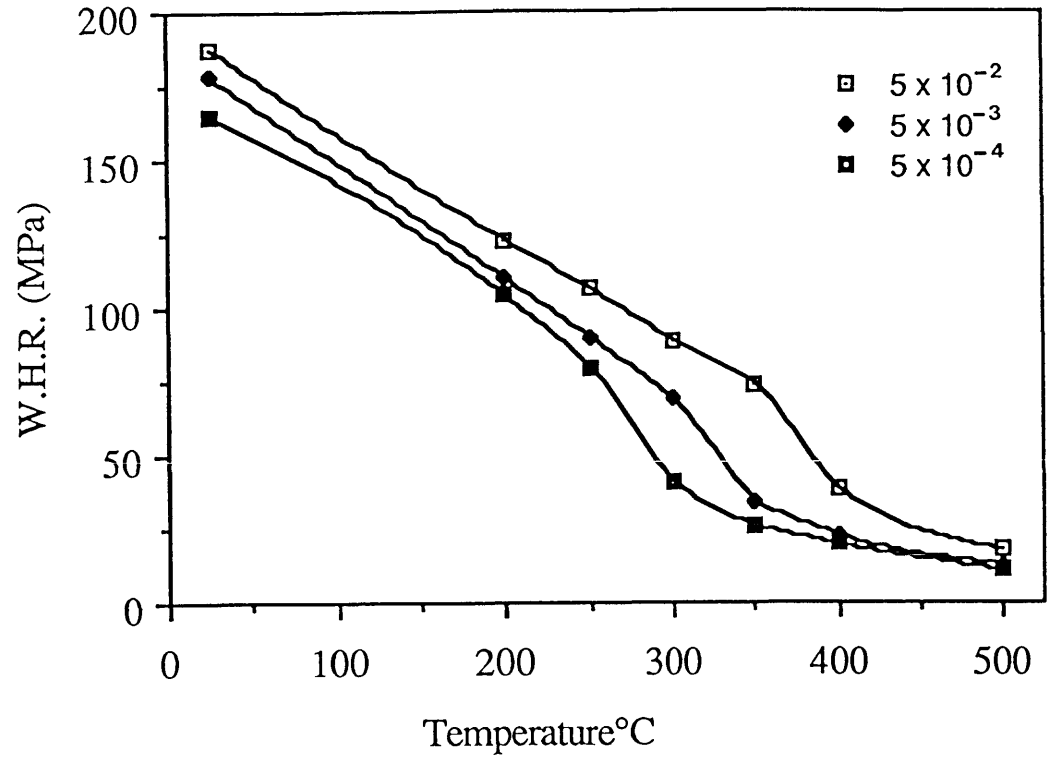


Fig. 3.18 Initial work hardening rates of the 2S/SiC composite as a function of temperature after compression testing at different strain rates.

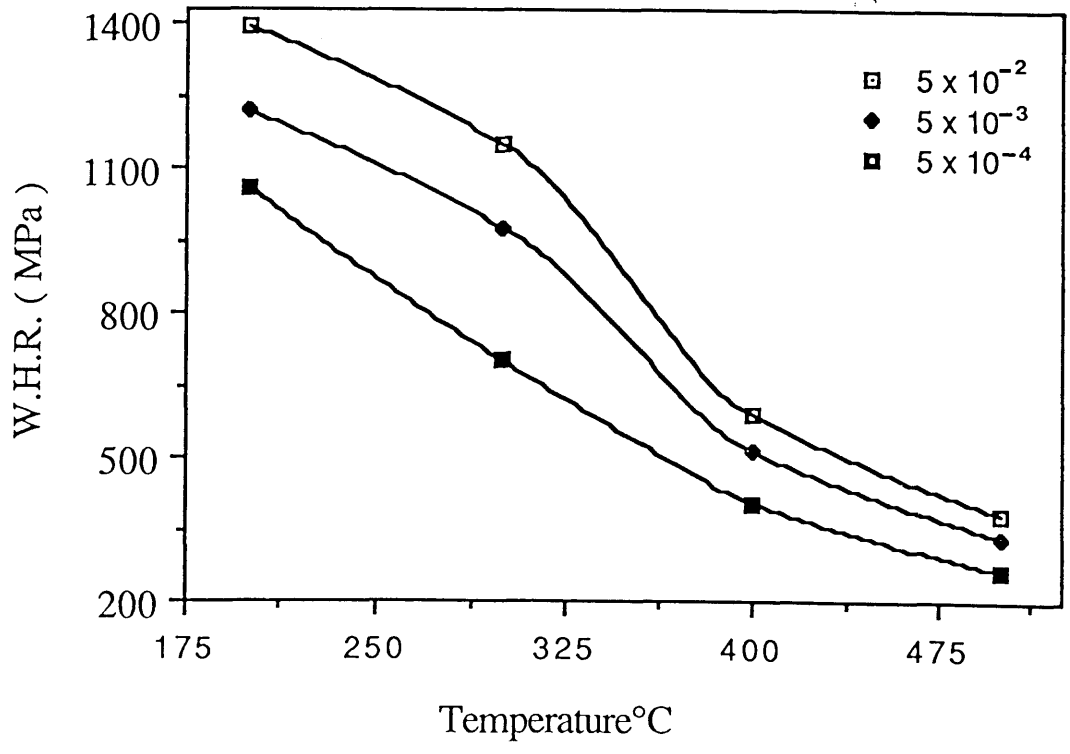


Fig. 3.19 Initial work hardening rates of the 2014/SiC composite as a function of temperature after compression testing at different strain rates.

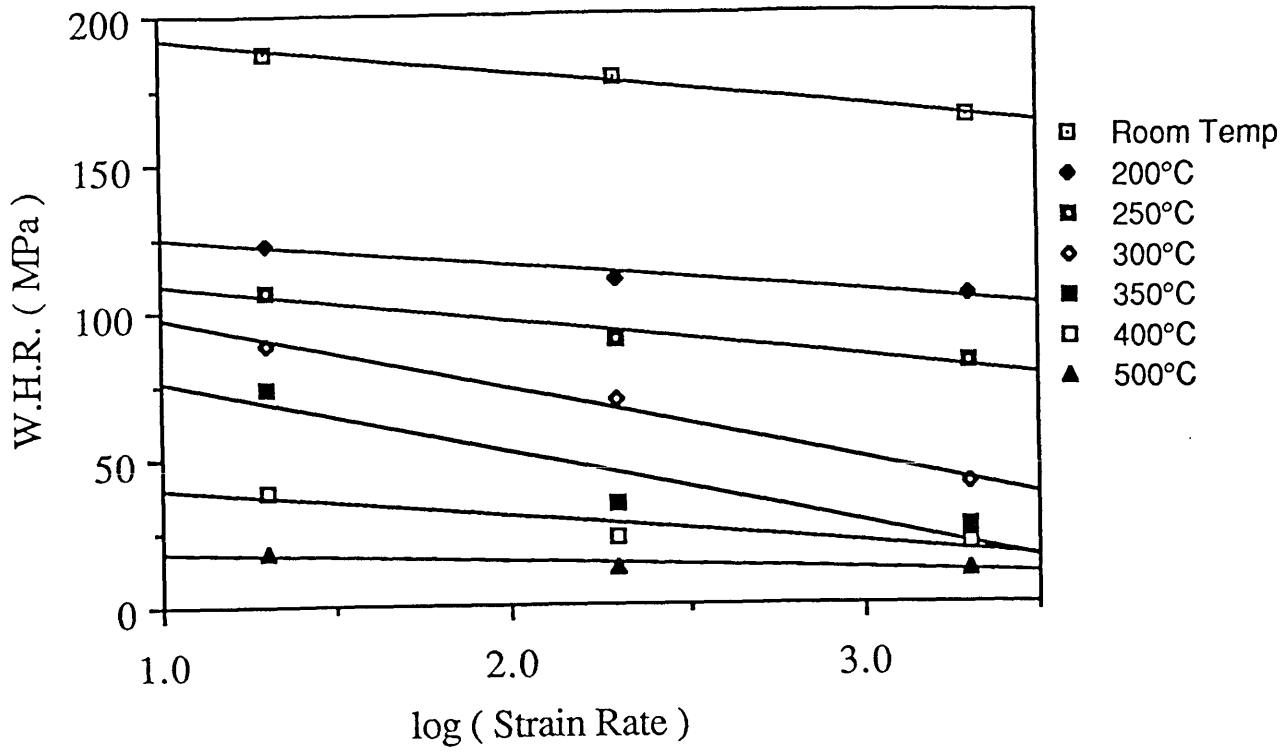


Fig. 3.20 Initial work hardening rates of the 2S/SiC composite as a function of strain rate after compression testing at different temperatures.

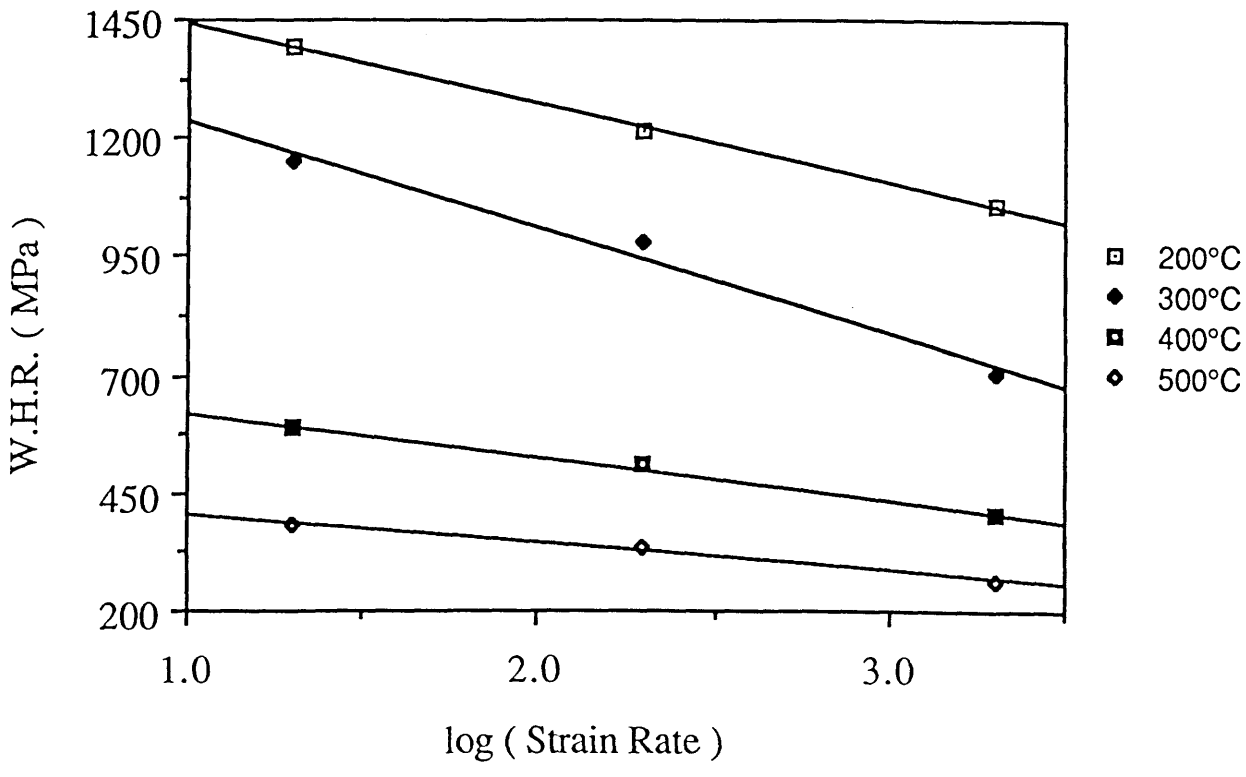


Fig. 3.21 Initial work hardening rates of the 2014/SiC composite as a function of strain rate after compression testing at different temperatures.

linear but the curves at intermediate temperatures such as between 250 to 350°C indicated sharp changes in this temperature range depending on strain rate.

3.3 Microstructural Studies of the Deformed Composites.

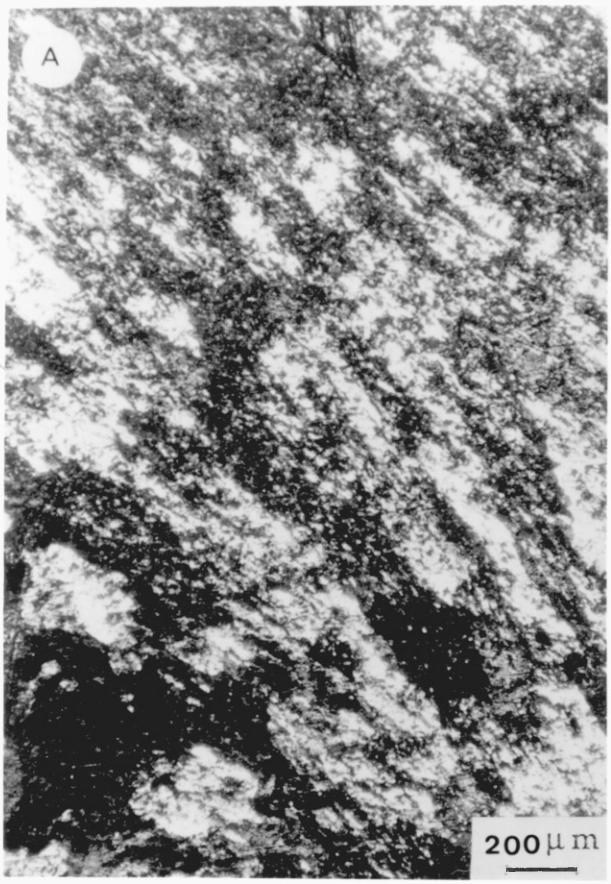
The microstructure of 2S/SiC and 2014/SiC composites prior to testing at various temperatures and strain rates, is shown in fig. 3.4 to 3.7 respectively in the optical and transmission electron micrographs.

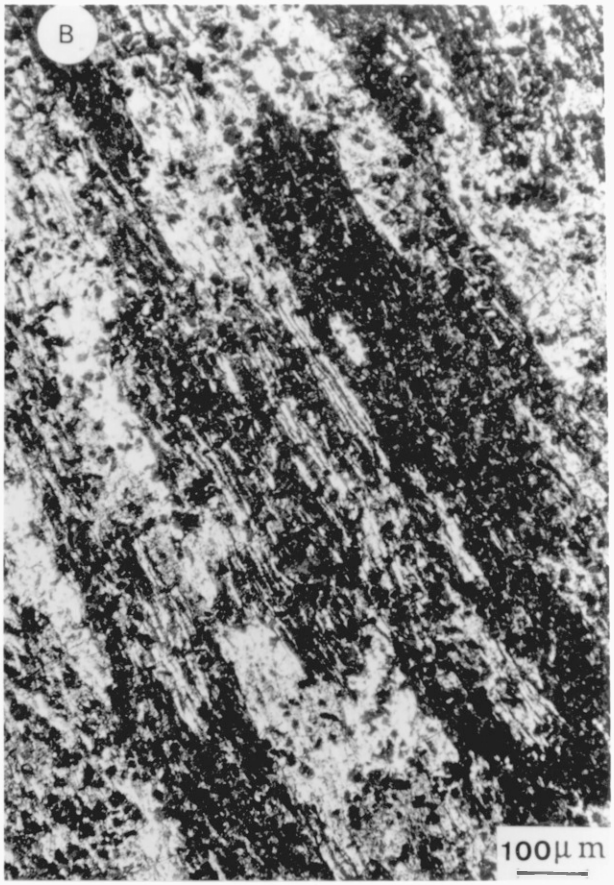
3.3.1 Optical Microscopy of 2S/SiC Composite Deformed in Compression.

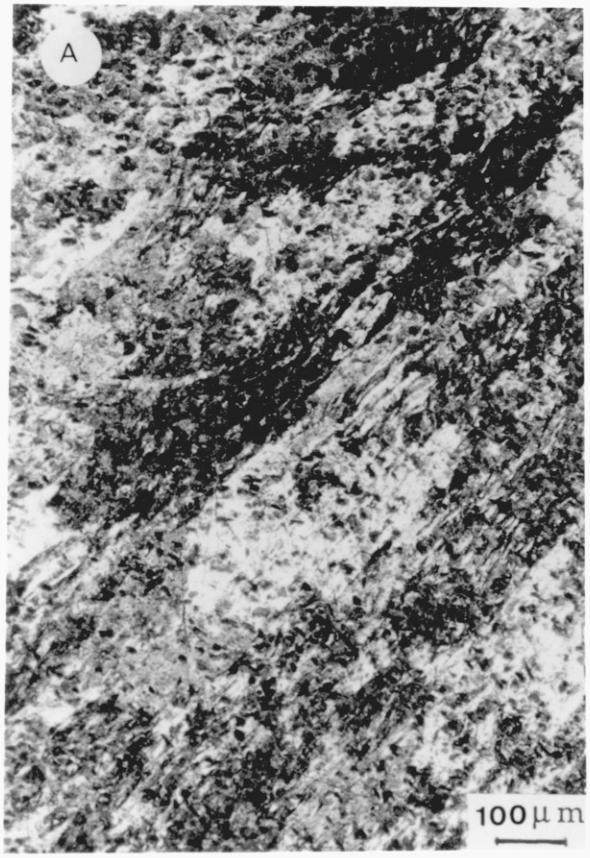
The composite specimens deformed between room temperature and 500°C displayed a deformed structure consisting of elongated grains aligned normal to the deformation direction (figs 3.22 to 3.26) with an average aspect ratio of about 3.5. The microstructure displayed fine deformation sub-grain banding in most of the grains in the specimens deformed at lower temperatures (figs. 3.22 to 3.24). Bands were visible up to 350°C in the specimens deformed at the lowest strain rate and up to 400°C in the specimens deformed at the highest strain rate. The banded structure grew coarser as the deformation temperature increased. However, in the specimensdeformed at or above 400°C at 5 x 10^{-4} and at 500°C at 5 x 10^{-2}, the structures were found to be different compared to that of specimens deformed below these temperatures. At 500°C, the microstructure had elongated grains with wavy boundaries, similar to those observed in

Fig. 3.23 Optical micrographs of the 2S/SiC composite after compression testing at 200°C at strain rates of (a) 5×10^{-2} and (b) 5×10^{-4} S^{-1}.

Fig. 3.24 Optical micrographs of the 2S/SiC composite after compression testing at 300°C at strain rates of (a) 5×10^{-2} and (b) 5×10^{-4} S^{-1}.


A
200 μ m


B
100 μ m


A
100 μ m

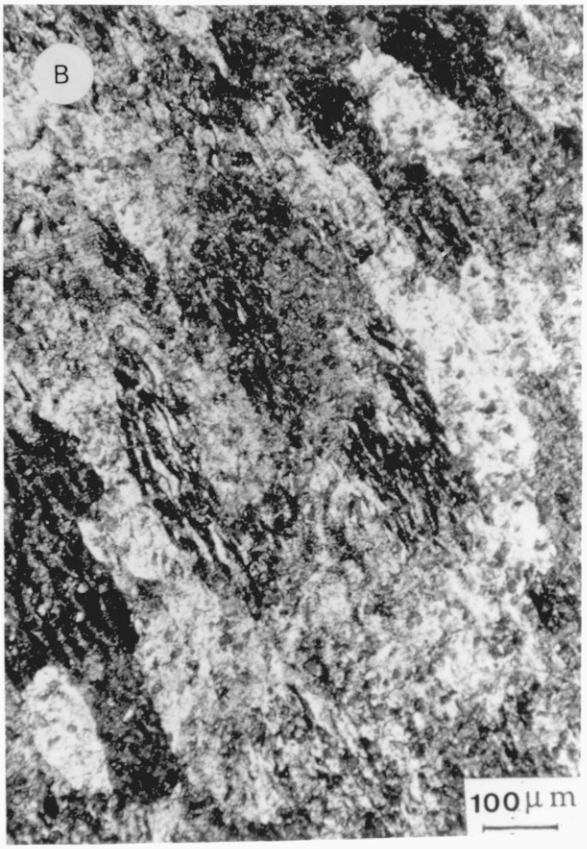
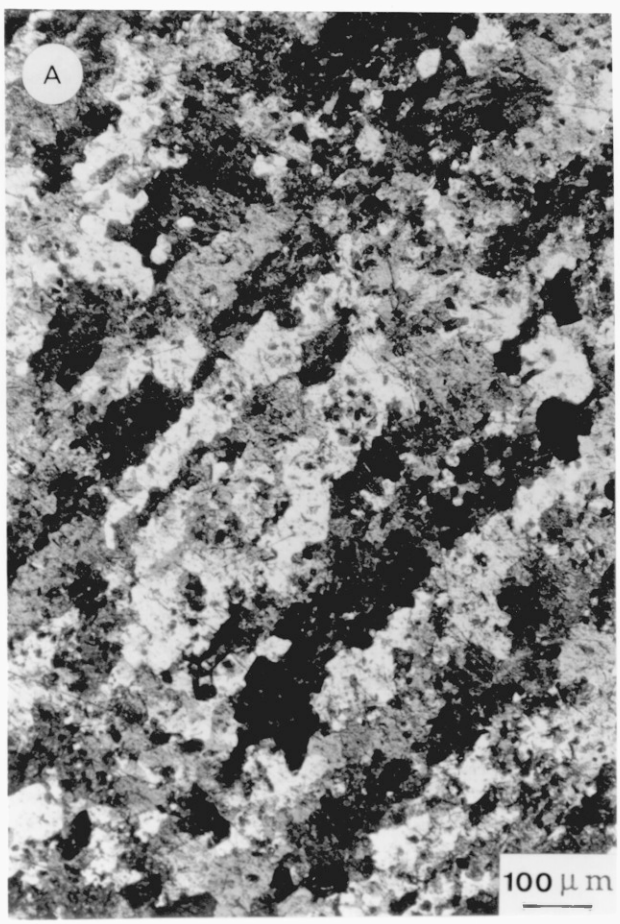

B
100 μ m

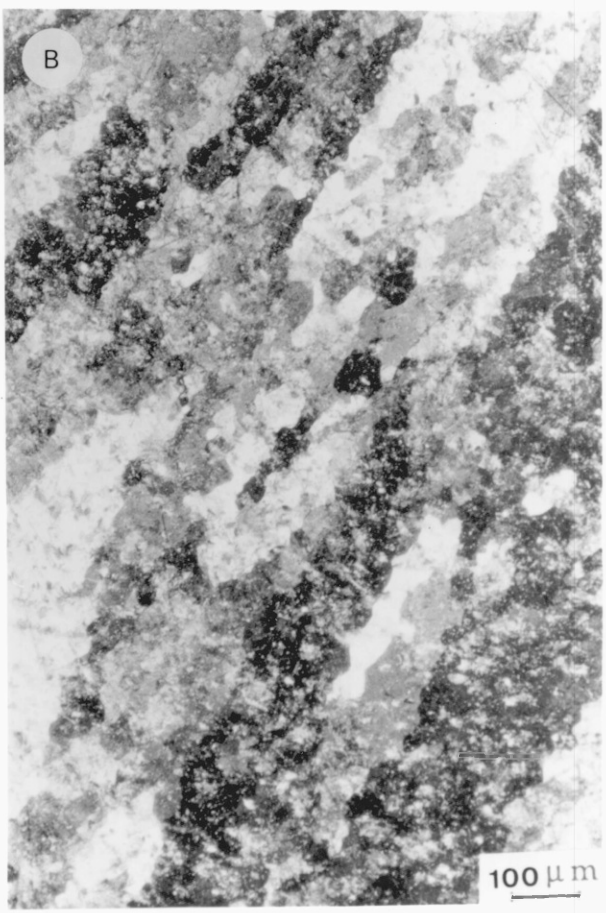
Fig. 3.25 Optical micrographs of the 2S/SiC composite after compression testing at 400°C at strain rates of (a) 5×10^{-2} and (b) 5×10^{-4} S^{-1}.

Fig. 3.26 Optical micrographs of the 2S/SiC composite after compression testing at 500°C at strain rates of (a) 5×10^{-2} and (b) 5×10^{-4} S^{-1}.


A
100 μ m


B
100 μ m


A
100 μ m


B
100 μ m

aluminium deformed at elevated temperatures (fig. 3.26). This effect was more pronounced in the specimen deformed at the slowest strain rate. A few small equiaxed grains were revealed in the optical microscopy of the specimen deformed at 500°C along with irregular elongated grains having serrated boundaries.

3.3.2 T.E.M. of 2S/SiC Composite Deformed in Compression.

Figs. 3.27 to 3.31 are a series of transmission electron micrographs showing microstructural development during different stages of deformation in the specimens deformed at temperatures between room temperature and 500°C at various strain rates.

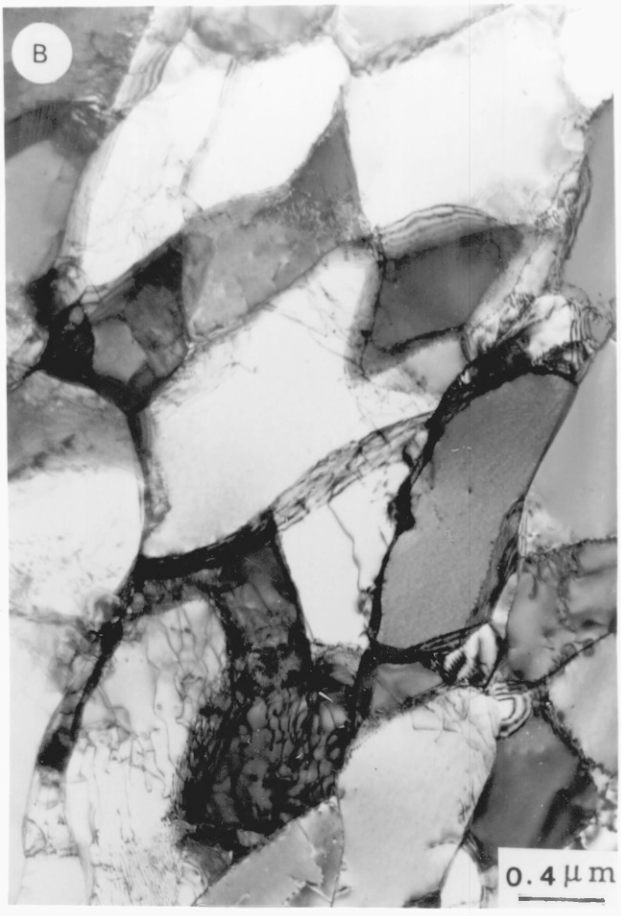
T.E.M. of the specimen deformed at room temperature revealed a dynamically recovered dislocation sub-structure which had a distinct cellular character with a high density of dislocations at the cell walls but with some free dislocations also within the sub-grains.The sub-grain boundaries become more sharply defined as the deformation temperature increased, as can be seen in fig. 3.27 to 3.29 for the specimensdeformed at 200 to 300°C.

A coarser sub-grain structure was found in the specimens deformed at 400 and 500°C (fig. 3.30 and 3.31). At these elevated temperatures, the dislocations as well as the sub-grain structure produced was associated with the dislocations generated from the SiC particles into the matrix due to the C.T.E. mismatch. At 500°C, a fine though not very distinct cell structure was observed in the matrix (fig. 3.31). The deformed grains exhibited well defined boundaries but the sub-grains had ill-defined boundaries.

Fig. 3.27 TEM of the 2S/SiC composite after compression testing at room temperature at strain rates of (a) 5×10^{-4} and (b) 5×10^{-2} S^{-1}.

Fig. 3.28 TEM of the 2S/SiC composite after compression testing at 200°C at strain rates of (a) 5×10^{-4} and (b) 5×10^{-2} S^{-1}.


A
1.0 μm

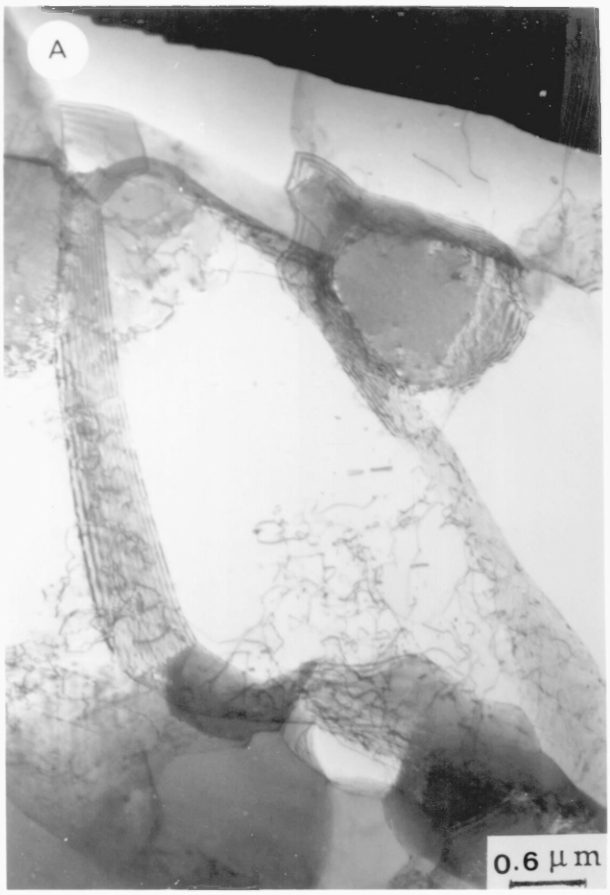

B
0.4 μm

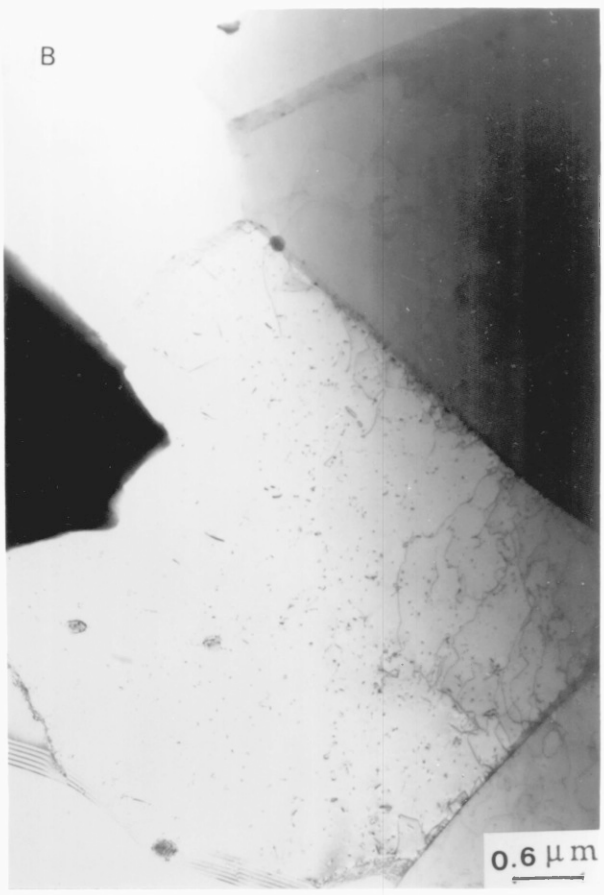

B
0.4 μm

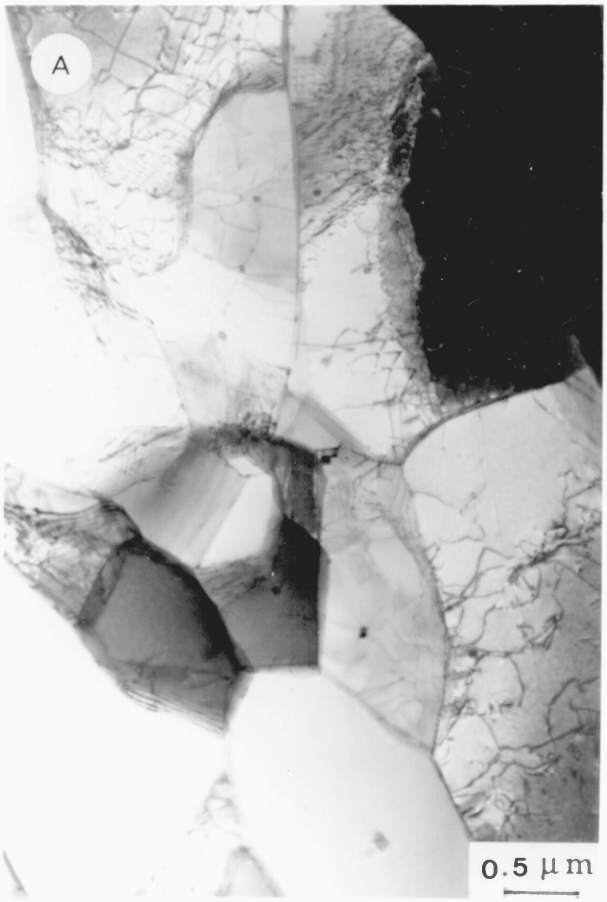

A
0.6 μm

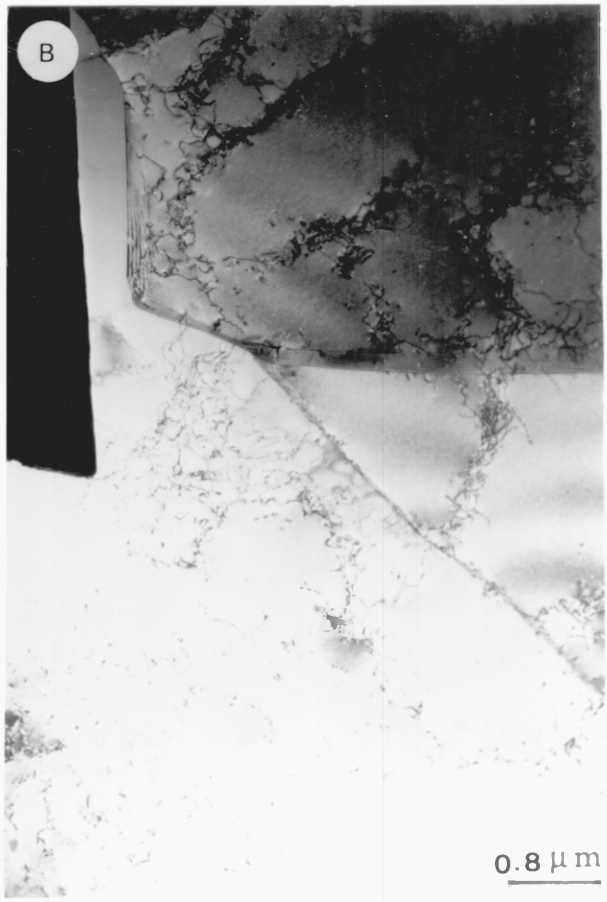
Fig. 3.29 TEM of the 2S/SiC composite after compression testing at 300°C at strain rates of (a) 5×10^{-4} and (b) 5×10^{-2} S^{-1}.

Fig. 3.30 TEM of the 2S/SiC composite after compression testing at 400°C at strain rates of (a) 5×10^{-4} and (b) 5×10^{-2} S^{-1}.


A
0.6 μm


B
0.6 μm


A
0.5 μm


B
0.8 μm

The average sub-grain size measured in specimens deformed between room temperature and 500°C at different strain rates is given in the table 3.1.

It is clear from the table that the sub-grains became larger as the deformation temperature increased.

3.3.3 Optical Microscopy of 2014/SiC Composite Deformed in Compression.

Figs. 3.32 to 3.35 show optical micrographs for 2014/SiC composite deformed at temperatures between 200 and 500°C at different strain rates.

The optical micrographs revealed elongated grains of a size around 100 μm. There were also grains observable in the microstructure which had an aspect ratio approaching unity. The starting material had structure with grains elongated parallel to the compression axis (fig. 3.4). Deforming these elongated grains in the opposite direction resulted in a more or less equiaxed grain structure (figs. 3.32 - 3.35).

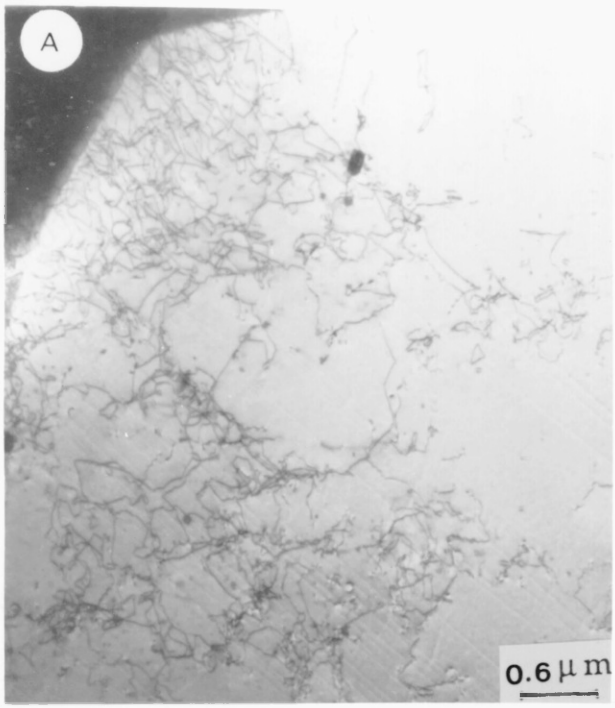
3.3.4 T.E.M. of 2014/SiC Composite Deformed in Compression.

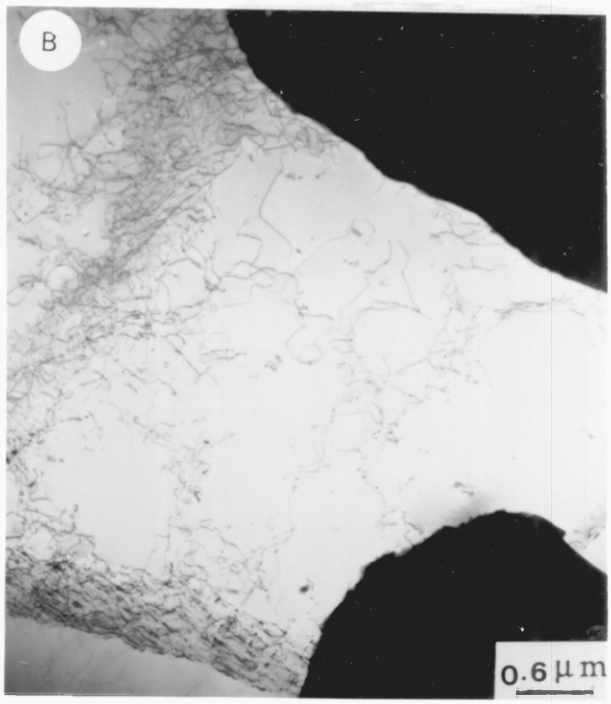
Microstructure of the specimen deformed at 200°C showed a mesh of high dislocation density distributed throughout the matrix (fig. 3.36). Very small precipitates appeared at this temperature which were uniformly dispersed and were effective in pinning dislocations and hence suppressing dynamic recovery. As a result, a structure without clear indication of sub-grain formation is produced.

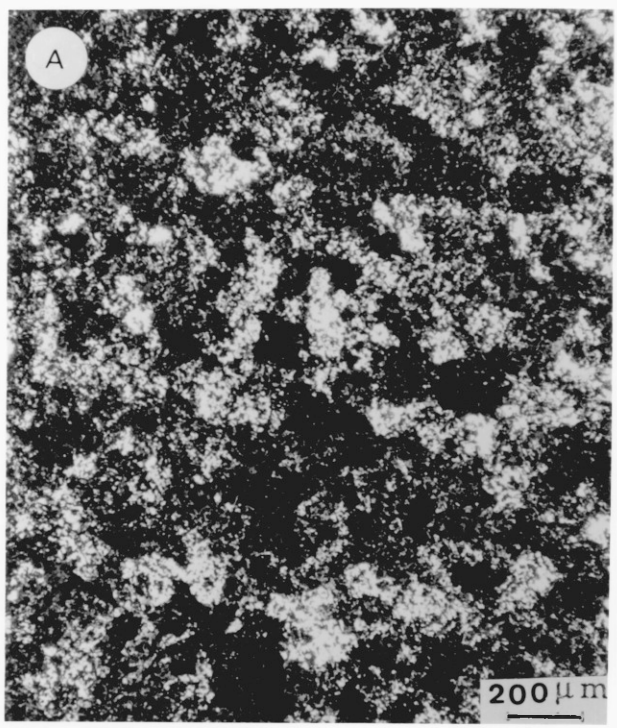
Fig. 3.31 TEM of the 2S/SiC composite after compression testing at 500°C at strain rates of (a) 5×10^{-4} and (b) 5×10^{-2} S^{-1}.

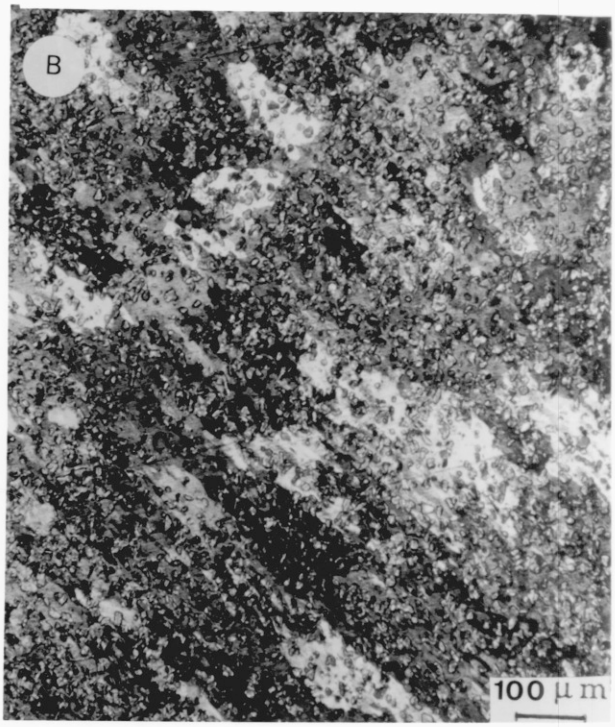
Fig. 3.32 Optical micrographs of the 2014/SiC composite after compression testing at 200°C at strain rates of (a) 5×10^{-4} and (b) 5×10^{-2} S^{-1}.

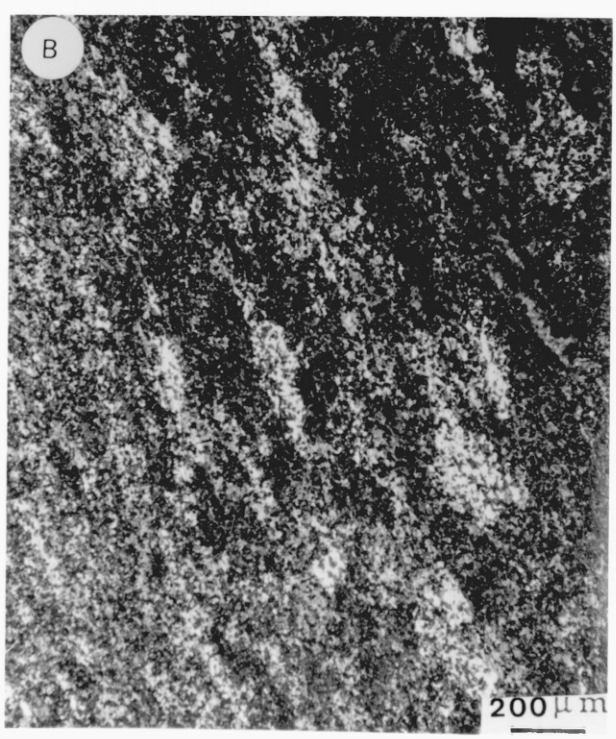
Fig. 3.33 Optical micrographs of the 2014/SiC composite after compression testing at 300°C at strain rates of (a) 5×10^{-4} and (b) 5×10^{-2} S^{-1}.


A
0.6 μm


B
0.6 μm


A
200 μm


B
100 μm


B
200 μm

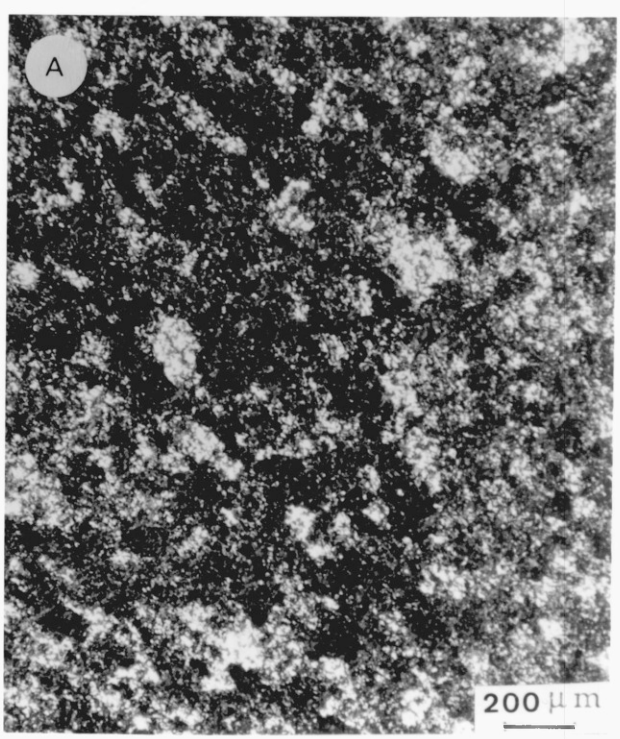
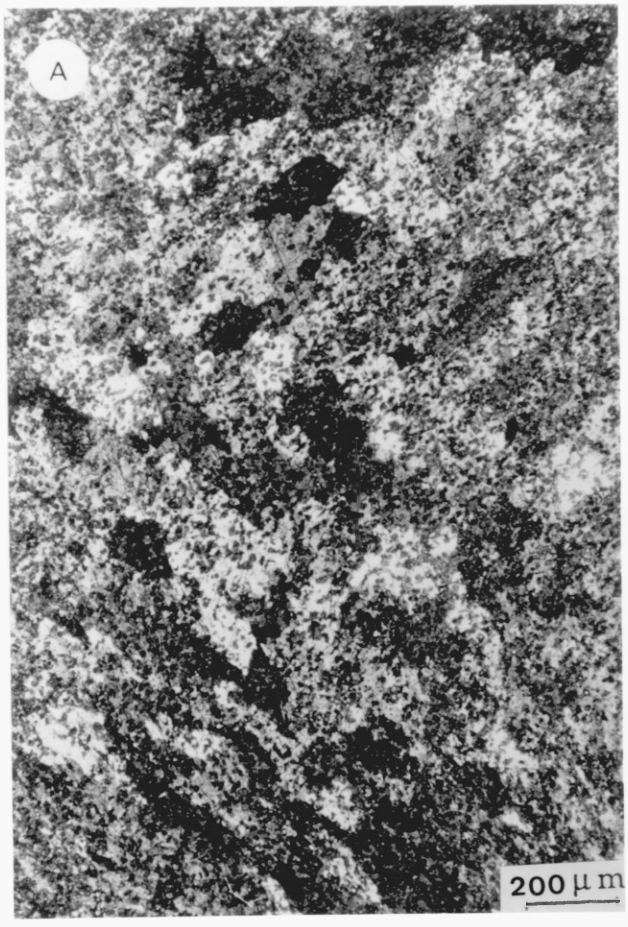
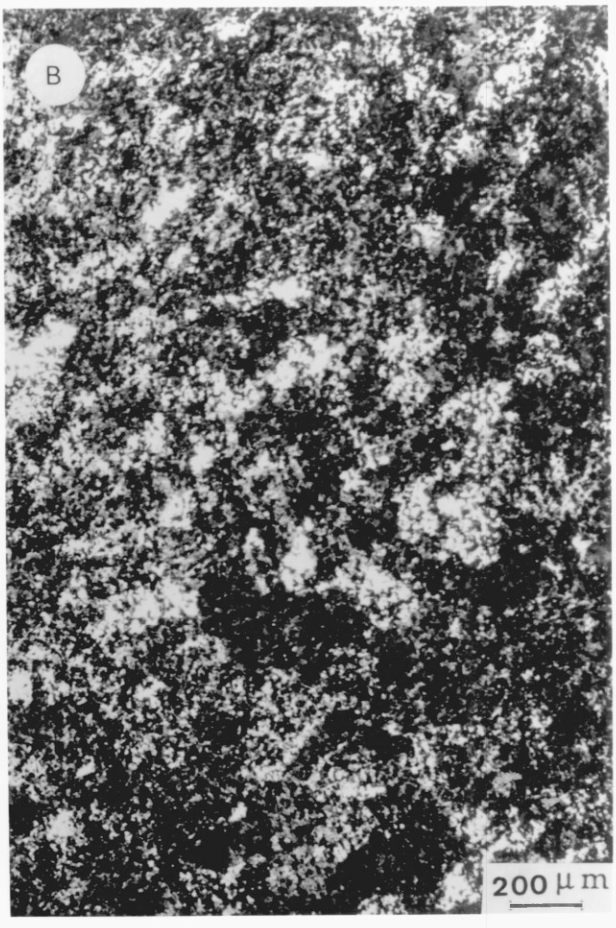
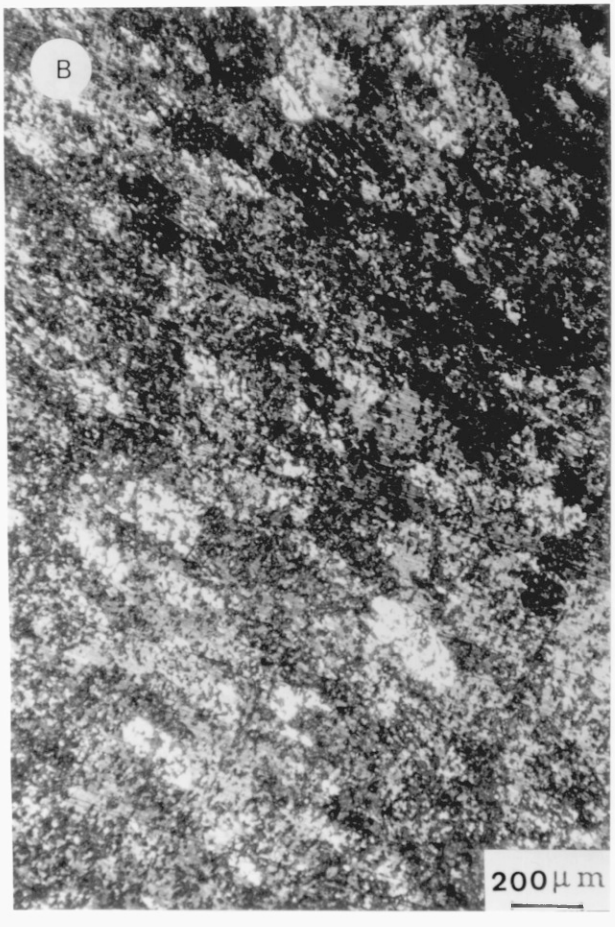

A
200 μm

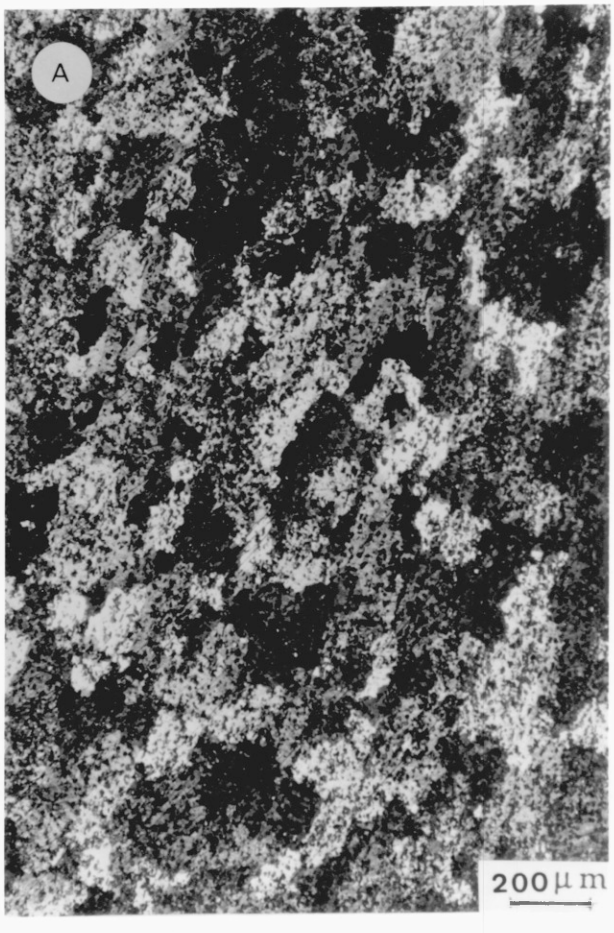
Fig. 3.34 Optical micrographs of the 2014/SiC composite after compression testing at 400°C at strain rates of (a) 5×10^{-4} and (b) 5×10^{-2} S^{-1}.

Fig. 3.35 Optical micrographs of the 2014/SiC composite after compression testing at 500°C at strain rates of (a) 5×10^{-4} and (b) 5×10^{-2} S^{-1}.


A
200 µm


B
200 µm


B
200 µm


A
200 µm

Upon increasing the deformation temperature to 300°C, there is evidence of recovery as sub-grains and sub-boundaries appear in preference to the randomly distributed dislocations. The specimen deformed at 300°C showed the first indications of a definite sub-grain structure (fig. 3.37). The sub-grain structure developed accompanied by coarsening of the precipitate size. The precipitates appeared to have an average size of 0.1 μm with some precipitates as large as about 1.0 μm. Sub-grain walls appeared to separate relatively dislocation free areas indicating that recovery had occurred.

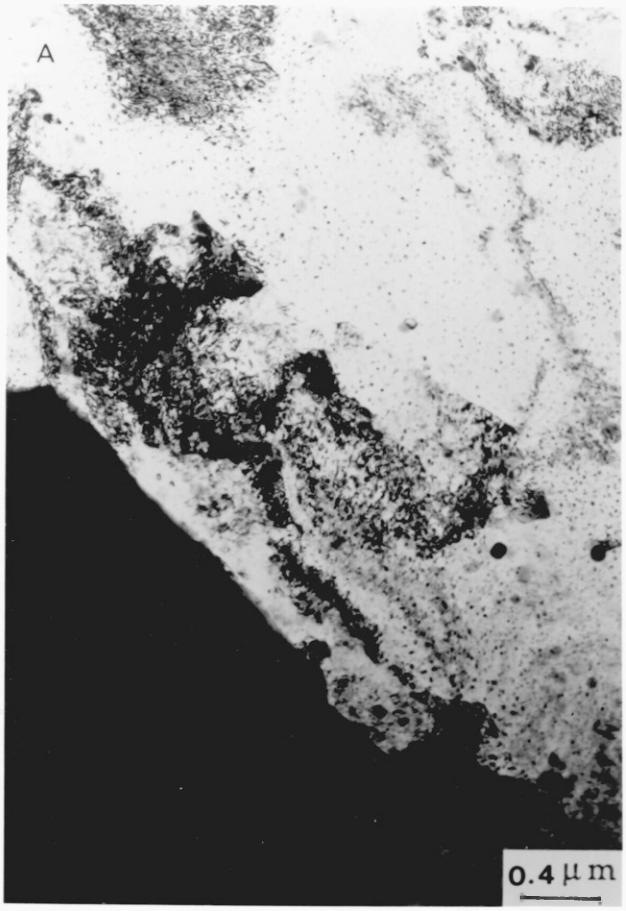
It is apparent from the figs. 3.38 to 3.39 for the specimens deformed at 400 and 500°C that as the deformation temperature increased, a distinct sub-grain structure began to form throughout the entire matrix. In the specimen deformed at 500°C, an extensive network consisting of tangled high density dislocations was observed within the grains (fig. 3.39), generated due to the C.T.E. mismatch during quenching from the high temperature.

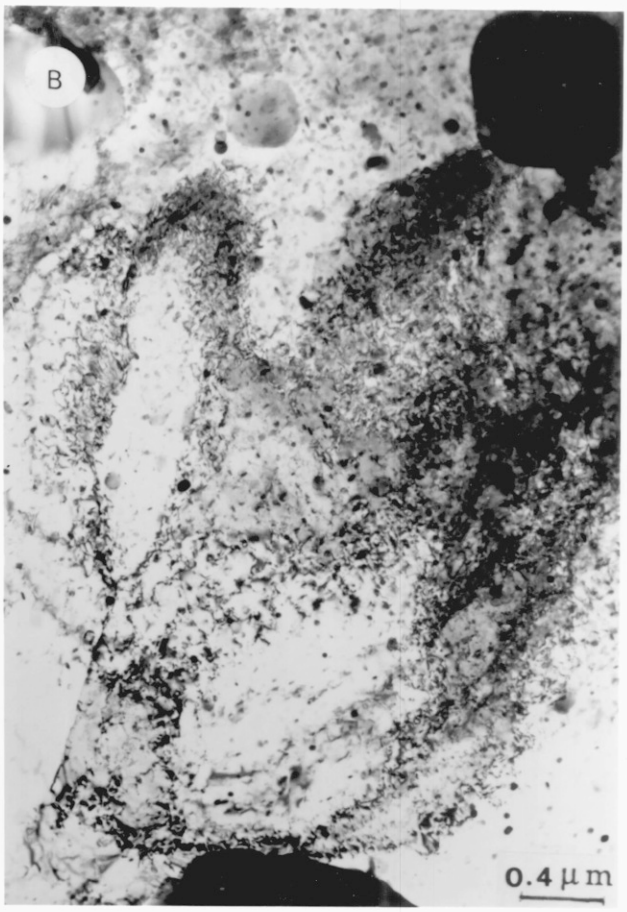
Precipitates appeared to play an important role in determining the deformation sub-structure by pinning the grain and sub-boundaries. The sub-grains exhibited large range of sizes apparently caused by the inhibition of the movement of dislocations due to the precipitates.

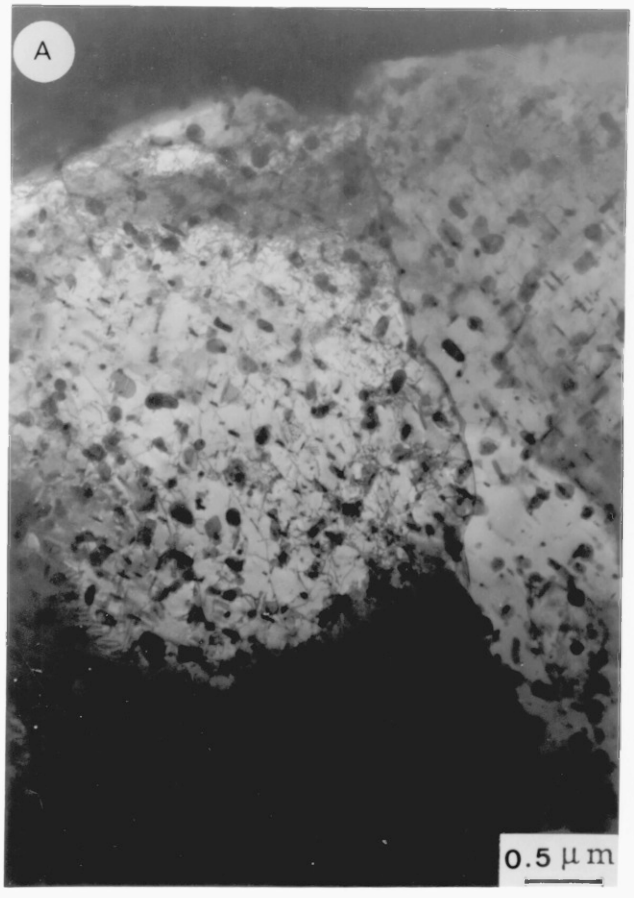
The average size of sub-grains formed during compression at different temperatures and strain rates is given in the table 3.2

Fig. 3.36 TEMof the 2014/SiC composite after compression testing at 200°C at strain rates of (a) 5 x 10^{-4} and (b) 5 x 10^{-2} S^{-1}.

Fig. 3.37 TEMof the 2014/SiC composite after compression testing at 300°C at strain rates of (a) 5 x 10^{-4} and (b) 5 x 10^{-2} S^{-1}.


A
0.4 μm


B
0.4 μm


A
0.5 μm

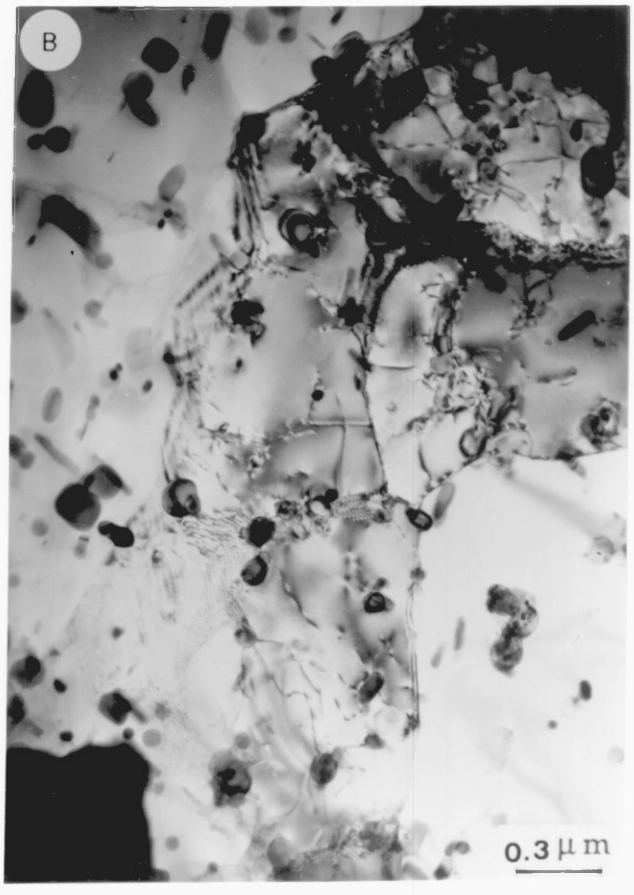
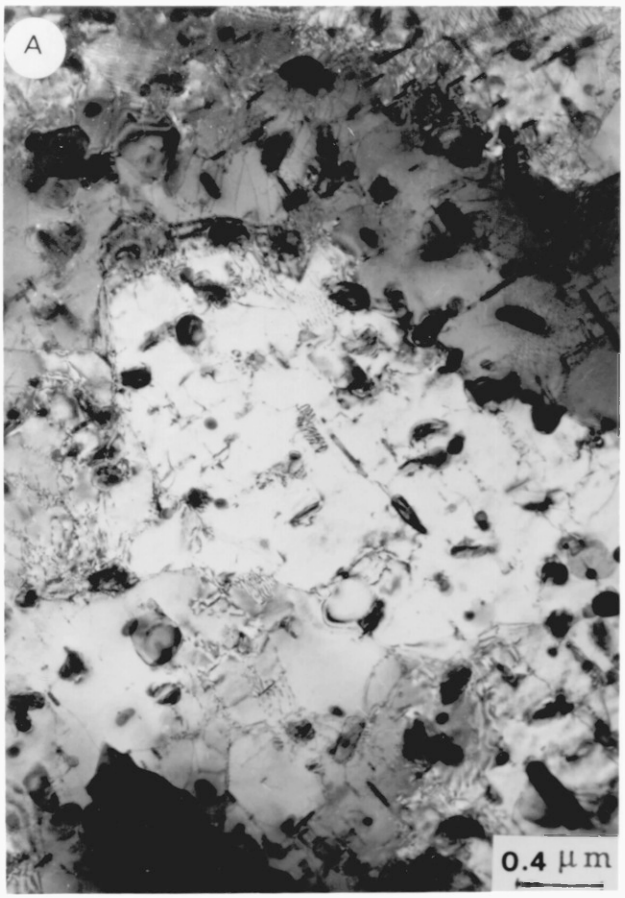
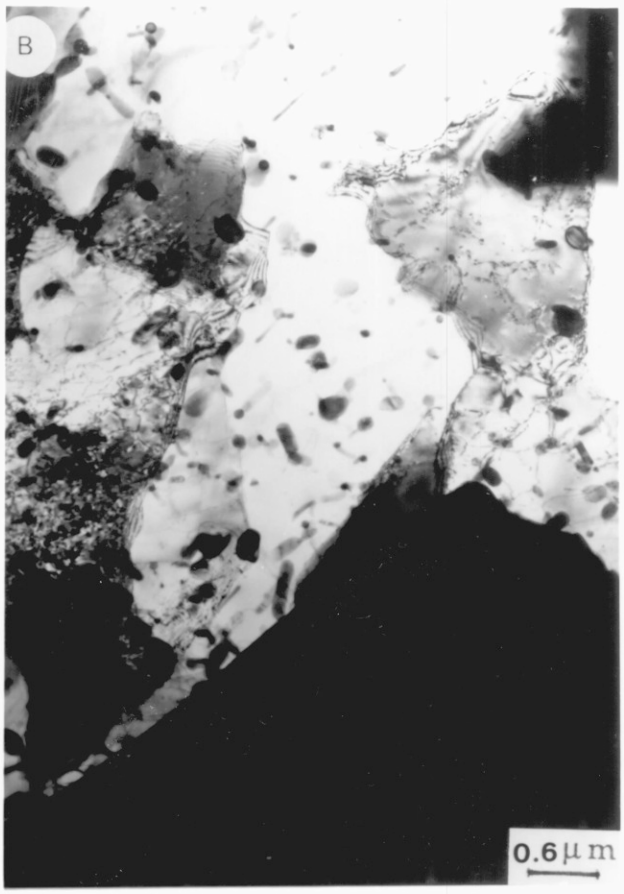

B
0.3 μm

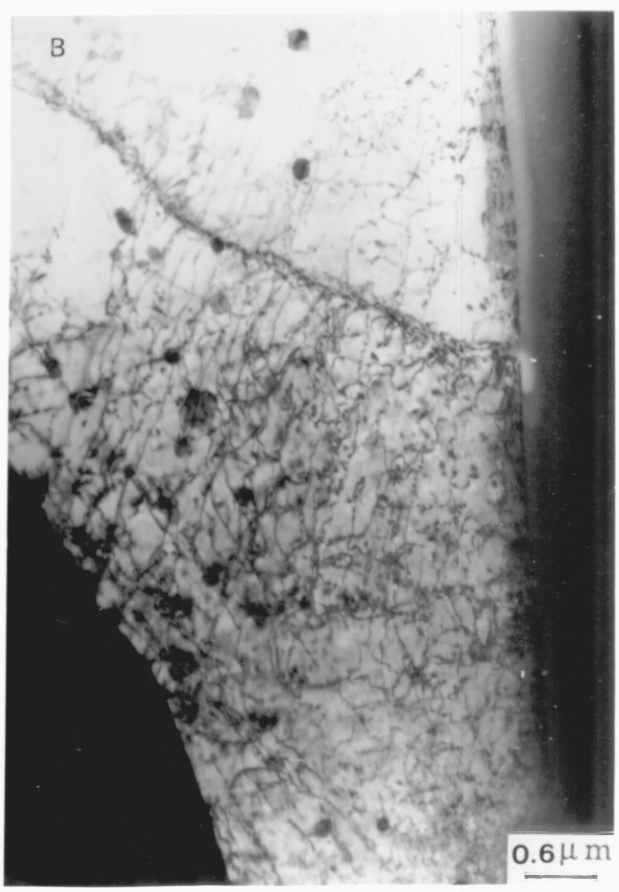
Fig. 3.38 TEMof the 2014/SiC composite after compression testing at 400°C at strain rates of (a) 5 x 10^{-4} and (b) 5 x 10^{-2} S^{-1}.

Fig. 3.39 TEMof the 2014/SiC composite after compression testing at 500°C at strain rates of (a) 5 x 10^{-4} and (b) 5 x 10^{-2} S^{-1}.


A
0.4 μm


B
0.6 μm


A
1.0 μm


B
0.6 μm

	Size of Sub-grains at Different Strain Rates	
Temperature°C	$5 \times 10^{-4}\ S^{-1}$ (μm)	$5 \times 10^{-2}\ S^{-1}$ (μm)
Room Temp.	0.74	0.69
200° C	1.2	0.87
300°C	1.6	1.12
400°C	2.7	1.6
500°C	2.8	1.9

Table 3.1 Average sub-grain size of the 2S/SiC composite deformed in compression at different temperatures and strain rates.

	Size of Sub-grains at Different Strain Rates	
Temperature°C	$5 \times 10^{-4}\ S^{-1}$ (μm)	$5 \times 10^{-2}\ S^{-1}$ (μm)
300°C	0.9	0.7
500°C	1.8	1.3

Table 3.2 Average sub-grain size of the 2014/SiC composite deformed in compression at different temperatures and strain rates.

CHAPTER 4

(RESULTS)

Tensile Testing and Fractography.

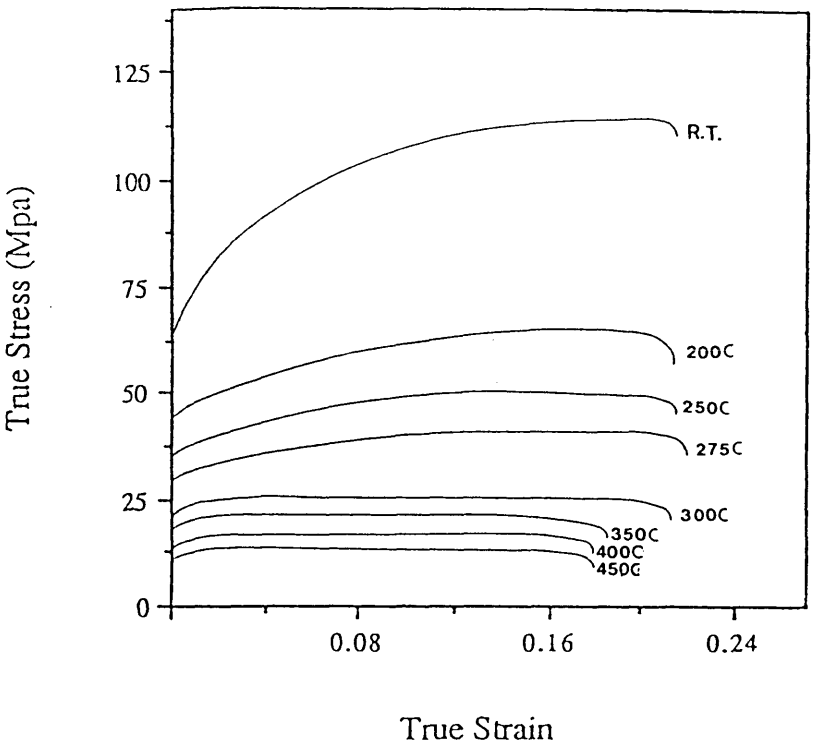
4.1 Stress Strain Behaviour of the Composites and the Matrix Alloys.

Variation in the true stress with true strain is shown in the figs. 4.1 and 4.3 for the 2S/SiC and 2014/SiC composites for tensile tests carried out at nominal strain rates between 5 x 10^{-2} and 5 x 10^{-4} S^{-1} at temperatures between room temperature and 450°C.

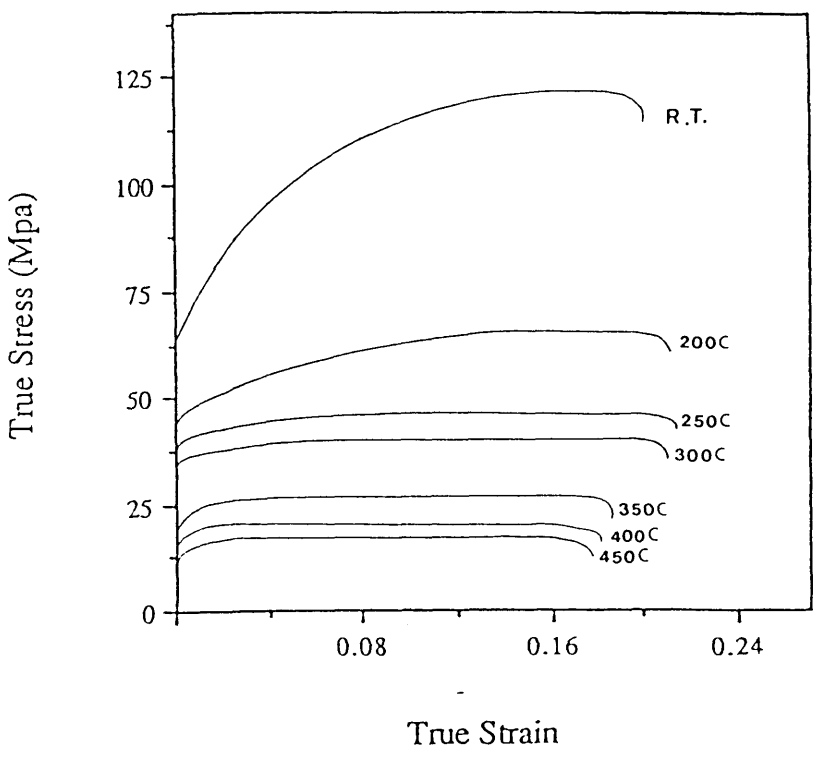
The curves obtained at lower temperatures showed a rapid increase of stress on straining. At elevated temperatures, there was an increase in stress followed by a constant stress level on further straining.

For comparative purposes, tensile tests have also been carried out on 2S and 2014 matrix alloys in the same range of temperature and strain rate, and the stress-strain curves are shown in figs. 4.2 and 4.4.

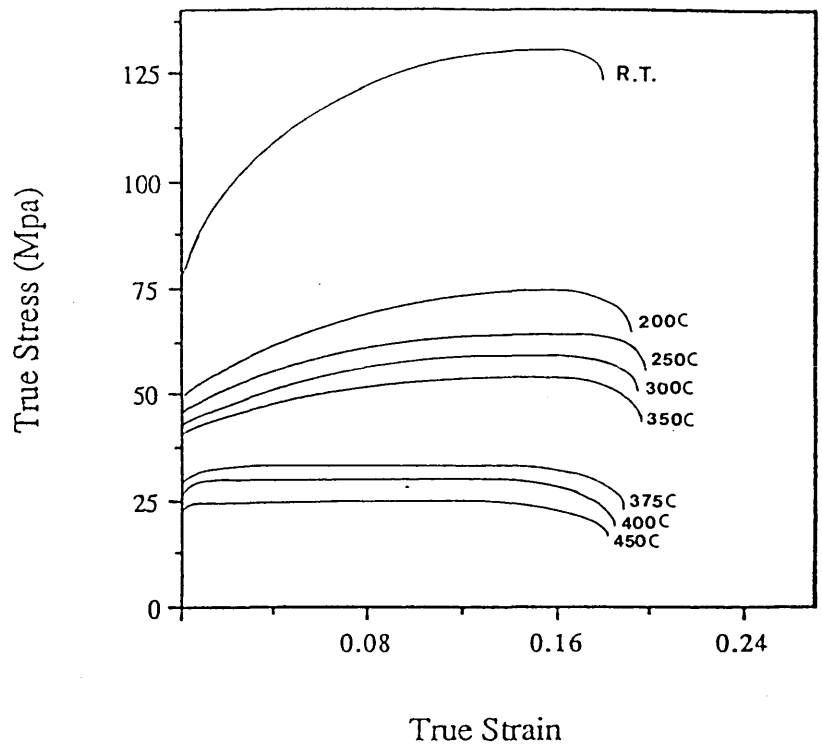
Data including the yield stress, maximum tensile stress and the amount of uniform elongation to failure obtained from the stress strain curves for 2S/SiC and 2014/SiC composites and their matrix alloys are summarised in tables 4.1 to 4.4. At the highest test temperature the evaluated yield stress and maximum tensile stress of the composites, especially the 2014/SiC composite, is not greatly different compared to the matrix alloys. However, at lower temperatures, the SiC reinforcement produces a marked increase in the strength but at the expense of a loss in ductility.


125
100
75
50
25
0
True Stress (Mpa)
R.T.
200C
250C
275C
300C
350C
400C
450C
0.08
0.16
0.24
True Strain

4.1 (a)

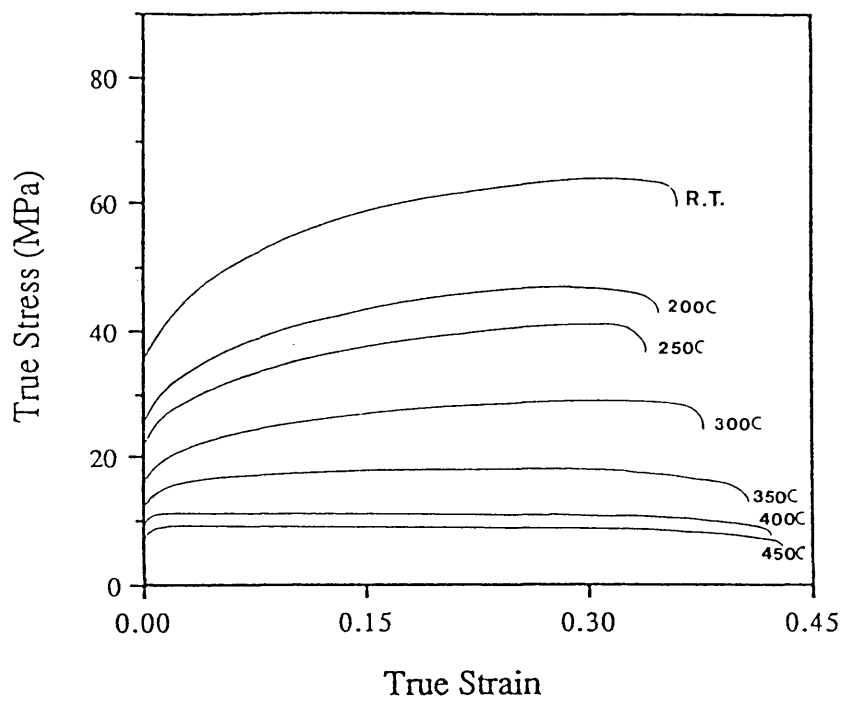

125
100
75
50
25
0
True Stress (Mpa)
R.T.
200C
250C
300C
350C
400C
450C
0.08
0.16
0.24
True Strain

4.1 (b)

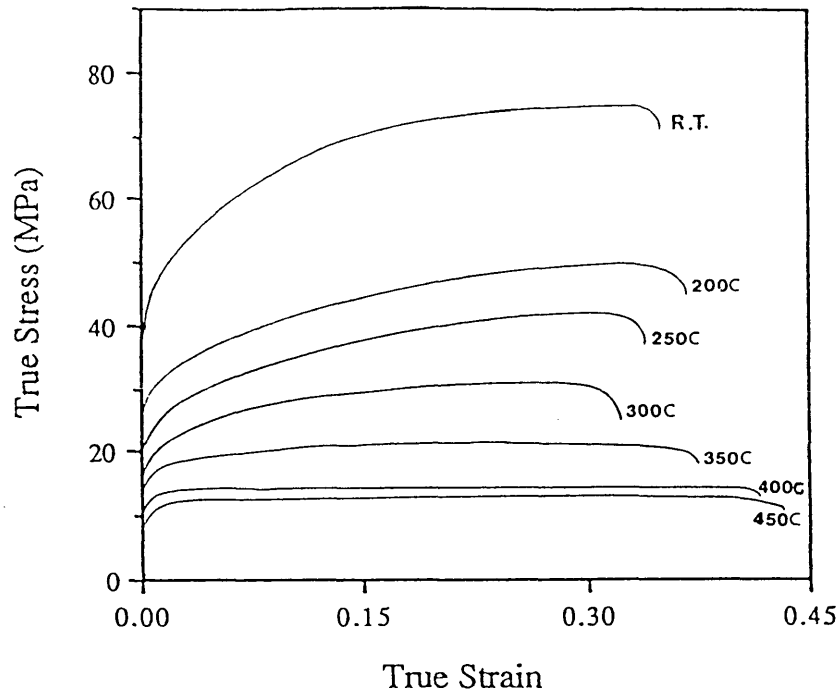


4.1 (c)

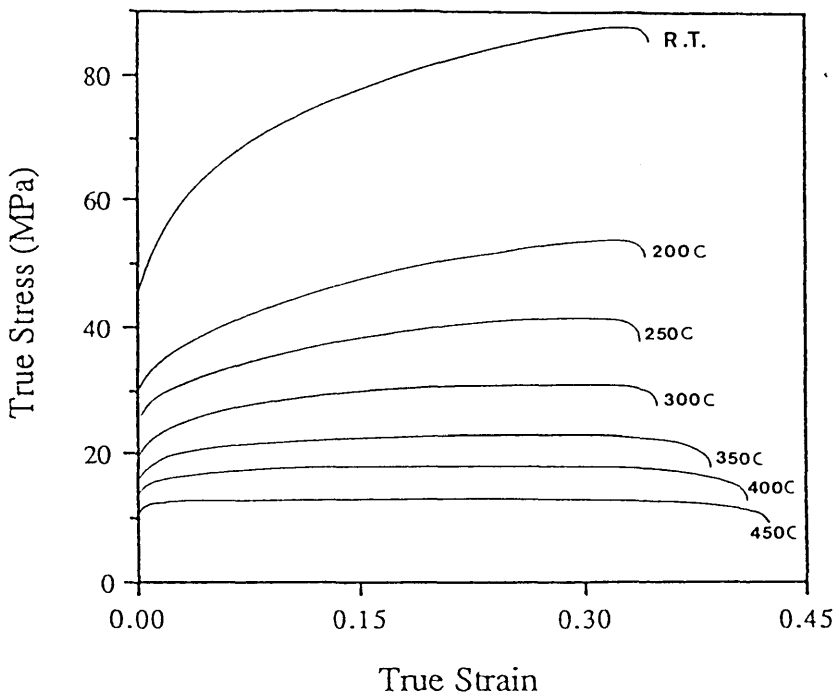
Fig. 4.1 True stress-strain curves of the 2S/SiC composite after tensile testing at temperatures between room temperature and 450°C at strain rates of (a) 5 x 10^{-4}, (b) 5 x 10^{-3}, and (c) 5 x 10^{-2} S^{-1}.



4.2 (a)

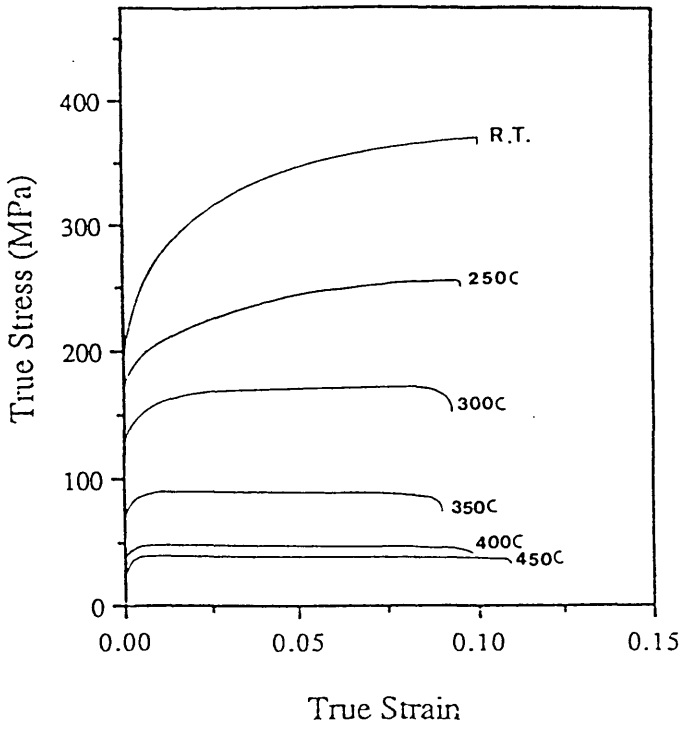


4.2 (b)

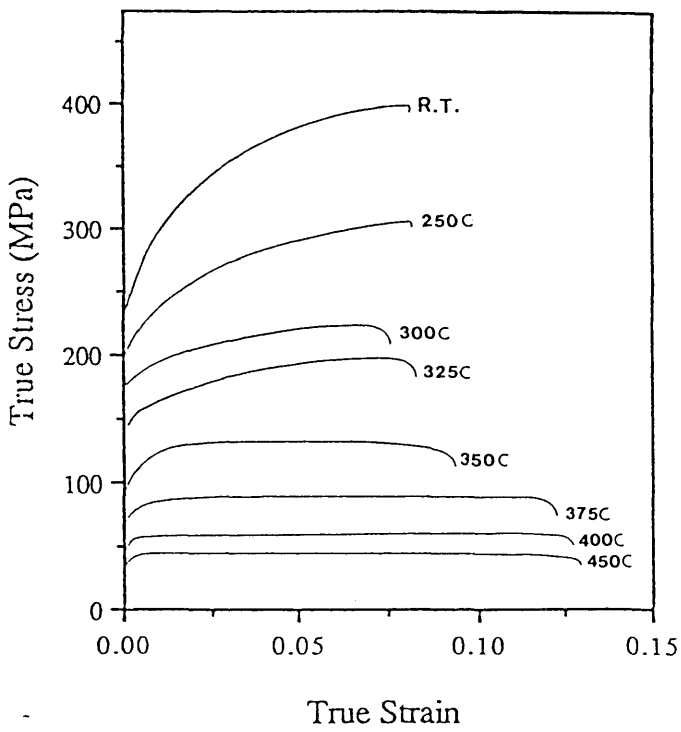


4.2 (c)

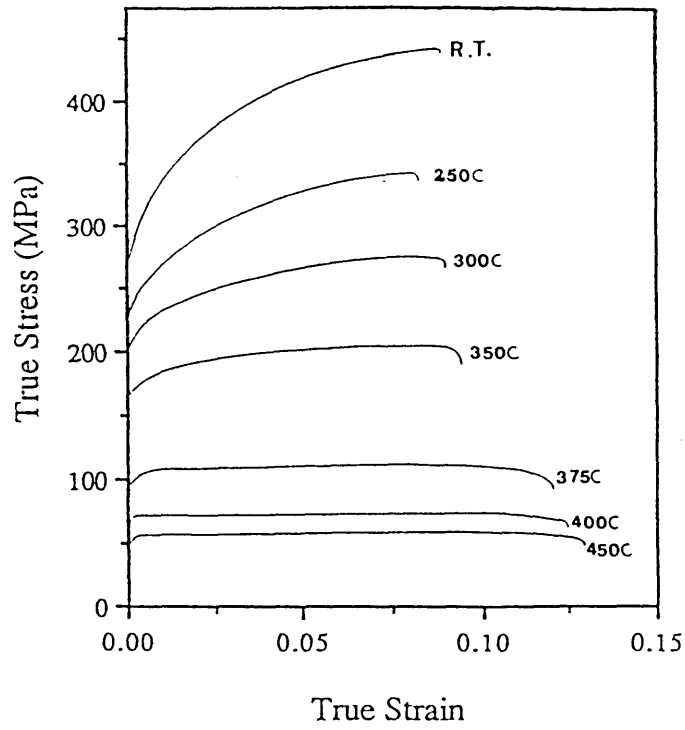
Fig. 4.2 True stress-strain curves of the 2S aluminium after tensile testing at temperatures between room temperature and 450°C at strain rates of (a) 5×10^{-4}, (b) 5×10^{-3}, and (c) 5×10^{-2} S^{-1}.


True Stress (MPa)
400
300
200
100
0
R.T.
250C
300C
350C
400C
450C
0.00
0.05
0.10
0.15
True Strain

4.3 (a)

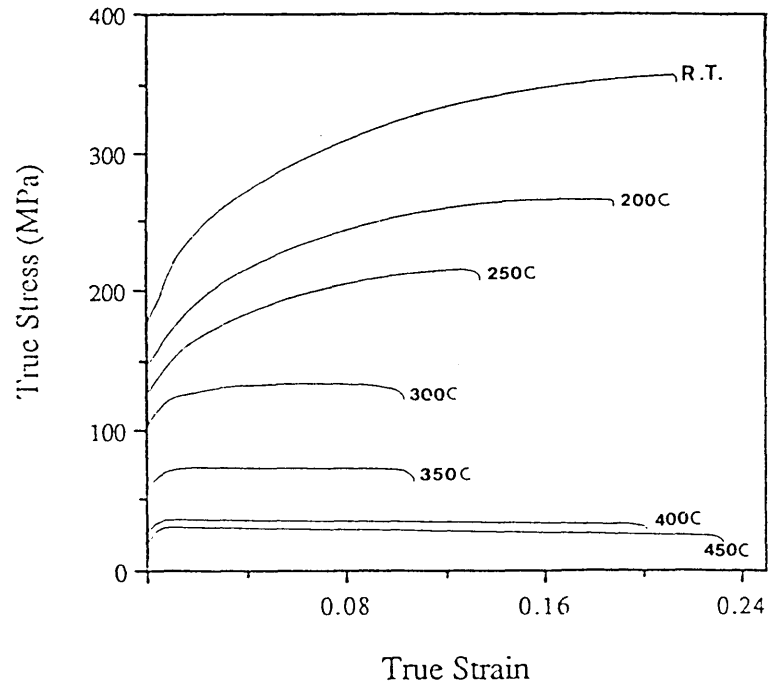

True Stress (MPa)
400
300
200
100
0
R.T.
250C
300C
325C
350C
375C
400C
450C
0.00
0.05
0.10
0.15
True Strain

4.3 (b)

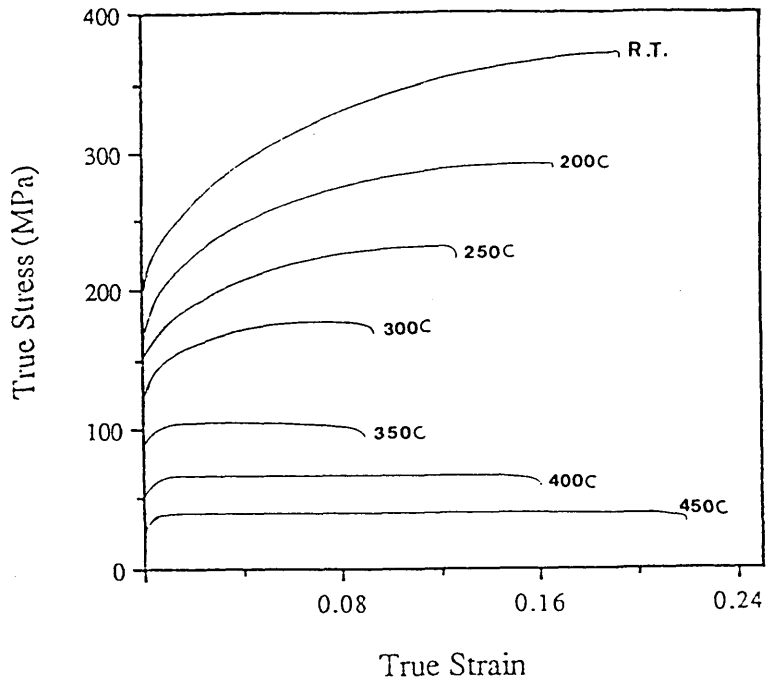


4.3 (c)

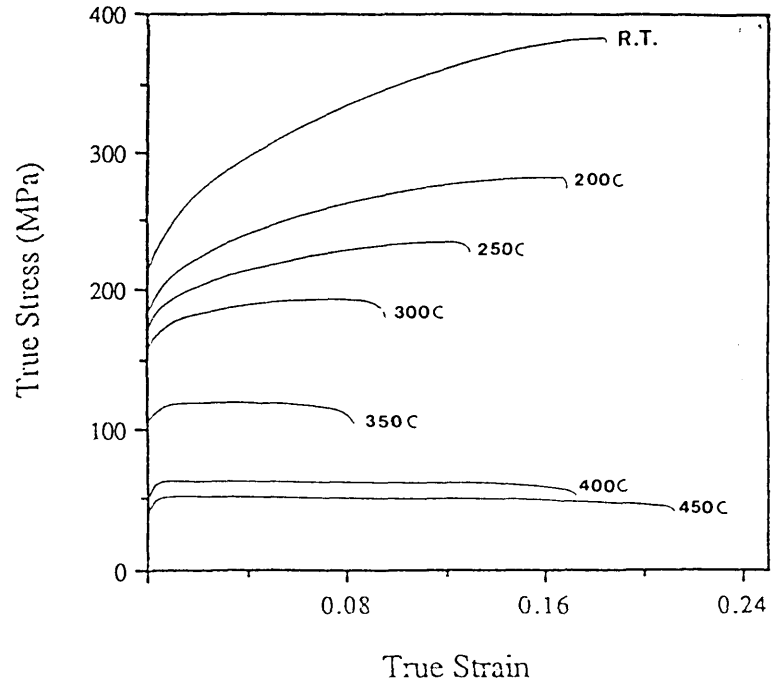
Fig. 4.3 True stress-strain curves of the 2014/SiC composite after tensile testing at temperatures between room temperature and 450°C at strain rates of (a) 5×10^{-4}, (b) 5×10^{-3}, and (c) 5×10^{-2} S^{-1}.



4.4 (a)



4.4 (b)



4.4 (c)

Fig. 4.4 True stress-strain curves of the 2014 alloy after tensile testing at temperatures between room temperature and 450°C at strain rates of (a) 5×10^{-4}, (b) 5×10^{-3}, and (c) 5×10^{-2} S^{-1}.

4.1.1 Yield Stress.

Modulus corrected yield stress was observed to decrease gradually in both composites on increasing the deformation temperature (figs. 4.5 and 4.6). There was then a rapid decrease in modulus corrected yield stress of the composites observed between 250 and 300°C for the lowest strain rate and between 350 and 400°C for the highest strain rate. The yield stress above these temperatures was again less temperature sensitive. The 2S matrix alloy in comparison showed little evidence of this effect and the yield stress decreased almost linearly with increasing temperature (fig. 4.7). The 2014 matrix alloy, however, displayed a relatively rapid fall which at higher temperatures again becomes steady (fig. 4.8)

The log. of yield stress as a function of strain rate is shown in figs. 4.9 to 4.12 for the composites and the matrix alloys deformed at different temperatures. The higher the strain rate, the greater the yield stress observed for a particular temperature.

4.1.2 Elongation

The tensile ductility data measured from the stress-strain curves of the 2S/SiC and 2014/SiC composites and their matrix alloys, is shown in the tables 4.1 to 4.4.

There was a limited ductility observed in the composites in the range of around 20 to 25 percent for the 2S/SiC composite and around 8 to 10 percent for the 2014/SiC. The 2S/SiC composite displayed a gradual drop in the amount of total elongation with increase in the temperature, however the composite 2014/SiC initially exhibited some decrease in the elongation

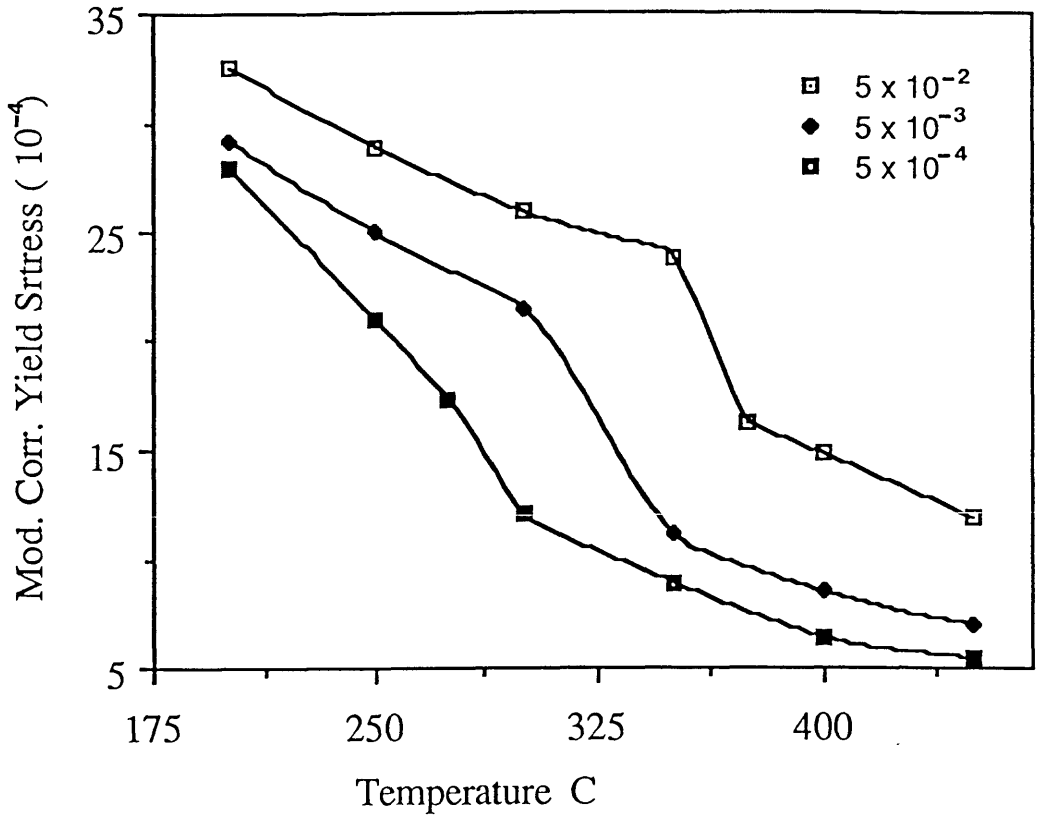


Fig. 4.5 Modulus corrected yield stress of the 2S/SiC composite as a function of temperature after tensile testing at different strain rates.

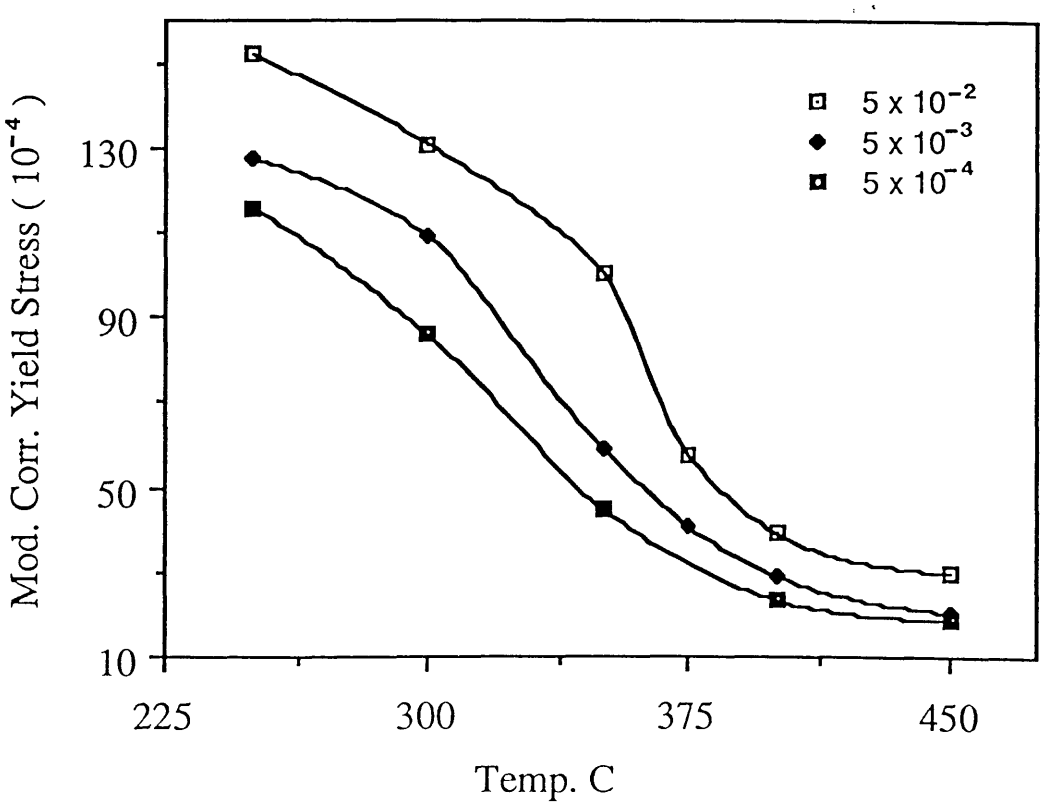


Fig. 4.6 Modulus corrected yield stress of the 2014/SiC composite as a function of temperature after tensile testing at different strain rates.

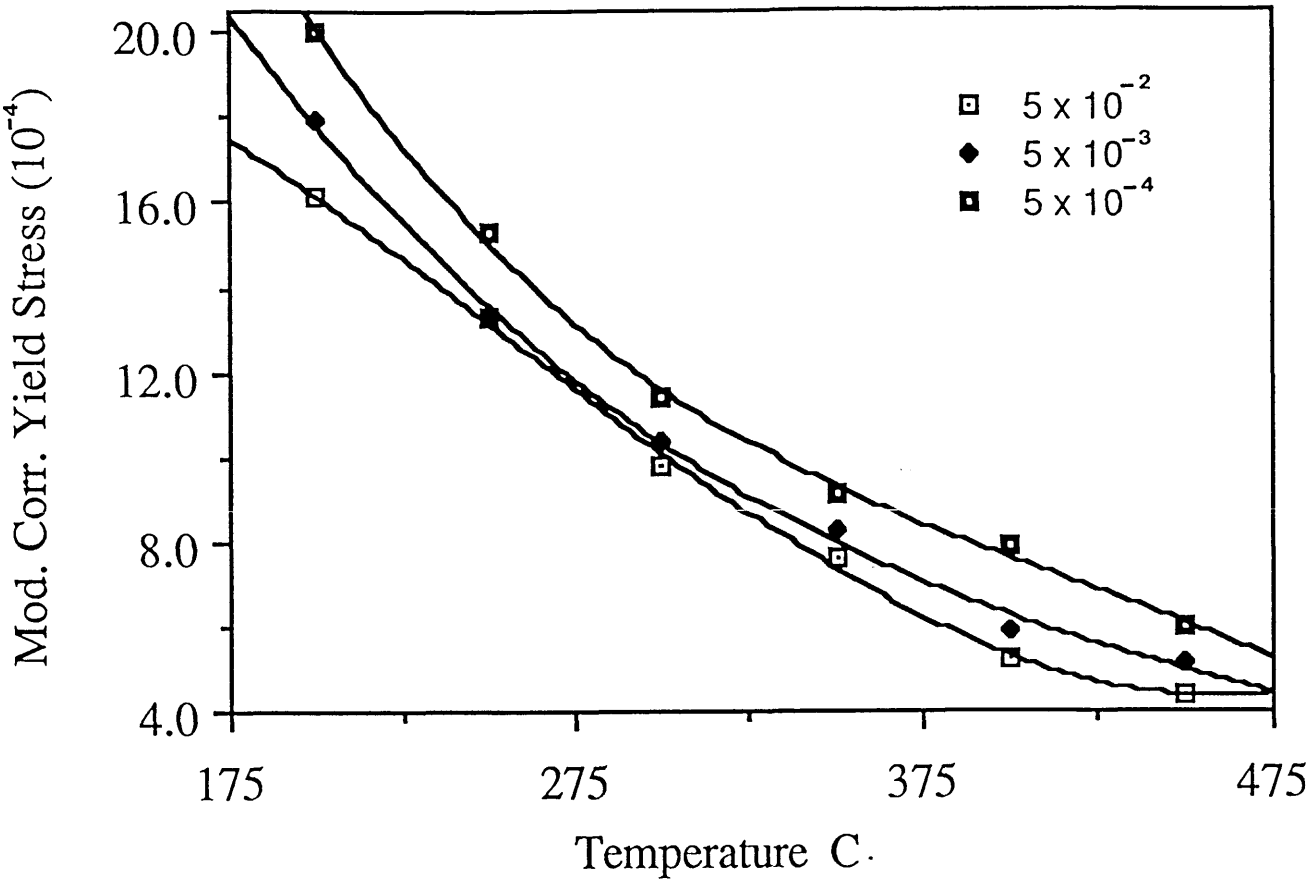


Fig. 4.7 Modulus corrected yield stress of the 2S aluminium as a function of temperature after tensile testing at different strain rates.

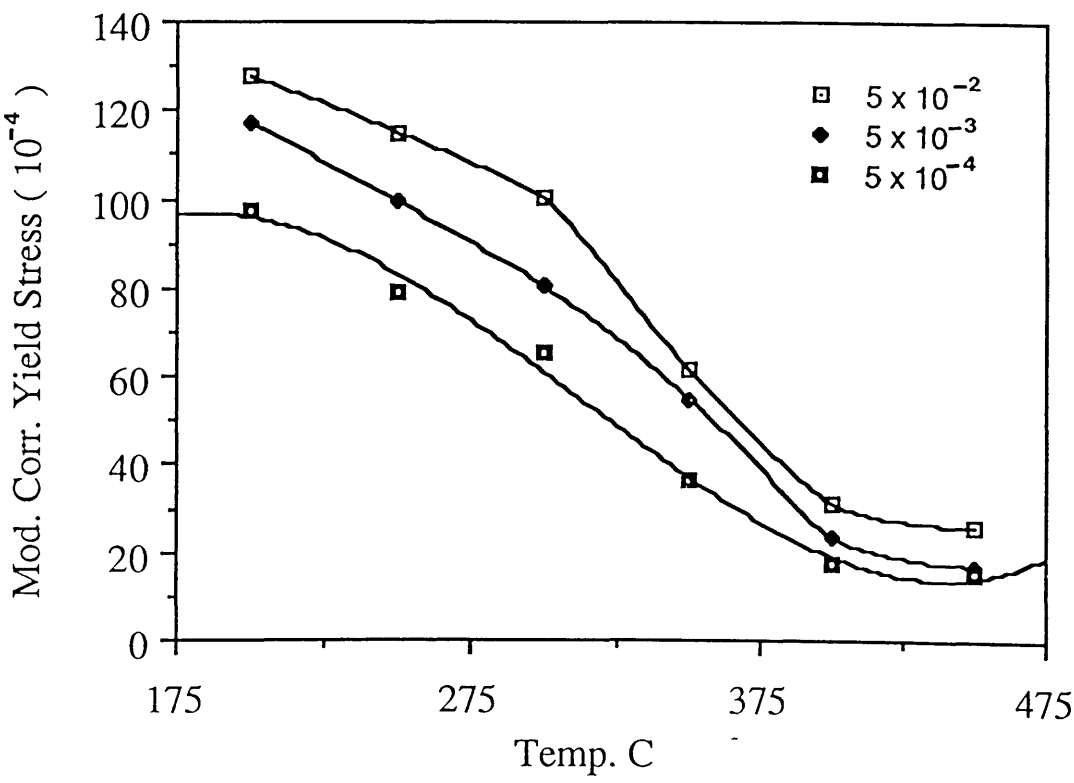


Fig. 4.8 Modulus corrected yield stress of the 2014 alloy as a function of temperature after tensile testing at different strain rates.

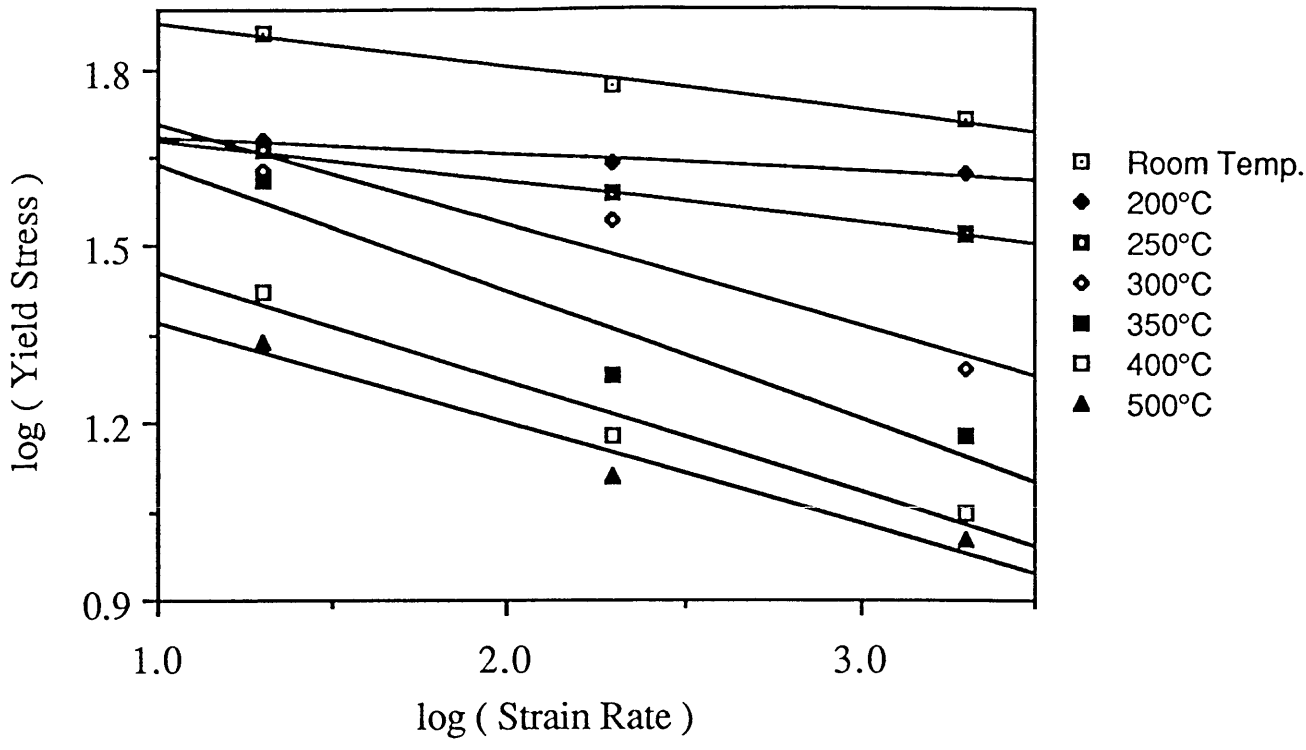


Fig. 4.9 Yield stress of the 2S/SiC composite as a function of strain rate after tensile testing at different temperatures.

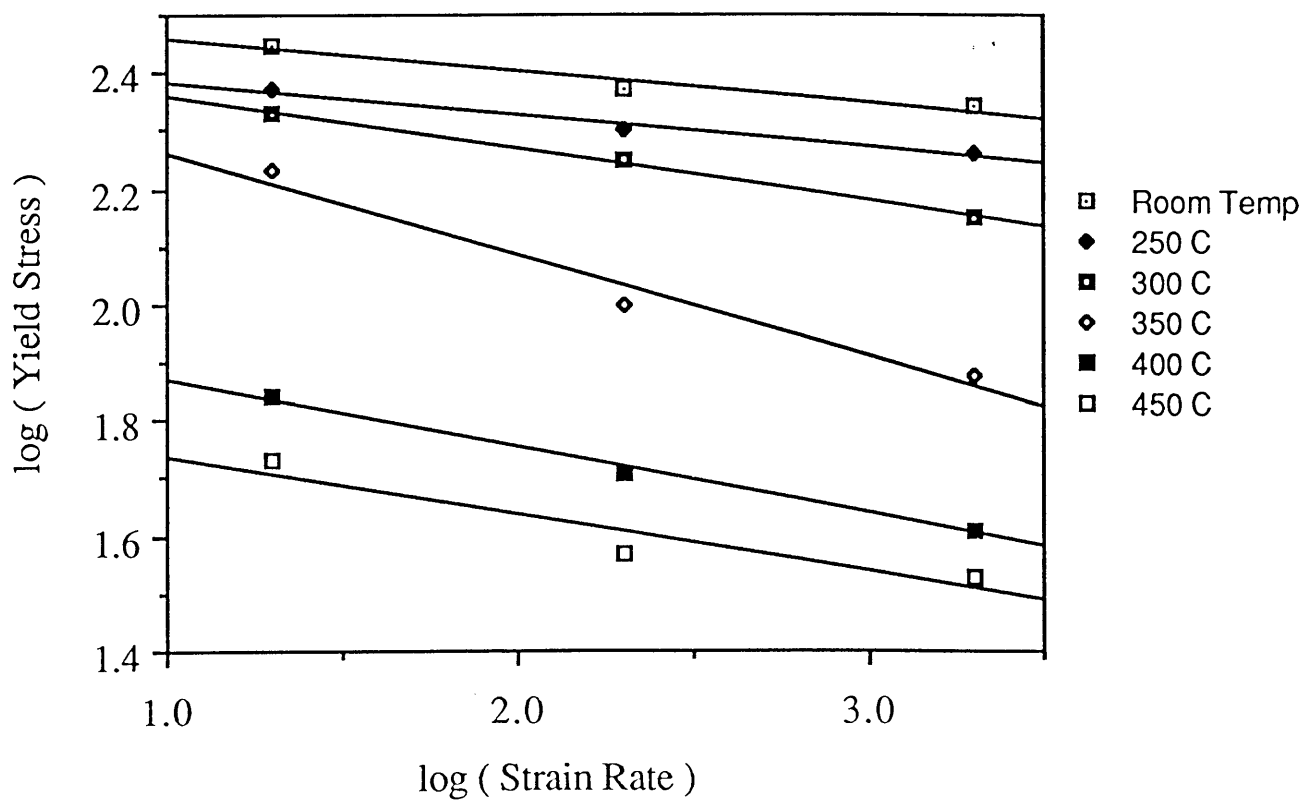


Fig. 4.10 Yield stress of the 2014/SiC composite as a function of strain rate after tensile testing at different temperatures.

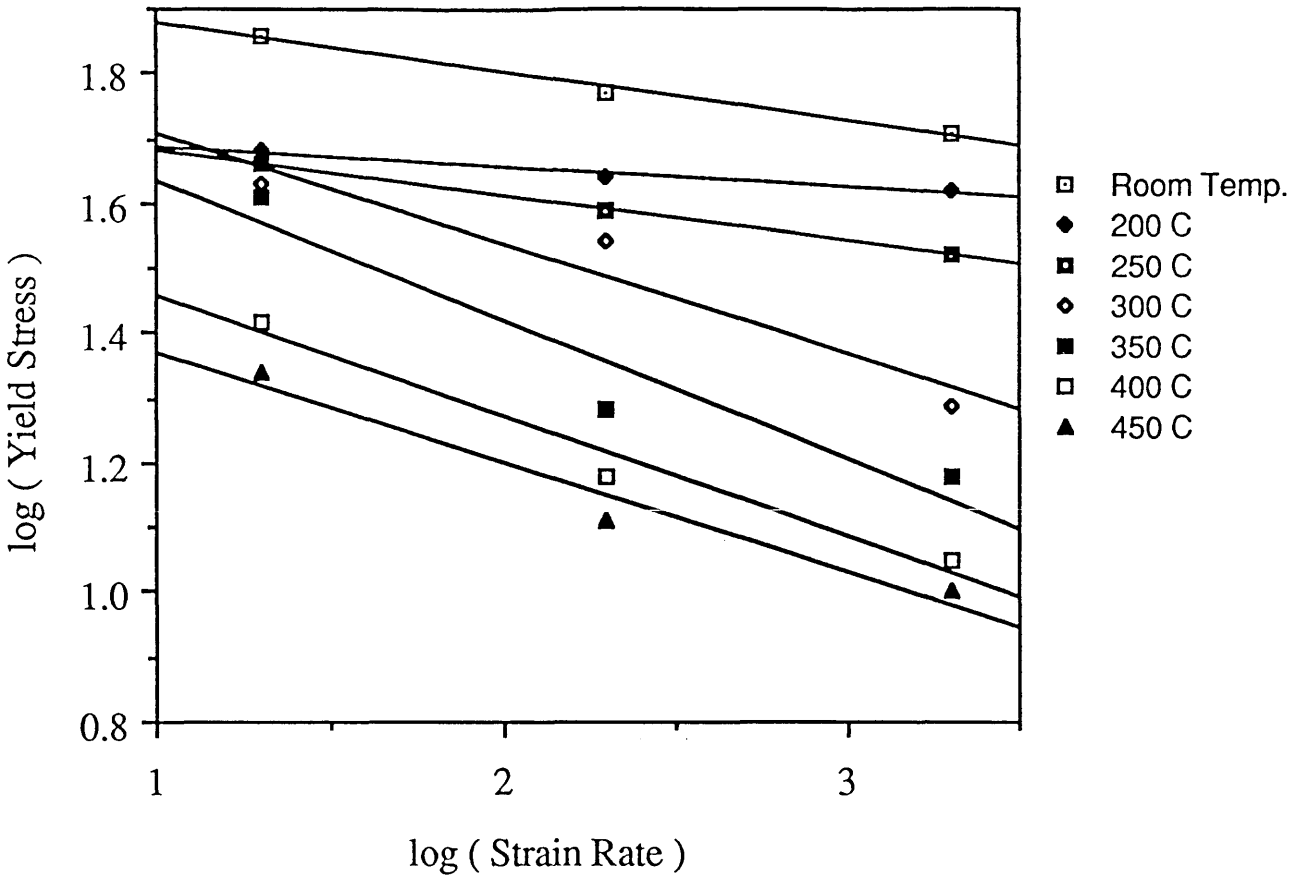


Fig. 4.11 Yield stress of the 2S aluminium as a function of strain rate after tensile testing at different temperatures.

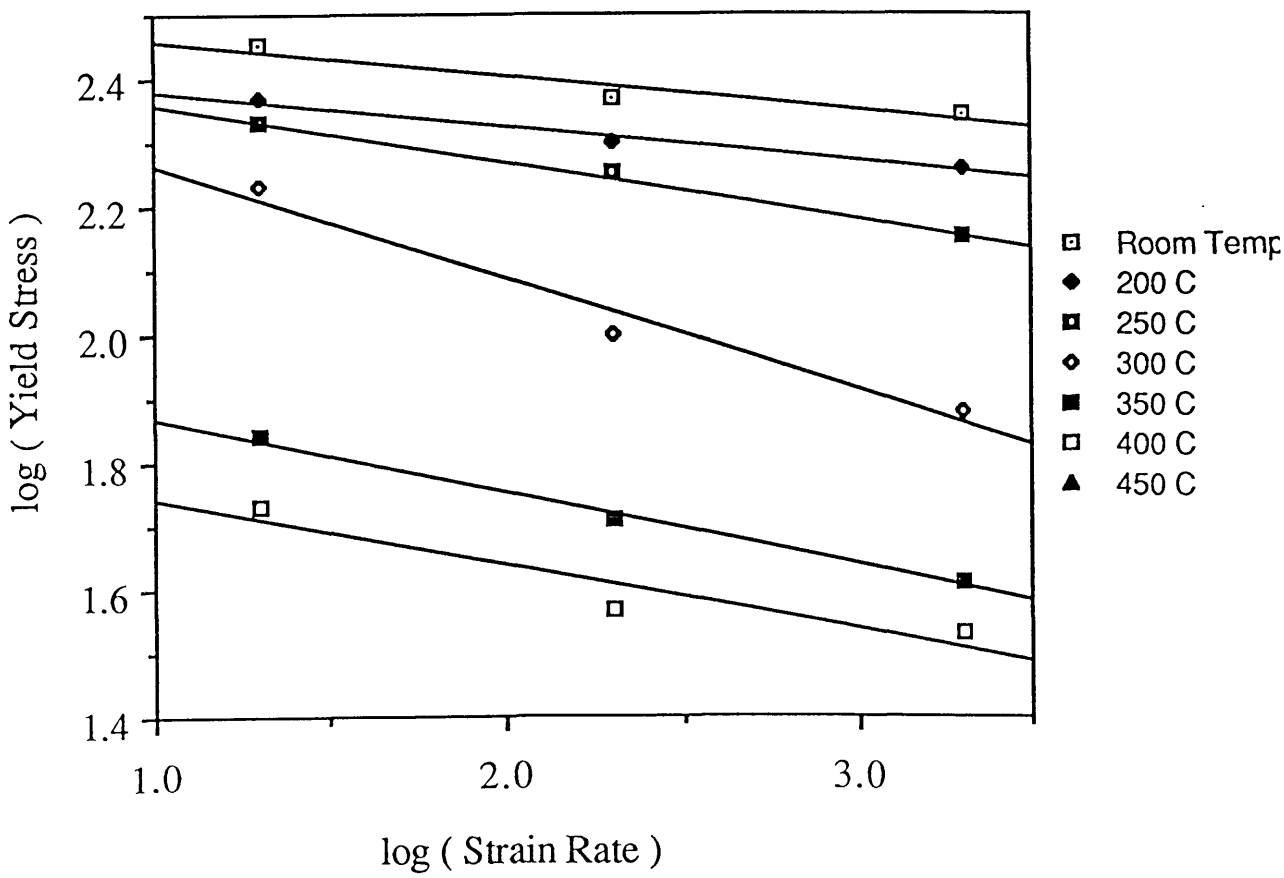


Fig. 4.12 Yield stress of the 2014 alloy as a function of strain rate after tensile testing at different temperatures.

but at temperatures above 350°C, a slight extended ductility was observed.

The 2014 matrix alloy also showed a similar ductility behaviour but with a relatively higher amount of ductility exceeding up to 24 percent. The 2S aluminium displayed the maximum ductility in the range of about 35 to 45 percent which increased from room temperature up to the final limit at the maximum conducted test temperature.

4.1.3 Work Hardening Rates.

Initial rates of work hardening measured for the tests conducted in a range of temperatures at various strain rates for 2S/SiC and 2014/SiC composites and their matrix alloys are given in figs. 4.13 to 4.16.

The composites exhibited much greater rates of work hardening as compared to the matrix alloys. On increasing the test temperature the work hardening rates showed a trend of initially a steady state region followed by a sharp decrease at a particular temperature, depending on strain rate, which once again becomes steady at elevated temperatures in the composites 2S/SiC and 2014/SiC . The 2014 matrix alloy showed a somewhat similar trend whereas the 2S alloy displayed a moderate and gradual drop of work hardening rates on increasing the deformation temperature.

The work hardening rates as a function of strain rate for the composites 2S/SiC and 2014/SiC and their matrix alloys is shown in figs. 4.17 to 4.20. The composites displayed a gradual change in the slope of the curves as the deformation temperature increased up to 350°C beyond which the curves show a relatively greater change in the slope. The curves for the matrix alloys, however, revealed a gradual variation in the slope of the curves throughout the test temperature range.

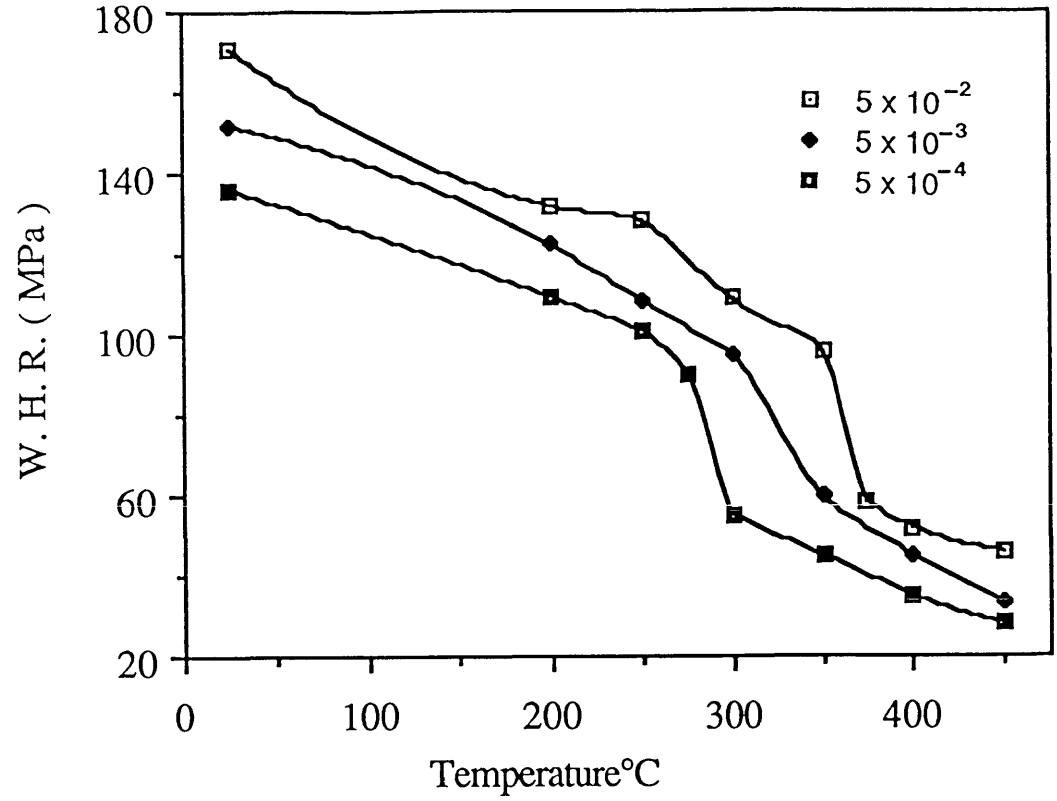


Fig. 4.13 Initial work hardening rates of the 2S/SiC composite as a function of temperature after tensile testing at different strain rates.

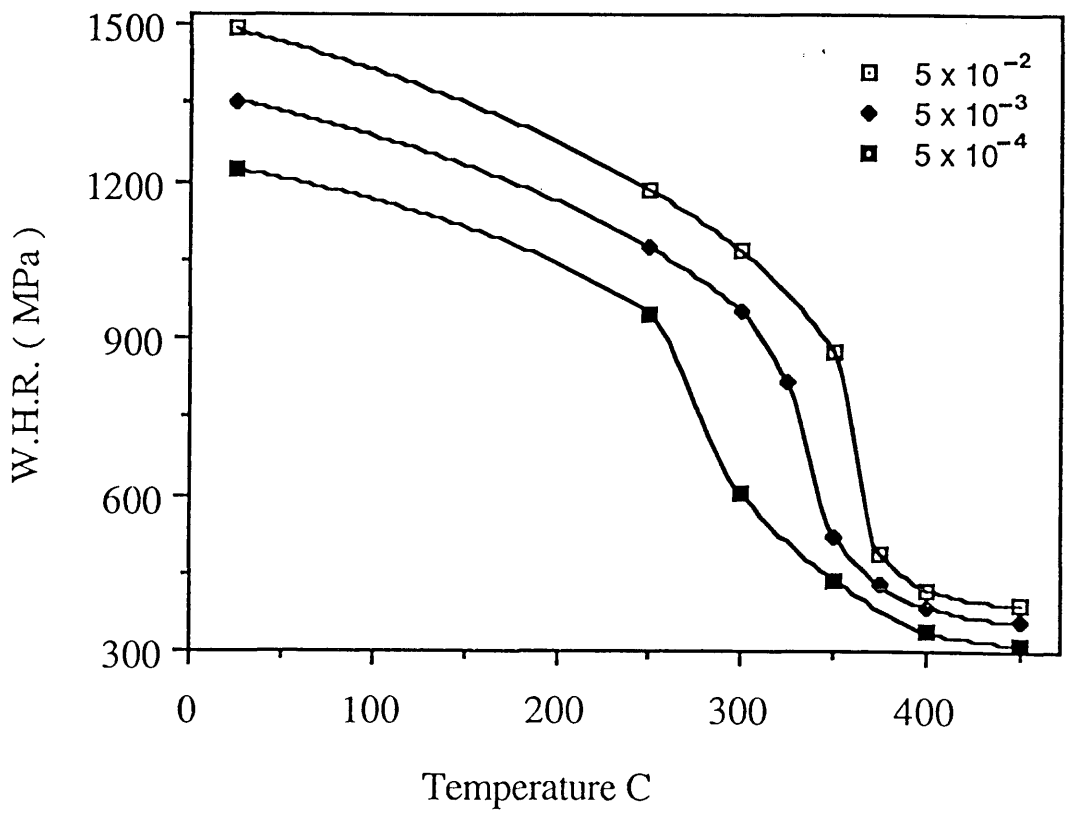


Fig. 4.14 Initial work hardening rates of the 2014/SiC composite as a function of temperature after tensile testing at different strain rates.

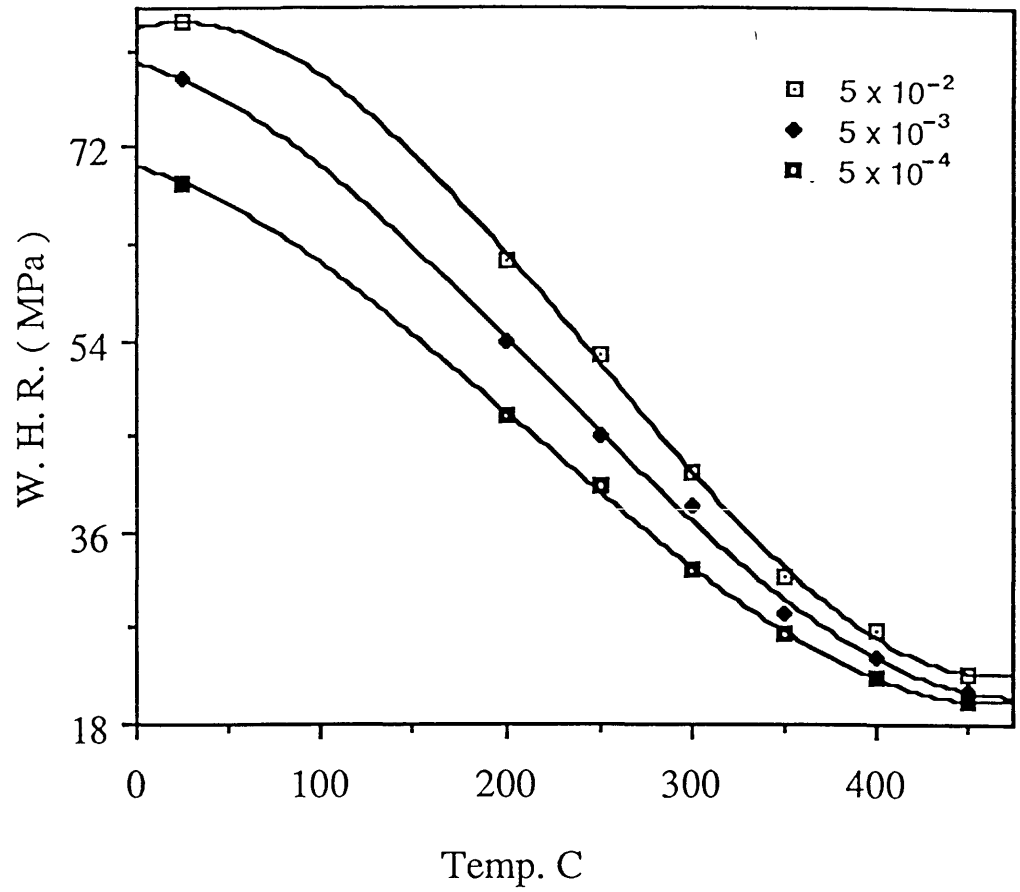


Fig. 4.15 Initial work hardening rates of the 2S aluminium as a function of temperature after tensile testing at different strain rates.

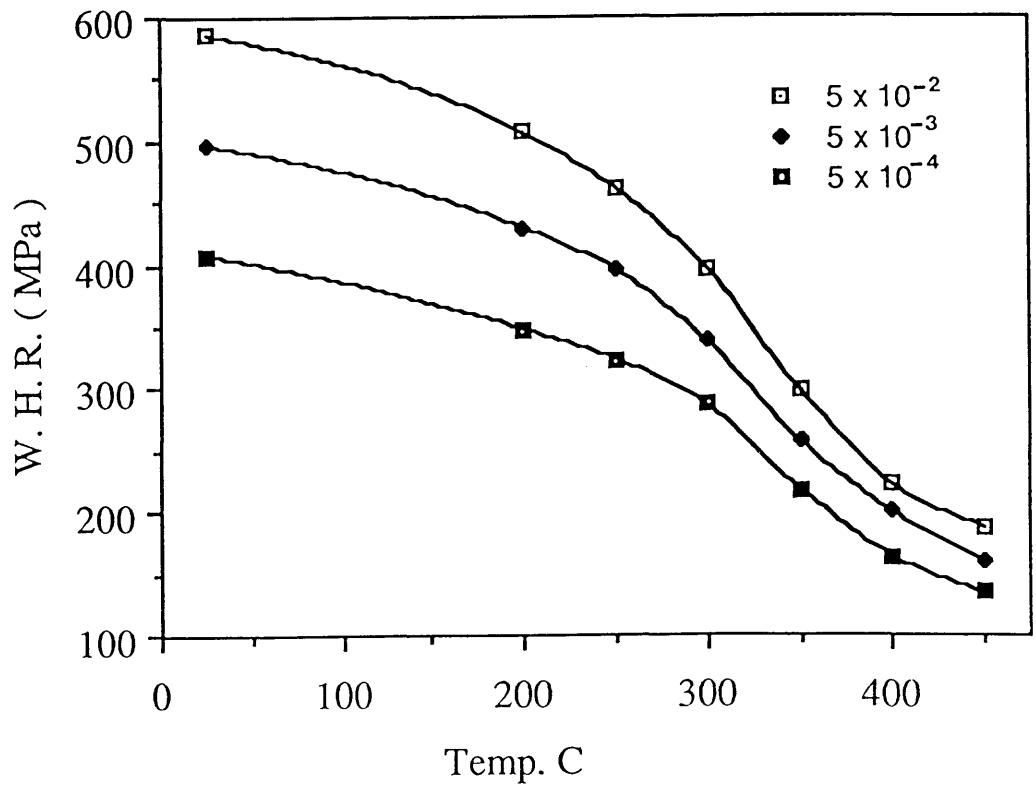


Fig. 4.16 Initial work hardening rates of the 2014 alloy as a function of temperature after tensile testing at different strain rates.

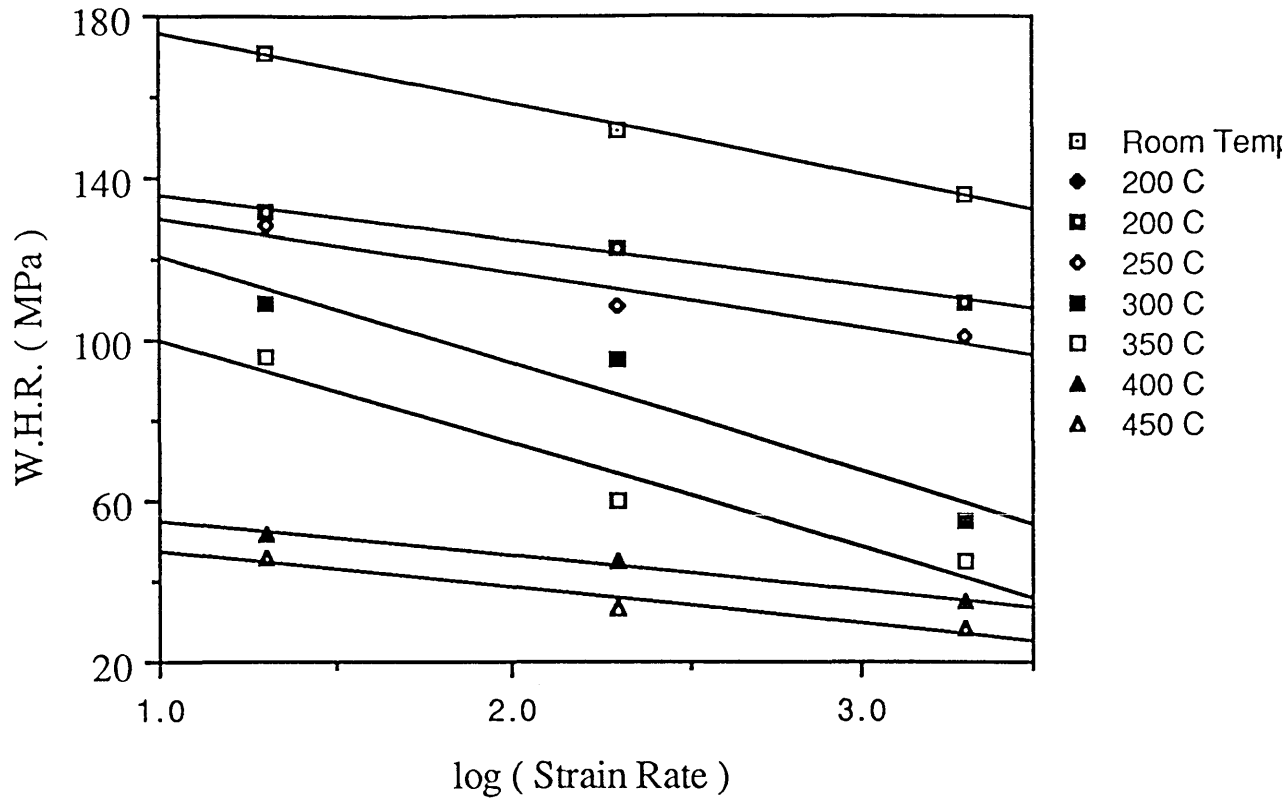


Fig. 4.17 Initial work hardening rates of the 2S/SiC composite as a function of strain rate after tensile testing at different temperatures.

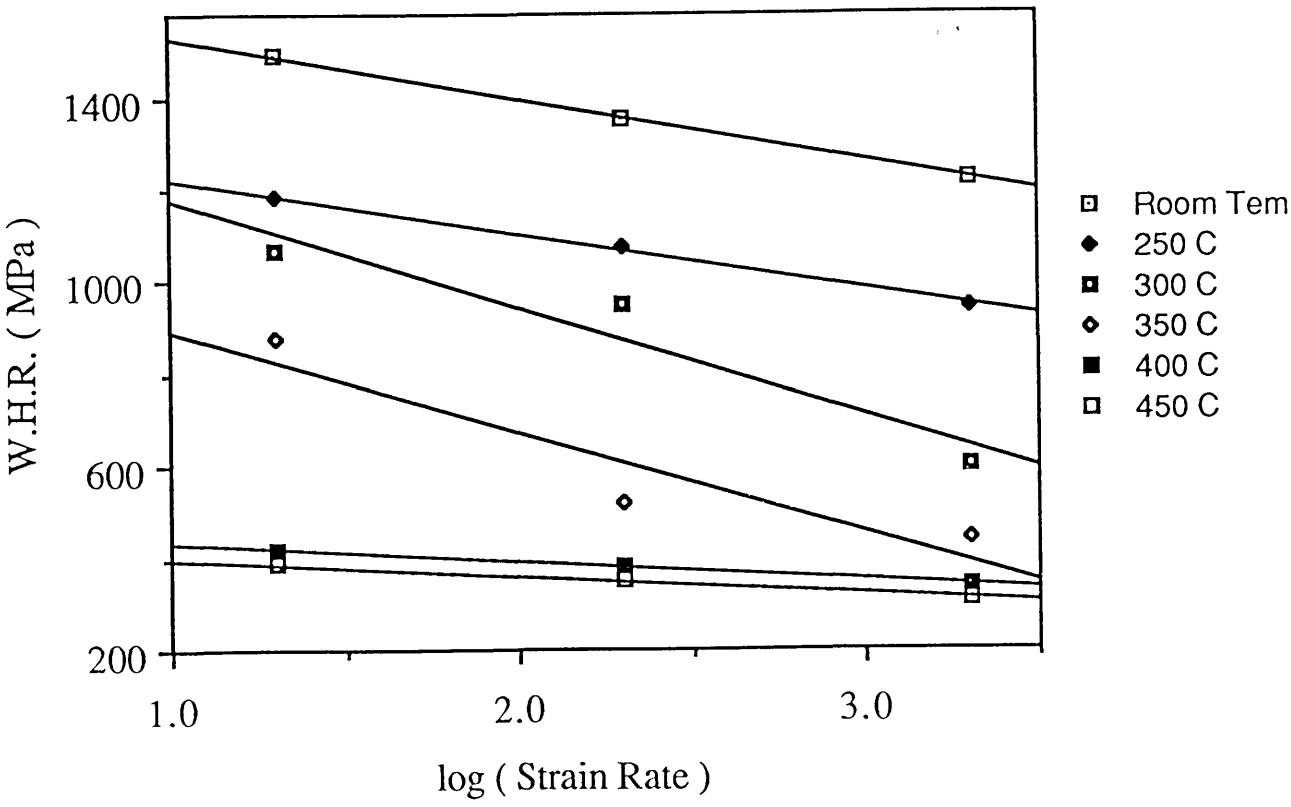


Fig. 4.18 Initial work hardening rates of the 2014/SiC composite as a function of strain rate after tensile testing at different temperatures.

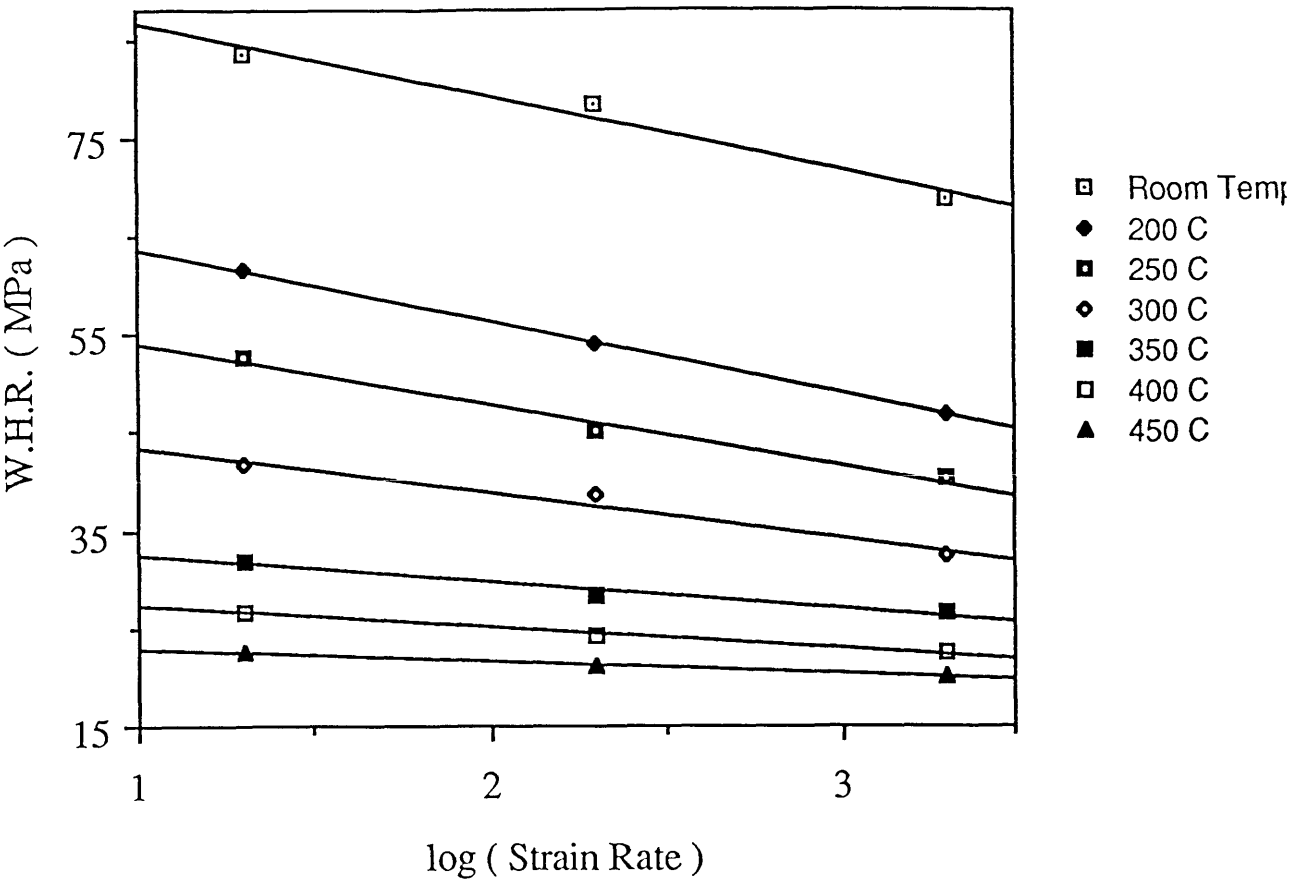


Fig. 4.19 Initial work hardening rates of the 2S aluminium as a function of strain rate after tensile testing at different temperatures.

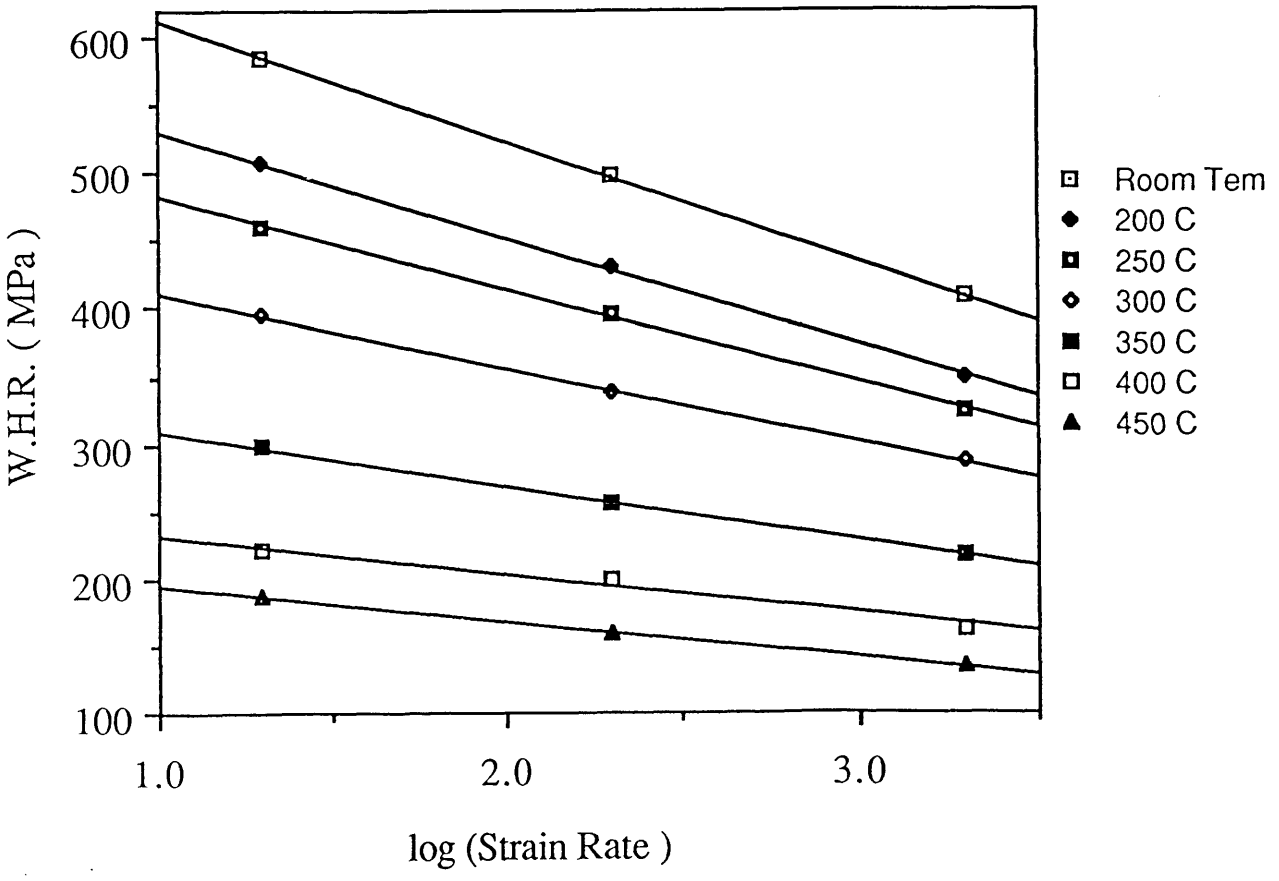


Fig. 4.20 Initial work hardening rates of the 2014 alloy as a function of strain rate after tensile testing at different temperatures.

Strain Rate = 5 X 10^{-2}				
Temperature°C	Y. S. (MPa)	U. T. S. (MPa)	W. H. R. (MPa)	True Strain
Room Temp.	72.51	130.60	171.0	0.20
200	48.80	73.40	131.7	0.22
250	45.50	63.20	128.2	0.22
300	42.50	58.20	108.8	0.22
350	40.67	52.60	96.0	0.22
375	28.10	31.80	58.5	0.21
400	26.40	29.30	52.0	0.21
450	22.00	24.20	46.0	0.20
Strain Rate = 5 X 10^{-3}				
Temperature°C	Y. S. (MPa)	U.T.S. (MPa)	W. H. R. (MPa)	True Strain
Room Temp.	59.69	123.60	152.0	0.23
200	43.44	65.70	122.2	0.24
250	39.35	52.80	108.4	0.25
300	35.29	45.70	95.0	0.24
350	18.97	27.90	59.6	0.21
400	15.20	19.60	45.1	0.21
450	12.92	17.30	33.5	0.21
Strain Rate = 5 X 10^{-4}				
Temperature°C	Y. S. (MPa)	U. T. S. (MPa)	W. H. R. (MPa)	True Strain
Room Temp.	52.1	115.8	136.0	0.250
200	47.7	62.8.	109.3	0.240
250	33.05	49.2	101.0	0.250
275	27.76	41.1	90.0	0.240
300	19.69	26.2.	55.1	0.240
350	15.21	21.0	44.85	0.200
400	11.37	16.15	35.2	0.190
450	10.15	10.14	28.0	0.190

Table 4.1 Tensile data obtained from the true stress-strain curves of the 2S/SiC composites deformed in tension.

Strain Rate = 5 X 10^{-2}				
Temperature°C	Y. S. (MPa)	U. T. S. (MPa)	W. H. R. (MPa)	True Strain
Room Temp.	44.10	78.30	83.7	0.36
200	29.90	54.70	61.5	0.36
250	24.08	41.28	52.7	0.35
300	18.70	30.60	41.6	0.36
350	15.55	23.01	31.8	0.41
400	14.03	18.60	26.7	0.43
450	11.08	13.21	22.7	0.45
Strain Rate 5 × 10^{-3}				
Temperature°C	Y. S. (MPa)	U. T. S. (MPa)	W. H. R. (MPa)	True Strain
Room Temp.	38.80	72.50	78.4	0.37
200	26.81	49.53	53.9	0.39
250	20.93	38.70	45.2	0.37
300	17.05	29.72	38.5	0.33
350	14.20	21.46	28.5	0.40
400	10.45	14.80	24.3	0.45
450	9.43	12.10	21.1	0.48
Strain Rate = 5 × 10^{-4}				
Temperature°C	Y. S. (MPa)	U. T. S. (MPa)	W. H. R. (MPa)	True Strain
Room Temp.	34.30	63.70	68.8	0.39
200	24.11	45.13	46.9	0.37
250	22.20	35.80	40.2	0.36
300	16.10	25.11	32.5	0.40
350	12.98	18.40	26.6	0.41
400	9.25	11.78	22.4	0.46
450	8.12	9.00	20.2	0.47

Table 4.2 Tensile data obtained from the true stress-strain curves of the 2S aluminium deformed in tension.

Strain Rate = 5×10^{-2}				
Temperature°C	Y.S. (MPa)	U. T. S. (MPa)	W. H. R. (MPa)	True Strain
Room Temp.	293.3			0.097
250	238.8	349.5	1185.0	0.077
300	214.3	282.9	1068.0	0.085
350	171.7	209.5	876.3	0.089
375	100.1	109.5	485.5	0.114
400	69.6	71.5	117.2	0.120
450	54.6	56.2	387.5	0.136
Strain Rate = 5×10^{-3}				
Temperature°C	Y.S. (MPa)	U. T. S. (MPa)	W. H. R. (MPa)	True Strain
Room Temp.	283.9			0.094
250	200.3	308.3	1074.0	0.088
300	179.5	226.7	951.2	0.081
325	145.4	201.7	816.7	0.088
350	100.1	135.7	522.2	0.088
375	70.5	88.8	426.2	0.128
400	51.8	56.4	385.0	0.138
450	37.5	39.2	355.1	0.143
Strain Rate = 5×10^{-4}				
Temperature°C	Y. S. (MPa)	U.T.S. (MPa)	W. H. R. (MPa)	True Strain
Room Temp.	218.5	376.6	1224.0	0.110
250	182.5	259.7	948.0	0.120
300	141.1	177.6	604.0	0.098
350	76.8	89.2	438.0	0.094
400	41.4	43.6	336.0	0.107
450	34.2	36.7	312.5	0.125

Table 4.3 Tensile data obtained from the true stress-strain curves of the 2014/SiC composites deformed in tension.

Strain Rate = 5×10^{-2}				
Temperature°C	Y. S. (MPa)	U. T. S. (MPa)	W. H. R. (MPa)	True Strain
Room Temp.	217.1	385.5	585.6	0.20
200	189.79	291.7	507.0	0.18
250	181.16	236.7	461.0	0.14
300	166.6	195.9	397.0	0.10
350	105.7	118.8	298.0	0.08
400	55.7	62.4	221.0	0.18
450	47.4	51.2	187.2	0.23
Strain Rate = 5×10^{-3}				
Temperature°C	Y. S. (MPa)	U. T. S. (MPa)	W. H. R. (MPa)	True Strain
Room Temp.	202.8	369.6	497.0	0.21
200	176.13	278.5	430.0	0.18
250	156.6	231.17	396.0	0.14
300	132.1.	178.7	338.0	0.10
350	99.26	106.9	257.0	0.095
400	41.6	50.4	199.0	0.16
450	31.2	35.7	159.0	0.23
Strain Rate = 5×10^{-4}				
Temperature°C	Y. S. (MPa)	U. T. S. (MPa)	W. H. R. (MPa)	True Strain
Room Temp.	182.100	356.200	408.0	0.23
200	145.600	267.600	349.0	0.20
250	124.030	221.170	424.0	0.14
300	107.810	139.300	287.0	0.10
350	62.350	76.400	218.0	0.095
400	30.740	34.200	163.0	0.16
450	27.700	31.600	135.0	0.23

Table 4.4 Tensile data obtained from the true stress-strain curves of the 2014 alloy deformed in tension.

4.2 Fractography

Fig. 4.21 to 4.36 illustrates the fracture characteristics of the composite 2S/SiC and 2014 /SiC tested at strain rates of 5×10^{-4} and 5×10^{-2} S^{-1} at different temperatures by observing single fracture surfaces or matching pairsof fracture surfaces under SEM.

Fractured specimens revealed a fine equiaxed dimple morphology indicative of fracture occurring in a ductile manner. Quantitative measurements of mean dimple diameter at different temperatures and strain rates are shown in table 4.5. The fractured surfaces exhibited similar dimple shape at the high temperatures as observed for the lower temperatures except for a slight increase in the dimple size at the high temperature. The fractured surfaces of the composite 2S/SiC showed a coarser dimple network as compared to that of the composite 2014/SiC. The size of the dimples at the 2S/SiC fractured specimen surfaces were of the similar order of the grain size. 2014/SiC, however, had a dimple size much smaller than this parameter.

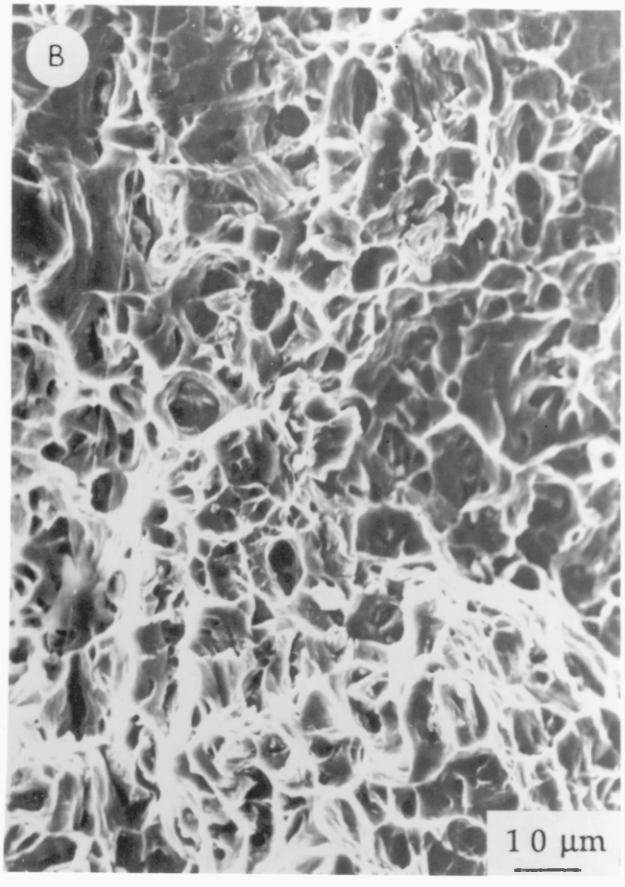
Fracture surfaces of the composites revealed slightly greater exposure of SiC particles at high temperatures, however, at low temperatures the particles were relatively less frequently observed on the fractured surface.

Fig. 4.21 SEM micrographs of the matching halves (a) and (b) of the 2S/SiC composite fracture surfaces after tensile testing at room temperature at a strain rate of $5 \times 10^{-4}\ S^{-1}$.

Fig. 4.22 SEM micrograph of the 2S/SiC composite fracture surface after tensile testing at 250°C at a strain rate of $5 \times 10^{-4}\ S^{-1}$.

Fig. 4.23 SEM micrograph of the 2S/SiC composite fracture surface after tensile testing at 350°C at a strain rate of $5 \times 10^{-4} S^{-1}$.


A
10 µm


B
10 µm


10 µm

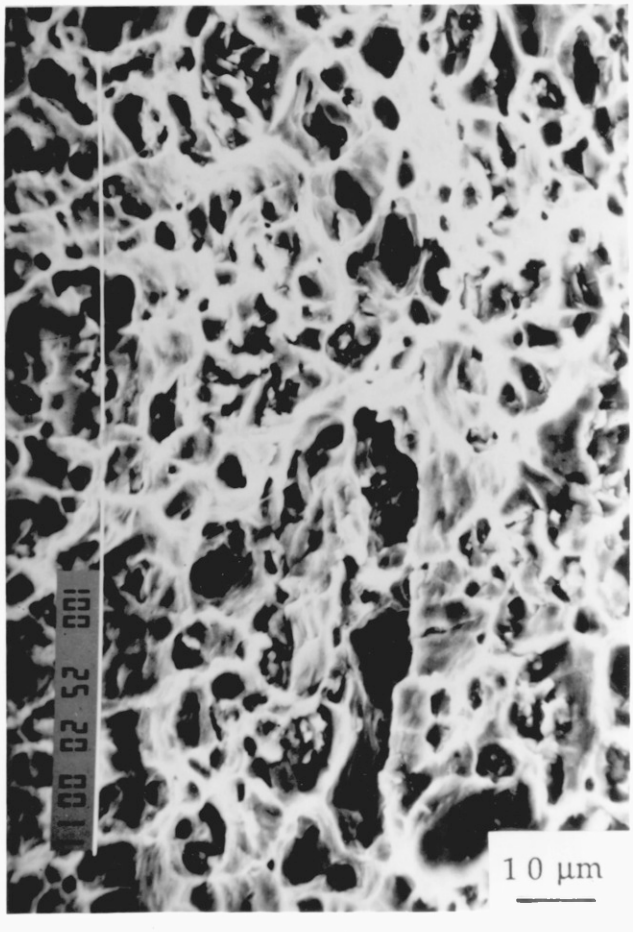
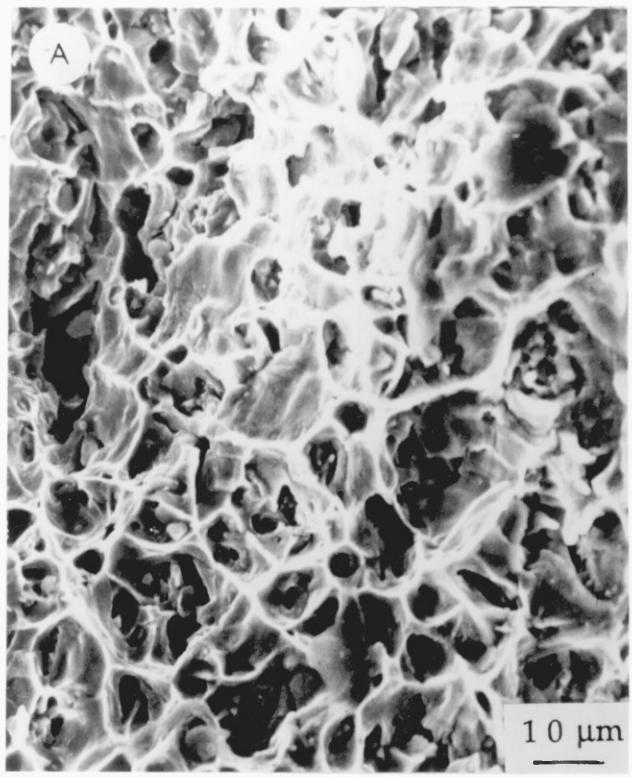
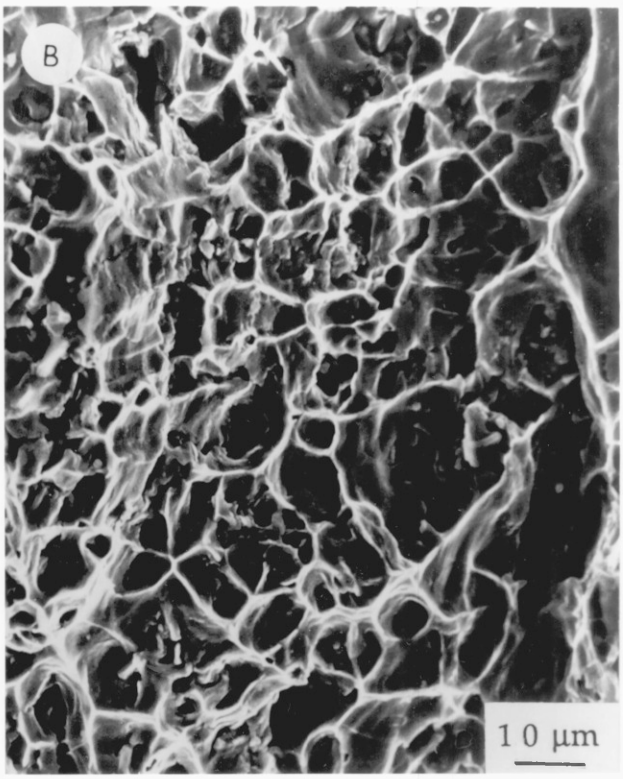
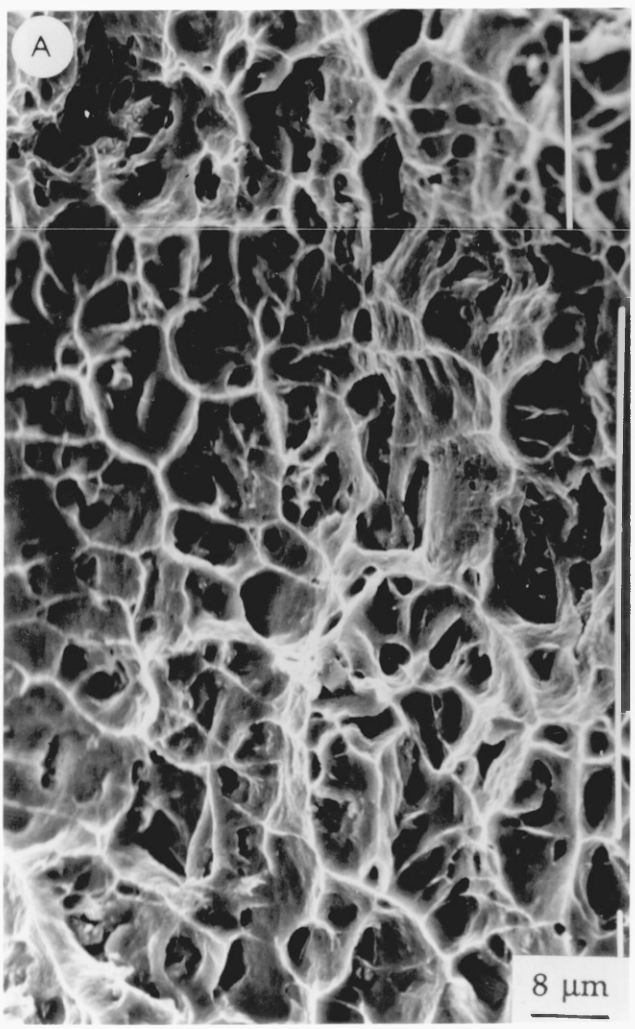

10 µm

Fig. 4.24 SEM micrographs of the matching halves (a) and (b) of the 2S/SiC fracture surfaces composite after tensile testing at 500°C at a strain rate of $5 \times 10^{-4}\ S^{-1}$.

Fig. 4.25 SEM micrographs of the matching halves (a) and (b) of the 2S/SiC fracture surfaces composite after tensile testing at room temperature at a strain rate of $5 \times 10^{-2}\ S^{-1}$.


A
10 µm


B
10 µm


A
8 µm

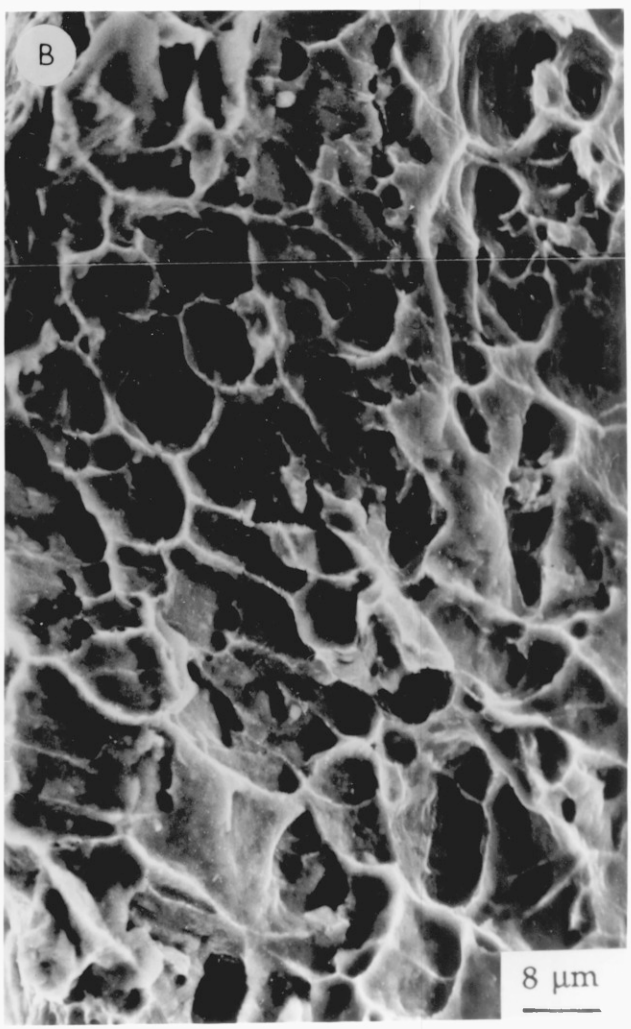
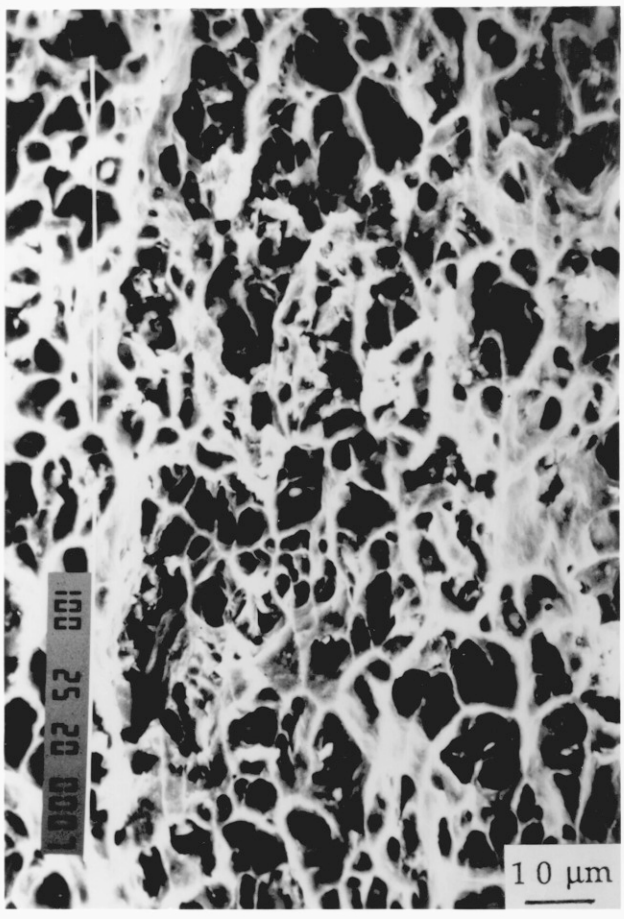

B
8 µm

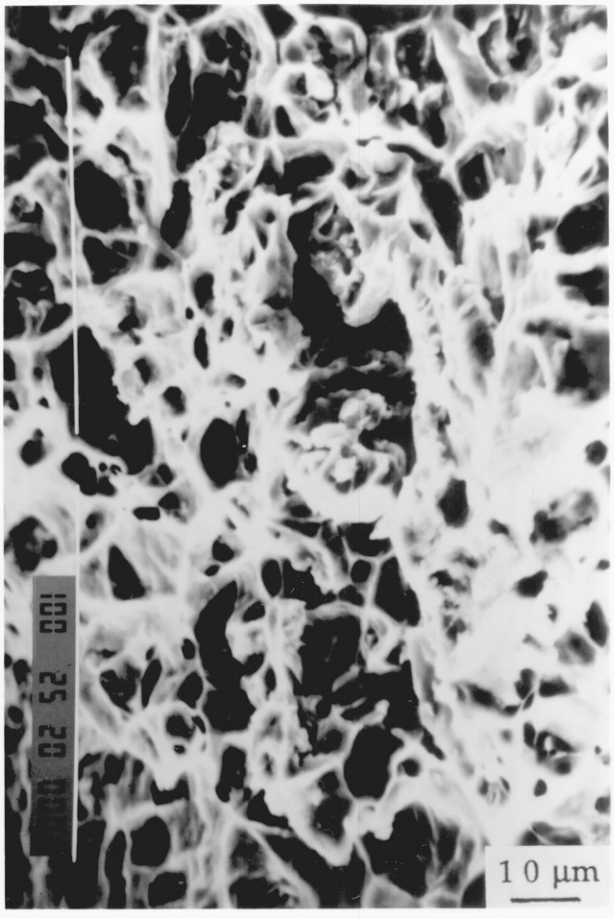
Fig. 4.26 SEM micrograph of the 2S/SiC composite fracture surface after tensile testing at 200°C at a strain rate of $5 \times 10^{-2} S^{-1}$.

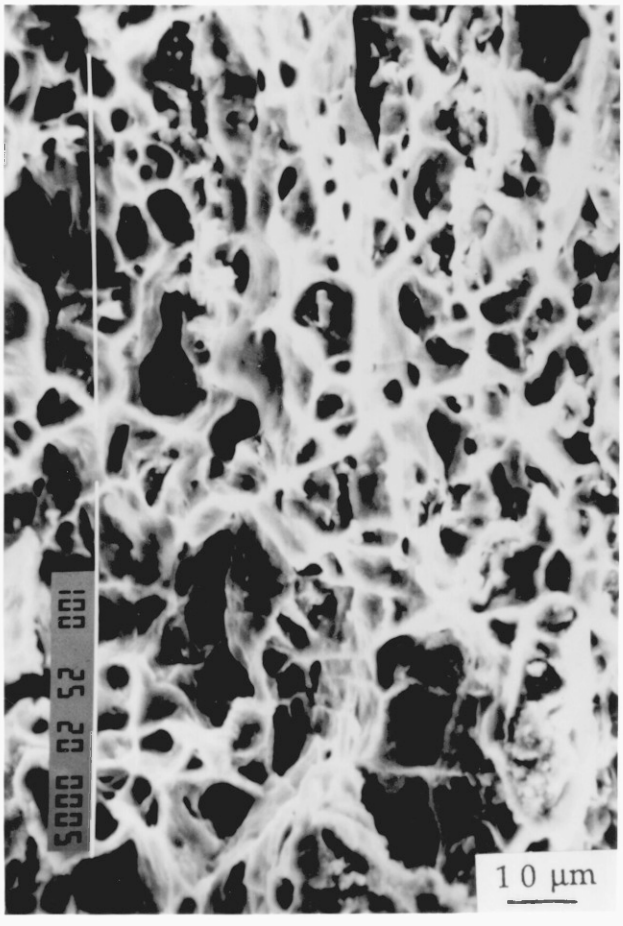
Fig. 4.27 SEM micrograph of the 2S/SiC composite fracture surface after tensile testing at 300°C at a strain rate of $5 \times 10^{-2} S^{-1}$.

Fig. 4.28 SEM micrograph of the 2S/SiC composite fracture surface after tensile testing at 400°C at a strain rate of $5 \times 10^{-2} S^{-1}$.

Fig. 4.29 SEM micrograph of the 2S/SiC composite fracture surface after tensile testing at 500°C at a strain rate of $5 \times 10^{-2} S^{-1}$.


10 µm


10 µm


10 µm

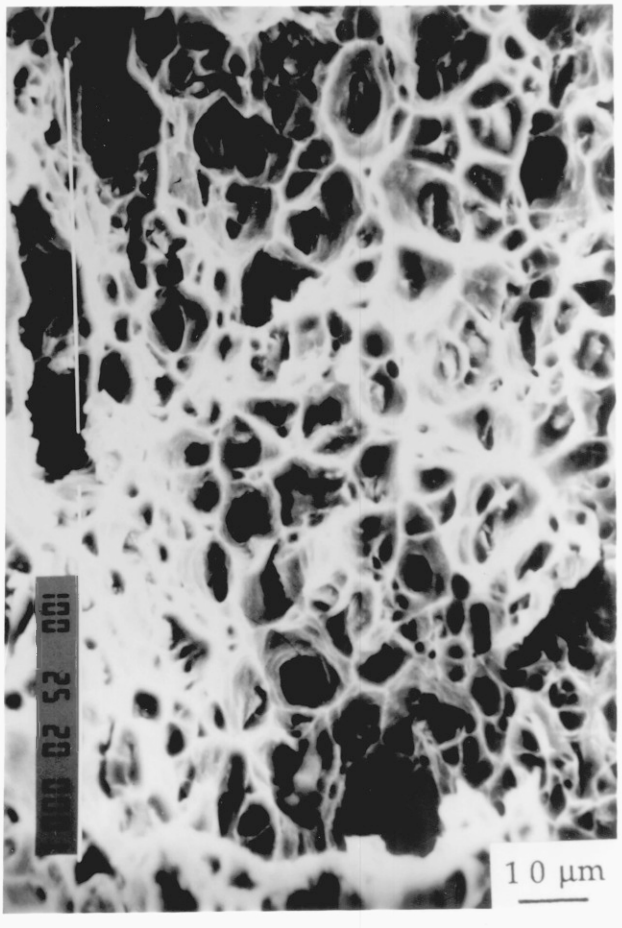
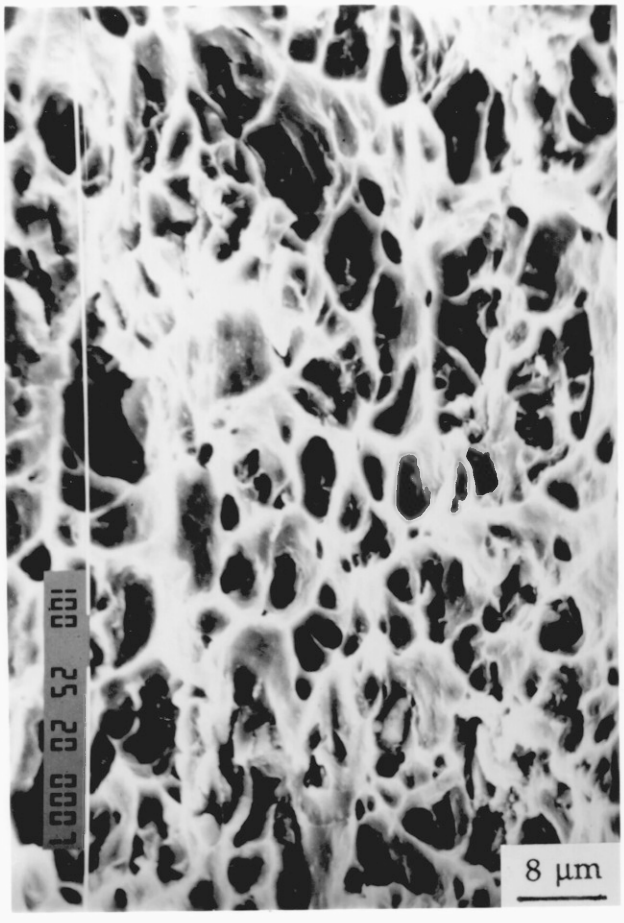

10 µm

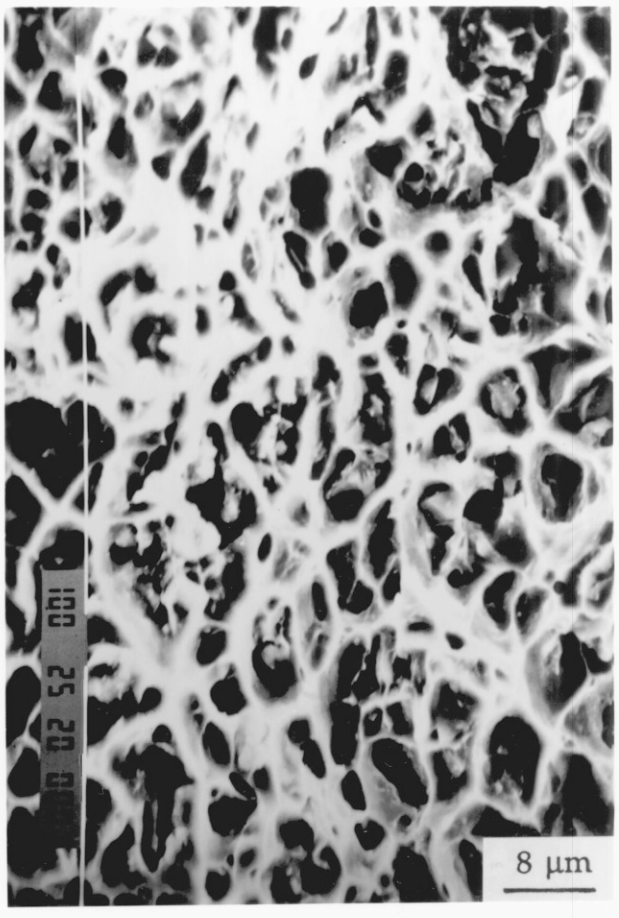
Fig. 4.30 SEM micrograph of the 2014/SiC composite fracture surface after tensile testing at room temperature at a strain rate of $5 \times 10^{-4} S^{-1}$.

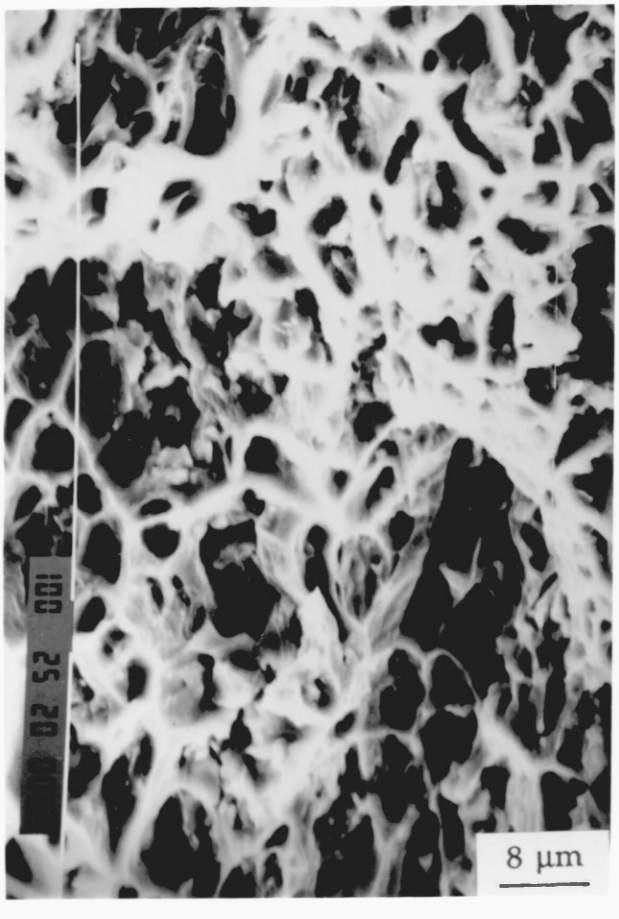
Fig. 4.31 SEM micrograph of the 2014/SiC composite fracture surface after tensile testing at 250°C at a strain rate of $5 \times 10^{-2} S^{-1}$.

Fig.4.32 SEM micrograph of the 2014/SiC composite fracture surface after tensile testing at 350°C at a strain rate of $5 \times 10^{-2} S^{-1}$.

Fig.4.33 SEM micrograph of the 2014/SiC composite fracture surface after tensile testing at 500°C at a strain rate of $5 \times 10^{-2} S^{-1}$.


8 µm


8 µm


8 µm

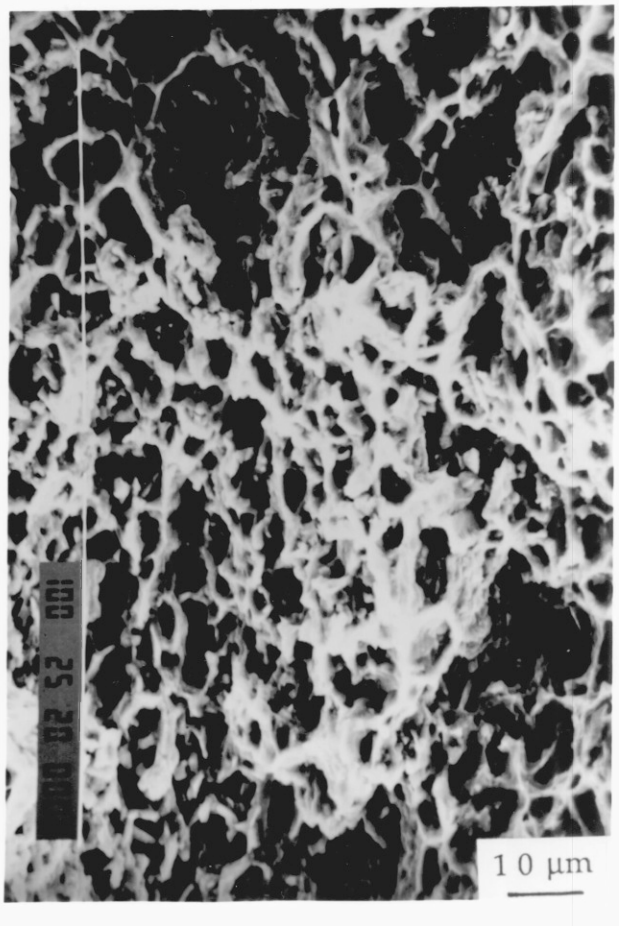
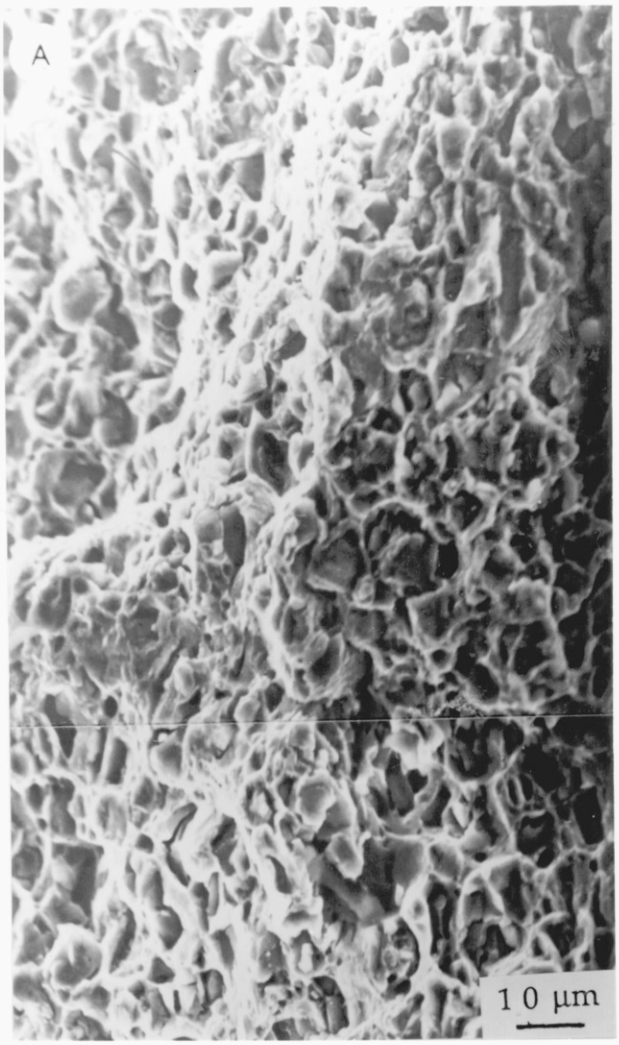
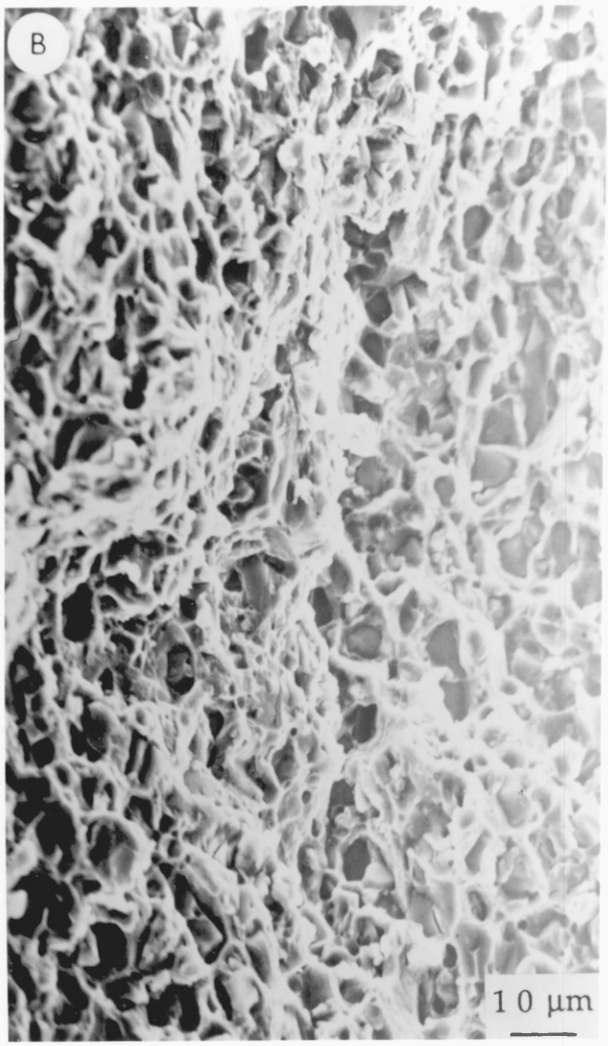

10 µm

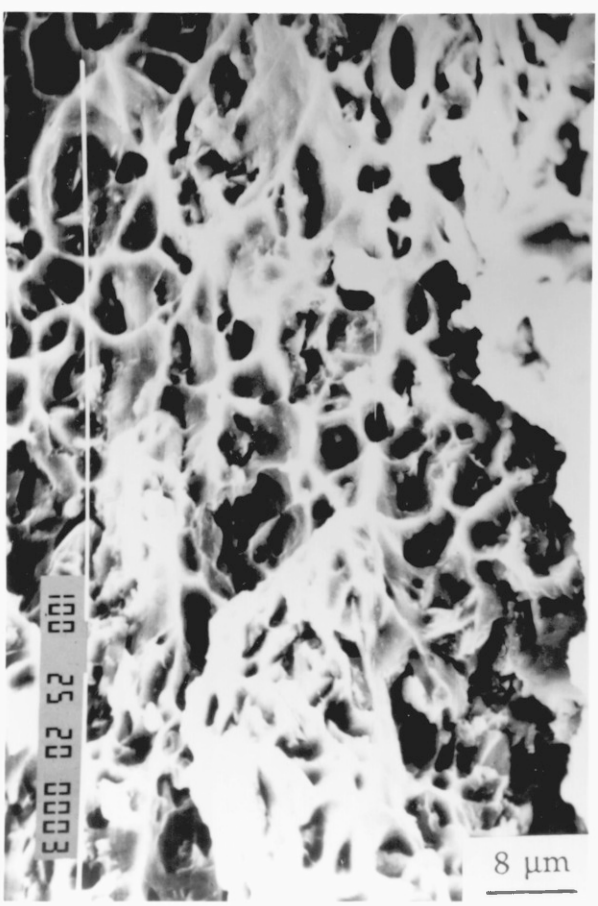
Fig. 4.34 SEM micrographs of the matching halves (a) and (b) of the 2014/SiC composite fracture surfaces after tensile testing at room temperature at a strain rate of $5 \times 10^{-2}\ S^{-1}$.

Fig.4.35 SEM micrograph of the 2014/SiC composite fracture surface after tensile testing at 300°C at a strain rate of $5 \times 10^{-2}\ S^{-1}$.

Fig. 4.36 SEM micrograph of the 2014/SiC composite fracture surface after tensile testing at 500°C at a strain rate of $5 \times 10^{-2}\ S^{-1}$.


A
10 µm


B
10 µm


8 µm

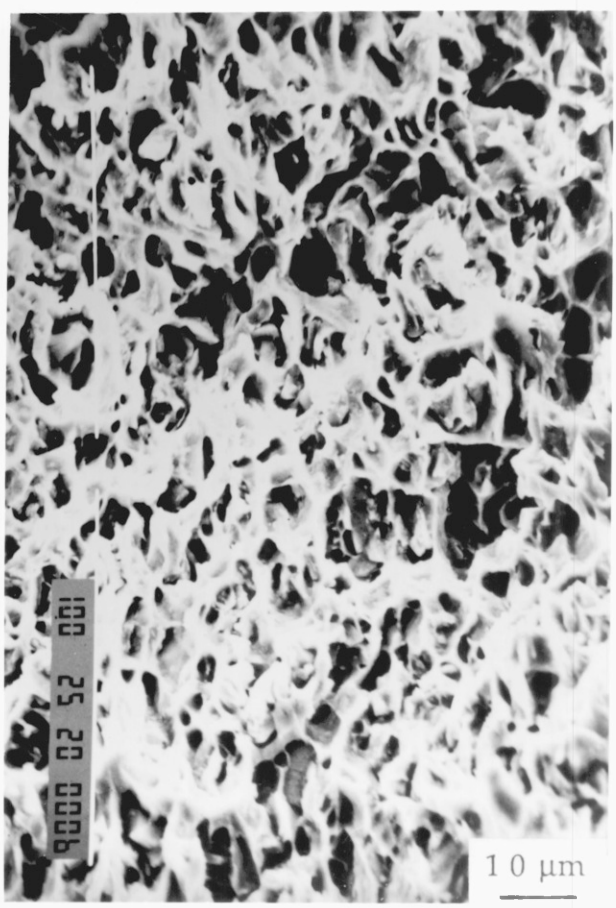

10 µm

Table 4.5 (a)

	Size of Dimples at Different Strain Rates	
Temperature°C	5×10^{-4} S^{-1} (μm)	5×10^{-2} S^{-1} (μm)
200° C	8.0	7.5
300°C	8.0	7.5
400°C	8.1	7.6
500°C	8.5	7.6

Table 4.5 (b)

	Size of Dimples at Different Strain Rates	
Temperature°C	5×10^{-4} S^{-1} (μm)	5×10^{-2} S^{-1} (μm)
200° C	5.9	5.8
300°C	6.2	5.8
400°C	6.3	6.1
500°C	6.5	6.1

Table 4.5 Average dimple size observed on the fracture surface of the composite (a) 2S/SiC and (b) 2014/SiC deformed in tension.

CHAPTER 5

(RESULTS)

Annealed Microstructure and Recrystallization of the Deformed Composites and their Matrix Alloys.

5.1 Introduction.

The presence of second phase particles can effectively modify the mechanisms and various aspects of recrystallization such as kinetics and the final grain size and therefore play an important role in the thermo-mechanical processing of many alloys. Particles are important in affecting both the deformation structure and recrystallization of the materials. Metal matrix composites when deformed and annealed, show recrystallization behaviour strongly influenced by the reinforcing SiC particles. The present study is concerned with the effect of these particles on the recrystallization of the 2S and 2014 matrix composites plus the complementary study of the recrystallization of the unreinforced matrix alloys as a comparison.

5.2 Hardness Measurements.

Isochronal hardness curves were determined for one hour annealing at different temperatures between 200 and 500°C for the composites 2S/SiC and 2014/SiC cold rolled 20, 35, 50, and 70 percent and the matrix alloys 2S and 2014 cold rolled 20, 50, and 70 percent using Vickers hardness measurements on polished sections.

Isothermal curves were obtained by measuring hardness against

varying annealing time for the composites 2S/SiC and 2014/SiC cold rolled 50 and 70 percent at 250 and 360°C.

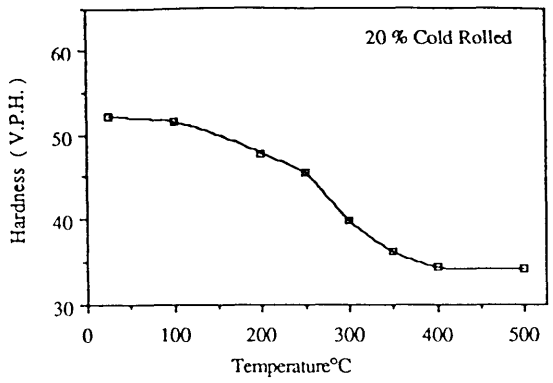
5.2.1 Isochronal Annealing of 2S (Composite and Matrix Alloy).

Figs. 5.1 and 5.2 show the variation of hardness as a function of temperature for both, the composite 2S/SiC and the matrix aluminium (2S) deformed to various amounts and annealed for one hour between 200 and 500°C. Fig 5.1 revealed that recrystallization occurred between 250 and 300°C for the composite. The higher the amount of rolling, the sharper the fall in the hardness curve until recrystallization is complete where the hardness curve again became steady.

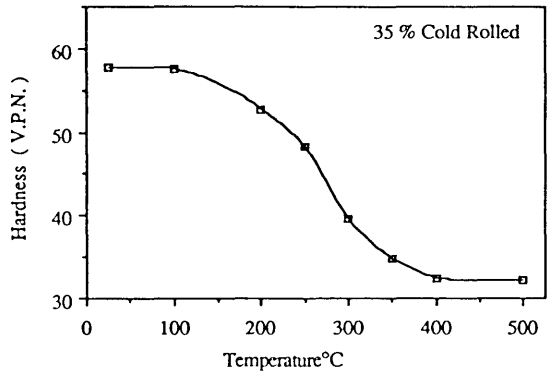
The unreinforced 2S alloy recrystallized at a temperature about 70 degrees higher than the composite at around 350°C (fig. 5.2).

5.2.2 Isochronal Annealing of 2014 (Composite and Matrix Alloy).

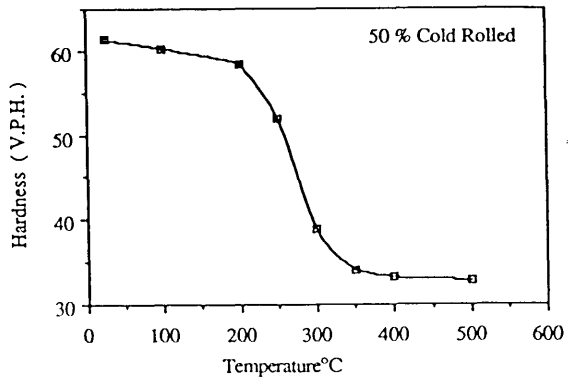
Results are plotted in figs. 5.3 and 5.4 as hardness versus annealing temperature for 2014/SiC and matrix alloy respectively. The decrease in the hardness in the curve for the composite 2014/SiC started at about 300°C and showing a drop down to 400°C after which at 425°C, the curve again started rising. The hardness of the specimen annealed at 500°C again rose to a higher value close to the cold rolled hardness level.



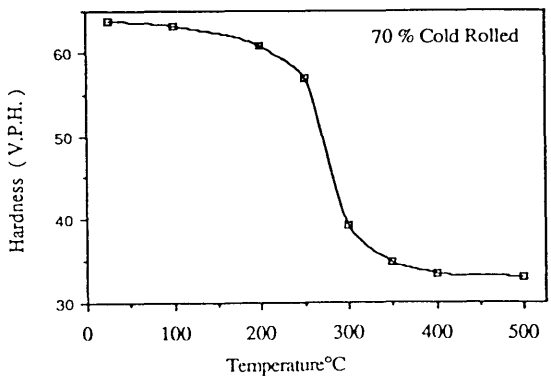
5.1 (a)



5.1 (b)

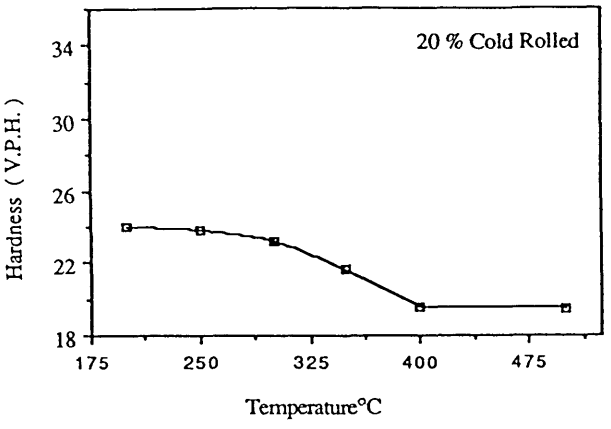


5.1 (c)

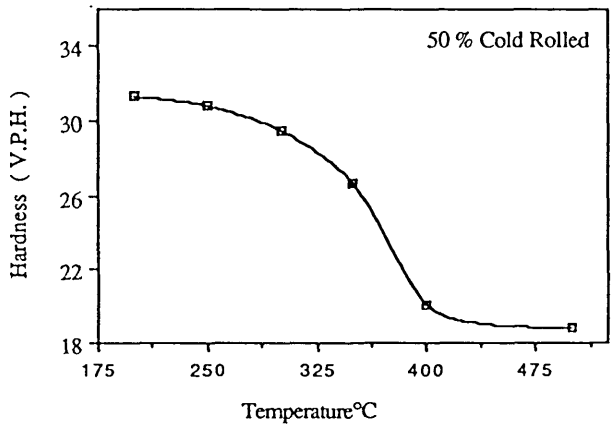


5.1 (d)

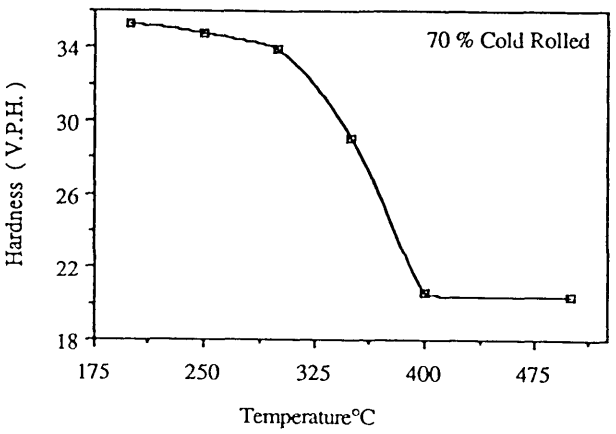
Fig. 5.1 Vickers hardness as a function of temperature for the 2S/SiC composite, cold rolled to (a) 20%, (b) 35%, (c) 50%, and (d) 70% and annealed for one hour.



5.2 (a)

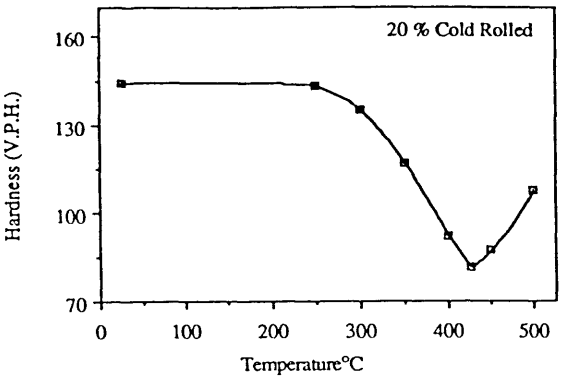


5.2 (b)

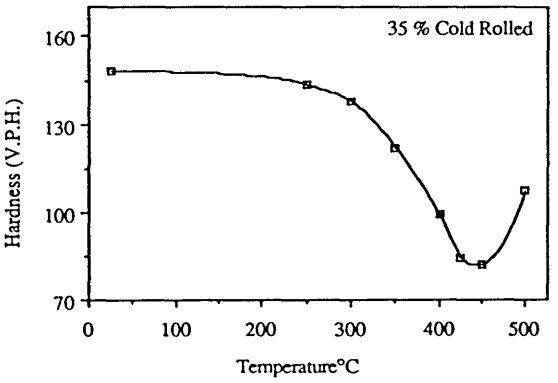


5.2 (c)

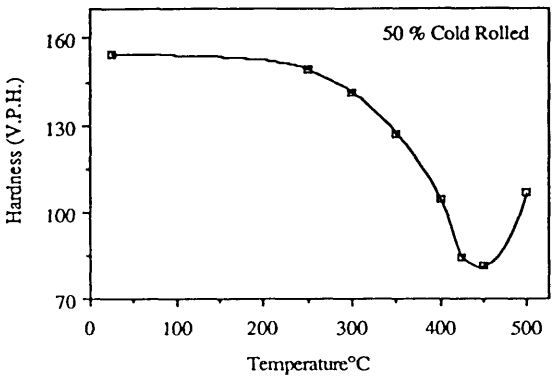
Fig. 5.2 Vickers hardness as a function of temperature for the 2S aluminium, cold rolled to (a) 20%, (b) 50%,and (c) 70% and annealed for one hour.



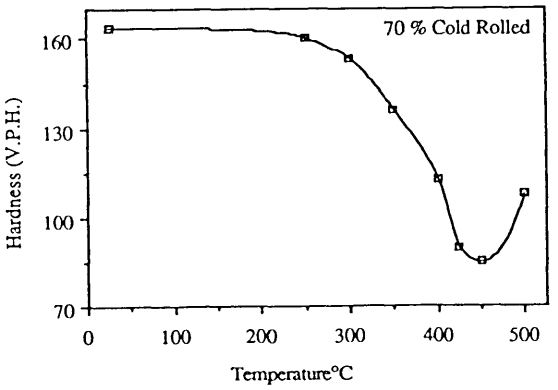
5.3 (a)



5.3 (b)

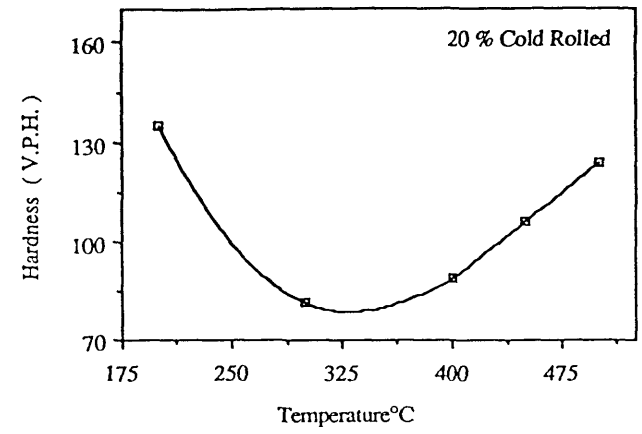


5.3 (c)

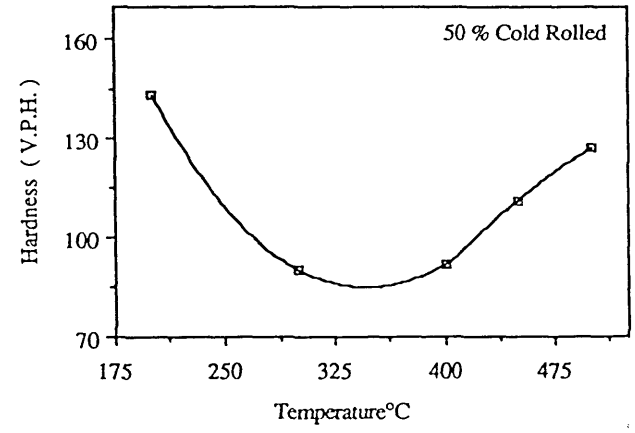


5.3 (d)

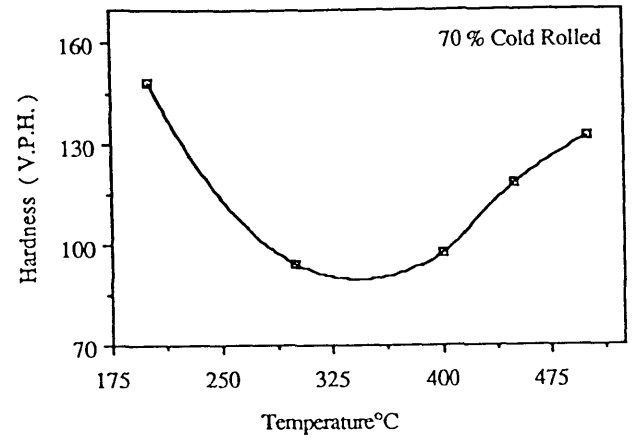
Fig. 5.3 Vickers hardness as a function of temperature for the 2014/SiC composite, cold rolled to (a) 20%, (b) 35%, (c) 50%, and (d) 70% and annealed for one hour.



5.4 (a)



5.4 (b)



5.4 (c)

Fig. 5.4 Vickers hardness as a function of temperature for the 2014 alloy, cold rolled to (a) 20%, (b) 50%,and (c) 70% and annealed for one hour.

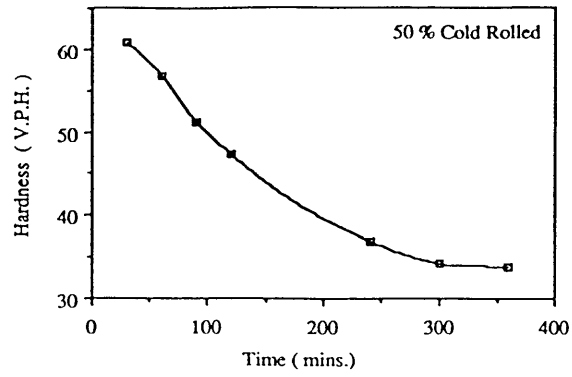
5.2.3 Isothermal Annealing of the Composites.

Figs. 5.5 and 5.6 show a similar trend of gradual fall in the hardness curves for 70 and 50 percent deformed 2S/SiC and 2014/SiC composites on isothermally annealing at 250 and 360°C up to 400 and 300 minutes respectively, and becoming level after 300 and 160 minutes respectively to indicate the completion of the recrystallization.

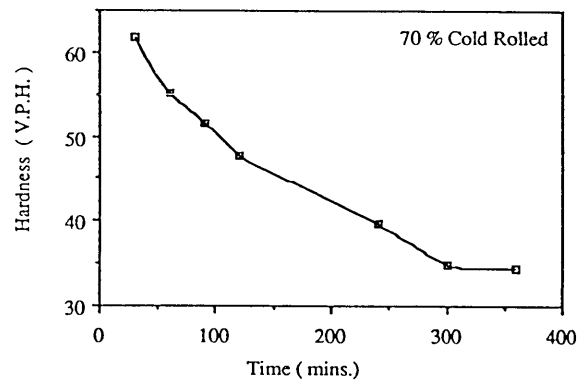
5.3 Effect of Strain and Annealing Temperature on the Microstructure During Recrystallization.

The aim of the investigation presented in this section is to examine the microstructural changes occurring in the composites which have been cold rolled to different amounts and then annealed at various temperatures. The optical microstructure of the hot rolled and annealed 2S/SiC and 2014/SiC composite prior to the cold rolling is shown in figs. 5.7 and 5.8.

Following the hot rolling, cold deformation of the 2S/SiC and 2014/SiC composites was carried out. This consisted of unidirectional rolling until total thickness reductions of 20, 35, 50 and 70 percent were obtained then the cold rolled material was annealed at temperatures between 200 and 500°C for one hour and water quenched. Unreinforced 2S and 2014 matrix alloys have been cold rolled to 20, 50 and 70 percent and similarly annealed for the comparison study.

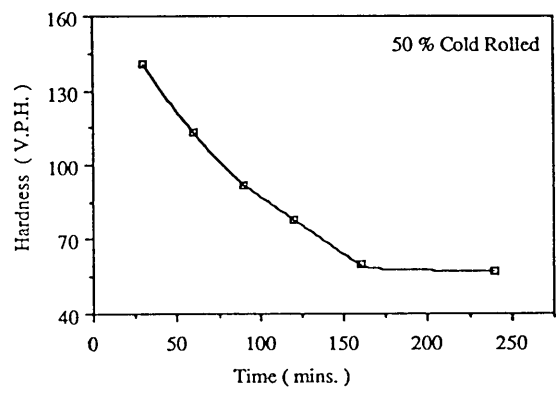


5.5 (a)

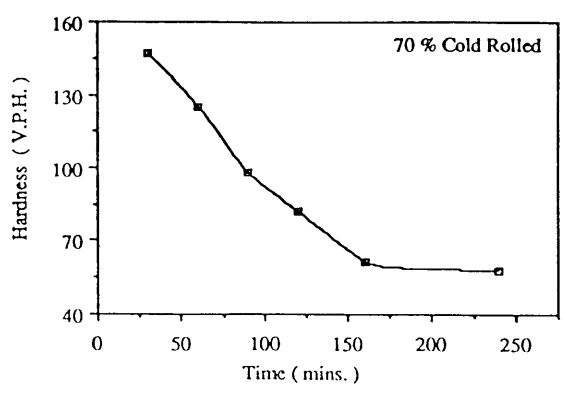


5.5 (b)

5.5 Vickers hardness as a function of time for the 2S/SiC composite, cold rolled to (a) 50% and (b) 70% and annealed at 250°C.



5.6 (a)



5.6 (b)

5.6 Vickers hardness as a function of time for the 2014/SiC composite, cold rolled to (a) 50% and (b) 70% and annealed at 360°C.

5.3.1 Observations Using Optical Microscopy for 2S (Composite and Matrix Alloy).

The structure of the cold rolled 2S/SiC composite consisted of grains which were elongated in the rolling direction (fig. 5.9).

Optical micrographs (fig. 5.10 to 5.13) show the microstructure of the composite 2S/SiC deformed 70, 50, 35, and 20 percent respectively which have been annealed at different temperatures in the range between 200 and 500°C for one hour. Annealing up to 250°C did not reveal any change in the microstructure compared to that at 200°C. A change was, however, observed in the structure between 250 and 300°C. Annealing at or above 300°C resulted in a fine equiaxed recrystallized grain structure achieved by introducing a large number of nucleation sites around SiC particles and the grain size corresponding to the distribution of the particles . The average grain size measurements (mean intercept length) for both the cold deformed unrecrystallized and completely recrystallized state for various cold reduction levels are given in the table 5.1 . The recrystallized grain size measurements given are the results taken from the samples annealed for one hour at 500°C which is observed to be the completely recrystallized state because fifty percent cold rolled 2S/SiC composite, when annealed at 300°C for 48 hours (fig. 5.17) resulted in the same average grain size as for that annealed at 500°C for one hour.

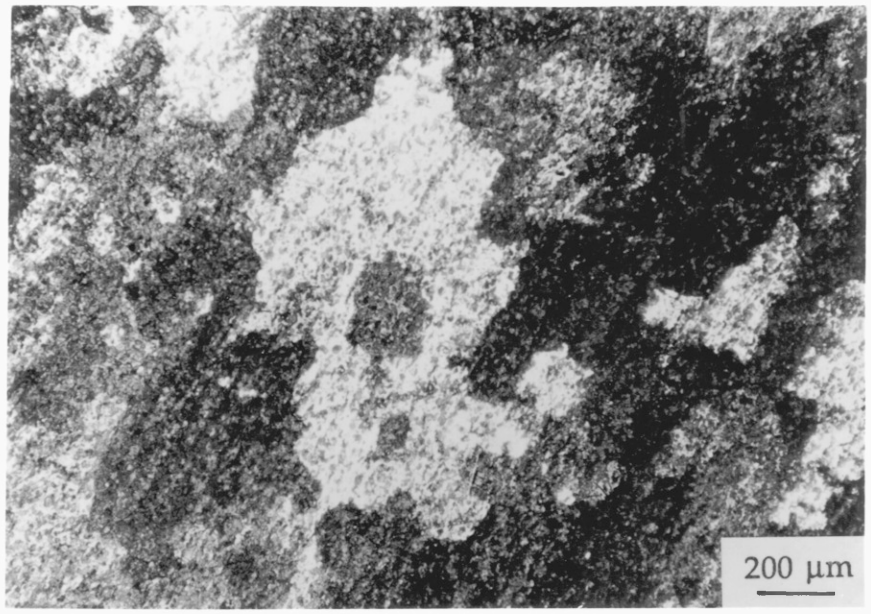
Table 5.1 shows that the average recrystallized grain size did not appreciably change as the amount of deformation decreased except for the specimen deformed 20 percent which had a significantly larger grain size.

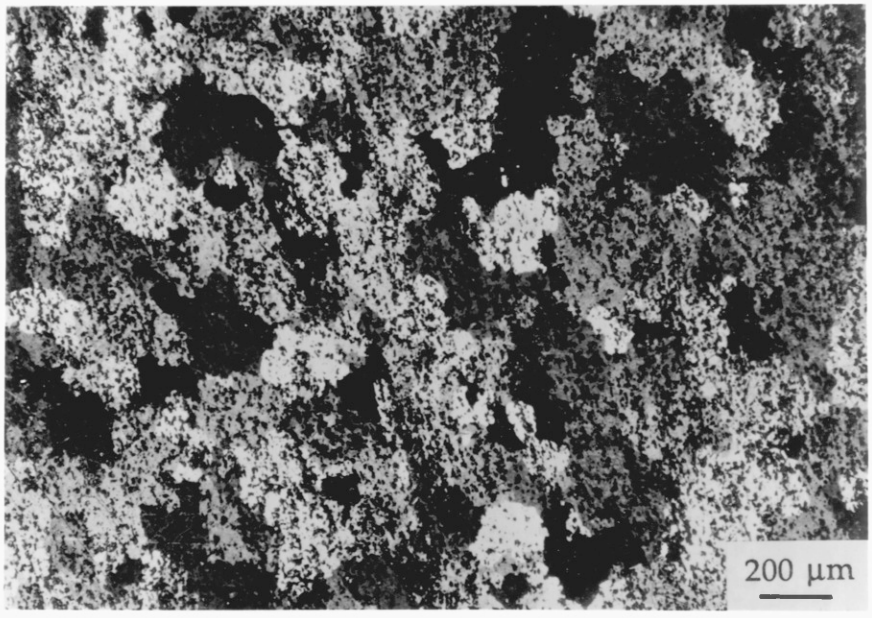
Figs. 5.14 to 5.16 show a series of optical micrographs illustrating the effect of annealing of 2S alloy which has been rolled 20, 50 or 70 % for one hour between 200 and 500°C. The 2S alloy, as revealed in these figs., started

Fig. 5.7 Optical micrograph of the 2S/SiC composite after 50% hot rolling.

Fig. 5.8 Optical micrograph of the 2014/SiC composite after 50% hot rolling.

Fig. 5.9 Optical micrograph of the 2S/SiC composite after 50% cold rolling.


200 µm


200 µm

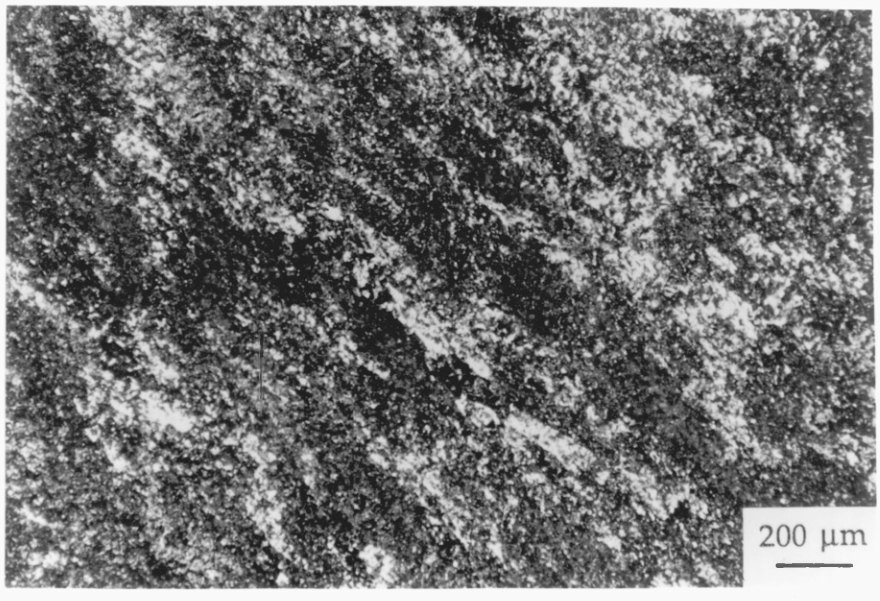

200 µm

Fig. 5.10 Optical micrographs of the 2S/SiC composite, 70 % cold rolled and annealed for one hour at (a) 200°C, (b) 300°C, (c) 400°C,and (d) 500°C.

5.10 (a)

5.10 (b)

5.10 (c)

5.10 (d)

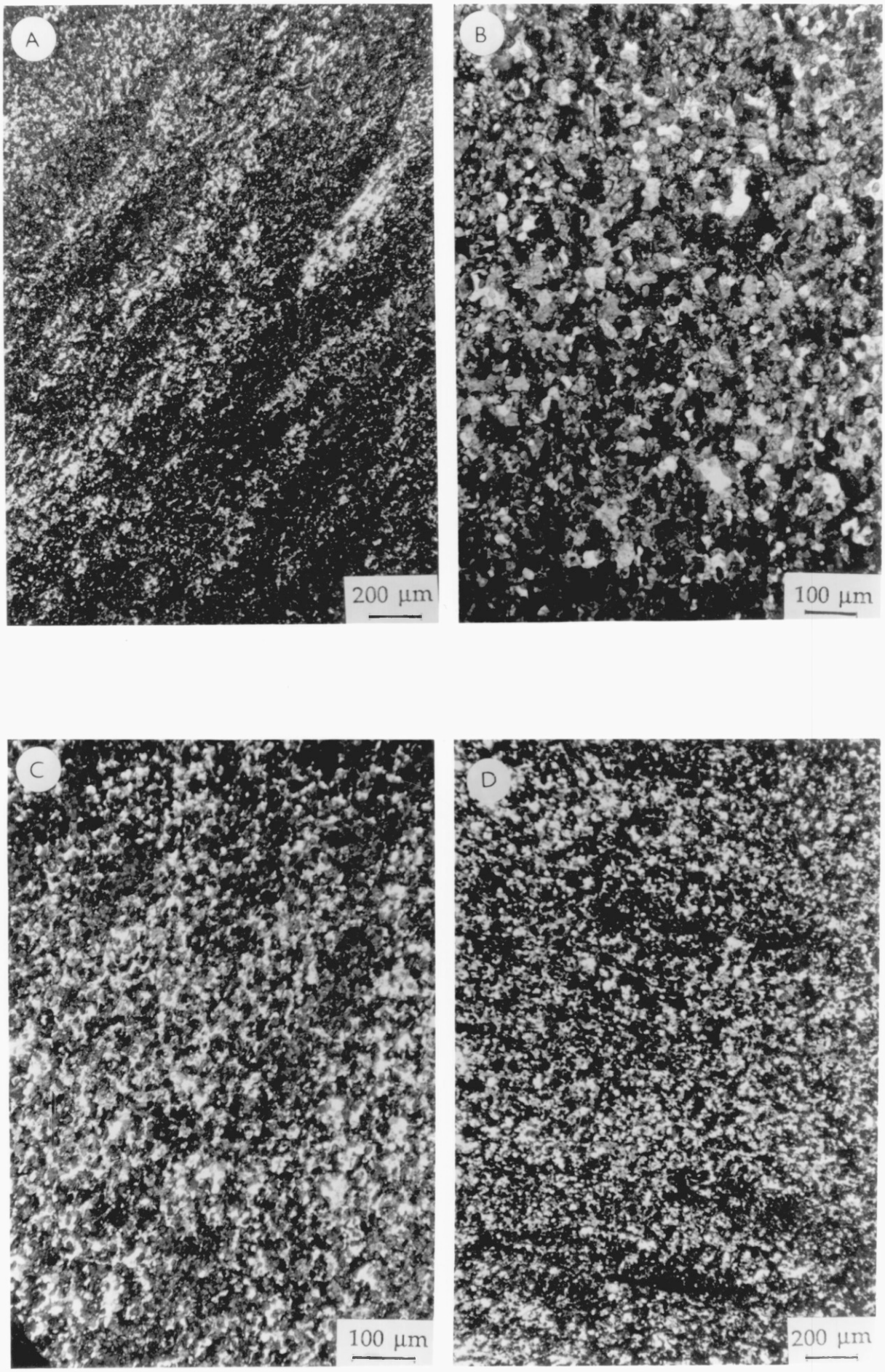

A
200 µm
B
100 µm
C
100 µm
D
200 µm

Fig. 5.11 Optical micrographs of the 2S/SiC composite, 50 % cold rolled and annealed for one hour at (a) 200°C, (b) 300°C, and (c) 400°C (d) 500°C.

5.11 (a)

5.11 (b)

5.11 (c)

5.11 (d)

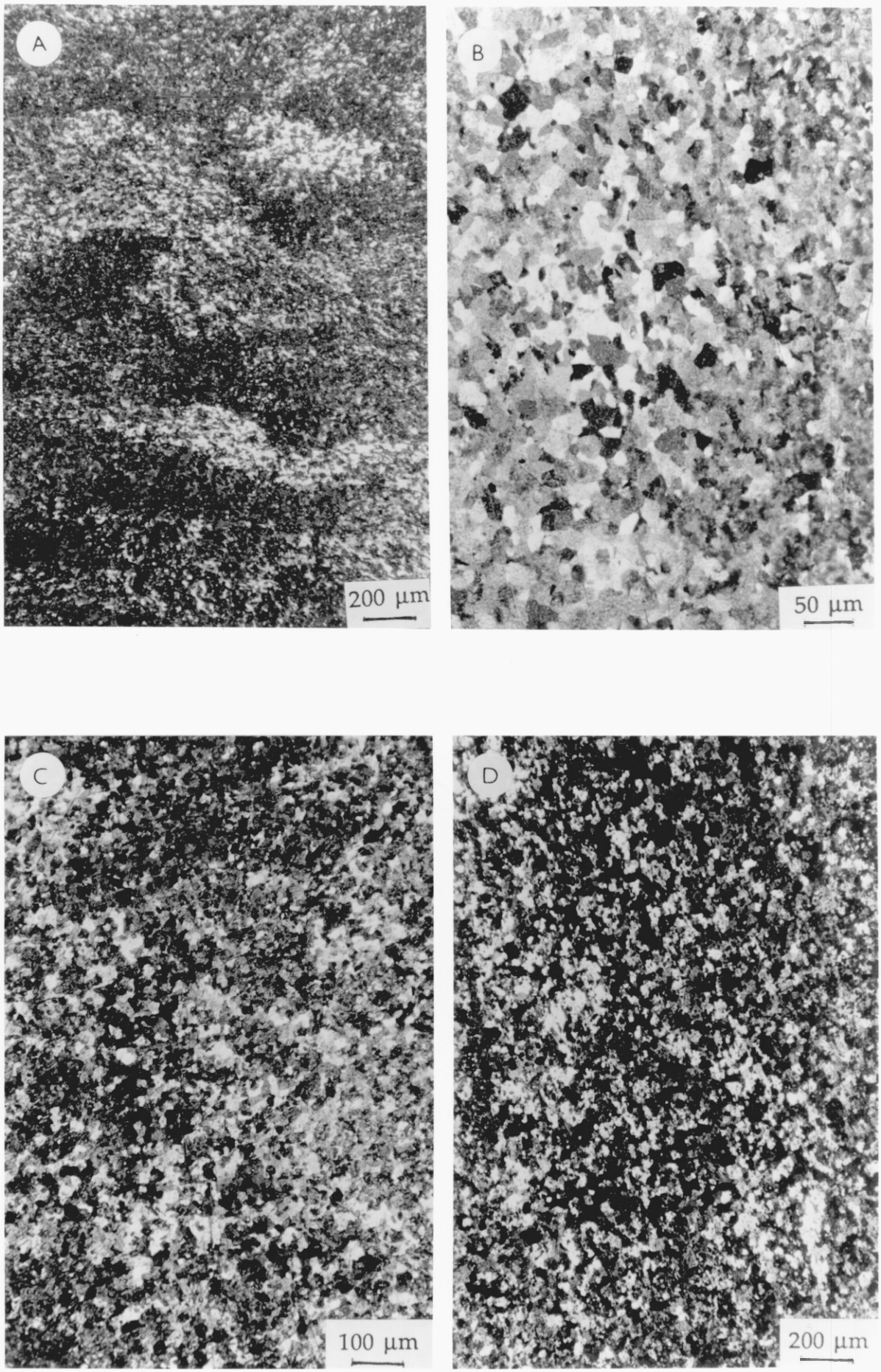

A
200 µm
B
50 µm
C
100 µm
D
200 µm

Fig. 5.12 Optical micrographs of the 2S/SiC composite, 35 % cold rolled and annealed for one hour at

(a) 200°C,

(b) 300°C, and

(c) 500°C.

Fig. 5.13 Optical micrographs of the 2S/SiC composite, 20 % cold rolled and annealed for one hour at

(a) 200°C,

(b) 300°C, and

(c) 500°C.

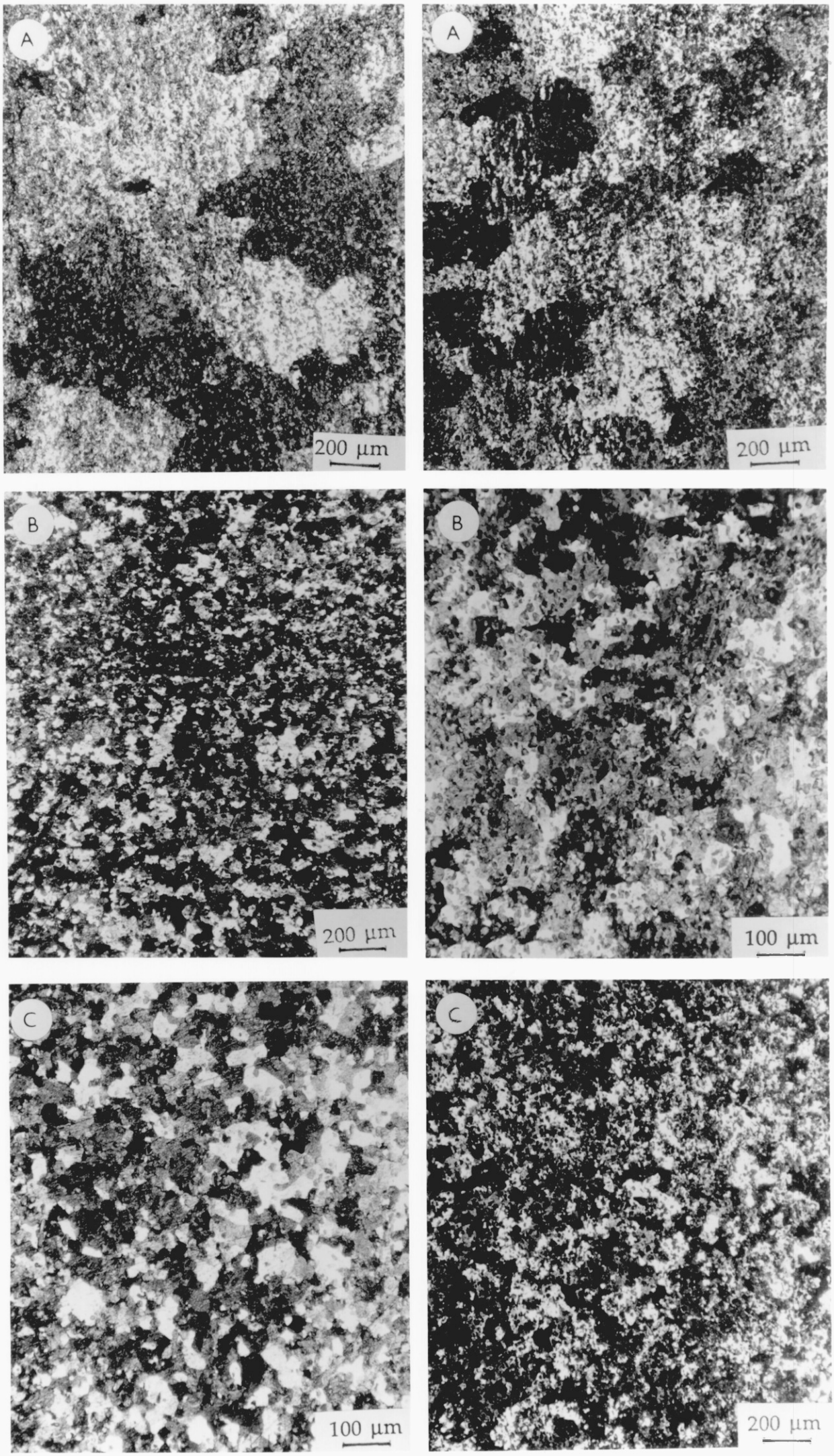
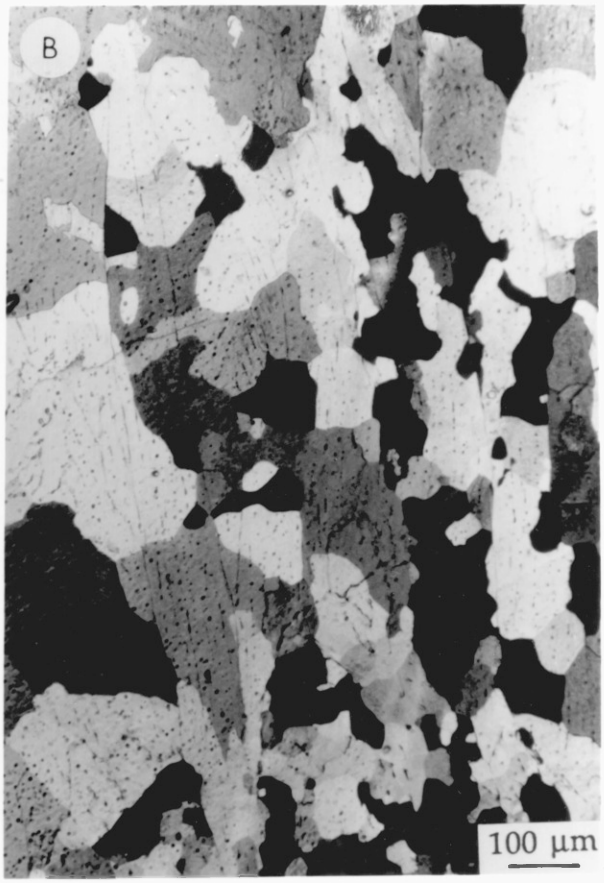

A
200 µm
A
200 µm
B
200 µm
B
100 µm
C
100 µm
C
200 µm

Fig. 5.14 Optical micrographs of the 2S aluminium, 70 % cold rolled and annealed for one hour at (a) 200°C and (b) 500°C.

Fig. 5.15 Optical micrographs of the 2S aluminium, 50 % cold rolled and annealed for one hour at (a) 200°C and (b) 500°C.


A
100 µm


B
100 µm


A
100 µm

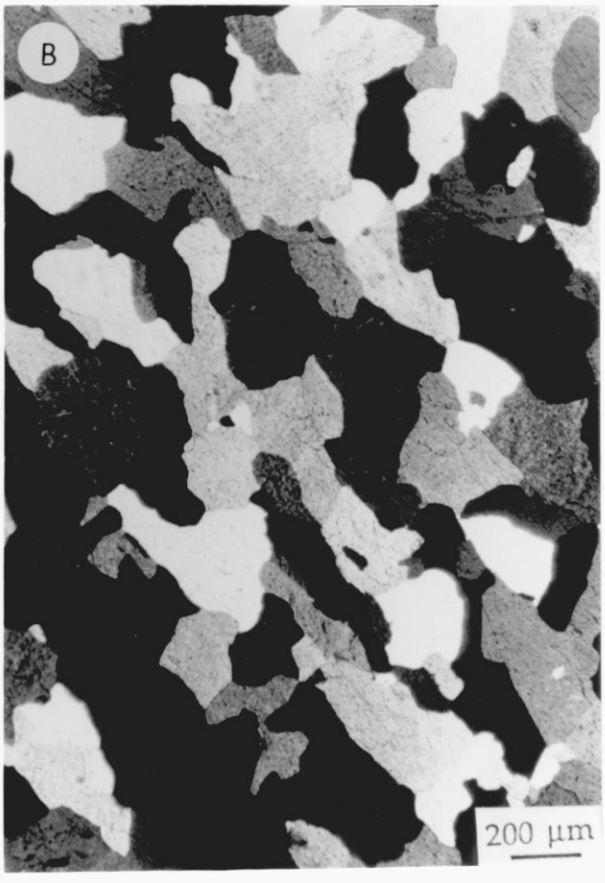
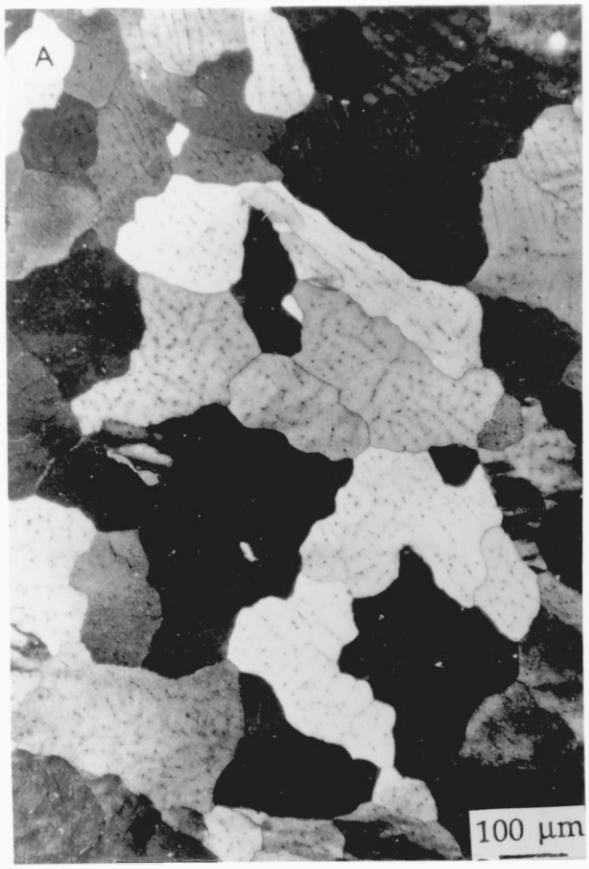
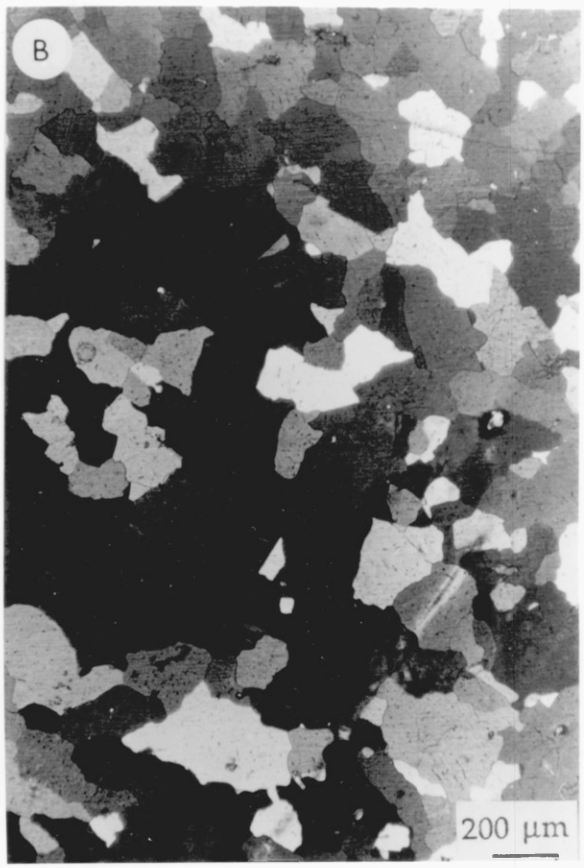

B
200 µm

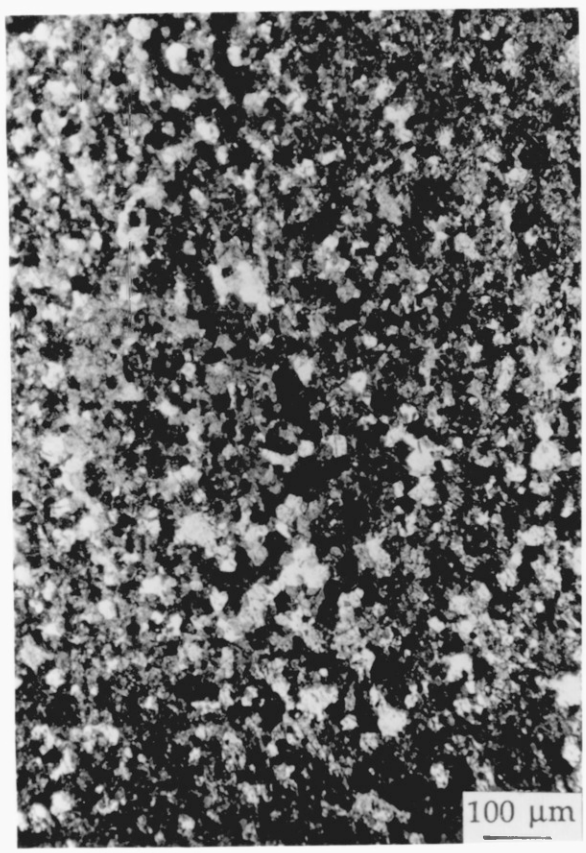
Fig. 5.16 Optical micrographs of the 2S aluminium, 20 % cold rolled and annealed for one hour at (a) 200°C and (b) 500°C.

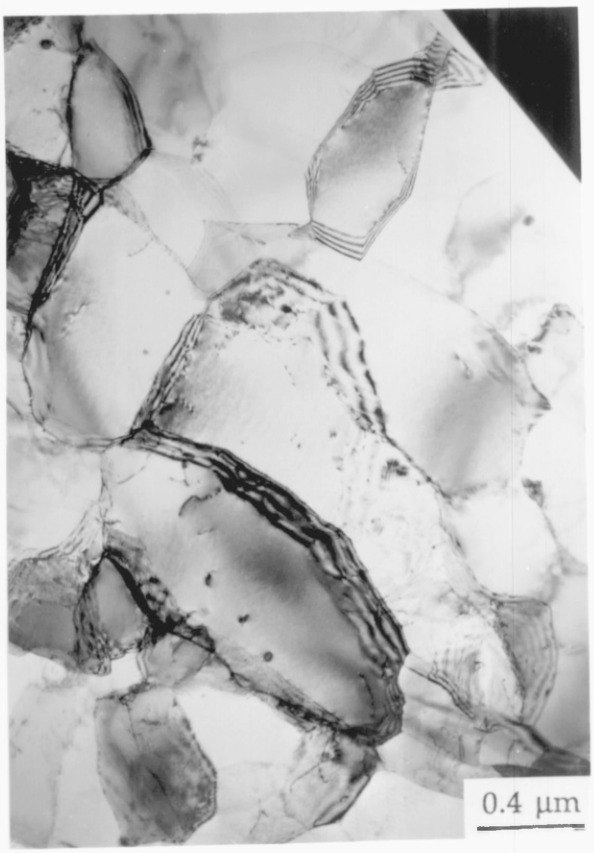
Fig. 5.17 Optical micrographs of the 2S/SiC composite, 50 % cold rolled and annealed for 48 hours at 300°C.

Fig. 5.18 TEM of the 2S/SiC composite after 50% cold rolling.


A
100 µm


B
200 µm


100 µm


0.4 µm

to recrystallize at 350°C and was completely recrystallized at 500°C. Unrecrystallized grains were elongated in the rolling direction and turned into small equiaxed grains after recrystallization but were about eight times greater in size compared to the recrystallized grain size of the composite 2S/SiC.

Table 5.2 shows the grain size of the unrecrystallized and recrystallized condition of 2S alloy annealed for various levels of cold reduction.

5.3.2. Observations Using T.E.M. For 2S/SiC Composite.

T.E.M. of the cold rolled 2S/SiC showed a deformed structure with well defined sub-grains of a very fine average size of 0.7 μm (fig. 5.18), indicative of rapid dynamic recovery. Similar structure persisted during annealing until recrystallized, as seen in the figs. 5.19 and 5.20 for 70 and 50 percent composites annealed at temperatures below 300°C. The average sub-grain size developed in 50 and 70 percent cold deformed 2S/SiC composite during annealing prior to recrystallization is given in table 5.3.

The recrystallized structure of the composite for 70 and 50 percent cold rolled and annealed for one hour at 400 and 500°C showed a dislocation density throughout the microstructure which gave the effect of the structure similar to the one recrystallized and cold deformed but with more evenly distributed dislocations and little substructure formation in the matrix. The dislocation density was relatively high near the particle / matrix interface indicating that the plastic flow had taken place from particle into the matrix during quenching.

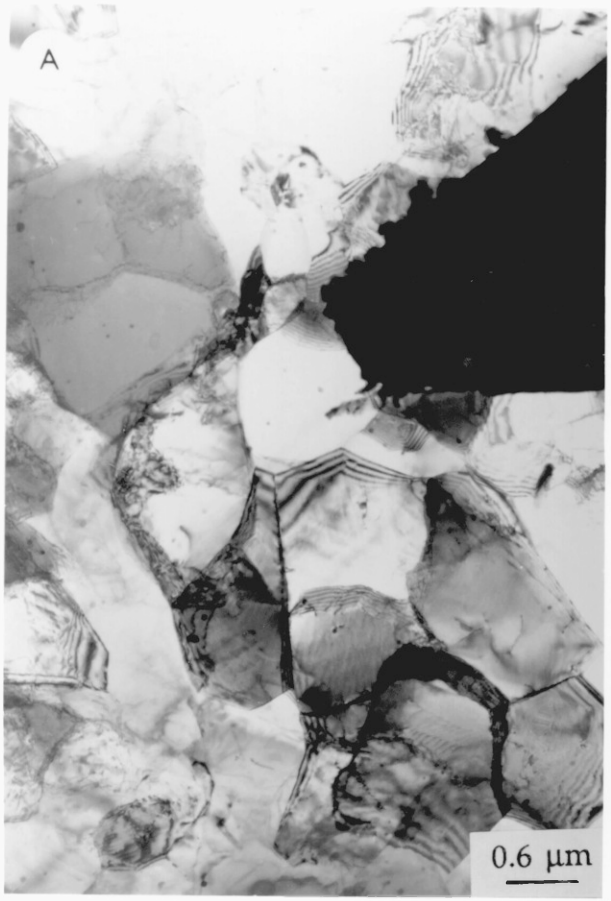
Fig. 5.19 TEMof the 2S/SiC composite, 70 % cold rolled and annealed for one hour at (a) 200°C, (b) 300°C, (c) 400°C, and (d) 500°C.

5.19 (a)

5.19 (b)

5.19 (c)

5.19 (d)


A
0.6 µm


B
1.0 µm


C
0.4 µm

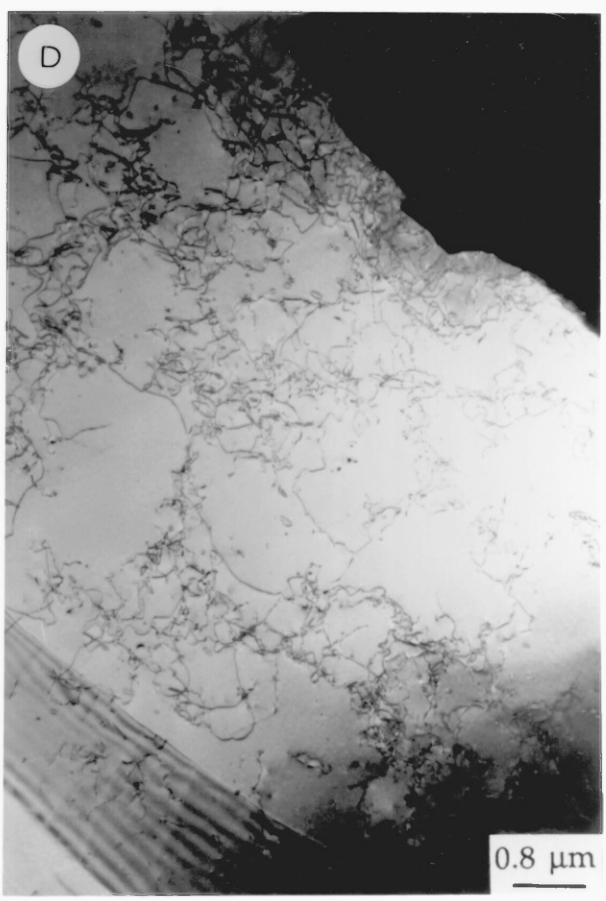

D
0.8 µm

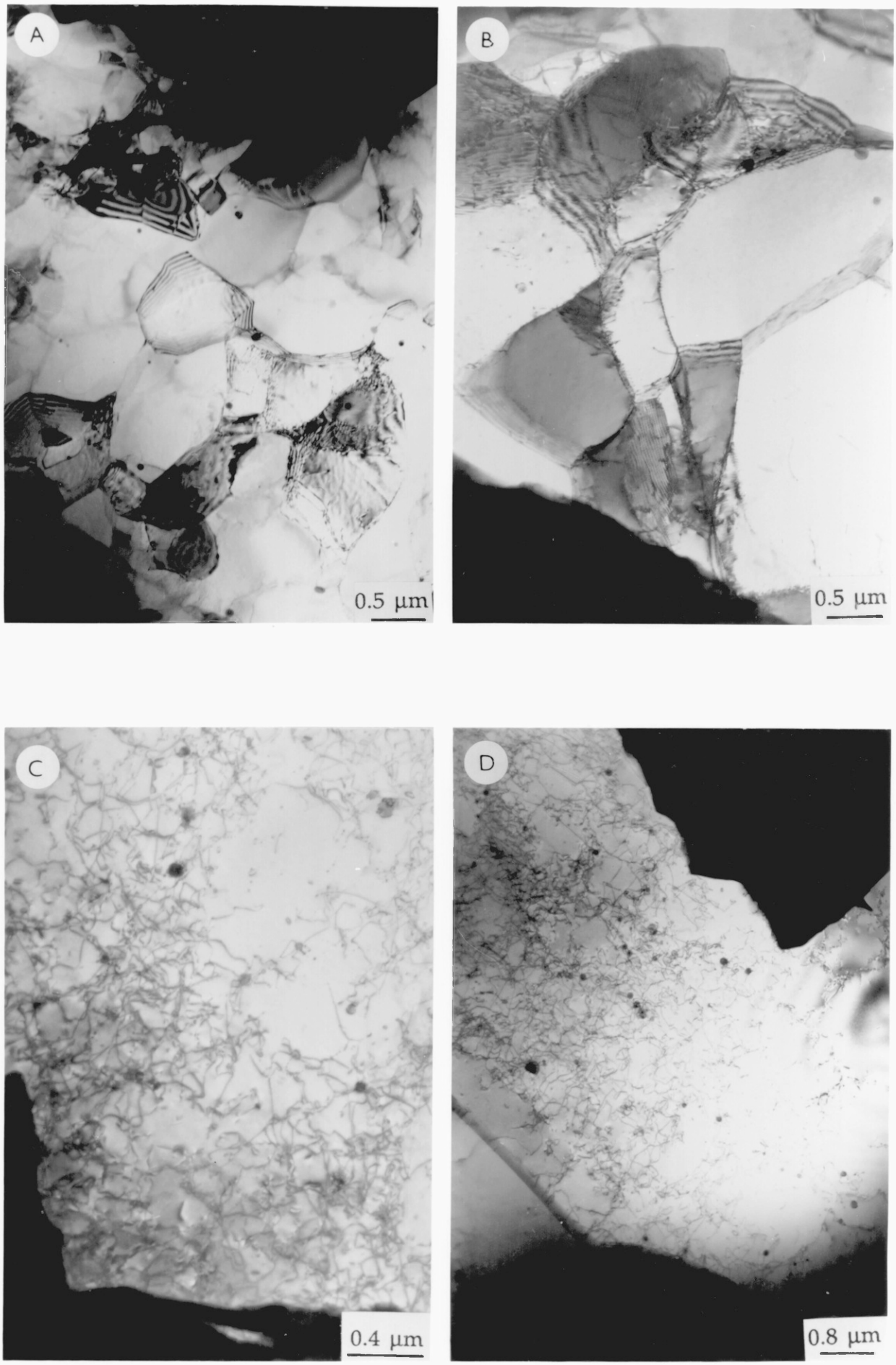
Fig. 5.20 TEMof the 2S/SiC composite, 50 % cold rolled and annealed for one hour at (a) 200°C, (b) 300°C, (c) 400°C, and (d) 500°C.

5.20 (a)

5.20 (b)

5.20 (c)

5.20 (d)


A
0.5 µm
B
0.5 µm
C
0.4 µm
D
0.8 µm

5.3.3 Observations Using Optical Microscopy for 2014 (Composite and Matrix Alloy).

The deformed microstructure of 2014/SiC composite after being 50 percent cold rolled is shown in fig. 5.21. Grains are elongated in the rolling direction with a size of 120 μm.

Microstructural development of the composite from the deformed structure produced by 50, 35, and 20 percent cold rolling to the recrystallized structure during annealing at temperatures between 200 and 500°C is shown in the figs. 5.22 to 5.24.

Grain size of cold rolled unrecrystallized and completely recrystallized conditions for the composite 2014/SiC annealed at different temperatures and various strain rates is shown in the table 5.4.

The grain size of the cold deformed 2014/SiC composite observed after recrystallization was of a comparable scale to that of the composite 2S/SiC.

The trend of very little decreasing in recrystallized grain size while increasing in strain in the 2014/SiC composite was also consistent with the observations for the 2S/SiC (table 5.1). There was, however, a difference in the recrystallization temperature for both composites as 2014/SiC started recrystallizing at about 370°C which was about 100°C more than the recrystallization temperature of the composite 2S/SiC.

The sequence of the microstructural progression of 50 and 35 % cold rolled 2014 matrix alloy during annealing for one hour between 200 and 500°C is shown in the optical micrographs (figs. 5.25 and 5.26).

In the unrecrystallized state, the microstructure consisted of large grains with a network of intermetallic precipitation structure apparent even after heavy cold deformation following hot rolling. The recrystallization started between 400 and 450°C and completely recrystallized at 500°C.

Fig. 5.22 Optical micrographs of the 2014/SiC composite, 50 % cold rolled and annealed for one hour at (a) 200°C, (b) 400°C, and (c) 500°C.

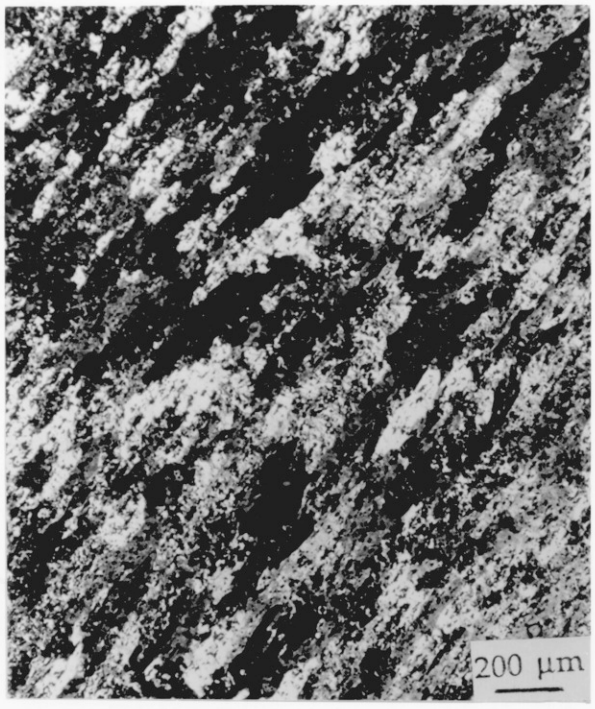
Fig. 5.21 Optical micrograph of the 2014/SiC composite after 50% cold rolling.

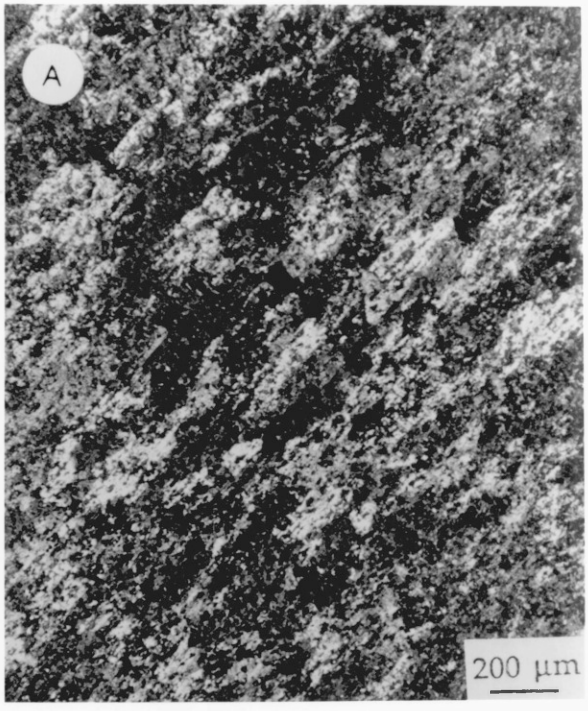
5.22 (a)

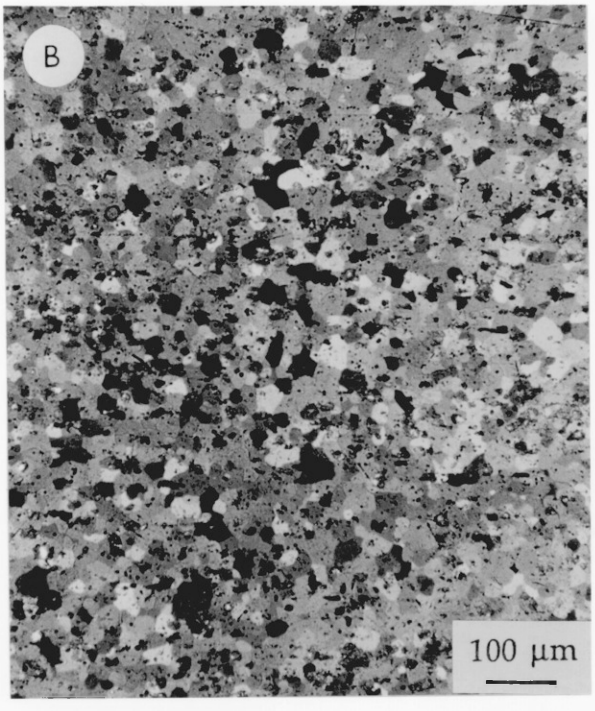
5.22 (b)

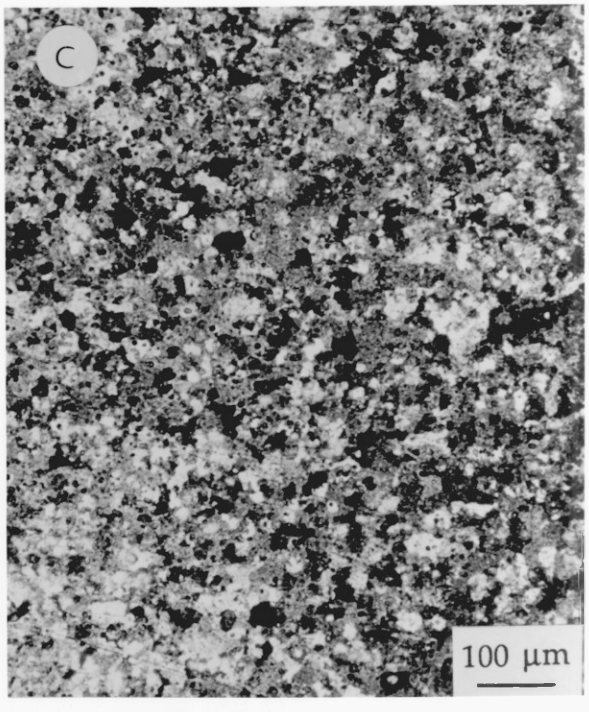
5.22 (c)

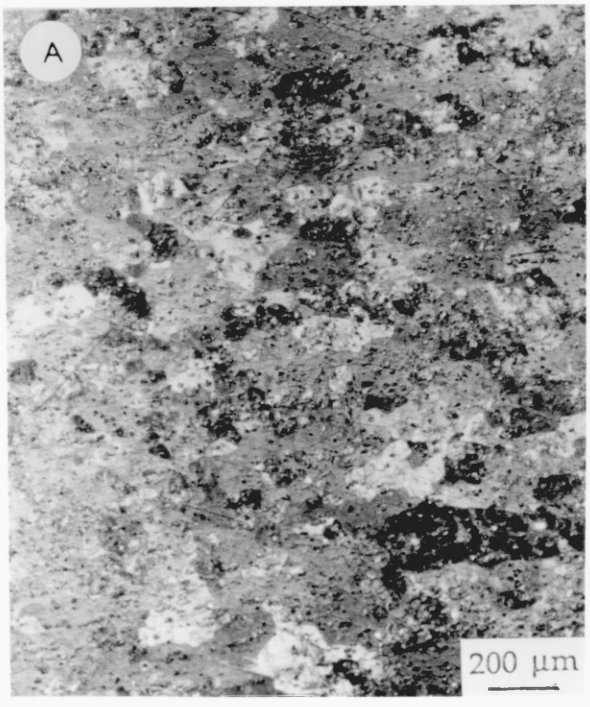
Fig. 5.23 Optical micrographs of the 2014/SiC composite, 35 % cold rolled and annealed for one hour at (a) 200°C, and (b) 500°C.


200 µm


A
200 µm


B
100 µm


C
100 µm


A
200 µm

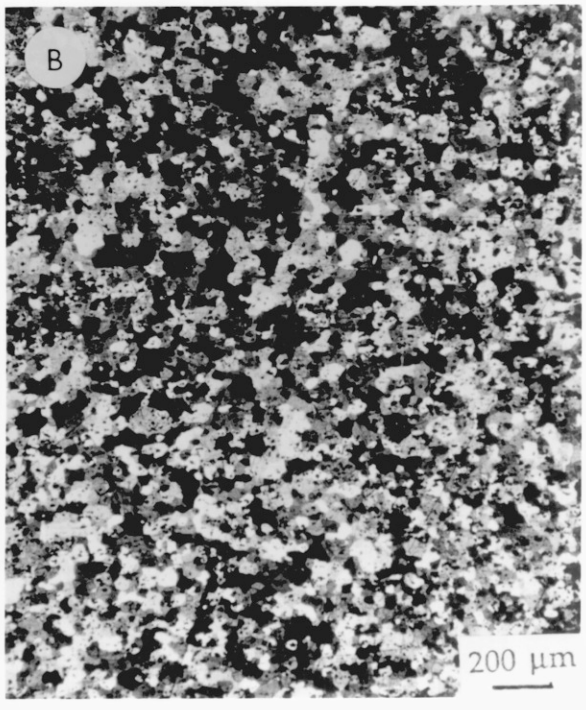
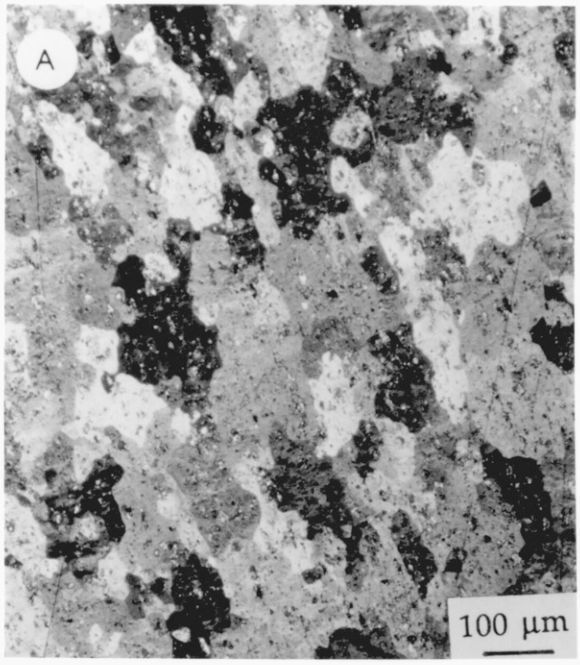
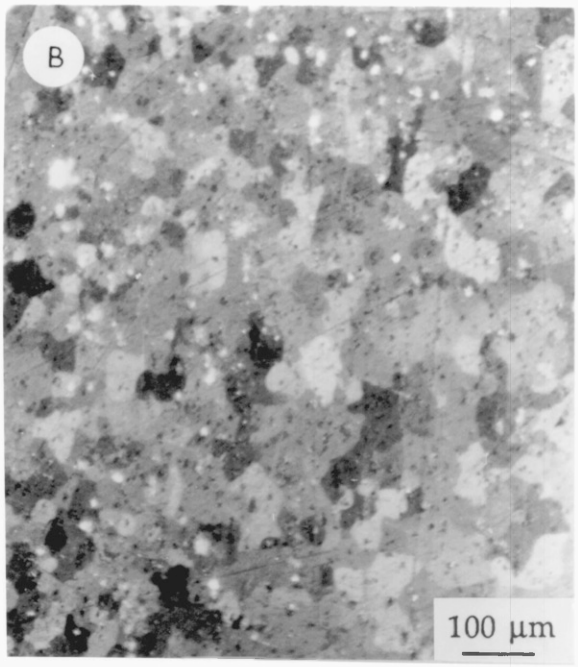

B
200 µm

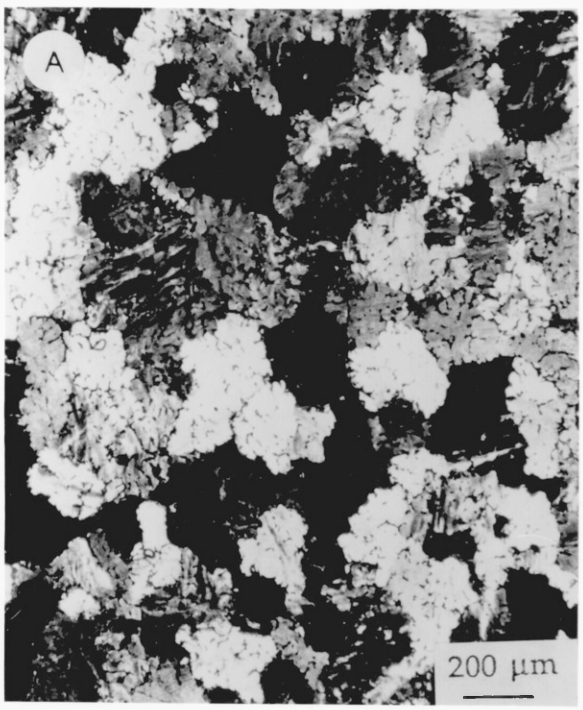
Fig. 5.24 Optical micrographs of the 2014/SiC composite, 20 % cold rolled and annealed for one hour at (a) 200°C and (b) 500°C.

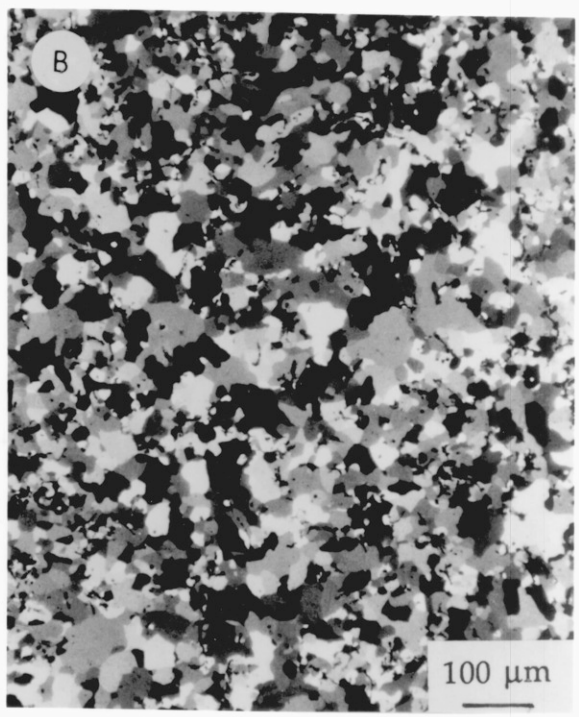
Fig. 5.25 Optical micrographs of the 2014 alloy, 50 % cold rolled and annealed for one hour at (a) 300 and (b) 500°C.

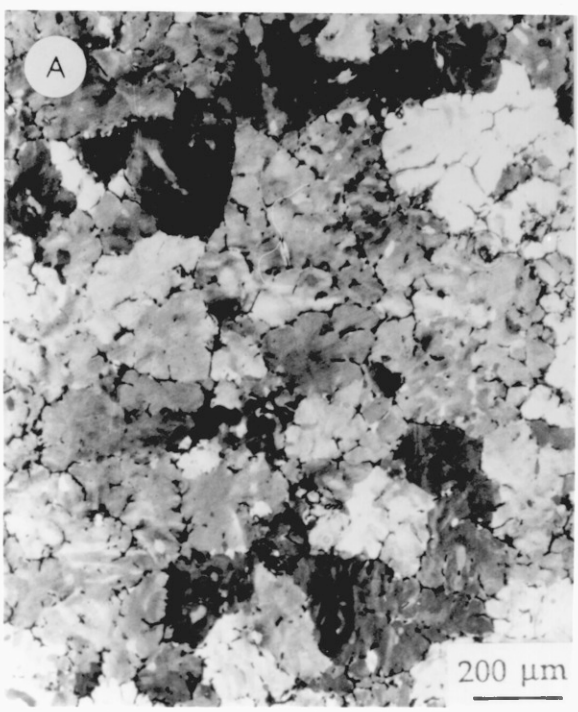
Fig. 5.26 Optical micrographs of the 2014 alloy, 35 % cold rolled and annealed for one hour at (a) 300 and (b) 500°C.


A
100 µm


B
100 µm


A
200 µm


B
100 µm


A
200 µm


B
100 µm

The average grain size of the 2014 alloy in unrecrystallized and recrystallized conditions is given in table 5.5 for the alloy deformed to various reductions and then annealed.

5.3.4. Observations Using T.E.M. for 2014/SiC Composite.

In the 50 percent cold rolled specimen, the microstructure indicated a high dislocation density in the form of a cloud-like dislocation network in the matrix and around particles (fig. 5.27). There was little indication of dislocation substructure development and a high density of undetectable individual dislocations spreaded around but relatively higher dislocation density near the particles.

The progressive development of microstructure towards recrystallization in 50 percent cold rolled 2014/SiC composite in response to annealing for one hour at temperatures between 200 and 500°C is determined in the series of T.E.M. micrographs in fig. 5.28.

As observed in the fig. 5.28(a) for the specimen annealed at 200°C, there was resistance to static recovery by the suppression of the annihilation process and instead of dislocations coalescing into cell walls, separating dislocation free areas, a dense cloud of unresolvable dislocations remained with fine precipitates formed at this temperature. A very high dislocation density made the transparent area very small in the foils, making thicker areas practically opaque.

At a temperature of 300°C where the precipitates start overaging in the 2014 alloy, precipitated intermetallic particles in a size range of 0.05 to 1.5 μm were observed with the majority of the precipitates of an average size of 0.1 μm along with the dislocations arranged to form separate sub-grain

walls (figs. 5.28 (b)).

Increasing the temperature led to the development of a distinct sub-grain structure with the initiation of recrystallization at both SiC and large intermetallic particles, occasionally present, as shown in figs. 5.28(c) and (d) for the specimen annealed at 400°C.

Figs. 5.28 (c), (d) and (e) showed the recrystallized microstructure formed by annealing at 400°C for one hour. A complex structure with different types of precipitates was observed, especially with the free dislocations which started to be generated within the grains due to the quenching effect. The presence of the precipitates appeared to slow down the recrystallization by pinning which affected the composite by delaying the recrystallization temperature until about 100°C above that of the composite 2S/SiC.

Finally, the specimen annealed at 500°C revealed a recrystallized structure having sharp boundaries and a high density of tangled dislocations in the form of both spiral and helical dislocations with line dislocations as well (figs. 5.28(f) and (g)). The presence of a great number of helical dislocations indicated the production of a high concentration of vacancies during annealing which had condensed during quenching to form loops and helices. There was a higher density of dislocation loops and tangles in the vicinity of the particles compared to the matrix regions away from the particles. There were undissolved Mn and Fe containing particles still observed at 500°C or even at higher temperatures, (fig. 5.28(g)).

Fig. 5.28 TEM of the 2014/SiC composite, 50 % cold rolled and annealed for one hour at (a) 200, (b) 300, (c) (d) (e) 400 and (f) (g) 500°C.

Fig. 5.27 TEM of the 2014/SiC composite after 50% cold rolling.

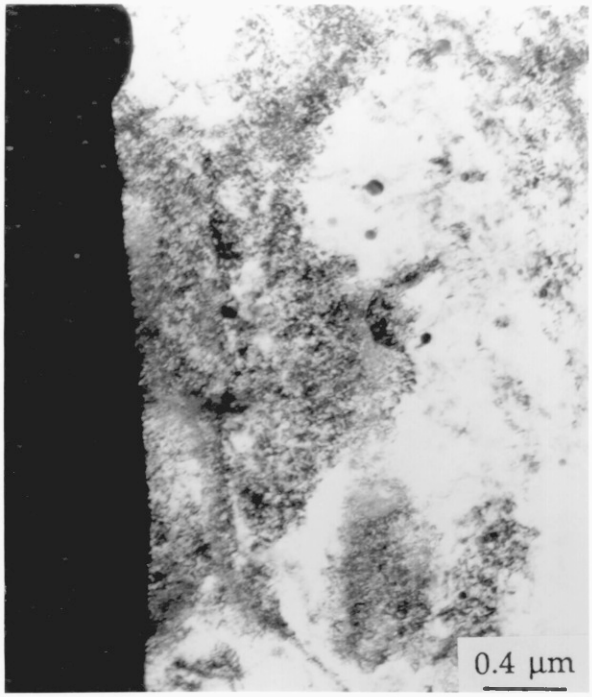
5.28 (a)

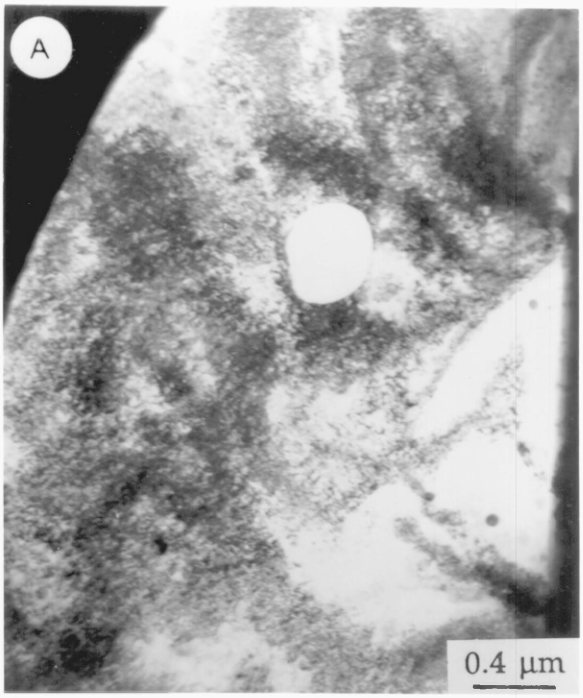
5.28 (b)

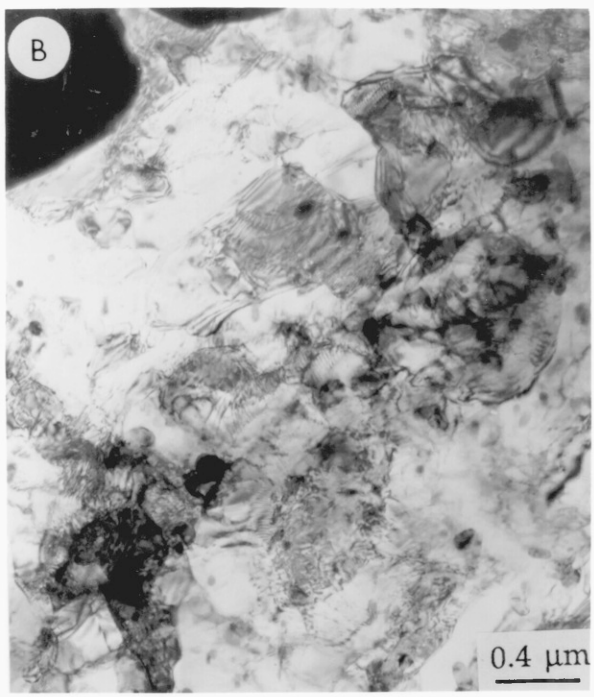
5.28 (c)

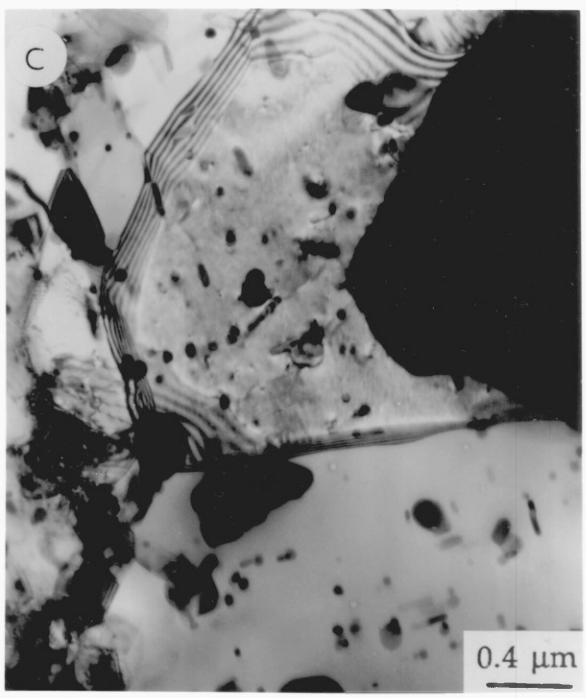
5.28 (d)

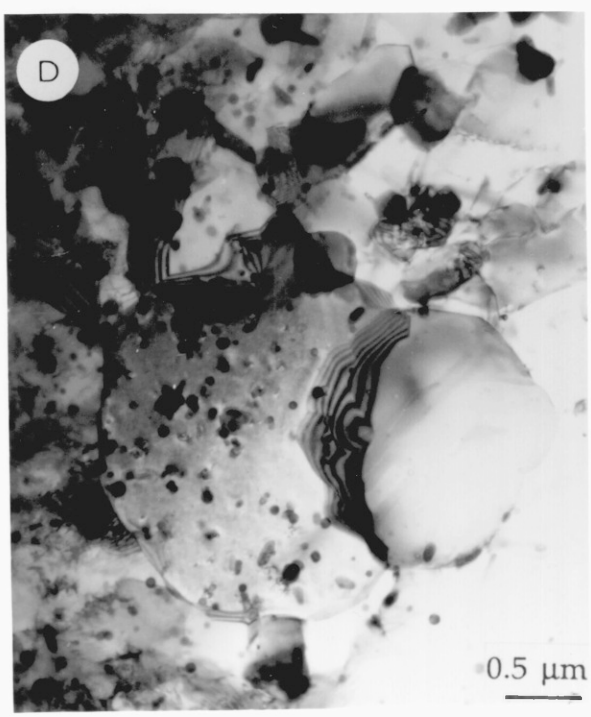
5.28 (e)

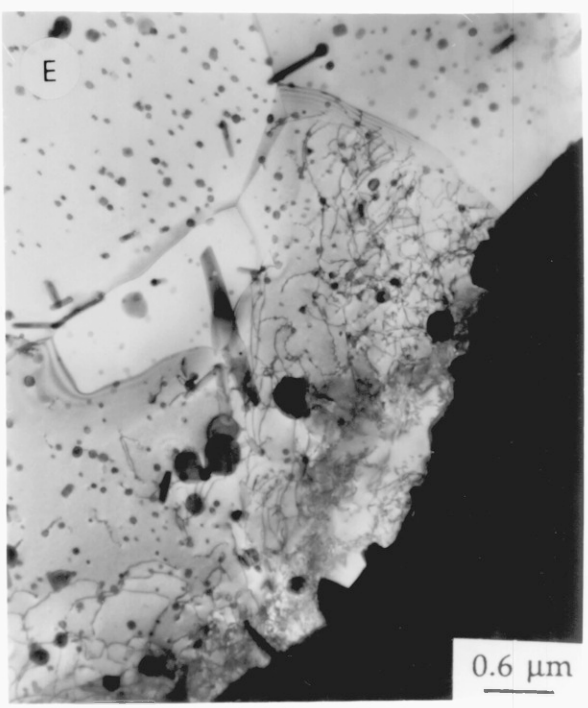

0.4 µm


A
0.4 µm


B
0.4 µm


C
0.4 µm


D
0.5 µm


E
0.6 µm

5.4 Effect of Heating Rate on the Recrystallization of the Composites.

Using the higher heating rate (100 K / S) with a salt bath, it was observed that the recrystallized grain size was smaller than in the case when the composite samples were recrystallized at a slower rate heat treatment (0.5 K / S) in an air furnace.

Optical micrographs 5.29 show the recrystallized microstructure of 2S/SiC and 2014/SiC composites which have been 50 percent cold rolled and isothermally annealed at 400°C for one minute in the salt bath. The resulting grain sizes measured for 2S/SiC and 2014/SiC composites recrystallized at a high heating rate were 15 and 20 μm respectively whereas the grain size for the same samples recrystallized in an air furnace was measured to be 23 (table 5.1) and 25 μm (table 5.4) respectively.

5.5 Effect of the Deformation Temperature on the Recrystallization of the Composite.

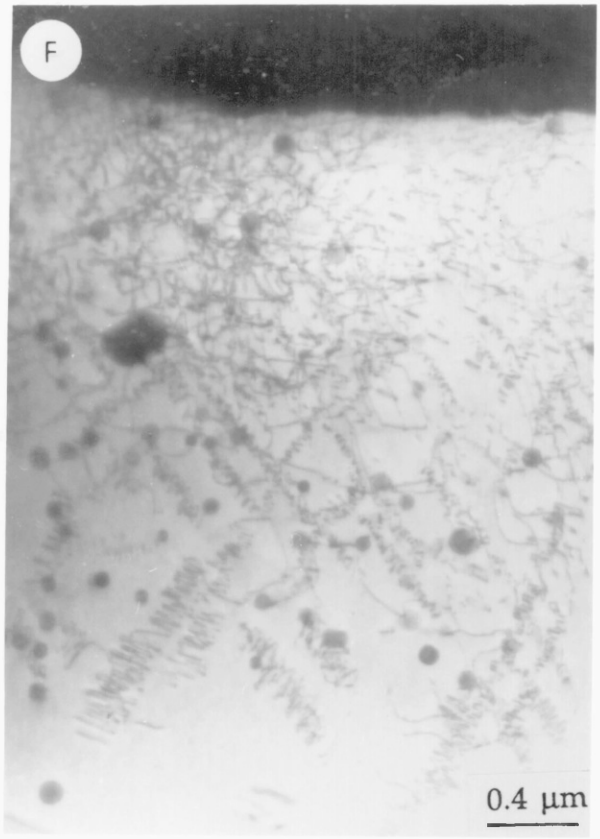
In this section we discuss how the deformation temperature affects the recrystallized microstructure of the metal matrix composites during subsequent static annealing.

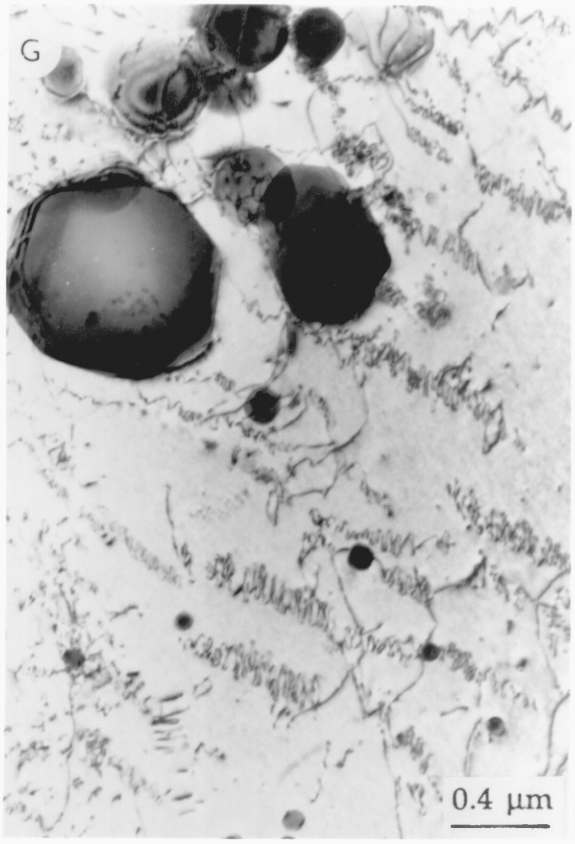
Specimens of the composite 2S/SiC which had been deformed at temperatures in the range between room temperature and 500°C to a strain of fifty percent at strain rates 5×10^{-4} and 5×10^{-2} S^{-1} in compression were all then annealed at 500°C for one hour and quenched. The resulting recrystallized microstructure of the samples is shown in the optical micrographs, fig. 5.30 to 5.35. As illustrated in these micrographs, the grain size of the samples deformed at a strain rate of 5×10^{-4} S^{-1} at

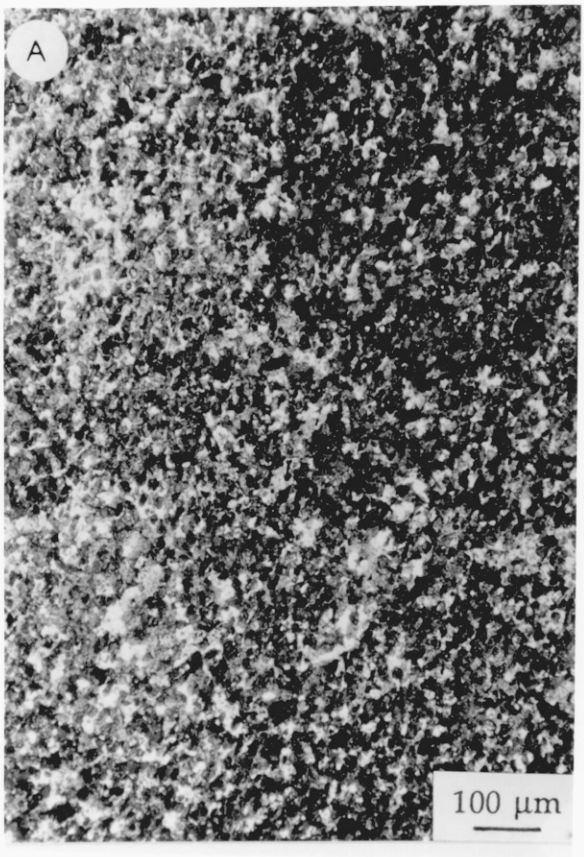
5.28 (f)

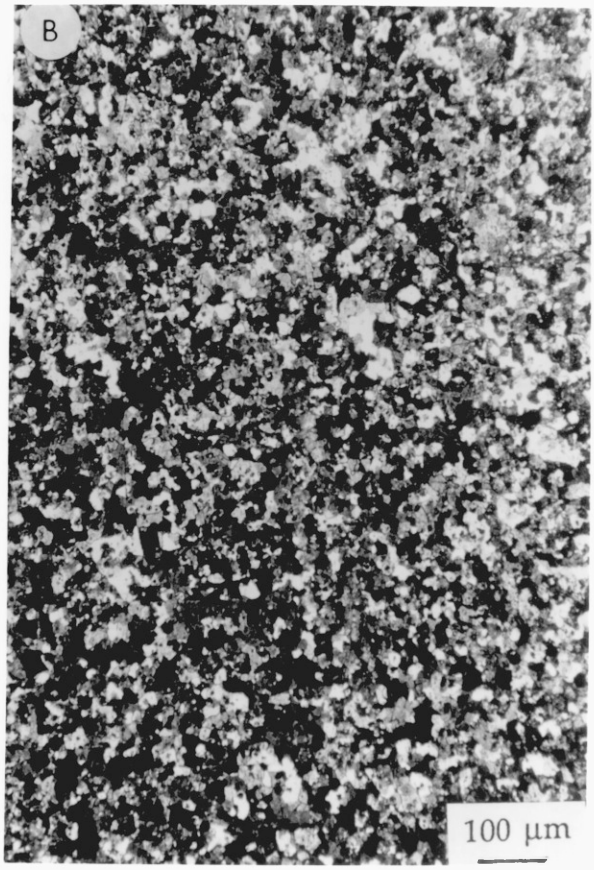
5.28 (g)

Fig. 5.29 Optical micrographs of the 50% cold rolled composites (a) 2S/SiC and (b) 2014/SiC, annealed for one minute in the salt bath at 350 and 400°C respectively.


F
0.4 µm


G
0.4 µm


A
100 µm


B
100 µm

temperatures between room temperature and 300°C and at 5 x 10^{-2} S^{-1} between room temperature and 400°C, and then subsequently annealed at 500°C appeared to be very fine in size and exhibited particle stimulated nucleation. The grain size measurements of the recrystallized samples annealed at 500°C showed a slight increase in the grain size as the deformation temperature increased up to 300°C for the specimen deformed at lower strain rates and 400°C for the higher strain rates, (shown in table 5.6), but past these deformation temperature limits, there was a drastic increase in the grain size of the composite. The samples deformed at or above 400°C and annealed for the lower strain rate and deformed at 500°C and annealed for the higher strain rate did not recrystallized due to particle stimulated nucleation. This illustrates the deformation temperature dependence of the final recrystallized grain size evolved during subsequent annealing in the composite for a particular strain rate.

Fig. 5.30 Optical micrographs of the composite 2S/SiC deformed in compression at room temperature at strain rates of (a) 5×10^{-4} and (b) 5×10^{-2} S^{-1} and subsequently annealed for one hour at 500°C.

Fig. 5.31 Optical micrographs of the composite 2S/SiC deformed in compression at 200°C at strain rates of (a) 5×10^{-4} and (b) 5×10^{-2} S^{-1} and subsequently annealed for one hour at 500°C.

Fig. 5.32 Optical micrographs of the composite 2S/SiC deformed in compression at 300°C at strain rates of (a) 5×10^{-4} and (b) 5×10^{-2} S^{-1} and subsequently annealed for one hour at 500°C.

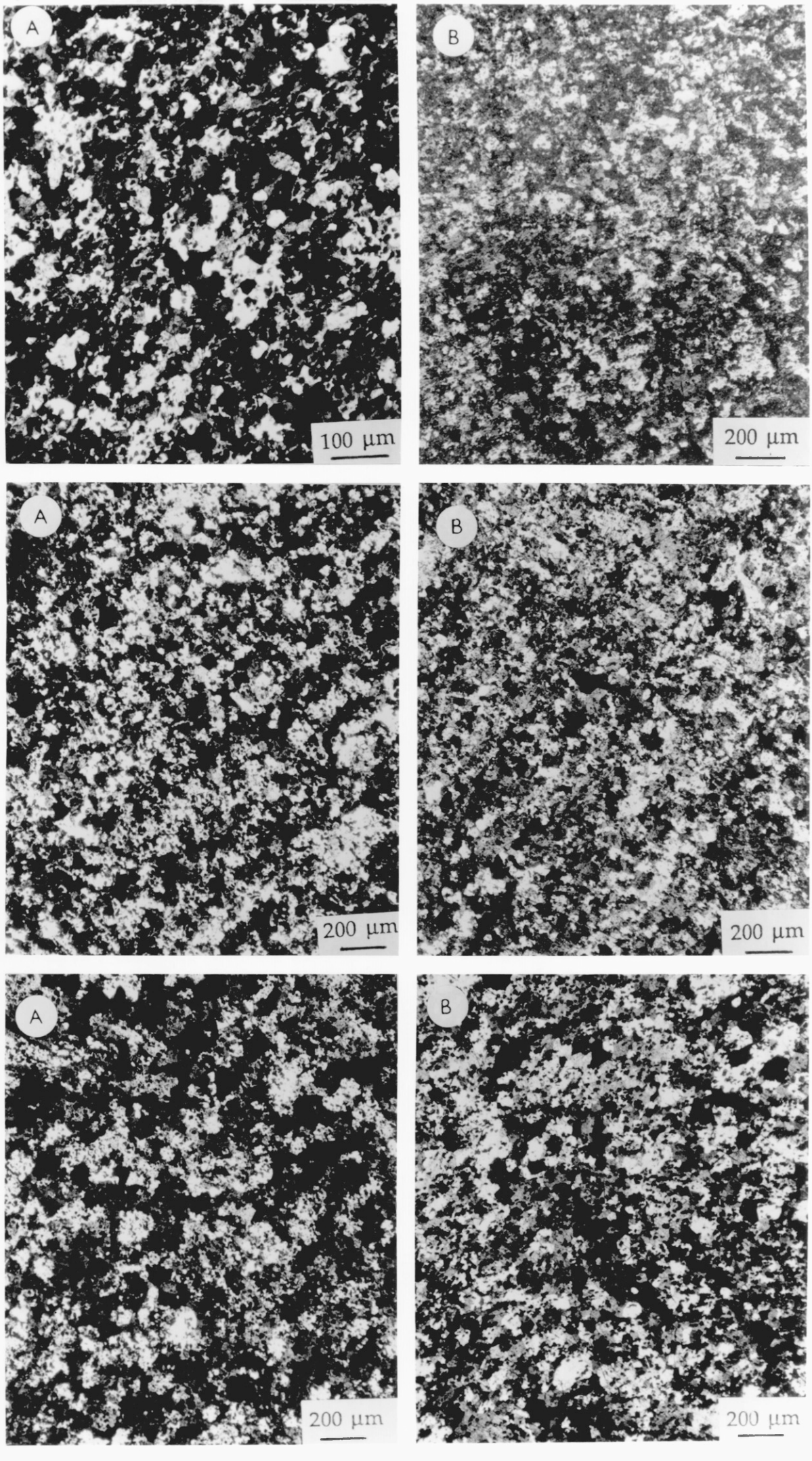
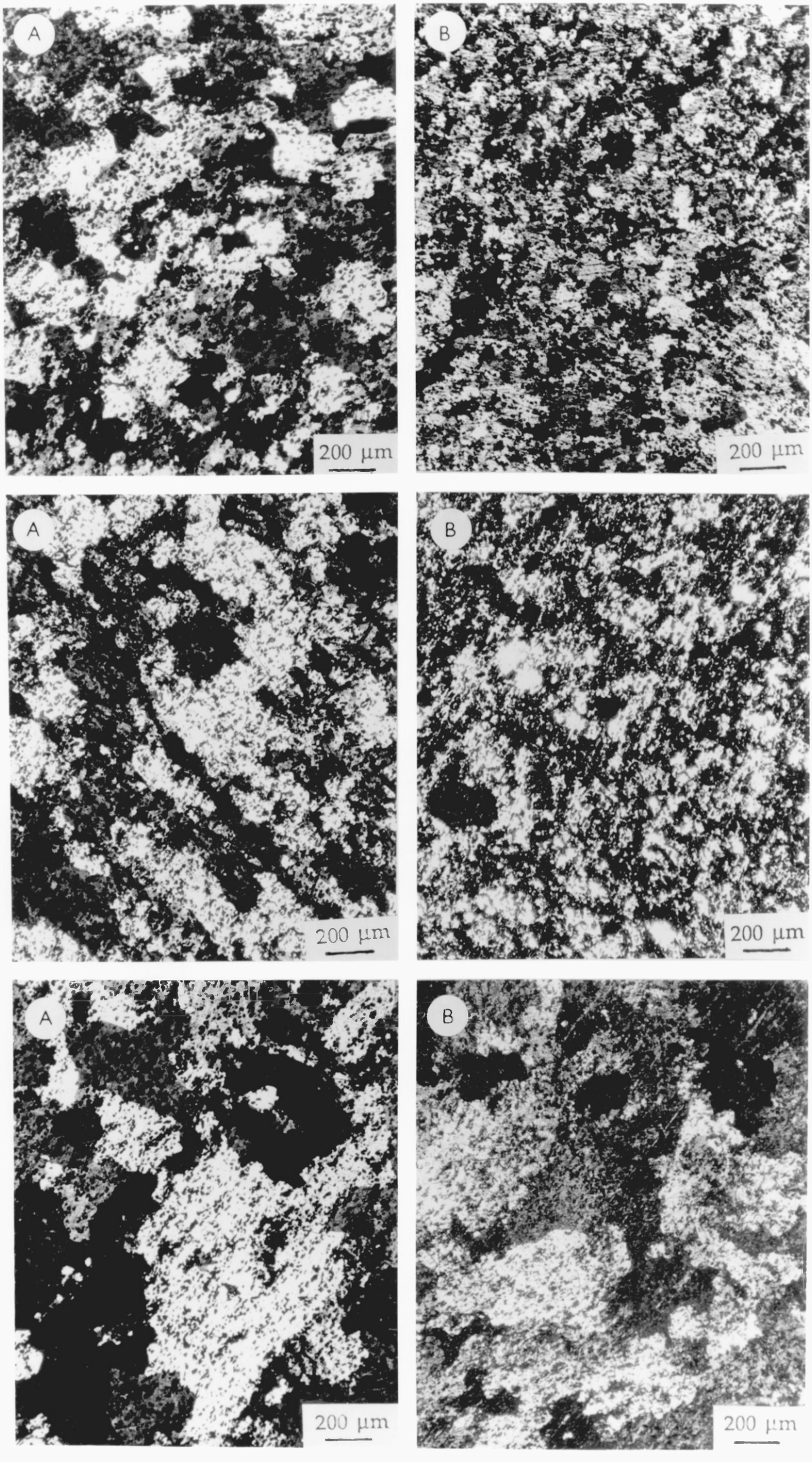

A
100 µm
B
200 µm
A
200 µm
B
200 µm
A
200 µm
B
200 µm

Fig. 5.33 Optical micrographs of the composite 2S/SiC deformed in compression at 350°C at strain rates of (a) 5 x 10^{-4} and (b) 5 x 10^{-2} S^{-1} and subsequently annealed for one hour at 500°C.

Fig. 5.34 Optical micrographs of the composite 2S/SiC deformed in compression at 400°C at strain rates of (a) 5 x 10^{-4} and (b) 5 x 10^{-2} S^{-1} and subsequently annealed for one hour at 500°C.

Fig. 5.35 Optical micrographs of the composite 2S/SiC deformed in compression at 500°C at strain rates of (a) 5 x 10^{-4} and (b) 5 x 10^{-2} S^{-1} and subsequently annealed for one hour at 500°C.


A
200 µm
B
200 µm
A
200 µm
B
200 µm
A
200 µm
B
200 µm

Amout of Cold Rolling (%)	Unrecrystallized Grain Size (μm)	Recrystallized Grain Size (μm)
20	140	45
35	140	29
50	165	23
70	170	23

Table 5.1 Average grain size of the 2S/SiC composite in unrecrystallized and completely recrystallized state.

Amout of Cold Rolling (%)	Unrecrystallized Grain Size (μm)	Recrystallized Grain Size (μm)
20	320	220
50	380	175
70	480	140

Table 5.2 Average grain size of the 2S aluminium in unrecrystallized and completely recrystallized state.

	Sub-grain Size at different Reductions	
Annealing Temp. °C	50 % (μm)	70 % (μm)
150	0.77	0.68
200	0.79	0.72
250	0.82	0.78

Table 5.3 Average sub-grain size developed in the 50 and 70 % cold deformed 2S/SiC composite during annealing prior to recrystallization.

Amout of Cold Rolling (%)	Unrecrystallized Grain Size (μm)	Recrystallized Grain Size (μm)
20	100	52
35	102	38
50	120	25
70	120	22

Table 5.4 Average grain size of the 2014/SiC composite in unrecrystallized and completely recrystallized state.

Amout of Cold Rolling (%)	Unrecrystallized Grain Size (μm)	Recrystallized Grain Size (μm)
20	220	72
50	220	55
70	230	50

Table 5.5 Average grain size of the 2014 alloy in unrecrystallized and completely recrystallized state.

	Grain size of the 2S/SiC composites specimens deformed at different temperatures and strain rates and subsequently annealed at 500°C.	
Temperature°C	$5 \times 10^{-4}\ S^{-1}$ (μm)	$5 \times 10^{-2}\ S^{-1}$ (μm)
200° C	30	33
250°C	42	38
300°C	55	43
350°C	65	43
400°C	120	65
500°C	170	160

Table 5.6 Grain size of the 2S/SiC composite deformed between room temperature and 500°C at different strain rates and subsequently annealed for one hour at 500C.

CHAPTER 6

(RESULTS)

Compression Testing and Microstructure of Al-Zr-Si Alloy

6.1 Annealed Microstructure.

Heat treatment of each alloy (i.e. Al-Zr, Al-Zr-Cu, and Al-Zr-Si alloys) resulted in the structure containing finely dispersed Al_3Zr particles (fig 6.8). The Al-Zr-Si alloy displayed a high density and a more uniform spatial distribution of the precipitates which is in accordance with the previous investigations (73, 165) that Si efficiently improves the density and distribution of Al_3Zr precipitates. In the TEM, the particles showed a characteristic strain field and a specific contrast effect as reported earlier (87, 152). The spherical Al_3Zr precipitates have a slightly larger cubic lattice parameter than the Al lattice and this gives rise to strain inside the matrix around precipitates resulting in a line of no contrast with dark contrast around it in the bright field image. This kind of diffraction contrast is typical for the particles having a coherency field around them (166). Specimens aged even up to 168 hours did not show a further appreciable change in the precipitate morphologies.

The precipitates were in the range of 50 to 100 Å although very occasionally, some relatively coarse precipitates were observed in the size range of 200 to 500 °A.

Due to a better and more uniform dispersion of fine Al_3Zr precipitates, the Al-Zr-Si alloy was selected to conduct the further study of elevated temperature deformation behaviour.

6.2 Hardness Testing.

Isochronal hardness measurements were made on Al-Zr, Al-Zr-Cu and Al-Zr-Si alloys in order to provide a general survey of the effects of the reactions in each alloy. Isochronal hardness measurements were taken after one hour holding at differing annealing temperatures between 200 and 600°C (fig. 6.1). Three of the alloys showed very little variation in the hardness up to 600°C, indicating the resistance of the alloys to recrystallization.

6.3 Mechanical Testing

Compression testing was performed on polycrystalline Al-Zr-Si alloy containing Al_3Zr second phase particles. True stress-strain curves are shown in fig 6.2 for the tests conducted at temperatures between 200 and 500°C at strain rates between 5×10^{-4} and 5×10^{-2} S^{-1}.

The stress strain curves for tests conducted at 400°C and 500°C at different strain rates showed a parabolic region up to strains of about 0.04, thereafter approaching a steady state. The 200 and 300°C curve did not show a clear steady state and exhibited an extended parabolic region.

The deformation in the steady state region of the curves for the tests performed at the temperatures of 400 and 500°C at a strain rate of 5×10^{-4} S^{-1}, the slowest strain rate conducted, displayed a complicated behaviour because of the occurrence of nonuniform deformation. A rise was followed by a decrease in the stress strain curve and then an increase in the flow stress was witnessed again. This behaviour was more pronounced at 400°C.

The alloy showed a significant temperature sensitivity in its yield stress

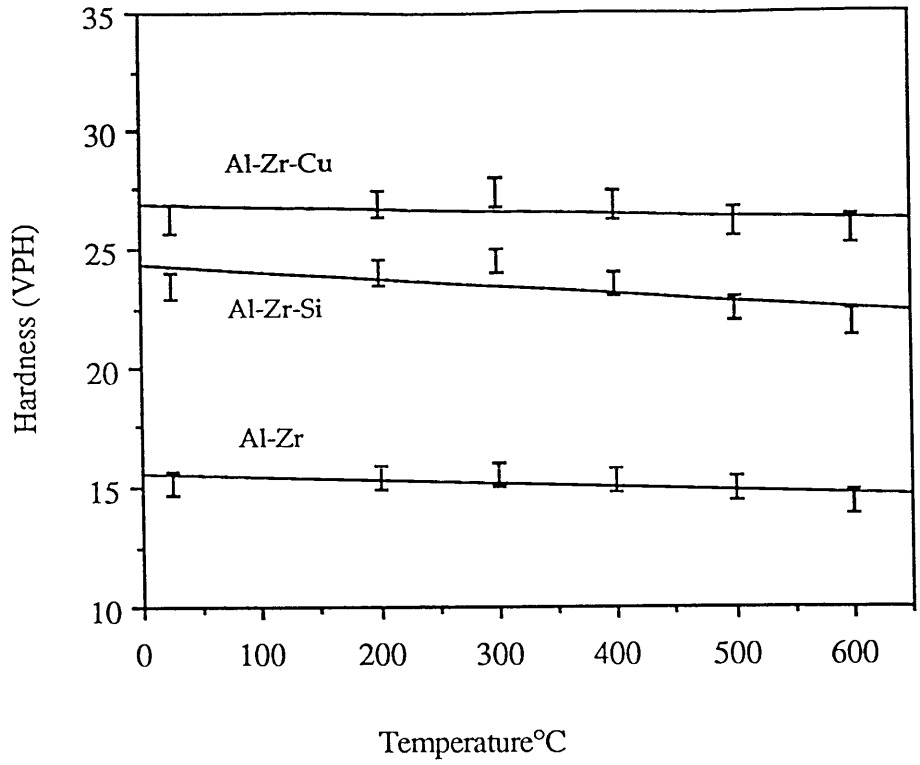
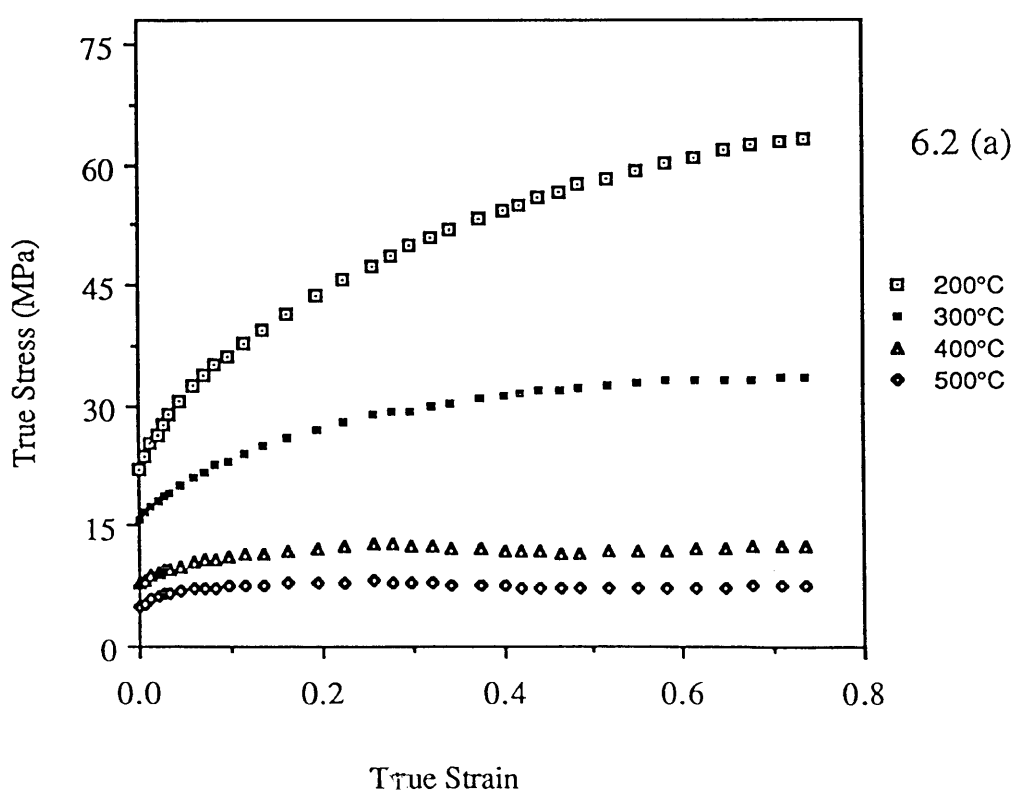
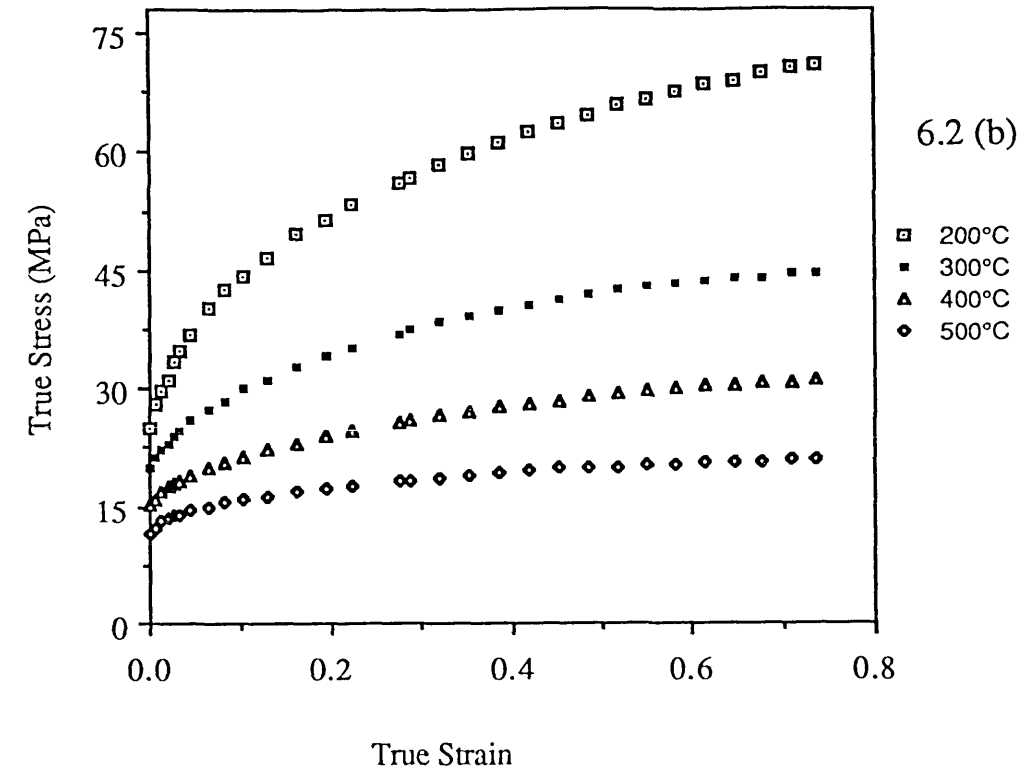


Fig. 6.1 Vickers hardness of the Al-Zr, Al-Zr-Si and Al-Zr-Cu alloys as a function of temperature.



6.2 (a)



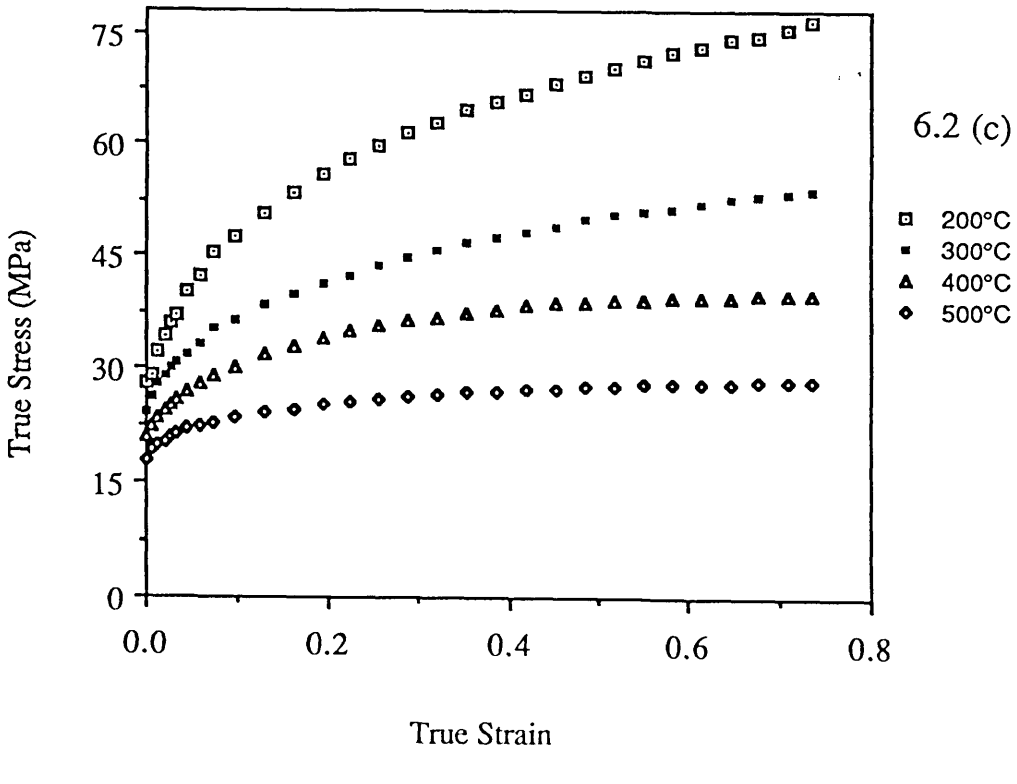


Fig. 6.2 True stress-strain curves of the Al-Zr-Si alloy deformed in compression at temperatures between 200 and 500°C at strain rates of (a) 5 x 10^{-4}, (b) 5 x 10^{-3}, and (c) 5 x 10^{-2} S^{-1}.

and a continuous drop in the modulus corrected yield stress was observed from the temperature 200°C to 500°C (fig. 6.3). A similar dependence of the yield stress was observed as a function of the strain rate (fig. 6.4).

Changes in the parabolic work hardening rates in the initial strain region (0.02-0.04) as a function of temperature are shown in fig. 6.7. There was a well defined regression in the work hardening rate between 300 and 400°C, however, the drop in the work hardening from 400°C to 500°C was relatively smaller and showed less temperature dependence.

Figure 6.5 shows the strain rate dependence of flow stress, and stress exponent, n, the slope of these curves was calculated to be 4.5 for the test temperatures above 300°C. By relating it to the slope of the curve ln $\dot{\varepsilon}$ vs. 1/T (fig. 6.6) and other parameters, the deformation process can be expressed by the following equation,

$$\dot{\varepsilon}^{\circ} = A\,\sigma^{n} \exp(-Q/RT)$$

here, $\dot{\varepsilon}^{\circ}$ is strain rate, A and n are constants, Q is the activation energy, R is the gas constant and T is absolute temperature.

Q in the present work for Al-Zr-Si alloy from the above relation was found to be 126 kJ $mole^{-1}$. The calculated value is slightly lower than the lattice diffusion activation energy which is 142 kJ / mole in pure Al (167).

6.4 Deformed Microstructure of the Al-Zr-Si Alloy.

Microstructural changes taking place during the deformation at temperatures between 200 and 500°C and at strain rates between 5×10^{-4} and 5×10^{-2} S^{-1} were investigated after interruption of the compression tests at a strain of 50 percent.

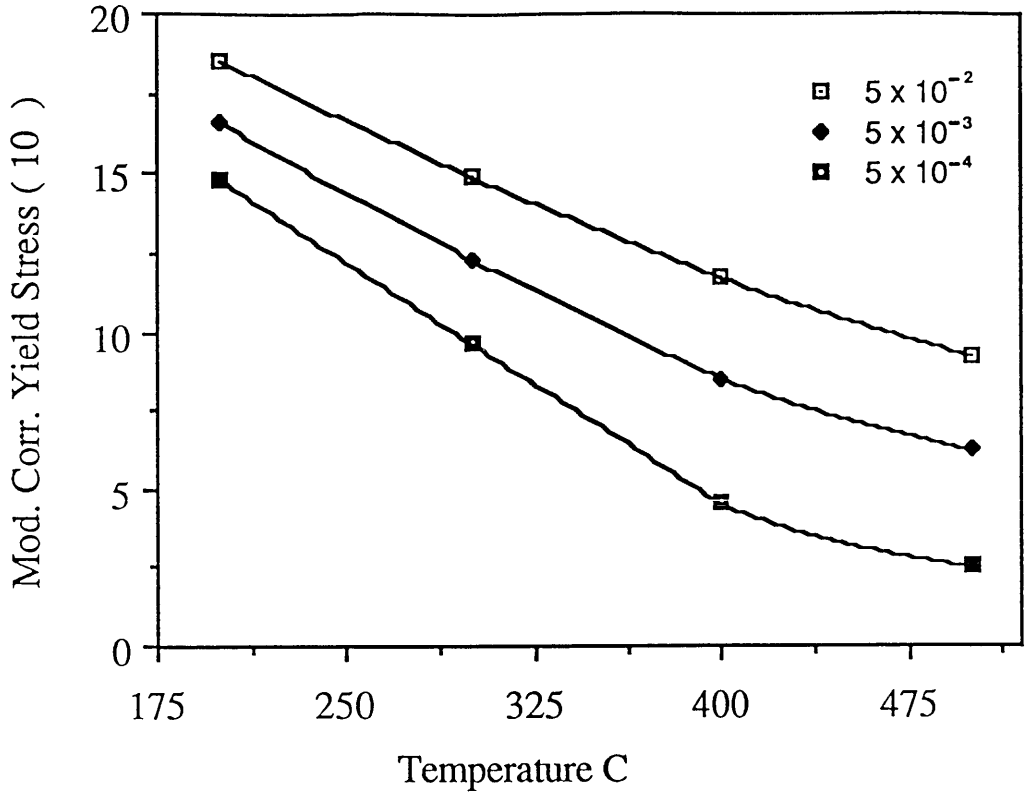


Fig. 6.3 Modulus corrected yield stress of the Al-Zr-Si alloy as a function of temperature after compression testing at different strain rates.

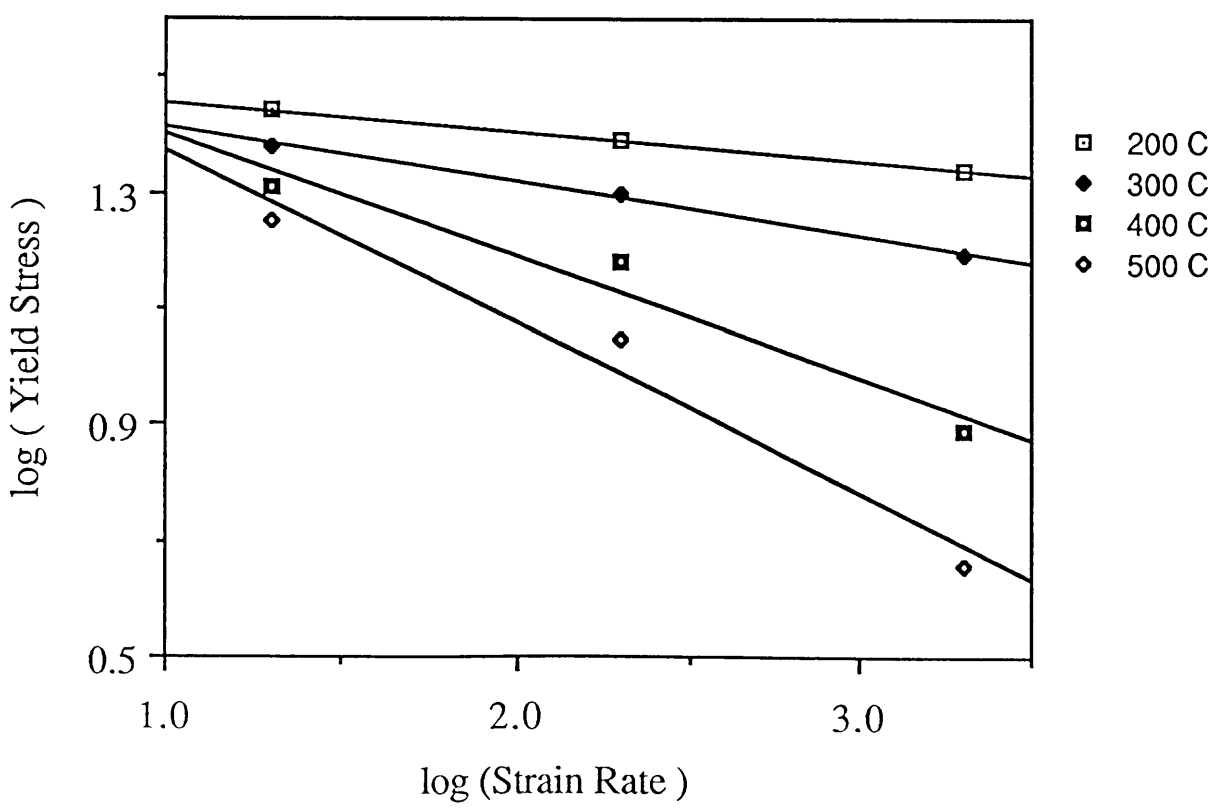


Fig. 6.4 Yield stress of Al-Zr-Si alloy as a function of strain rate deformed in compression at different temperatures.

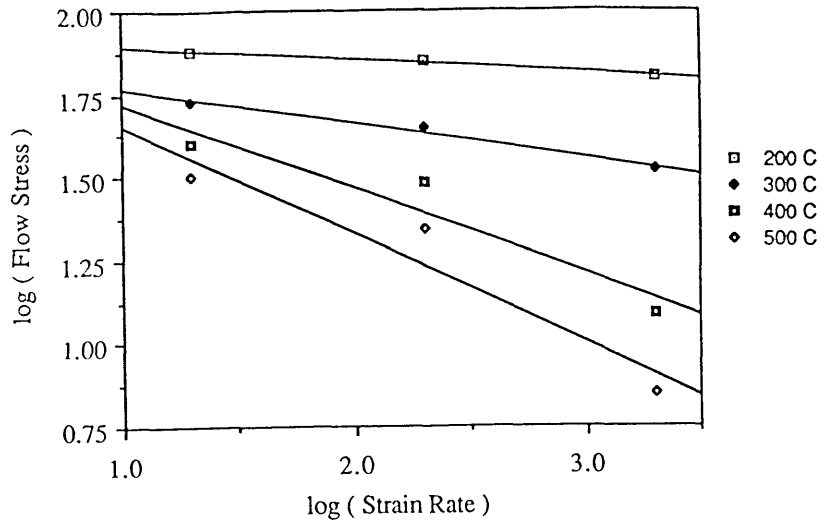


Fig. 6.5 Flow stress of Al-Zr-Si alloy as a function of strain rate deformed in compression at different temperatures.

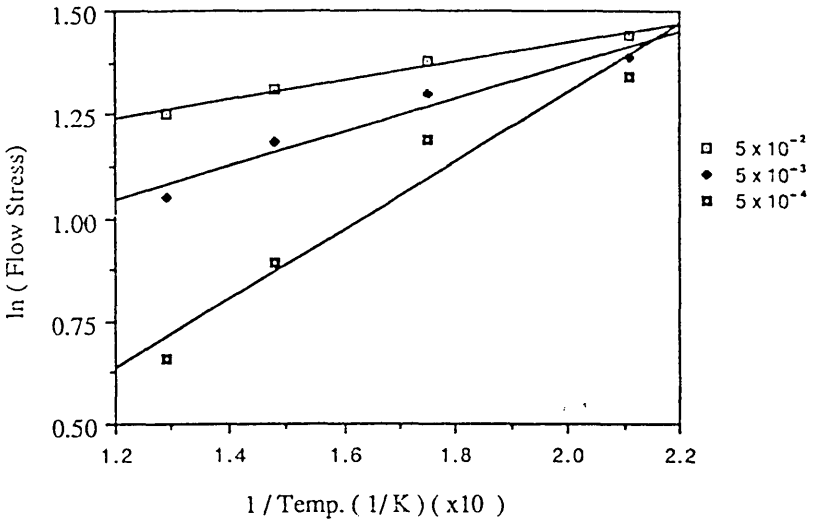


Fig. 6.6 Flow stress of the Al-Zr-Si alloy as a function of reciprocal of temperature after compression testing at different strain rates.

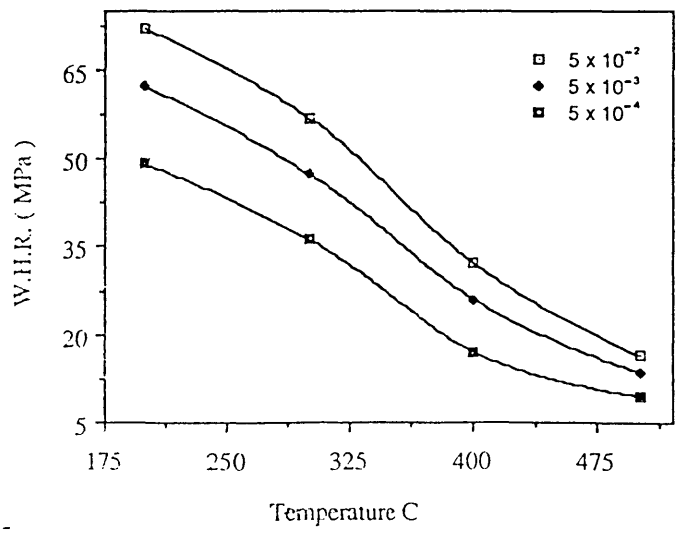


Fig. 6.7 Initial work hardening rates of Al-Zr-Si alloy as a function of temperature after compression testing at different strain rates.

6.4.1 Optical Microscopy

Optical microstructure are presented in figs. 6.9 to 6.12 to illustrate the range of effects seen in the specimens deformed 50 percent in compression at temperatures between 200 and 500°C and at strain rates between 5 x 10^{-4} and 5 x 10^{-2} S^{-1}. At the low temperatures of 200 and 300°C, clearly elongated grains with a feathery substructure arranged in the form of patchwork arrays appeared in the specimens (figs. 6.9 and 6.10). The sub-grain shape was seen to become more equiaxed and larger with increasing temperature and decreasing strain rate as a result of dynamic recovery (table 6.1). In the specimens deformed at the temperature of 500°C at the slowest strain rate of 5 x 10^{-4} (fig. 6.12), the substructure was very clearly equiaxed and had a coarser substructure compared to the specimens deformed at relatively lower temperatures and at higher strain rates.

In the specimens deformed at elevated temperatures at or above 400°C, the local deformation structure appeared to have been modified near the grain boundaries (fig. 6.13). Layers of fine elongated bands with a sharp contrast, were seen in the region near some grain boundaries which were observed to consist of small sub-grains whose size was smaller than the cells in the interior of the grains. Such fine sub-grains were sometimes observed originating at triple points (fig. 6.13 (c)). This kind of effect near the grain boundaries was seen to be more pronounced at 400 or 500°C but at lower temperatures such as at 300°C, this phenomenon was much restricted and was not clearly observed. The specimens deformed at the highest temperature of 500°C at a strain rate of 5 x 10^{-4} S^{-1}, the modified structure around the grain boundaries was relatively clear but the constituent sub-grains within the elongated bands appeared to be getting broken up into fragments.

Fig. 6.8 TEM micrographs showing the distribution of Al_3Zr precipitates in (a) (b) Al-Zr-Si, (c) A -Zr, and (d) Al-Zr-Cu alloys.

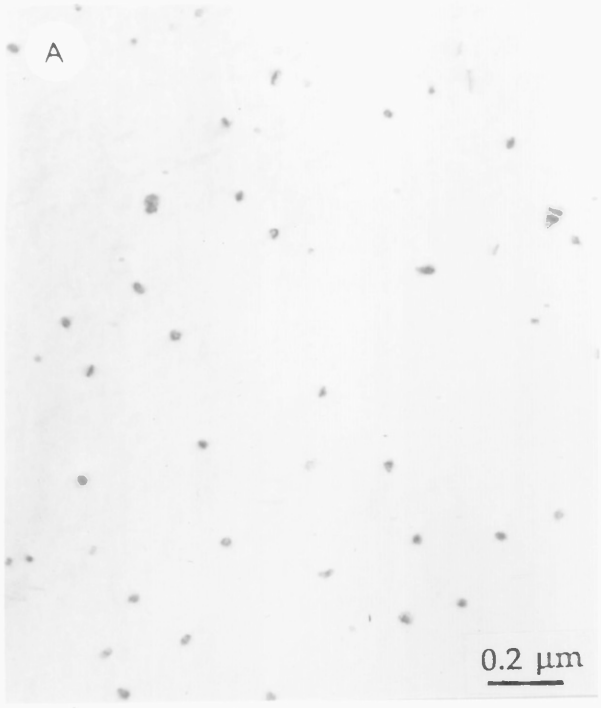
6.8 (a)

6.8 (b)

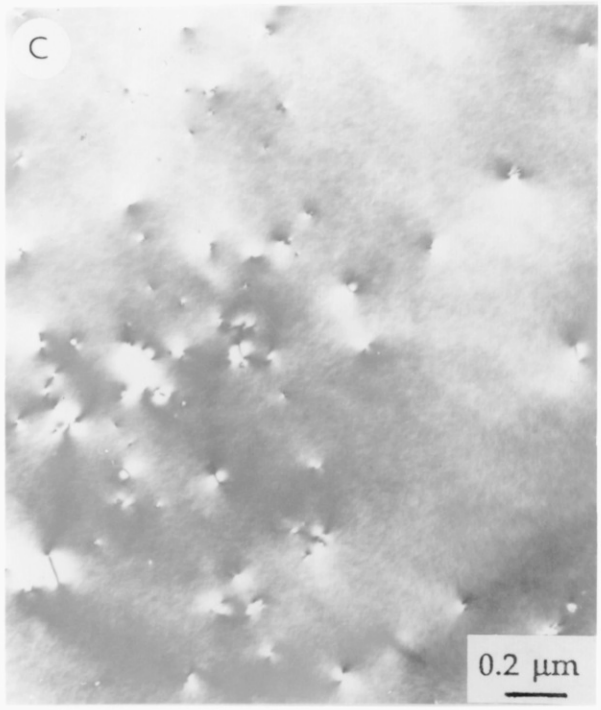
6.8 (c)

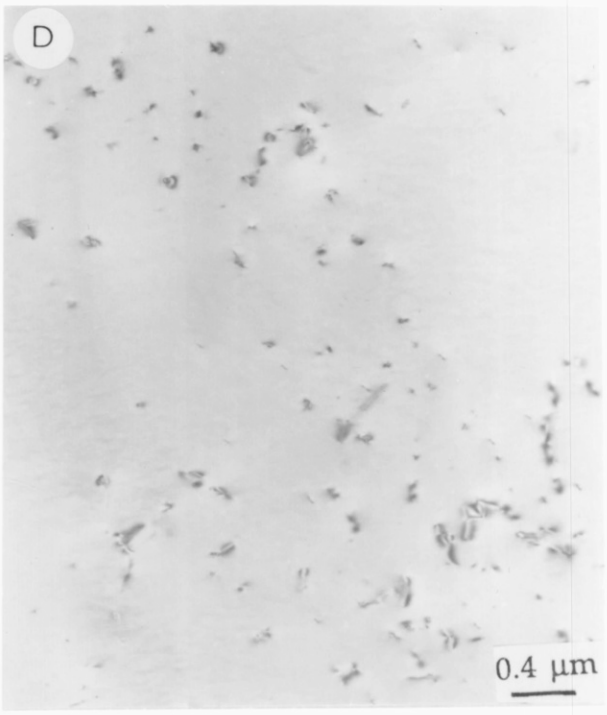
6.8 (d)

Fig. 6.9 Optical micrographs of the Al-Zr-Si alloy after compression testing at 200°C at strain rates of (a) 5×10^{-4} and (b) 5×10^{-2} S^{-1}.


A
0.2 μm


B
0.4 μm


C
0.2 μm


D
0.4 μm


A
200 μm

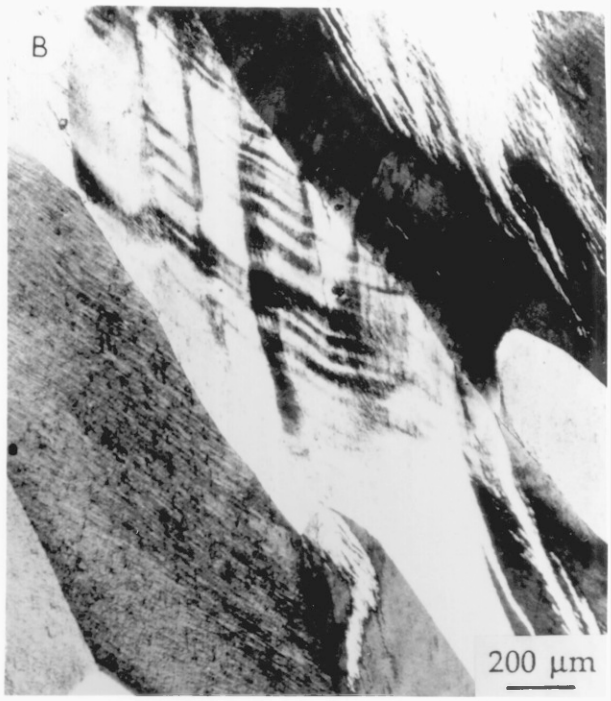

B
200 μm

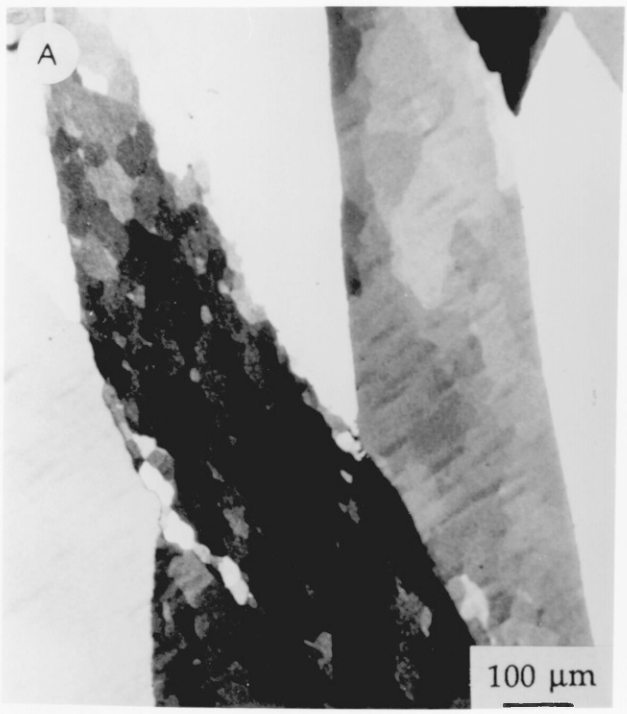
Fig. 6.10 Optical micrographs of the Al-Zr-Si alloy after compression testing at 300°C at strain rates of (a) 5×10^{-4} and (b) 5×10^{-2} S^{-1}.

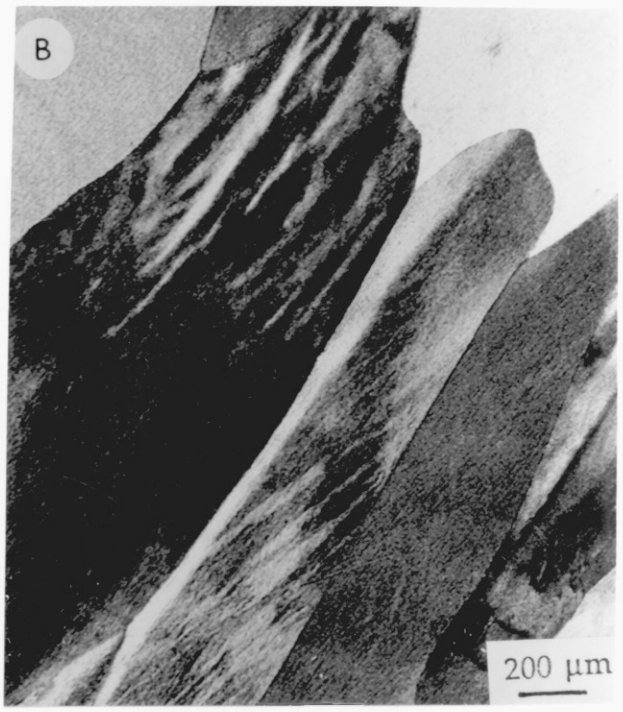
Fig. 6.11 Optical micrographs of the Al-Zr-Si alloy after compression testing at 400°C at strain rates of (a) 5×10^{-4} and (b) 5×10^{-2} S^{-1}.

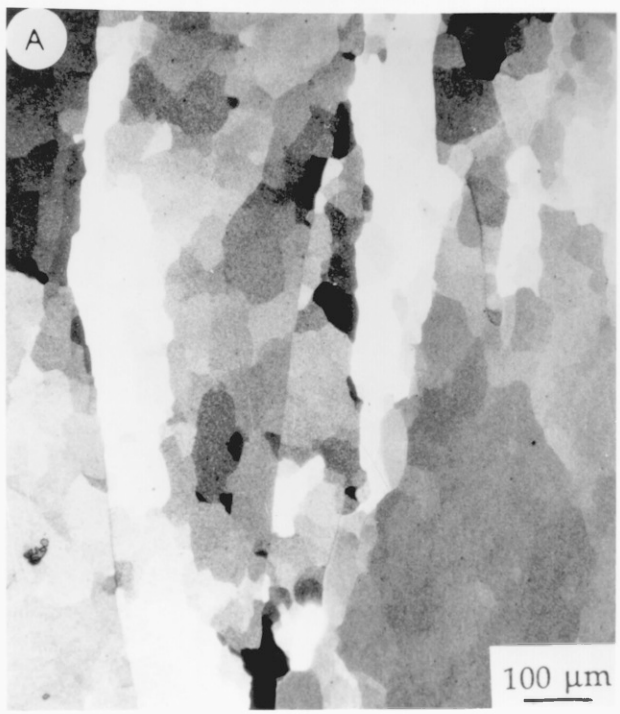
Fig. 6.12 Optical micrographs of the Al-Zr-Si alloy after compression testing at 500°C at strain rates of (a) 5×10^{-4} and (b) 5×10^{-2} S^{-1}.


A
100 µm


B
200 µm


A
100 µm


B
200 µm


A
100 µm

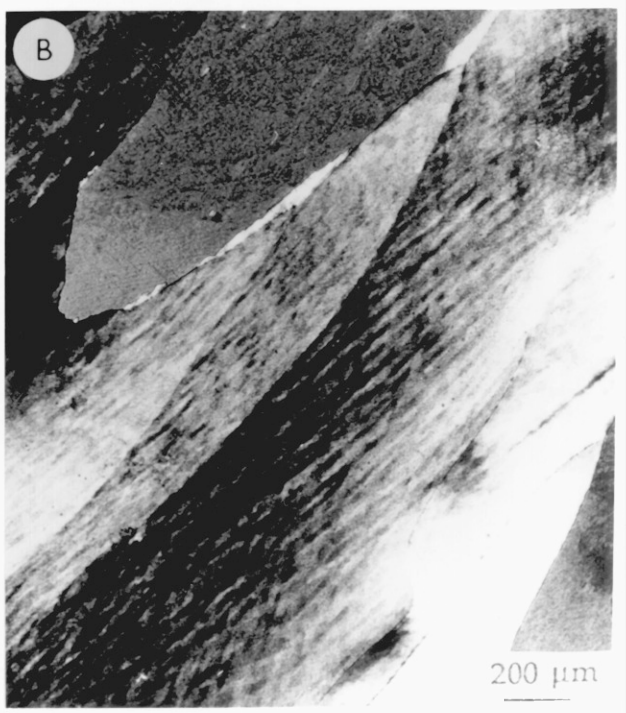

B
200 µm

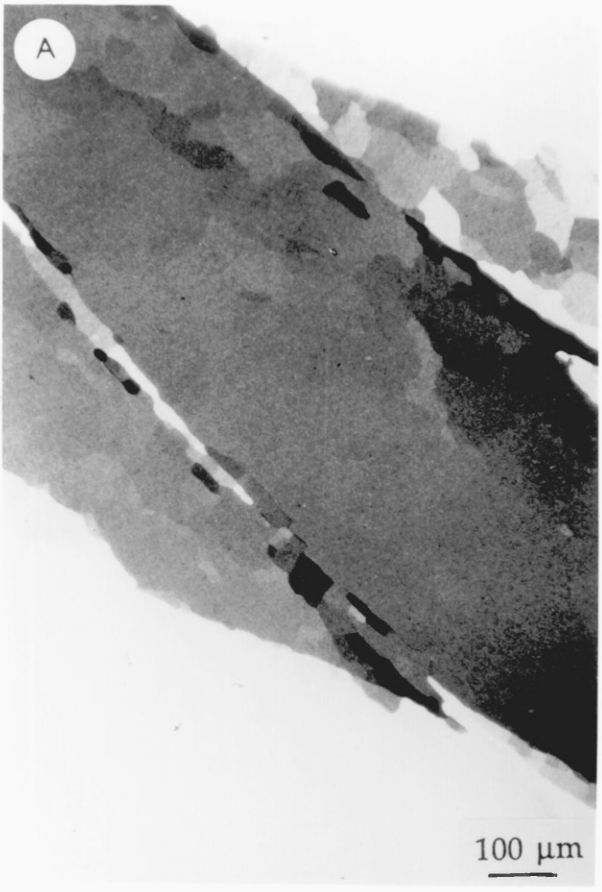
Fig. 6.13 Optical micrographs of the Al-Zr-Si alloy showing heterogeneous substructure developed adjacent to the grain boundaries after deformation at (a) 400°C at 5 x 10^{-4} S^{-1}, (b) 400°C at 5 x 10^{-4} S^{-1}, (c) 500°C at 5 x 10^{-3} S^{-1}, and (d) 400°C at 5 x 10^{-2} S^{-1}.

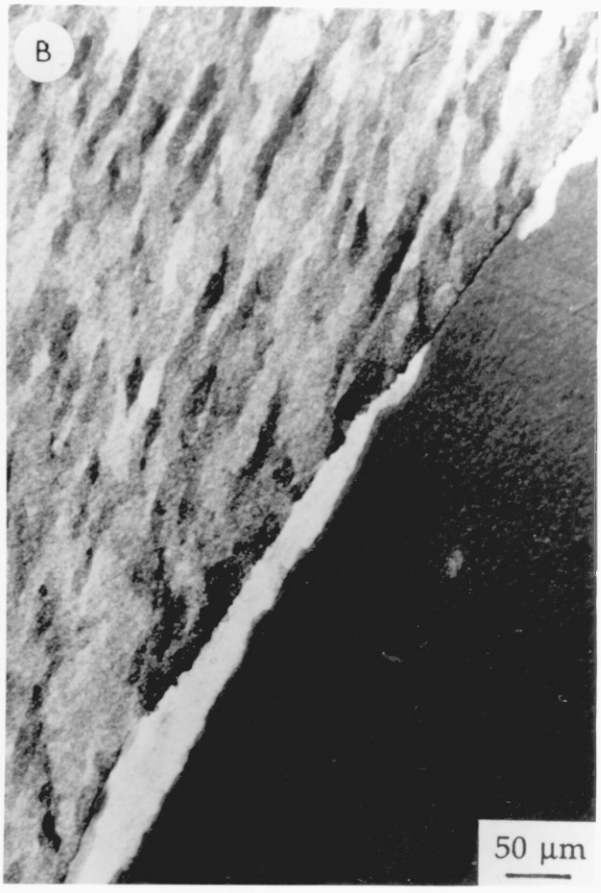
6.13 (a)

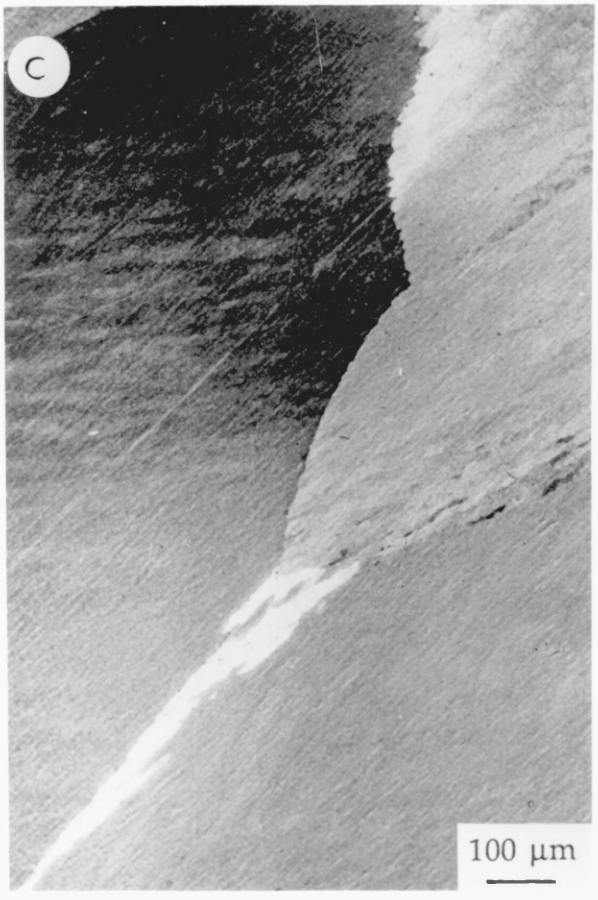
6.13 (b)

6.13 (c)

6.13 (d)


A
100 µm


B
50 µm


C
100 µm


D
100 µm

6.4.2 Transmission Electron Microscopy.

Observations of the deformed substructure of the Al-Zr-Si alloy in the temperature range of 200 to 500°C at various strain rates have been made by the technique of transmission electron microscopy.

At temperatures of 200 and 300°C, the deformed substructure was seen to be similar to that typical of the low temperature deformed substructure of aluminium alloys (figs. 6.14-6.15). The resultant structure had a low dislocation density within the sub-grains and sharp sub-boundaries.

The resulting deformed structure generated at 400 and 500°C may significantly distinctive to that generated during the deformation at lower temperatures (figs. 6.16 - 6.17). The microstructure revealed coarser sub-grains with low dislocation density walls. Sub-boundaries at the highest deforming temperature of 500°C appeared to become more regular (fig. 6.17). An increase in the sub-grain size was observed on increasing the deformation temperature and decreasing strain rate, as shown in the table 6.1.

More inhomogeneous distributions of free dislocation tangles within the sub-grains, extending around the Al_3Zr particles were found in the specimens deformed at 400 and 500°C compared to those deformed at lower temperatures. The microstructure revealed that dislocation movement was impeded by the presence of small finely dispersed particles and as a result an extra high dislocation density was created in the material associated with the particles.

The heterogeneous dislocation structure in the area adjacent to a boundary was different from that inside the grains in the specimens deformed at high temperatures. Pileups of many heterogeneously evolved dislocations were seen around the boundary region which tended to form

small elongated cells parallel to the grain-boundaries. This type of divergent deformation sub-structure observed near the grain-boundaries, is depicted in fig. 6.18. Such a structure was also occasionally observed to be present in the specimens deformed at low temperatures at low strain rates (fig. 6.18 (e)) but not as clearly developed as at higher temperatures. Dislocations in the grain-boundary areas were usually observed in the form as if they were linking the boundaries with the Al_3Zr particles present in the adjacent zones. The apparent effect of the particles on grain boundaries was to hinder the grain boundary and dislocation mobility by effectively pinning them which gave rise to the formation of the heterogeneous deformation structure at the boundaries.

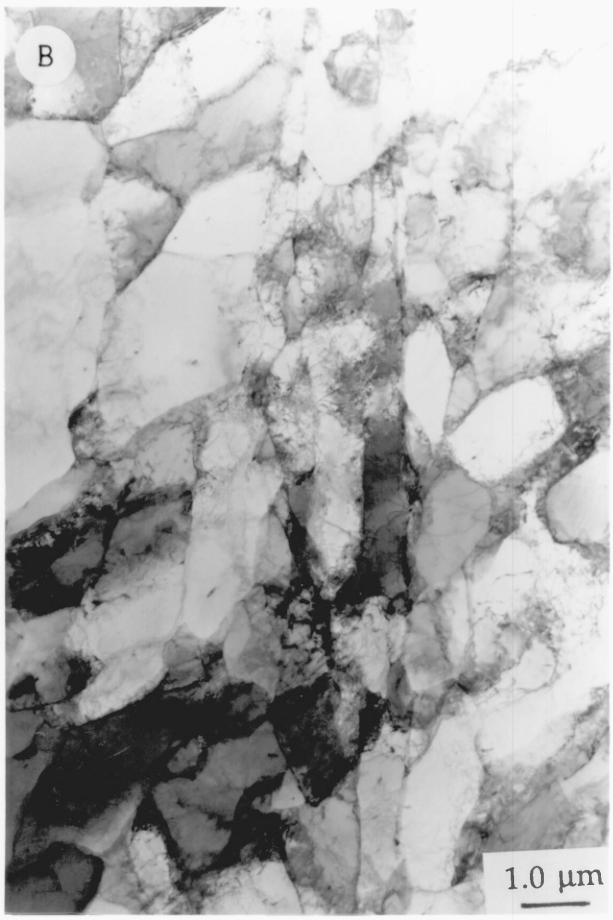
Temperature°C	Strain Rate S^{-1}		
	5×10^{-4} (μm)	5×10^{-3} (μm)	5×10^{-2} (μm)
200	2.2	1.3	0.95
300	9.8	2.4	1.9
400	4.7	3.8	2.4
500	12.5	4.6	3.9

Table 6.1 Sub-grain size of the Al-Zr-Si alloy deformed in compression at different temperatures and strain rates.

Fig. 6.14 TEM of the Al-Zr-Si alloy after compression testing at 200°C at strain rates of (a) 5×10^{-4} and (b) 5×10^{-2} S^{-1}.

Fig. 6.15 TEM of the Al-Zr-Si alloy after compression testing at 300°C at strain rates of (a) 5×10^{-4} and (b) 5×10^{-2} S^{-1}.


A
1.0 µm


B
1.0 µm


A
1.5 µm

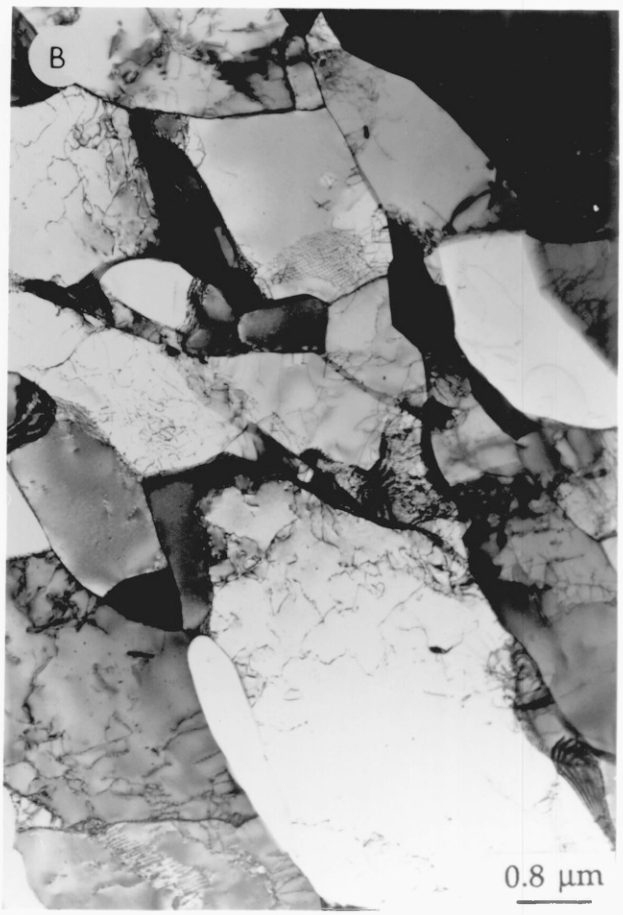
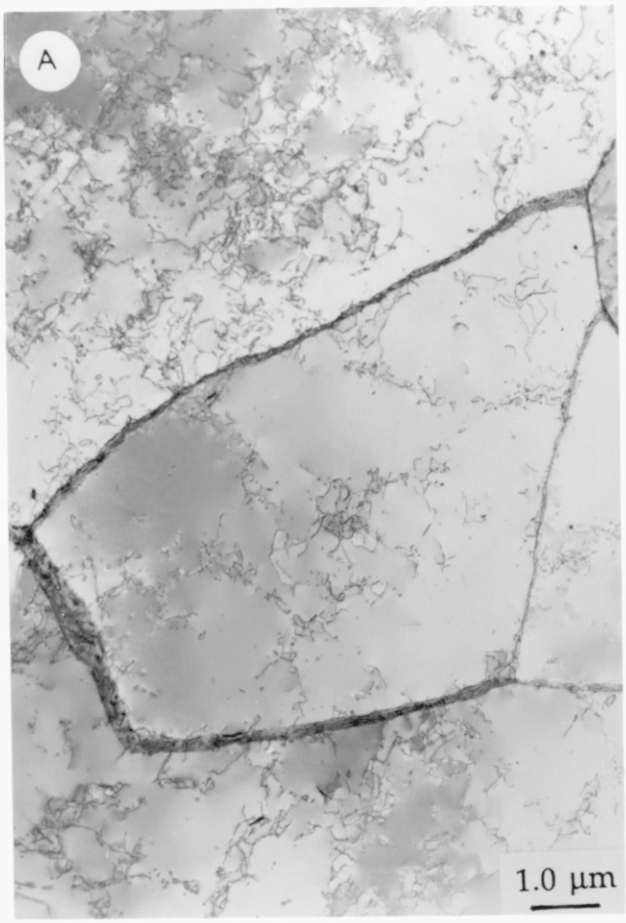
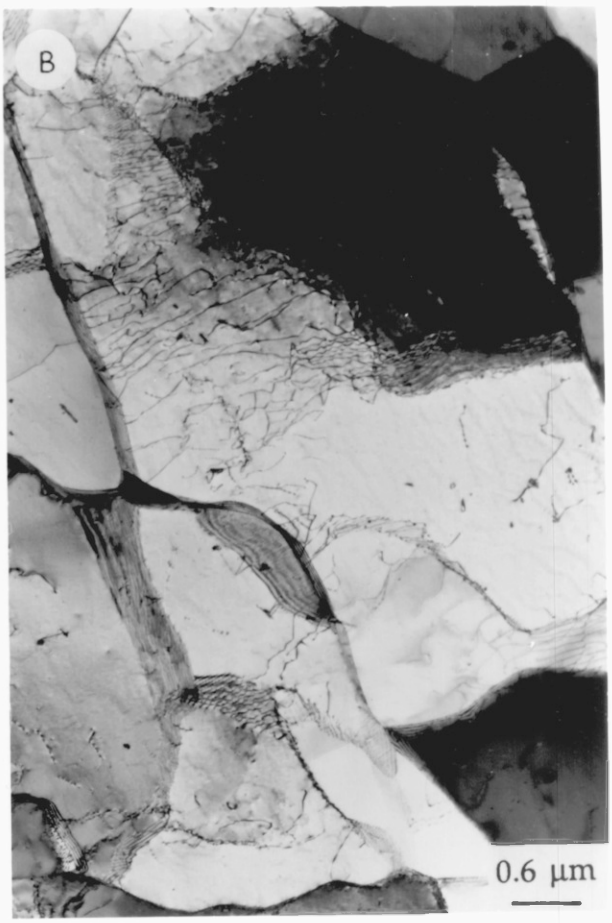
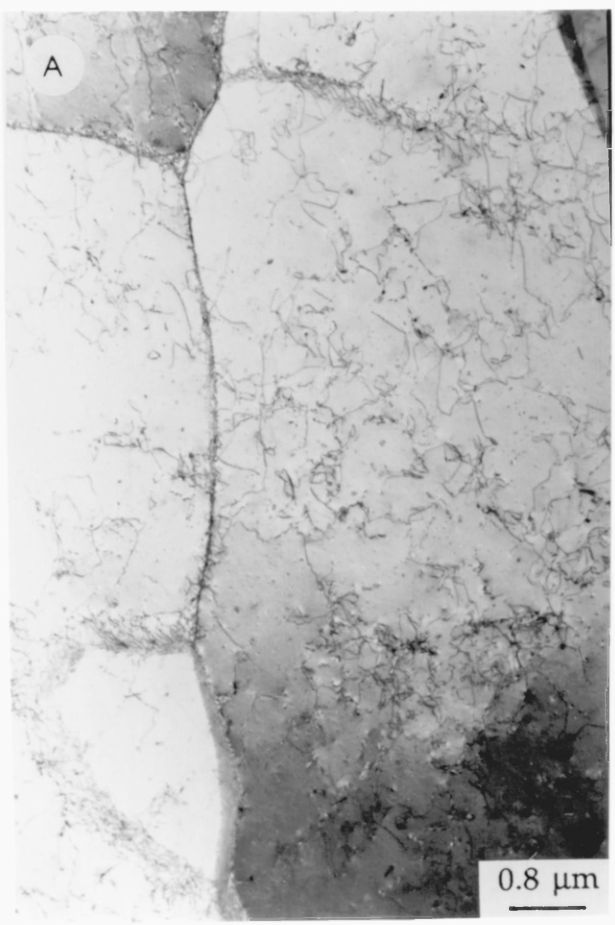

B
0.8 µm

Fig. 6.16 TEM of the Al-Zr-Si alloy after compression testing at 400°C at strain rates of (a) 5×10^{-4} and (b) 5×10^{-2} S^{-1}.

Fig. 6.17 TEM of the Al-Zr-Si alloy after compression testing at 500°C at strain rates of (a) 5×10^{-4} and (b) 5×10^{-2} S^{-1}.


A
1.0 µm


B
0.6 µm


A
0.8 µm

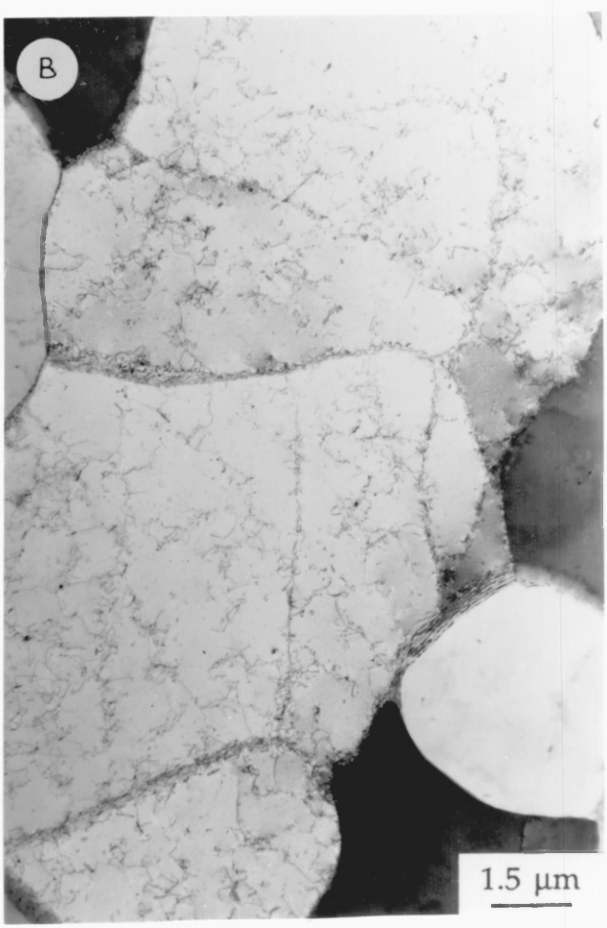

B
1.5 µm

Fig. 6.18 TEM of the Al-Zr-Si alloy showing heterogeneous substructure developed adjacent to the grain boundaries after deformation at (a) (b) 500°C at 5 x 10^{-4} S^{-1}, (c) (d) 400°C at 5 x 10^{-4} S^{-1}, (e) 300°C at 5 x 10^{-3} S^{-1}, and (f) 500°C at 5 x 10^{-2} S^{-1}.

6.18 (a)

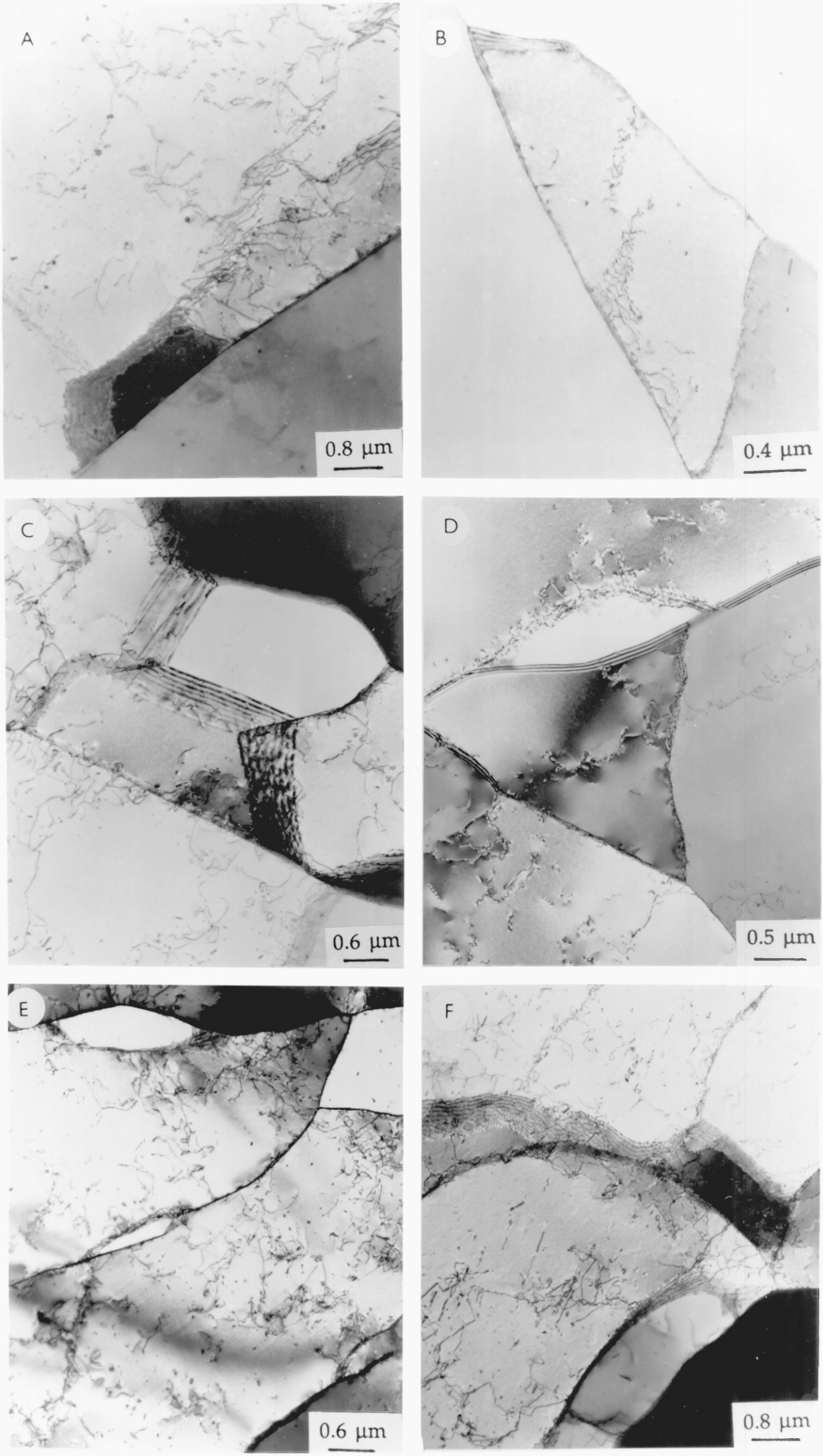
6.18 (b)

6.18 (c)

6.18 (d)

6.18 (e)

6.18 (f)


A
0.8 μm
B
0.4 μm
C
0.6 μm
D
0.5 μm
E
0.6 μm
F
0.8 μm

CHAPTER 7
DISCUSSION

7.1 Strength of the Composites at Low Temperature.

The experimental results of the mechanical testing of both the 2S/SiC and 2014/SiC composites, and their unreinforced alloys clearly indicate (see section 4.1) that the addition of SiC particles has markedly improved the strength of the composites over the unreinforced matrix alloys at low temperatures. This result is in accordance with the reported mechanical properties results of the aluminium matrix/SiC composites (124, 131, 144, 168).

The observed increase in the strength of the aluminium/SiC composites over the unreinforced aluminium comes as a result of combined interactions and contributions from more than one elementary hardening mechanism such as that due to the action of SiC particles acting as dislocation barriers during deformation, the generation of high dislocation density as a result of the large difference in the thermal expansion coefficients between Al matrix and SiC particles, the effect from grain and sub-grain structure evolved as a result of the thermo-mechanical processing of the composites, the precipitation strengthening in case of the Al alloy matrix composites, and arising from the internal residual stresses in the matrix from the inhomogeneous deformation gradients of the particles and the matrix.

7.1.1 Rule of Mixtures.

Since Al/SiC alloys have been defined as composites, therefore it may be possible to calculate their strength from the strength contributions provided by the different constituents of the composites.

Assuming a perfect distribution of a second phase embedded in a metal matrix. When a load is applied on the composite, the stress is transferred from the matrix to the particles, by an interfacial shear stress generated by strain in the matrix. The load transferred will be the sum of the load carried by the matrix and the reinforcement. This in general is given by

$$\sigma = v_p \sigma_p + (1 - v_p) \sigma_m$$

where v_p is the volume fractions of particles and σ_p and σ_m are the strengths of the particles and the matrix. This model has been commonly applied (128, 168) to calculate the strength of the composites.

Applying a similar approach of rule mixtures to the composite 2S/SiC, the total strength obtained was 380 MPa, found by inserting the values of strength and volume fraction of each constituent. This value is much higher than the experimentally obtained values. It is not clear whether the inappropriate calculated result is due to improper representation of the particle distribution, incorrect strength values of SiC used or due to a combination of any other factors. Moreover, as explained by Humphreys (128), this model based on load transfer from matrix to reinforcement through interface is invalid in case of particles due to their small aspect ratio and in turn having small $\overset{a}{\lambda}$ interface for load transfer. This model also assumes that a good stress transfer across the matrix-reinforcement interface can be achieved and the quality of of the interface is uniform. In practice, a very poor understanding of the interface exists. This approach of calculating the strength of the composites therefore, is not very accurate and

reliable.

7.1.2 Internal and Residual Stresses.

The presence of a second-phase in an alloy, with a large difference in the thermal expansion coefficients, becomes a source of dislocation generation due to stresses caused by differential contraction on cooling from an elevated fabrication temperature. In the Al/SiC composites, which have a similar characteristic of having a large discrepancy between thermal expansion coefficients of the metallic and ceramic phases (10 : 1 ratio), when cooled from an elevated temperature, the generation of internal stresses resulting from the differential shrinkage is expected to produce some degree of plastic strain and enhanced dislocation density in the matrix (124, 125). The evidence of SiC particles leading to an increased dislocation density in an aluminium matrix is given in figs. 3.6 and 3.7 for the composites 2S/SiC and 2014/SiC which have been annealed to recrystallization and then quenched.

It has been extensively reported (169, 170) that the dislocations have a strong effect on the mechanical properties of metals and a high density of the dislocations could result in the strengthening of the composites. The generation of a high dislocation density, induced by the difference between the thermal expansion coefficients of Al and SiC in Al/SiC composites on cooling from the thermal treatments is reported to be responsible for an increase in the strength relative of the unreinforced aluminium. (124, 126, 131, 171). The higher the cooling rate, the greater the dislocation density generated and in turn more the strengthening induced by dislocations. Humphreys (128) has reported that in the Al/SiC composites, a higher yield stress is expected when quenched from 550°C compared to that quenched

from 200°C. Derby et al. (127) has also shown that the quenched in dislocations can give rise to the strength increment by establishing a relationship between hardness and quench temperature.

The increase in strength due to dislocation density can be given by the following expression, supposing that the dislocations are uniformly distributed.

$$\tau = \alpha G b (\rho)^{1/2}$$

where α is a constant frequently referred to as dislocation strengthening efficiency and is 1.25 for aluminium (57), G is shear modulus, b is Burger's vector, and ρ is the dislocation density.

Inserting the calculated values of the dislocation density in the above equation, the calculated strength increment values of 50 and 40 MPa were obtained for the composites 2S/SiC and 2014/SiC respectively. These values suggest that the fraction of strengthening, due to the dislocations generated during quenching, is an important fraction but does not completely account for the total strength improvement of the composites.

The unrelieved residual stresses arise in the early stages of deformation in the matrix due to the remainder of the stresses at the particle/matrix interface of the composites which could not be recovered in the form of quenched-in dislocations by any of the plastic relaxation mechanisms. The rise in the back stress in the matrix will increase misfit and hence increase the difficulty of movement for further dislocations. The internal misfit stresses have been calculated based on Eshelby's (44) theory of misfitting elipsoidal inclusions and applied to Al/SiC composites to predict the strength (168, 171). Humphreys (128) suggested that this factor has a small influence on the strength of the particulate metal matrix composites.

7.1.3 Particle Strengthening.

The presence of second-phase particles creates a resistance to the movement of dislocations. The effectiveness of the second phase in obstructing the dislocation movement determines the improvement in strength of a material. For impenetrable equiaxed particles, the dislocations are forced to bypass the particles and leave residual Orowan loops encapsulating them. The improvement in the strength related to the formation of Orowan loops is given by

$$\tau = G\,b/\lambda$$

where G is the shear modulus, b is Burger's vector and λ is the average spacing between the particles in the slip plane. This equation defines the strong dependence of strengthening on λ.

Using the measured average separation of SiC particles in the composite 2S/SiC, of 30 μm the predicted improvement in the strength according to the above equation would be 5 MPa which obviously is too small when compared to the actual increase in the strength observed between the composites and the unreinforced matrix materials. In fact large SiC particles in the Al matrix generate complex dislocation networks around themselves as a result of deformation and the CTE effect. Description of the deformation process in terms of Orowan loop formation would not be appropriate in this situation. Moreover, a number of SiC particles in these high volume fraction composites lie on the boundaries so it is difficult for the Orowan mechanism to operate and significantly contribute towards the strengthening.

7.1.4 Grain and Sub-Grain Strengthening.

The particulate Al/SiC composites generally have a very small grain size, typically around 10 μm as a result of the thermo-mechanical process involving cold deformation followed by recrystallization annealing. A marked increase in the strength would be expected in the composites with this range of grain size on applying Hall-Petch equation.

A number of studies have verified the validity of the Hall-Petch type equation (60, 173, 174, 175), expressing the relationship between the strength increment and grain size.

$$\tau = K(d)^{-1/2}$$

K is a constant whose value for high angle boundaries varies between 0.07 and 0.04 $MN/m^{3/2}$ (58, 175, 176) depending on the amount, shape and spacing of the second phase particles.

In the present studies, the composites 2S/SiC and 2014/SiC had an average grain size of 165 and 120 μm respectively, prior to testing, as a result of hot rolling and annealing. The expected strength contribution from this large grain size in these composites from applying the above equation is very insignificant compared to the actual difference between the strengths of the composites and the unreinforced matrix alloys. Similar results have also been reported previously; Hansen (57) shows that a deviation from the above equation exists with a large grain size as the strengthening effect decreases rapidly with increasing grain size. These composites, if otherwise processed to obtain a fine grain size, would be expected to show grain structure strengthening. It has also been reported (57) that the grain boundary strengthening becomes absent in aluminium when deformed at strains more than 15 % or if the size of the second phase is very large (> 1 μm). This effect is described to be due to the dominance of other mechanisms in the matrix such as an increase in the dislocation density. This

reason could also account for the small strength contribution from the grain boundary effect.

Sub-grain size is also observed to influence the strengthening of Al in a similar way to grain size (53). The transmission electron microscopy of the composites 2S/SiC and 2014/SiC shows that the enhanced dislocation density gets arranged as a result of dynamic recovery into a sub-grain structure in the size range of one μm. The strength increment expected from this sub-grain size was calculated to be 30 MPa. The flow stress value is estimated to be 130 MPa for aluminium with this sub-grain size range from the correlation established by McQueen et al. (66) between steady state flow stress and mean sub-grain diameter for a variety of deformation conditions and metals (fig. 7.1).

7.1.5 Combination of the Strengthening Mechanisms.

The strength of composites is frequently expressed by a treatment which simply involves the summing of the different individual hardening mechanisms linearly (176, 177). Applying this linear additivity method to predict the total ultimate strength of the composite 2S/SiC gave a value of 160 MPa. The strength increment contributions due to dislocation density, sub-grain structure and SiC particles have already been calculated to be equal to 50, 30, and 5 MPa respectively for the composite 2S/SiC. Adding these values to the ultimate tensile strength of the unreinforced 2S aluminium, which is 74 MPa, the ultimate tensile strength of the composite is found to be 160 MPa. Similarly, the ultimate tensile strength calculated for the composite 2014/SiC is 540 MPa. The predicted values are higher than the experimental results.

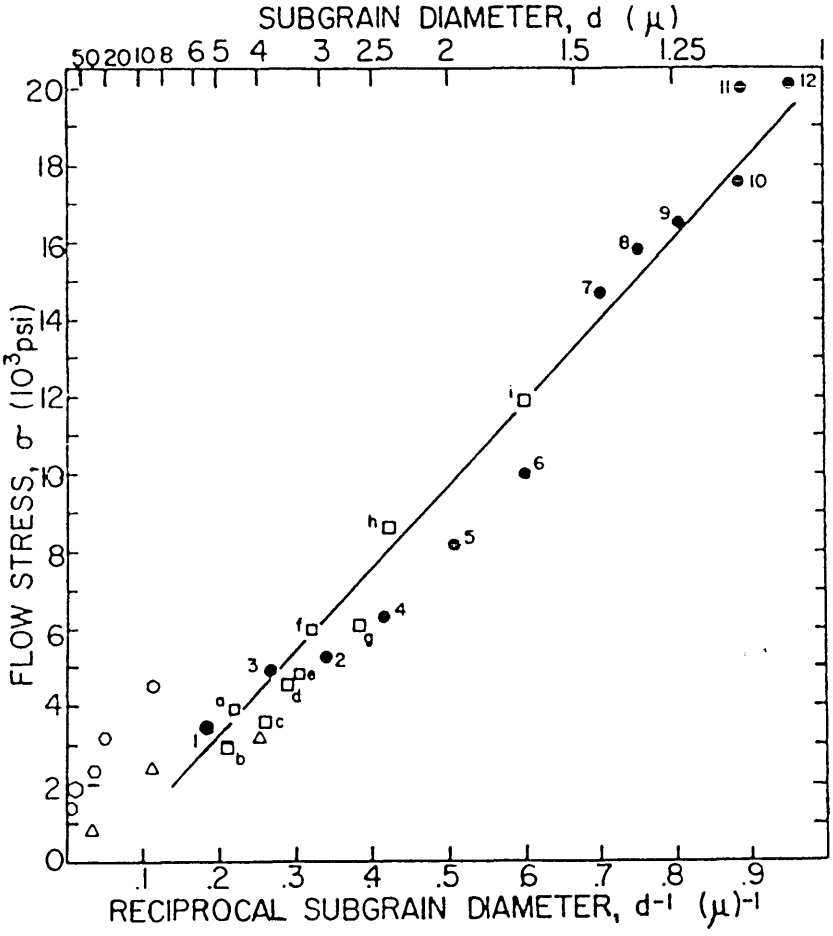


Fig. 7.1 Correlation between steady state flow stress and mean subgrain diameter for a variety of deformation conditions and metals (66).

The contributions of these factors of course combines to improve the strength of the composites. The presence of SiC particles significantly modifies the process of strengthening due to contributions of different factors by generating a high dislocation density during cooling. This complicates the combination of different strengthening mechanisms, as the same dislocation population is superimposing its effect on different mechanisms. This high dislocation density also modifies the transformation reactions such as those affecting the precipitation sequence in the alloy matrix of the composites (121, 178), altering the deformed sub-structure, or forming a superimposed sub-structure due to some polygonization of the dislocations. This situation makes the theoretical prediction differ from the experimental results due to difficulty in clearly separating the complex mutual interactions of different components.

The contribution of various strengthening mechanisms in Al/SiC composites, therefore, may not be a linear sum of the magnitude of all the individual factors (2), due to the way these different mechanisms interact with each other during the strengthening process. The resultant strengthening contributed, for instance, by the components such as impenetrable particles and dislocation density is best represented as the square root of the sum of the squares of these individual factors. The contributions due to other factors such as grain boundaries, weak penetrable particles, etc. are generally added linearly (2) to provide a reasonably simple and accurate prediction of the strength. However, it will need a great deal of effort to improve the existing methods to find the exact strength of the materials, considering the details of the complex micromechanisms responsible for strengthening.

7.2 Work Hardening of the Composites at Low Temperature.

It has been observed (131) that aluminium/SiC composites exhibit greater initial work hardening rates than the unreinforced matrix alloys. This is in agreement with the present investigations on the 2S/SiC and 2014/SiC composites and their alloys (see section 4.1.3).

The particles which do not deform during deformation have the most pronounced effect on work hardening in the early stages of deformation. However, at large strains, these particles do not affect work hardening significantly (2, 16, 62).

In the early stages of deformation, the load is transferred from the inside of the matrix to the particles, which act as barriers to the moving dislocations. This could result in either Orowan loop formation or in the starting of some other equivalent dislocation mechanism such as the generation of primary and secondary prismatic loops. In aluminium matrix composites containing large SiC particles the description of work hardening in terms of Orowan loops may not be appropriate, but due to the complex dislocation interactions at the particles, the concept of internal stresses due to unrelaxed strain can still be applicable in the initial stages of deformation.

The main contribution to internal stresses in two phase alloys is considered to be the mean matrix stress (179). The mean stress arises from a uniform stress generated throughout the matrix to compensate for the stresses within the undeformed particles due to the unrelaxed dislocation structure around the particles. The mean stress according to (42, 43) is given by

$$\tau = \gamma G f \varepsilon$$

where f is volume fraction, ε is unrelaxed strain, γ is an accommodation factor which relates the elastic strain in the particles to the plastic strain in the matrix and is of order of 0.5 for spherical particles and

G is shear modulus. If the elastic constant of the particles differs from that of the matrix then a modification is required to replace G with an effective G*, taking the inhomogeneous deformation into account (10). The value of G* is found to be 2 (128) for Al/SiC composites.

The mean stress as predicted by the above equation acts to oppose the further deformation of the matrix and the material hardens rapidly on increasing strain in the early stages of deformation.

A break down of initial linear hardening occurs on further straining and stress to cause hardening is no more proportional to strain (50). The stress-strain curve at large strain becomes parabolic due to onset of relaxation of large stresses at the particle matrix interface by generating complex dislocation tangles.

Work hardening by the dislocations stored within the matrix between the particles to accommodate the imposed strain gradients is discussed by Ashby (18) in terms of a parameter recognised as geometrically necessary dislocations. These are generated to relieve the stress and maintain the compatibility between the non-deforming, incoherent and hard particles and the matrix during plastic deformation. The process of the generation of geometrically necessary dislocations is particularly amplified in Al/SiC composites by dilation due to differential thermal expansion.

The density of geometrically necessary dislocations induced as a result of the strain gradient differences between the matrix and the second phase particles is given by

$$\rho^G = 4 f \varepsilon / r b$$

A rapid storage of dislocations at large particles occurs. The TEM of the composites 2S/SiC and 2014/SiC show evidence of the existence of high dislocation densities in the matrix around the particles.

The increase in work hardening due to the dislocation density is given

by a commonly observed relationship which gives flow stress proportional to the square root of the dislocation density.

$$\tau = \alpha G b (\rho^G)^{1/2}$$

Inserting the expression for the density of geometrically necessary dislocations, one obtains

$$\tau = \alpha G (f b \varepsilon / r)^{1/2}$$

This expression shows that the particle size and the volume fraction influence the flow stress. Assuming that these factors are constant, a plot of flow stress against $\varepsilon^{1/2}$ represents parabolic hardening. Several authors have studied work hardening rates of many alloys, relating flow stress to $\varepsilon^{1/2}$ for single crystals (180), and also for polycrystalline materials (181). Plots of stress against $\varepsilon^{1/2}$ for the composites 2S/SiC and 2014/SiC at ambient temperature are given in figs. 7.2 and 7.3.

At very large strains, a deviation from Ashby's hardening model is observed (38, 39, 182) which is attributed to the onset of dynamic recovery of the forest of geometrically necessary dislocations through the formation of a cell structure. This effect can be observed in the stress-strain curves of the two phase materials which become parallel to those of single phase materials at large strains (183). The present studies on the composites, especially when deformed in compression (where larger strains were obtained than in tension), show more evident deviation in the stress-strain curves. These findings agree with with the microstructural observations made of the composites deformed in compression (e.g. figs. 3.22 and 3.28), which clearly show a dynamically recovered cell structure developed after large strains.

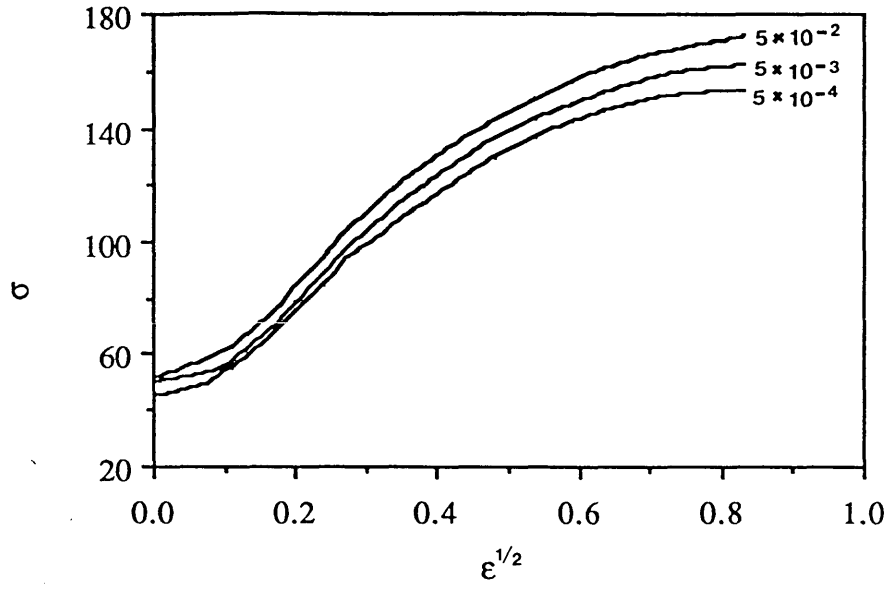


Fig. 7.2 σ vs. $\varepsilon^{1/2}$ curves of the composites 2S/SiC deformed in compression at ambient temperature at different strain rates.

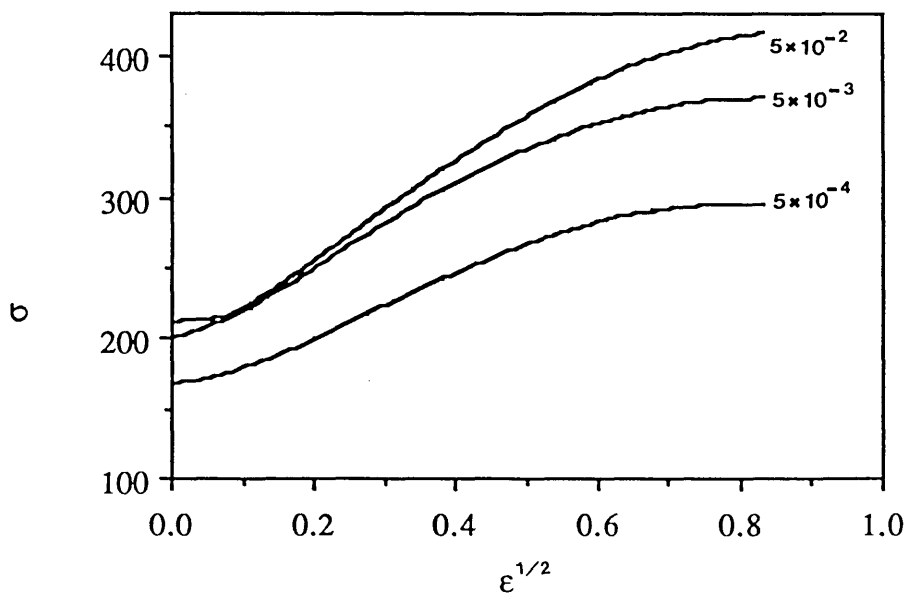


Fig. 7.3 σ vs. $\varepsilon^{1/2}$ curves of the composites 2014/SiC deformed in compression at ambient temperature at different strain rates.

7.3 Mechanical Properties of the Composites at Elevated Temperatures.

In order to evaluate the mechanical properties of the 2S and 2014 aluminium alloy matrix / SiC composites at high temperatures, tests were carried out on alloys reinforced with and without SiC particles . Tension as well as compression tests were used. The results are given in section 3.2 and 4.1.

Several authors have suggested (128, 184) that the mechanical behaviour of alloys containing non-deforming second phase particles can be generally categorized into three distinct temperature regions known as low, medium and high temperature domains, based on the different dislocation mechanisms involved at various temperatures.

At low temperatures, the composites exhibit a high yield stress and flow stress. The SiC particles act as dislocation barriers during deformation and confer a substantial improvement in the strength of the composites over the unreinforced matrix alloys (see section 7.1). The stress-strain curves at low temperatures do not show a true steady state and fracture during the tensile tests is observed while the curve is still rapidly rising. This shows that the addition of the large volume fraction of SiC particles greatly increases the hardening of the composites and reduces their ductility.

On increasing temperature, the modulus corrected yield stress for the composites remains constant until a temperature is reached at which it begins to drop rapidly (figs. 3.10, 3.11, 4.5, and 4.6). Several authors (10, 17, 37) have discussed the substantial drop observed in the yield stress in two phase alloys on increasing the temperature. Most investigations of the high temperature strength of the two phase alloys have been centered on copper single crystals containing SiO_2 particles. It has been observed that the normalized yield stress is constant up to ≈ 400 K owing to Orowan loops

and the yield stress has been shown to correspond to the Orowan stress. Beyond this temperature, the curve is observed to fall rapidly. The theories account this effect to the climb of dislocations, whether through bulk (124, 185) or pipe diffusion (17, 37). The maximum stress is found to drop to one half of the Orowan stress observed at low temperatures.

It would not be correct to apply this treatment to the composites which have a very complex dislocation structure around SiC particles generated through the combination of deformation and CTE effects. But whatever mechanism may be envisaged, the fall in the strengthening of course involves the climb of dislocations around particles by lattice diffusion. The value of stress exponents at elevated temperature is found to be 6.5 and 6.8 for the composites 2S/SiC and 2014/SiC. These values are between 4 and 7 (186). The activation energy calculated is close to that for the self diffusion of pure aluminium. This supports the view that dislocation climb controlled by lattice diffusion dominates the high temperature deformation process. The thermally assisted dislocations climb over the particles easily and annihilate more frequently. The strength of the composites is controlled by the strength of the matrix. At temperatures near 500°C, the strength of the composites is observed to be similar to that of the matrix materials. The strength advantage gained at room temperature from SiC particles is lost at elevated temperatures. The properties of the matrix may then determine the strength of the composites. These results are consistent with the observations made by Jarry et al. and Nieh et al (129, 187).

The stress-strain curves of the composites deformed at elevated temperatures show a steady state attained during straining which indicates that recovery effects are introduced. These arise from the rearrangement and annihilation of mobile dislocations, which balance the dynamic strengthening (104). The TEM observations show evidence of the

dynamically recovered substructure in the composites developed on increasing the deformation temperature (see section 7.5).

7.4 Work Hardening of the Composites at Elevated Temperatures.

Initial work hardening rates of the composites 2S/SiC and 2014/SiC and their matrix alloys have been measured as a function of temperature and strain rate and are shown in figs. 3.18, 3.19, 4.13, and 4.14. The curves clearly show that at low temperatures, the work hardening rates of the composites are greater than those of the matrix alloys, but as the temperature increases, a drastic change occurs between 275 and 375°C, depending on strain rate, where the work hardening rates of the composites drop significantly and become similar to those of the matrix materials. This indicates that there is a transition existing in the mechanical behaviour of the composites at a particular temperature, depending on strain rate. This change in the mechanical behaviour as a function of temperature for a particular strain rate and particle size can be interpreted in terms of dislocation particle interactions.

At low temperatures, dislocations bypass the particles, leaving Orowan loops accumulated around them. This results in high local stresses at the particles and leads to plastic relaxation of the dislocations around the particles. At large particles ($> 0.1\mu m$), the relaxed structure appears in form of local lattice rotation (2, 3). This gives a large initial work hardening of the materials.

With increasing temperature, the dislocations arriving at the particles

start climbing instead of accumulating. This leads to a loss of particle induced work hardening, and the work hardening of the alloy drops to a value similar to that of the matrix. Several authors have studied the conditions under which the stresses built up around the particles as a result of dislocation accumulation during deformation may be removed by thermal diffusion (2, 3, 62). Hirsch et al. (30) explained the removal of dislocation loops by dislocation core diffusion. This process explained the low temperature recovery of work hardening only in alloys containing small particles. Ashby (32) considered the process of climb to occur in the form of surface diffusion. Koeller et al. (24) and Mori et al. (188) discussed the process in terms of diffusional relaxation of high local stresses at the particle matrix interface. The process of dislocation climb at the particle matrix interface is only operative at low temperatures. Humphreys et al. (7) quantified the behaviour in terms of the initiation of diffusional relaxation by dislocation climb due to bulk or interface diffusion or both.

This explanation, based on situations in which dislocations either accumulate at, or climb away from, the particles, suggests that the mechanical behaviour of alloys containing large non-deformable particles can be divided into two regions of temperature and strain rate, depending on the particle size.

In the low temperature and high strain rate region, the dislocation particle interaction leads to the formation of a complex dislocation structure adjacent to the particles which significantly alters the mechanical behaviour of the material.

In the high temperature and low strain rate region, no dislocation structure is formed because the rate of removal of dislocations is greater than the rate of accumulation around particles owing to the diffusion-controlled climb of dislocations.

The transition in the mechanical behaviour as a result of bulk and interface diffusion occurs at a value of strain rate given by Humphreys and Kalu (7).

$$\varepsilon^{\circ} = [K_1 \exp.(-Q_v / R T) / T d^2] + [K_2 \exp.(-Q_i / R T) / T d^3]$$

Q_v and Q_i are the activation energies for bulk and surface diffusion and K_1 and K_2 are constants.

The first term represents volume diffusion and the second term represents boundary diffusion and will be very small for large particles (> 1 μm) (128).

This model has been verified for aluminium alloys with a range of particle sizes (0.5 to 10 μm) and containing a low volume fraction of second phase particles (7). In the present work, this model is applied to the aluminium matrix composites containing large SiC particles. The transition temperatures in the mechanical behaviour of the composites at different strain rates predicted according to the above equation, using the values of K_1 and K_2 applicable to a matrix of pure aluminium (7), are shown in table 7.1.

A good agreement is found between the experimental and theoretical transition temperatures of aluminium matrix SiC composites. It is also found that the high volume fraction composites obey the theory of the transition in mechanical behaviour determined for dilute aluminium alloys (7).

The significant influence of the large SiC particles on elevated temperature mechanical behaviour of the composites suggests that consideration of the transition theory is of great practical importance in optimising the processing route of the two phase aluminium alloys.

Humphreys (128) has explained the conditions, as shown in fig. 7.4, needed to predict the critical transition temperature for a particular particle size and strain rate, based on the above equation, for the particulate metal matrix composites. The results of the present study, as shown in table 7.1, correspond well with these conditions. The construction of such a diagram can be used to forecast the right conditions of the critical temperature and strain rate for the composites to be successfully hot worked. It also shows that the area between the melting temperature of the composite and the allowable hot working region above the transition temperature becomes narrower as the particle size increases.

7.5 Microstructural Developments during Elevated Temperature Deformation of the Composites.

The microstructural variations were followed by optical and TEM examinations of the composites 2S/SiC and 2014/SiC deformed in compression at different temperatures and strain rates to a strain of fifty percent.

The optical microstructure of the deformed composite 2S/SiC revealed that the originally coarse equiaxed grains (165 μm dia.) had been elongated in the direction normal to the compression axis. (figs. 3.22 to 3.26). The composite 2014/SiC after deformation, however, exhibited more or less equiaxed grains due to deformation of the grains already elongated in a direction parallel to the deformation axis (see section 3.3.3).

The results are similar to those found for aluminium hot deformed to higher strain levels (189) showing that a constant grain size persists while

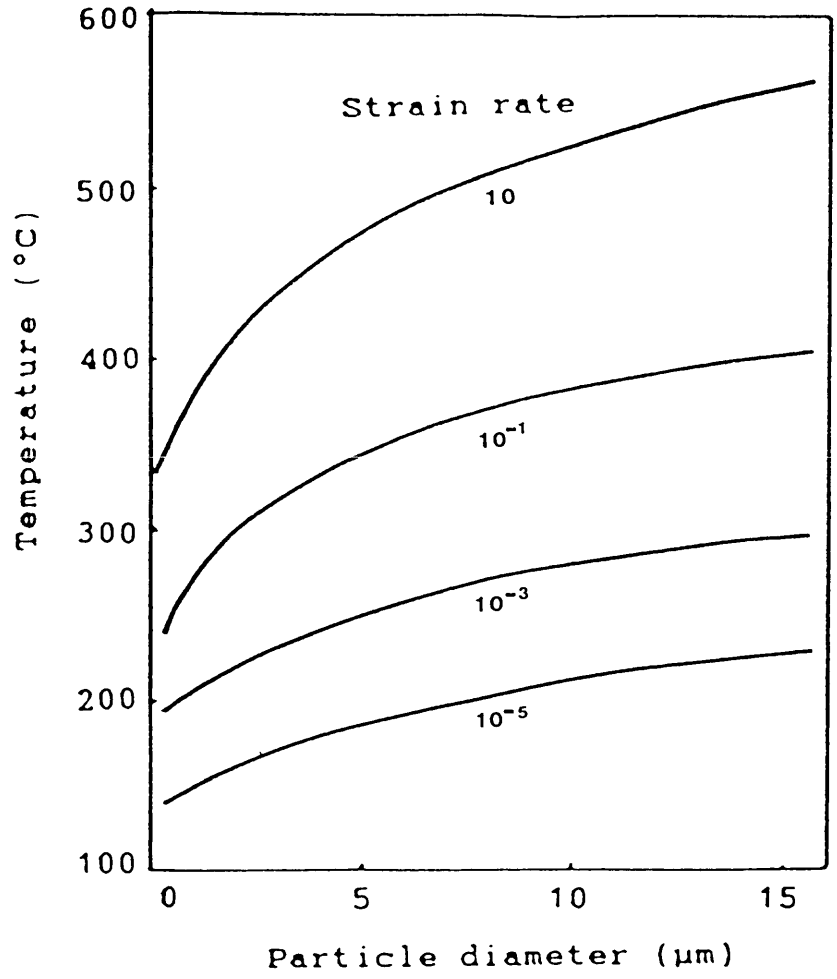


Fig. 7.4 The critical temperature below which stresses will accumulate at the particles (128).

Strain Rate (s^{-1})	Experimental Transition Temperature (°C)	Theoratical Transition Temperature (°C)
5×10^{-4}	375 - 400	370 - 390
5×10^{-3}	325 - 350	320 - 340
5×10^{-2}	275 - 300	275 - 300

Table 7.1 Experimentally measured and theoretically predicted temperatures of the transition in the mechanical behaviour of the composites.

deforming at various temperatures due to the absence of recrystallization. This indicates that dynamic recovery is the sole restoration mechanism during the deformation of the composites at various temperatures.

A few small equiaxed grains were observed in the optical micrographs of the composite 2S/SiC along with the widespread elongated grains having wavy grain boundaries (e.g. figs. 3.25 and 3.26). Such small equiaxed grains are commonly observed following high temperature deformation of aluminium and its alloys and have been interpreted as being due to dynamic recrystallization (190). Humphreys (191, 192) explained that this could be due to the impingement of scalloped grain boundaries at large strains rather than the formation of new grains.

The optical microscopy of the deformed 2S/SiC composite having a large grain size revealed the existence of strain inhomogeneities in form of deformation bands within the grains around particles (figs. 3.22 to 3.25). There is little information available about the effect of particles on the development of substructural features such as shear bands in the grains (193).

A study of the variations in the substructure with temperature at different strain rates in the composite 2S/SiC shows that the sub-grains are elongated at low temperatures similar to those observed in pure aluminium deformed at low temperatures (189). The composite 2014/SiC deformed at low temperatures was found to consist of a high density of dislocations along with fine precipitates, distributed randomly within the matrix instead of forming a well defined cell structure (fig. 3.36). The dispersion of fine precipitates retards the movement of the dislocations during deformation, resulting in the prevention of the dislocation rearrangements necessary to form sub-grains normally observed in aluminium (194) as a result of dynamic recovery.

On increasing the deformation temperature, the substructure of the composites was found to be transformed from elongated sub-grains to coarser and more equiaxed ones. This change observed in the composites has a similar dependance on the temperature and strain rate as observed for pure aluminium. This is attributed (189, 194, 195, 196) to the strong dependance of the dislocation distribution and rearrangement on temperature. The large dislocation density produced during deformation at elevated temperatures can be readily annihilated and rearranged into ordered patterns due to thermally assisted cross-slip and climb of the dislocations into low energy configurations, resulting in the formation of equiaxed sub-grains. It has been reported (105) that in Al deformed above 400°C, the shape of the sub-grains remains equiaxed over a wide range of strains although the grains increasingly become elongated with strain. The composite 2014/SiC deformed at elevated temperatures did not exhibit as uniform a size of the recovered sub-grains as observed in the composite 2S/SiC. The presence of fine precipitates in the matrix of the composite 2014/SiC restricts both the movement of dislocations and reformation of the sub-boundaries during dynamic recovery by pinning them and tends to stabilize the heterogeneous substructure defined by the distribution of the precipitates (197).

The observation of the substructural variations occurring during deformation at different temperatures indicates that there is a distinct enlargement in the sub-grain size on increasing the deformation temperature from 300 to 400°C (table 3.1). The transition in the mechanical behaviour of the composites from a low temperature to a high temperature region is also observed in this temperature range and is reported (7) to be due to increase in the ability of dislocations to avoid particles by diffusion controlled climb instead of being accumulated at the particles. The reduced capability of the SiC particles to restrict dislocation

movement at high temperatures allows dislocation mobility to be enhanced. The dislocations annihilate and form into sub-grain structures more readily. The degree of dynamic recovery increases and therefore the sub-grains formed at temperatures above the transition are enlarged and more equiaxed.

7.6 Effect of Quenching on the Microstructure of the Composites.

An important structural feature observed in the TEM of the specimens deformed at 400 and 500°C is the presence of a significantly higher level of redundant dislocation density within the recovered sub-grains. The specimens deformed during elevated temperature compression tests were quenched to terminate the test. This causes the generation of a high dislocation density in the matrix which is attributed to the large ratio of thermal expansion coefficients (10 : 1) between Al and SiC (124). Therefore the observation of a high dislocation density within the substructure is in fact a structure introduced duringquenching superimposed on the original dynamic structure generated as a result of the elevated temperature deformation.

The composite 2S/SiC shows a relatively homogeneous distribution of dislocations inside the grains in the matrix. The composite 2014\SiC, however, shows a relatively higher dislocation density near the SiC particles compared to areas away from the particles. The types of the dislocations observed in the composite 2014\SiC consist of ine dislocation loops and helical dislocations along with long straight dislocations and are different

compared to those observed in the composite 2S\SiC . The observations (198) of the quenched in dislocations in Al-Cu alloys have shown that an excessive concentration of vacancies is retained in solution, associated with the solute atoms after quenching from high temperatures. Whereas in pure Al, the vacancies can anneal out by climb. The condensation of supersaturated vacancies in the alloys results in the in formation of collapsed discs. These interact with dislocations emitted from the SiC particles in the matrix due to the CTE effect and form interwined helices and rows of loops, such as observed in the microstructure of the recrystallized and quenched 2014\SiC composite. The friction experienced by the dislocations in the matrix of the 2014 alloy due to intermetallic precipitates, causes higher concentrations of the quenched-in dislocations to be retained in the vicinity of the SiC particles.

7.7 Fractography of the Composites.

The SEM examinations of tensile fracture surfaces of the composites were made by using single and both half matching fracture surfaces in order to observe a clear picture of the fracture mechanism. It was difficult to identify a significant population of SiC particles on the fracture surfaces, suggesting that the fracture was caused by matrix failure. However, the observations of some fractured particles detected on the fracture surfaces and the evidence from the particle size analysis (fig. 3.3) under different processing conditions showed that the fracturing of the SiC particles does occur during deformation. These results indicate that the fracture of the composites is controlled by a combination of void nucleation in the matrix and the fracture of the particles.

A majority of fracture studies have been carried out on the low volume fraction materials (199) and it is reported (128) that the second phase particles assist in void nucleation during deformation at a critical strain and, on further straining, the voids will grow to a critical size in the length equal to interparticle spacing for interlinkage. The fracture is then controlled by the process of void growth.

In high volume fraction materials such as Al/SiC composites, the void nucleation is a more critical stage relative to that of void growth (128, 200). It is due to the reduced interparticle spacing which requires the amount of critical growth strain needed to be reduced. It is reported (200) that as the volume fraction reaches 0.16, assuming a uniform particle size and spacing, the amount of critical growth becomes zero.

In high volume fraction composites, the damage may also be expected by rapid accumulation of localised stress concentration due to an overlap of the plastic zones around particles. The impingement of plastic zones prevents stress relaxation during further straining and raises local stress rapidly until a critical value where fracture occurs (25, 128, 201).

In Al/SiC composites, regions of microstructure form where SiC particles, due to their high volume fraction, may cluster and have greater local volume fractions. Such areas are observed in the optical microscopy of composites in the present work (figs. 3.1 and 3.2). Increased stress concentration in these areas can give rise to initiation of fracture (140, 146).

The tensile fracture surfaces of the composite 2S/SiC show large dimples with an average size of 8 μm and small dimples for 2014/SiC with a size of about 5.5 μm. The intermetallic precipitates in the matrix of 2014/SiC have an effect of additional strengthening and determine the extent of void growth by their dispersions. The void growth is then very limited in the presence of small intermetallic precipitates along with SiC particles and hence showing smaller dimple size on the fracture surface.

The fracture surfaces at high temperatures revealed relatively more SiC particle exposure compared to those at room temperature. Similar observations have been previously reported in Al/SiC composites (129, 137, 200). This is suggested (137) to be as a result of sliding and decohesion between aluminium matrix and SiC particles at high temperatures.

7.8 Recrystallization Behaviour of the Composites.

The reinforcement of the large SiC particles markedly modifies the recrystallization behaviour of the aluminium matrix as a result of the formation of complex local lattice rotated deformation zones at the particles after deformation which represent the sites of high local strain energy. These deformation zones can potentially provide sites for the initiation of recrystallization (93). The driving force for the recrystallization arises from the strain gradient arising from the of dislocation density difference between the particle matrix interface and in the matrix away from the particles.

The accelerated recrystallization behaviour of the composite 2S/SiC and the temperature at which recrystallization takes place is observed to be similar to those of dilute two phase Al alloys, containing large Si particles (93), which undergo particle stimulated nucleation of recrystallization. A rapid fall in the isochronal curves (figs. 5.1) is observed at 270°C which is about 75 degrees lower than the recrystallization temperature of the unreinforced 2S aluminium. The hardness experiments are consistent with the metallographic results.

Similarly the composite 2014/SiC recrystallizes at 370°C, approximately 75 degrees lower than the recrystallization temperature of the unreinforced 2014 alloy but 100 degrees higher than the recrystallization temperature of the composite 2S/SiC. The 2014/SiC composite contains a dispersion of fine precipitates in the matrix which influence the recrystallization process over a large temperature range during annealing. Studies on the recrystallization behaviour of similar alloys containing both large and small particles (101) have shown that nucleation of recrystallization occurs at large particles, although the

kinetics of the recrystallization are controlled by fine dispersions.

TEM studies of the composite 2S/SiC show that on raising the annealing temperature, the ability of dislocations to change their configuration into fewer, simpler and more compact networks is increased by cross-slip and climb. The thermally activated formation of well defined substructure is indicative of recovery. The composite 2014/SiC, however, at low annealing temperatures consisted of areas of high dislocation density and a dispersion of very fine precipitates with little evidence that any substructure formed. The dispersion of fine precipitates prevents the long distance rearrangements necessary for dislocations to form sub-grains. Increasing the deformation temperature further leads to a coarsening of the fine precipitates and dislocations become unpinned. This assists dislocation activity in the matrix and sub-grain formation commences.

Increase in the temperature causes the sub-grain size to increase until the progress of recovery is terminated by the process of recrystallization.

After recrystallization, the composite 2S/SiC and 2014/SiC revealed a fine equiaxed grain structure. The recrystallized grain size, in the case of particle stimulated nucleation of recrystallization, can be related to the particle size and distribution in terms of the following expression, assuming one grain is nucleated per particle (128).

$$D = d\,(1-f)^{1/3}/\,f^{1/3}$$

where d is the particle size and f is the volume fraction.

Putting the required values in the above expression, the recrystallized grain sizes obtained for the composites 2S/SiC and 2014/SiC are 20 and 25 μm respectively. These results are in close agreement to the experimentally observed recrystallized grain sizes in the composites.

Since there are many factors which may influence the process of recrystallization such as the annealing temperature, additional alloying

elements, heating rate, deformation temperature, the amount of deformation prior to recrystallization, and the ability of large particles (> 3 μm) to nucleate more than one grain (54), etc. Therefore, the above equation can be regarded as merely indicating the correct trend in the change of the grain size due to the process of the particle stimulated recrystallization rather than the absolute values of grain size (128).

7.9 Effect of Amount of Cold Deformation on the Recrystallization of the Composites.

The recrystallization kinetics and the grain size of the composites 2S/SiC and 2014/SiC deformed to high strain levels of 50 and 70 % were found to be almost identical to those of 35 % deformed composites. Such a result would not be expected for conventional two phase aluminium alloys in which the recrystallized grain size is dependent on prior cold deformation : the higher the amount of strain, the smaller the grain size. This behaviour of the composites may be explained in relation to the driving force for recrystallization. The driving force in a single phase alloy for recrystallization is provided entirely by the dislocations stored as a result of deformation. In two phase alloys, there are additional dislocations relieved at coarse particles in the form of geometrically necessary dislocations to maintain the continuity during deformation (18). The density of these dislocations is proportional to a parameter which is the ratio of particle volume fraction to particle size. This factor may be very significant in the high volume fraction composites. In Al/SiC composites, the local dislocation density in the vicinity of the SiC particles would not only be a

function of applied strain, volume fraction and particle size but also depend on the complex dislocation structure introduced due to CTE mismatch (124). Therefore even at low applied strains, the SiC particles have a major influence on the formation of large number of dislocation structures, there being a more potential nucleation sites, at the particle matrix interface rather than a uniform distribution of dislocations through the matrix. The Al/SiC composites are, therefore, expected to store a significant amount of strain energy, in the form of large and complex dislocation networks, which can be above the critical levels even at a low strains to facilitate rapid recrystallization initiation. The lack of room temperature recovery effects allowsthe dislocation density to saturate at low strains which can provide a strong driving force equivalent to that generated at higher strains in conventional alloys and the recrystallized structure forms rapidly. The composites 2S/SiC and 2014/SiC containing a high volume fraction of large SiC particles have interparticle spacing 30 and 55 μm respectively. The interparticle spacing effectively controls the grain structure. The recrystallized grain size in an alloy containing a high volume fraction of large particles is expected to be of the order of interparticle spacing with little further growth occurring (8). This results in a uniform recrystallized grain size in Al/SiC composites which is insensitive to variations in the strain levels prior to recrystallization.

The recrystallized grain size in the composites deformed less than 35 % however, revealed a grain size of about 50 μm after annealing. This is larger than those obtained in the recrystallized composite specimens which have been subjected to greater amounts of cold deformation. This indicates deviation from the insensitivity observed in the recrystallized grain size in the more highly deformed composites. According to the diagrammatic explanation given by Humphreys (202) (Fig. 1.10), the composite

(7). It is shown that at low temperatures, the dislocations interact with particles and accumulate at the particle matrix interface which results in the formation of complex rotated zones at the particles. Annealing low temperature deformed composites, containing local lattice rotations associated with the particles which are a prerequisite for particle stimulated nucleation, leads to a small grain size due to an increase in the concentration of viable nuclei for recrystallization with little further grain growth due to control by the interparticle spacing.

However, above the transition temperature, where diffusion in the matrix is sufficient for dislocations to be able to climb away at the particles at a faster rate than they accumulate at the particles, complete recovery occurs at the particle matrix interface and hence no deformation zones are formed at the particles. Therefore on the subsequent annealing of the composite specimens deformed above the transition temperature, the particle stimulated nucleation of recrystallization would not occur and the resulting grain structure possesses a large grain size.

A slight increase in the subsequently recrystallized grain size is observed on increasing the deformation temperature up to the transition temperature. This is expected to be due to moderate changes in the deformation zones through some recovery. Thermally assisted cross-slip of dislocations is observed to take place in Al at intermediate temperatures (203). This can recover some stress concentration in the regions of high dislocation density at relatively high deformation temperatures. Its effects on potential nucleation sites results in a moderate increase in the recrystallized grain size. It is also shown (7) that the critical particle size to nucleate recrystallization increases rapidly with increasing temperature. This implies that for a constant particle size, the ability of the particles to provide recrystallization nuclei decreases with increasing temperature. This may effect the nucleation and result in a slight increase in the recrystallized

containing about 10 μm size particles deformed to a strain of 20 % are not expected to show recrystallization stimulated by particles. Therefore due to the absence of particle stimulated recrystallization, the nucleation rate is not enhanced any more by the particles and the grain structure observed is larger in the recrystallized composites deformed 20 % compared to those deformed to higher strains.

7.10 Effect of Deformation Temperature on the Subsequent Recrystallization of the Composites.

The effect of deformation temperature is an important variable affecting the final grain size on subsequent recrystallization. A difference in the grain growth kinetics was observed after recrystallization in the 2S/SiC composite specimens when deformed below or above a temperature range of 300 and 400°C, depending on the strain rate (figs. 5.30 - 5.35). The deformation temperatures at which a change in the subsequently annealed grain structure occurs, is comparable to the temperatures at which the transition in mechanical behaviour of these composites is observed to occur.

The specimens which were deformed below the transition temperature, show a small grain size whereas those deformed above the transition temperature after annealing displayed a large grain size of about 200 μm. These results supplement some other results where a small grain size was observed on annealing the cold rolled composites (fig. 5.11(c) & 5.22(c)) and a large grain size on annealing hot rolled composites (fig. 3.4 & 3.5). These results indicate that the deformation behaviour of the composites can be divided into two temperature regimes, depending on the strain rate similar to that suggested for Al alloys containing large particles

grain size on increasing the deformation temperature up to the transition temperature whereafter a major change occurs in the recrystallized grain size.

7.11 High Temperature Deformation of Al-Zr-Si Alloy.

Hot deformation tests of Al-Zr-Si alloy were conducted at temperatures between 200 and 500°C at strain rates between 5 x 10^{-4} and 5 x 10^{-2} S^{-1} (fig. 6.2). True stress-strain curves exhibit a general view of variation in the mechanical properties of this alloy at different temperatures and strain rates. The curves at higher temperatures reveal a trend of dynamically softening and attaining a steady state. The curves show that there is nonuniform deformation in the specimens deformed at 400 and 500°C at a strain rate of 5 x 10^{-4} S^{-1} above a strain of about 0.25. The flow stress at higher strain rates at these temperatures and at lower temperatures is observed to be uniform. It is reported (68) that fine coherent Al_3Zr dispersed particles redissolve in aluminium during boundary migration during early stages of deformation at high temperatures and re-precipitate during later stages of deformation. This phenomenon is reported on the basis of TEM observations of the migrating grain boundaries in the hot deformed Al-Zr alloys which on one side show precipitate free areas and on the other side, the precipitates exist in the form of dispersions. However, the present investigations of hot deformed Al-Zr-Si alloy in different conditions did not reveal large differences in the precipitate distributions on two sides of the grain boundaries between the neighbouring grain. If it is supposed that such a phenomenon does exist, the fall in flow stress during nonuniform deformation then may be associated with the reversion of the

precipitates into the solution and rise due to re-precipitation of the Al_3Zr precipitates. This is analogous to the observations where mobile dislocations during deformation are reported (204) to get pinned due to to diffusion of impurities on the dislocations and as a result, a jerky flow is observed.

Variation of the yield stress as a function of temperature is usually divided into three regions. At low temperature, the yield stress is temperature independent. In the medium range, the yield stress is very much dependent on the temperature and falls sharply. This is generally attributed to climb of dislocations around particles which is on high enough frequency to make the stress to drop significantly. At higher temperatures, the yield stress is again found to be little affected by the temperature and is found to be approximately one half of the Orowan stress in the single crystals (10, 37).

The curves for the modulus corrected yield stress in the range of 200 to 300°C in this work show a continuous drop which is more prominent at the lowest strain rate due to diffusion readily occurring in the specimens and dislocation loops climbing away from the particles.

A simple relation between flow stress, strain rate and temperature is given by the following equation (104).

$$\dot{\varepsilon}^{\circ} = A \sigma^{n} \exp.(- Q / R T)$$

Where A and n are the material constants, Q is the activation energy, R is the gas constant and T is absolute temperature. The equation has been found to fit the data of most of metals and their alloys (104, 167). This equation is used to analyse the correlation of temperature, strain rate and flow stress and by putting appropriate values, the activation energy at high temperatures was found to be 126 KJ/mole.

The initial parabolic work hardening rates were found to be very sensitive to the temperature in the range of 300 and 400°C. The size of

Al_3Zr particles is too small to form complex rotated zones around them during deformation at low temperatures. The particles may block the mobile dislocations and form primary and secondary dislocation structure around them at low temperatures which by interfering the dislocation movement, provide increased hardening of the alloy. At elevated deformation temperatures, where volume diffusion plays an important role, the dislocations may climb the particles readily through interface or / and bulk diffusion (7) which is responsible for initial work hardening rates to fall at high temperatures.

7.12 Microstructure of the Deformed Al-Zr-Si alloy.

Optical micrographs of Al-Zr-Si alloy revealed large elongated grains in the specimens deformed in compression at different temperatures and strain rates.

The specimens deformed at 200 and 300°C show a banded substructure within the grains, very similar to that in pure Al deformed at low temperatures. At higher temperatures i.e. 400 and 500°C, the poligonization is enhanced. The substructure appeared is coarse and gradually becoming more equiaxed. At 500°C, the individual sub-grains can be clearly distinguished. Increase in the temperature increases the thermal activation and resulting in dynamically recovered coarser and equiaxed structure.

TEM of the Al-Zr-Si alloy tested at 200 and 300°C revealed sharp elongated sub-grain walls similar to that in pure Al deformed at low temperatures. Dynamic recovery during deformation causes dislocations to annihilate and rearrange them in form of sub-grains with low density interiors and neatly arranged walls (205, 206).

On increasing the deformation temperature, the initial elongated sub-grains convert into larger and more equiaxed sub-grains, as observed in Al-Zr-Si alloy deformed at 400 and 500°C (figs. 6.16 and 6.17). The sub-grain size of Al-Zr-Si alloy has a similar dependence on temperature and strain rate as for single phase Al (75) and shows the increase in rate of rearrangement of dislocations with increase in temperature. This is due to diffusion being the rate controlling mechanism (205) and dislocations may climb away easily whereas at low temperatures, the rate controlling mechanism is only dislocation glide and cross-slip.

During deformation, a density of free dislocations within the sub-grains, higher than generally present in single phase Al, is noted to be introduced in the Al-Zr-Si alloy associated with Al_3Zr particles. These dislocations appear to increase with increase in temperature. The microstructural evidence suggests that the dislocations are anchored by the particles which give rise to a high dislocation density during straining.

It is reported (69, 70, 207) that Al_3Zr particles strongly prevent the formation of the dynamically recovered structure in Al alloys containing Zn, Mg or Cu which may either lower the stacking fault energy of aluminium or provide large particles which encourage recrystallization during deformation. In the present investigations, the Al_3Zr particles are observed to interact with moving dislocations and boundaries. The particles affect the dislocations sinking into the sub-boundaries and therefore at high temperatures, less dense walls are observed along with an excessive dislocation density associated with the particles. This is the extent to which Al_3Zr particles are observed to interfere with dynamic recovery in the present work and the microstructure shows a well developed substructure. The diffusion controlled climb assists dislocations to get unlocked from the dislocation pile-ups at the particles. The freeing of dislocations from the

particles allowsthem to align together and annihilate one another leading to dynamic recovery.

The microstructural variations developed in the deformed Al-Zr-Si alloy are comparable to those evolved in the composite 2S/SiC deformed at similar deformation temperatures and strain rates. However the only distinguishing factor in the microstructures of the both materials is the presence of different forms of free dislocations within the sub-grains. In Al-Zr-Si alloy, the dislocation tangles observed within the sub-structure are those associated with Al_3Zr particles due to the pinning effect whereas in the composite, the excessive high dislocation density is due to the CTE effect generated during quenching.

7.13 Heterogeneous Deformation at the Grain Boundaries During Elevated Temperature Deformation of the Al-Zr-Si Alloy.

Deformation in Al-Zr-Si alloy deformed at high temperatures observed in the optical microscopy shows significantly heterogeneous structure in the grain boundary region. Plastic accommodation in this region takes the form of localised elongated deformation bands consisting of fine sub-grains. This type of heterogeneous structure varying from edge to the grain interior have been frequently observed in Al-Mg alloys (186, 187) and reported to be due to the differential local deformation in the grain-boundary region. This kind of modified microstructure developed near the grain-boundaries is at a much finer scale than in the interior of the grains and is observed in Al-Zr-Si alloy at 400 and 500°C. The contrast in the optical micrographs for this area in the polarized light suggests that

there is a different orientation gradient of these bands compared to the grain interior. These bands are more prominent at higher temperatures and lower strain rates but at 300°C, this phenomenon is very restricted as the overall sub-grain size in the specimens deformed is much smaller than those deformed at much higher temperatures, therefore, even if there were some heterogeneous deformation around the boundaries at low temperatures, it would not be prominently distinguished.

TEM observations afford a little information on how this substructure is formed at the grain-boundaries. It is considered from the observations that the particles are perhaps contributing to the formation of small sub-grains in the boundary region by interfering the movement and readjustment of the dislocations introduced in this area by stress concentration. Particles, if present near the grain-boundaries, reduce the capability of dislocations to sink into the boundaries (208) and give rise to a dislocation density in the boundary region. The existence of dislocations tangles lying parallel and near the grain-boundaries has been observed in the present work. It is thought that when such dislocation tangles decorated by Al_3Zr particles near the grain-boundaries get interlinked, this results in the formation of small sub-grains near the grain-boundaries. The sub-grains formed in this way on the boundaries show that the dislocation tangles and dispersed particles are present within the structure as well. The higher the temperature and lower the strain rate, the clearer this heterogeneous structure present.

CHAPTER 8
Conclusions and Proposals for Further Work.

8.1 Conclusions.

1. The composites 2S/SiC and 2014/SiC were deformed in uniaxial tensile and compression tests, at temperatures between room temperature and 500°C at strain rates between 5×10^{-4} and 5×10^{-2} S^{-1}. Similar tests on 2S and 2014 unreinforced matrix alloys have also been carried out for comparative purposes and true stress-strain curves were obtained. The true stress-strain curves of the composites at low temperatures were characterised by a parabolic hardening, but, at higher temperatures, the curves showed an increase in stress followed by a constant level on further straining.

2. The yield stress of the composites was less temperature dependent at lower temperatures but it showed a rapid decrease in the temperature range between 300 and 400°C, depending on strain rate. The yield stress above this temperature was again temperature independent. The unreinforced 2S and 2014 alloy showed a gradual decrease in the yield stress throughout the temperature range.

3. At low temperatures, the SiC particles produced a marked increase in the strength of the composites as a result of high dislocation density, substructure strengthening and internal stresses induced by differential thermal expansion coefficients of Al and SiC. At elevated temperatures, however, the yield stress and ultimate tensile stress of the composites is not greatly different in comparison to the matrix.

4. The values of activation energy for hot working were calculated to be 148 and 154 KJ/mole for the hot worked composites 2S/SiC and 2014/SiC respectively.

5. The initial work hardening rates of the composites were much greater compared to the unreinforced alloys at low temperatures.

6. The initial work hardening rates of the composites remained temperature independent with increasing temperature up to a limit in the temperature range between 300 and 400°C, depending on strain rate, where the work hardening rates dropped sharply as a consequence change in the nature of dislocation-particle interactions. This transition in the mechanical behaviour of the composites is reported (7) to be due to the onset of stress relaxation, caused by climb of dislocations controlled by bulk or / and interface diffusion, over the particles at a particular temperature, depending on particle size and strain rate. At temperatures above the transition temperature, the work hardening curves of the composites were again less temperature sensitive.

7. The experimentally measured temperatures for the transition in the mechanical behaviour of the composites reasonably agree with those predicted, according to the model given by Humphreys (7), for the conventional low volume fraction two phase alloys.

8. The composites showed a limited ductility compared to the unreinforced matrix alloys at low temperatures.

9. The fracture surfaces of the composites revealed fine equiaxed dimples , indicative of fracture occurring in a ductile manner. The initiation of fracture in the composites is expected to be a consequence of particle cracking and void nucleation adjacent to the particles.

10. The optical microscopy of the composites deformed in compression a different temperatures and strain rates showed deformed elongated grains with a banded substructure within at low temperatures. This substructure coarsened, as a result of dynamic recovery on increasing temperature, or decreasing strain rate.

11. TEM of the composite 2S/SiC deformed at temperatures between room temperatures and 500°C showed dynamically recovered substructure which became coarser and more equiaxed with increase in temperature.

12. TEM of the composite 2014/SiC deformed at low temperatures showed a mesh of high dislocation density and uniformly dispersed fine precipitates which pinned dislocations and suppressed dynamic recovery. However, on increasing the deformation temperature above 200°C, the dynamic recovery was evidenced in form of a sub-grain structure and the intermetallic precipitates coarsened in the matrix.

13. The hardness measurements as a function of temperature and metallography, for the composites and the matrix alloys deformed to various amounts of cold deformation revealed that the composites 2S/SiC and 2014/SiC recrystallized at temperatures of about 270 and 370°C respectively, whereas, the unreinforced 2S and 2014 alloys recrystallized at 350 and 425°C respectively.

14. Optical microscopy showed that, in both the composites 2S/SiC and 2014/SiC, large cold deformed elongated grains converted into a fine equiaxed grain structure after recrystallization. The fine recrystallized grains formed as a result of particle stimulated nucleation whose growth was related to the interparticle spacing.

15. The measured recrystallized grain size and recrystallized temperature of the composites was found to fit well with the predicted values according to the model given (128) for low volume fraction Al alloys containing large particles.

16. The recrystallized grain size of both the composites was found to be insensitive to the amount of prior cold deformation on subsequent annealing , if deformed by more than 20 %. This is suggested to be as a result of the high stored energy coming from the high dislocation density

due to the high volume fraction of the particles and the CTE effect, which, even at lower deformation levels, is sufficient to initiate particle stimulated nucleation of recrystallization.

17. TEM of the cold deformed 2S/SiC composite during annealing, at low temperatures below recrystallization temperature, revealed a fine sub-grain structure which coarsened on increasing temperature. At temperatures above the recrystallization temperature, a recrystallized microstructure was observed with a high density of dislocations within the grains. This originated during quenching, performed after annealing, as a result of difference in the thermal expansion coefficients between Al and SiC.

18. TEM of the cold deformed and annealed 2014/SiC revealed that the static recrystallization was suppressed during annealing at low temperatures by pinning effect of the fine precipitates in the alloy matrix. However, on increasing the annealing temperature, a distinct sub-grain structure developed as the precipitates started to overage. On annealing above 350°C, a recrystallized structure appeared with a high superimposed dislocation density. The quenched-in dislocations in the microstructure of the composite 2014/SiC were in the form of helices and spirals which formed due to the interaction of condensation of vacancies and dislocations during quenching, their density was higher near the particle-matrix interface.

19. The microscopy of the composites showed that the composite 2014/SiC recrystallized at 370°C, about 100 degrees higher than the recrystallization temperature of the composite 2S/SiC. This is attributed to the presence of the intermetallic precipitates present in the 2014 alloy matrix which slowed down the recrystallization by pinning of dislocations and sub-boundaries.

20. The cold deformed 2S/SiC composite annealed at a higher heating rate in a salt bath furnace resulted in a finer recrystallized grain size compared to that recrystallized at a slower heating rate in an air furnace.

21. On subsequent annealing of the composite 2S/SiC deformed at temperatures above the transition, a large recrystallized grain size was obtained, but, those deformed below the transition temperature yielded a very fine particle stimulated recrystallized grain structure on subsequent annealing.

22. Al-Zr-Si alloy displayed a high density and uniform distribution of Al_3Zr precipitates. The addition of Si appeared to improve the dispersion of fine Al_3Zr particles.

23. Al-Zr-Si alloy, deformed in compression at 200 and 300°C, showed an extended parabolic region in the true stress-strain curves. In the curves for the specimens deformed at 400 and 500°C, a steady state tends to occur after a small amount of deformation.

24. With the deformation of Al-Zr-Si alloy in the steady state, curves for the tests performed at temperatures of 400 and 500°C, and at a strain rate of 5×10^{-4} S^{-1}, showed a non-uniform deformation behaviour.

25. A continuous fall in the modulus corrected yield stress of Al-Zr-Si alloy is observed in the temperature range form 200 to 500°C.

26. Variations in the initial work hardening rates as a function of temperature in Al-Zr-Si alloy showed a well defined drop in the temperature range between 300 and 400°C, however, the work hardening rates were less temperature dependent above or below this temperature range.

27. The activation energy of the hot deformed Al-Zr-Si alloy was calculated to be 126 KJ/mole which is slightly lower than the self diffusion activation energy of pure Al.

28. The optical and transmission electron microscopy of Al-Zr-Si alloy showed that the deformed substructure at low temperatures was very similar to that of pure Al and the substructure became coarser and more fully polygonized as the deformation temperature was increased. At 400 and 500°C, a clear large and equiaxed substructure was observed.

29. The presence of fine Al_3Zr particles in Al-Zr-Si alloy tended to form dislocation tangles within the sub-grains by pinning of mobile dislocations and resulted in a much larger dislocation density in the hot deformed microstructure.

30. A prominent heterogeneous deformation structure is observed in Al-Zr-Si alloy at 400 and 500°C in form of layers of very fine sub-grains, adjacent to grain boundaries, which are smaller than the sub-grains in the interior of grains. TEM observations revealed that the heterogeneous substructure near the boundaries appeared to be formed by the pinning effect of the dislocations by the particles. This resulted in the formation of dislocation pile ups, parallel to the boundaries, which by interconnection during deformation were gradually converted into sub-grains.

8.2 Proposals For Further Work.

Aluminium alloy / SiC particulate composites show considerable promise as a structural material. They are destined to become very popular within the next few years. An increasing demand for higher performance composites makes it necessary to carry out systematic and analytic research in order to develop the optimum properties and thermo-mechanical processing routes and achieve the highest quality materials. In the present work, the basic micro-mechanisms operating during high and low temperature deformation and during subsequent recrystallization of the composites have been discussed while the areas of research that still require further understanding are outlined in this section.

Al/SiC composites in some cases are expected to behave superplastically at elevated temperatures. Some additional mechanical tests on a wider range of temperatures and strain rates on these composites will hopefully provide a better understanding of the effect of large second phase particles on superplasticity. This will help to optimise the thermo-mechanical processing route for these materials.

Crystallographic texture develops develops when two phase alloys are deformed at different temperatures or when annealed after deformation. An investigation on the textural development in hot and cold deformed and subsequently annealed composites is required to be carried out in order to understand how the dispersion of a high volume fraction of SiC particles influences the development of texture during various forming operations. This study could be used as a comparison with corresponding results from a study of microstructural development.

A detailed study is needed to understand the fracture behaviour of the composites with particular attention being paid to the role of the SiC

particles as to whether decohesion occurs at the particle-matrix interface or particles crack during failure of the composites. This will help in overcoming the principle problem of low ductility and low fracture toughness of these materials.

A more detailed and systematic study of the dislocation activity and microstructural development during hot deformation in Al/SiC composites using TEM in a more quantitative manner is needed. It will clarify the situation as to whether or not the presence of large, second phase particles affects the initiation of dynamic recrystallization in Al alloys.

It would also be useful to provide information about the inhomogeneous structure observed near the grain boundaries in the Al-Zr-Si alloy studied. This could be achieved through detailed investigations of the role of fine Al_3Zr particles on the development of heterogeneous microstructure and a quantitative study involving measurement of the misorientations between the sub-grains.

REFERENCES

1 Martin, J. W.; "Micromechanisms in Particle Hardened Alloys", Cambridge Univ. Press, 1980.
2 Humphreys, F. J.; In "Dislocations and Properties of Real Materials, The Inst. of Met., London, 1985, 175.
3 Brown, L. M.; Proc. 5th Int. Conf. on Strength of Metals and Alloys, Aachen, 3, 1984, 1551.
4 Embury, J. D.; Met. Trans., 16A, 1985, 2191.
5 Pederson, O. B. and Brown, L. M.; Proc. 4th Int. Riso Symp. on Met., Roskilde, 1983, 83.
6 Gerold, V. and Brown, L.M.; Proc. 4th Int. Riso Symp. on Met., Roskilde, 1983, 79.
7 Humphreys, F. J. and Kalu, P. N.; Acta Met., 35, 1987, 2815.
8 Humphreys, F. J.; Met. Sc., 13, 197, 136.
9 Kelly, A. and Nicholson, R. B.; Progress in Mat. Phys., 10, 1963, 151.
10 Brown, L. M. and Ham, R. K.; In "Strengthening Methods in Crystals", eds. Kelly, A and Nicholson, R. B., Elsevier, 1971, 12.
11 Orowan, E.; Symposium on Internal Stresses, Inst. of Met., London, 1948, 451.
12 Foreman, A. J. E. and Makin, M. J.; Phil. Mag., 14, 1966, 911.
13 Kocks, U. F.; Acta Met., 14, 1966, 1629.
14 Hirsch, P. B. and Humphreys, F. J.; Proc. Royal Soc., A318, 1970, 45.
15 Hirsch, P. B.; J. Inst. of Met., 86, 1957, 7.
16 Humphreys, F. J. and Martin, J. W.; Phil. Mag., 16, 1967, 927.
17 Humphreys, F. J., Hirsch, P. B. and Gould, D.; Proc. 2nd Int. Conf. on Strength of Metals and Alloys, 1982, Asilomer, 1970, 550.
18 Ashby, M.F. and Johnson, L.; Phil. Mag., 21, 1970, 399.
19 Ashby, M.F.; Phil. Mag., 14, 1966, 1157.
20 Brown, L. M. and Stobbs, W. M.; Phil. Mag., 34, 1976, 351.
21 Humphreys, F. J.; Acta Met., 27, 1979, 1801.
22 Humphreys, F. J. and Stewart, A. T.; Surface Sc., 31, 1972, 927.
23 Porter, J. R. and Humphreys, F. J.; Met. Sc., 13, 1979, 83.
24 Koeller, R. C. and Raj, R.; Acta Met., 26, 1978, 1551.
25 Goods, S. H. and Brown, L. M.; Acta Met., 27, 1979, 1.
26 Brownrigg, A., Spitzig, W. A., Richmond, O., Terlink, D. and Martin, J. W.; Acta Met., 31, 1983, 1141.
27 Brown, L. M. and Embury, J. D.; Proc. 3rd Int. Conf. on Strength of Metals and Alloys, Cambidge, 1, 1973, 164.

28 Rice, J. R. and Tracey, D. M.; J. Mech. Phy. Solids, 17, 1969, 201.
29 McClintock, F. A.; In "Ductility", 1968, 255.
30 Hirsch, P. B. and Humphreys, F. J.; In "Physics of Strength and Plasticity", ed. Argon, A., MIT Press, 1969, 189.
31 Humphreys, F. J. and Hirsch, P. B.; Phil. Mag., 34, 1976, 373.
32 Ashby, M. F.; USA Office of Naval Research Contract No. N00-14-67-A-0289-0010-NR-031-503, 1969.
33 Brown, L. M.; Proc. 5th Int. Conf. on Strength of Metals and Alloys, Aachen, 3, 1884, 1551.
34 Humphreys, F. J.; Ann. Chi. Fr., 5, 1980, 25.
35 Gould, D., Hirsch, P. B. and Humphreys, F. J.; Phil. Mag., 30, 1974, 1353.
36 Atkinson, J. D., Brown, L. M. and Stobbs, W. M.; Phil. Mag. 30, 1974, 1247.
37 Shewfelt, R. S. W. and Brown, L. M.; Phil Mag., 35,1977, 945.
38 Anand, L. and Gurland, J.; Acta Met, 24, 1976, 901.
39 Lloyd, D. J. and Kenny, D.; Acta Met., 28, 1980, 639.
40 Fisher, J. C., Hart, E. W. and Pry, R. H.; Acta Met., 1, 1953, 511.
41 Hart, E. W.; Acta Met., 20, 1972, 275.
42 Brown, L. M. and Stobbs, W.M.; Phil. Mag., 21, 1970, 399.
43 Brown, L. M. and Stobbs, W.M.; Phil. Mag., 23, 1971, 1201.
44 Eshelby, J. D.; Proc. Royal Soc., A241, 1957, 376.
45 Hazzledine, P. M. and Hirsch, P. B.; Phil. Mag., 30, 1974, 331.
46 Silcock, J. M.; Acta Met., 8, 1960, 589.
47 Brimhall, J. L. and Huggins, R. A.; Trans AIME, 233, 1965, 1033.
48 Price, R. J. and Kelly, A.; Acta Met., 11, 1963, 915.
49 Lloyd, D. J.; Acta Met., 25, 1977, 459.
50 Nourbakhsh, S. and Nutting, J.; Acta Met., 28, 1984, 357.
51 Baker, I. and Martin, J. W.; Met. Sc., 17, 1983, 459 & 469.
52 Klein, M. J. and Huggins, R. A.; Acta Met., 10, 1962, 55.
53 Hansen, N.; Powder Met., 12, 1969, 23.
54 Hansen, N.; Acta Met., 29, 1981, 65.
55 Sundberg, M., Sundberg, R. and Jacobson, B.; Jern. kont Ann., 155, 1971, 1.
56 Humphreys, F. J.; Acta Met., 20, 1972, 1801.
57 Hansen, N.; Acta Met., 25, 1977, 863.
58 Lloyd, D. J. and Martin, J. W.; Mat. Sc. & Engg., 46, 1980, 1.
59 Hansen, N. and Bay, B.; J. Mat. Sc., 7, 1972, 1351.
60 Hansen, N. and Ralph, B.; Acta Met., 30, 1982, 411.
61 Baker, I. and Martin, J. W.; Proc. 6th Int. Conf. on Strength of Metals and Alloys, Melbourne, 1, 1981, 487.
62 Stewart, A. T. and Martin, J. W.; Acta Met., 23, 1975,1.
63 Stobbs, W. M.; Phil Mag., 30, 1973, 1073.

64 Mori, T., Okabe, M. and Mura, T.; Acta Met., 28, 1980, 319.
65 Stanford-Beale, C. A. and Clyne, T. W.; Proc. 9th Int. Riso Symp. on Met., Roskilde, 1988, 479.
66 McQueen, H. J. and Jonas, J. J.; In "Plastic Deformation of Materials", ed. Arsenault, R. J., Academic Press, New York, 1975, 416.
67 Irvine, K. J., Gladman, T., Orr, J. and Pickering, F. B.; J. Iron & Steel Inst., 208, 1970, 717.
68 Nes, E.; J. Mat. Sc., 13, 1978, 2052.
69 Watts, B. M., Stowell, M. J., Blaike, B. L. and Owen, D. J. E.; Met. Sc., 10, 1976, 189 and 198.
70 Grimes, R., Stowell, M. J. and Watts, B. M.; Met. Tech., 3, 1976, 154.
71 Nes, E.; Met. Sc., 13, 1979, 211.
72 Nieh, T. G., Rainen, R. A. and Chellman, D. J.; Proc. 5th Int. Conf. on Composite Materials, San Diego, 1985, 825.
73 Takashi, A and Komori, S.; J. Jpn. Light Metals, 18, 1968, 428.
74 Jones, A. R. and Hansen, N.; Proc. 1st Int. Riso Symp. on Met., Roskilde, 1980, 13.
75 McQueen, H. J. and Hocket, J. E.; Met. Trans., 1A, 1970, 2997.
76 Jones, A. R., Ralph, B. and Hansen, N.; Met. Sc. 13, 1979, 149.
77 Rollason, T. C. and Martin, J. W.; J. Mat. Sc., 5, 1970, 127.
78 Baker, I. and Martin, J. W.; Proc. 1st Int. Riso Symp. on Met., Roskilde, 1980, 27.
79 Hansen, N.; Trans AIME, 245, 1969, 2061.
80 Mould, P. R. and Cotteril, P.; J. Mat. Sc., 2, 1967, 241.
81 Hansen, N.; Mem. Sci. Rev. Met., 1975, 189.
82 Gatti, A. and Fullman, R. L.; Trans AIME, 215, 1959, 344.
83 Doherty, R. D. and Martin, J. W.; J. Inst. of Met., 91, 1962-63, 332.
84 Preston, O. and Grant, N. J.; Trans AIME, 236, 1966, 1302.
85 Ryum, N.; Met. Report . ARL/Met. 64, Aeronautical Labs., Australia, 1967.
86 Chin, L. L. and Grant, N. J.; Powd. Met., 10,1967, 344.
87 Ryum, N.; Acta Met., 17, 1969, 269.
88 Zener, C.; see Smith, C. S., Trans AIME, 175, 1948, 15.
89 Chopra, O. K. and Niessen,P.; J. Mat. Sc., 9, 1974, 297.
90 Humphreys, F. J. and Martin, J. W.; Acta Met, 13, 1966, 775.
91 Leslie, W. C., Michalak, J. T. and Aul, F. W.; "Iron & its Dilute Solid Solutions", Interscience, New York, 1963, 119.
92 Gawne, D. J. and Higgins, G. T.; J. Mat. Sc., 6, 1971, 4031.
93 Humphreys, F. J.; Acta Met., 25, 1977, 1323.

94 Bay, B. and Hansen, N.; Met. Trans. 10, 1978, 279.
95 Morris, L. R.; Proc. 4th Int. Conf. on Strength of Metals and Alloys, Nancy, 1976, 649.
96 Ball, M. D. and Morris, P. L.; In "Electron Microscopy", ed. Sturgess, J. M., Microscopy Soc. of Canada, 1978, 622.
97 Nes, E.; Acta Met., 24, 1976, 391.
98 Nes, E.; Proc. 1st Int. Riso Symp. on Met., Roskilde, 1980, 85.
99 Nes, E.; Proc. Int. Conf. on Superplasticity, Grenoble, 1985, 1.
100 Morris, P. L. and Ball, M. D.; Proc. 1st Int. Riso Symp. on Met., Roskilde, 1980, 97.
101 Chan, H. M. and Humphreys; Acta Met., 32, 1984, 235.
102 Jonas, J. J., Sellars, C. M. and McG.Tegart, W. J.; Met. Rev., 14, 1969, 1.
103 Omerod, H., Tobolova, Z. and Cadek, J.; J. Inst. Met., 92, 1962-63, 297.
104 Sellars, C. M. and McG.Tegart, W. J.; Mem. Sci. Rev. Met., 200, 1966, 1044.
105 McQueen, H. J.; Met. Forum, 4, 1981, 81.
106 Stuwe, V. H. P. and Drube, B.; Z. Metalknde., 58, 1967, 499.
107 Lutton, M. J. and Sellars, C. M.; Acta Met., 17, 1969, 1033.
108 Sah, J. P., Richmond, J. R. and Sellars, C. M.; Met. Sc., 8, 1974, 325.
109 Sakai, T. and Jonas, J. J.; Acta Met., 32, 1984, 198.
110 McQueen, H. J. and Bergerson, S.; J. Mat. Sc., 6, 1977, 807.
111 McG.Tegart, W. J.; J. Metals Australia, 3 (1), 1971, 3.
112 Petkovik, R. A., PhD Thesis, McGill Univ., Montreal, 1975.
113 Bromley, R. and Sellers, C. M. ; Proc. 3rd Int. Conf. on Strength of Metals and Alloys, Cambridge, 2, 1973, 380.
114 Sheppard, T. and Zaidi, M. A.; Met. Sc., 17, 1983, 481.
115 Bricknell, R. H. and Edington, J. W.; Met. Trans., 10A, 1979, 1257.
116 Sheppard, T. and Tutcher, M. G.; Met. Sc., 14, 1980, 589.
117 Evengelista, E., McQueen, H. J. and Bonetti, E.; Proc. 4th Int. Riso Symp. on Met., Roskilde, 1983, 243.
118 Kalu, P. N. and Humphreys, F. J.; Proc. 7th Int. Riso Symp. on Met., Roskilde, 1986, 93.
119 Divecha, A. P., Fishman, S. G. and Dermarker, S. D.; J. Met., 33, 1981, 12.
120 Webster, D.; Met. Trans., 13A, 1982, 1511.
121 Nieh, T. G. and Karlak, R. F.; Scripta Met., 18, 1984, 25.
122 Froes, F. J. and Pickens, J. R.; J. Met., 36, 1884, 14.
123 Hasson, D. F., Hoover, S. M. and Crowe, C. R.; J. Mat. Sc., 20, 1985, 4147.
124 Arsenault, R. J. and Fisher, R. M.; Scripta Met., 17, 1983, 67.

125 Vogelsang, M., Arsenault. R. J. and Fisher, R. M.; Met. Trans, 17A, 1986, 379.
126 Arsenault, R. J. and Shi, N.; Mat. Sc. & Engg., 81, 1986, 175.
127 Nardone, V. C. and Prewo, K. M.; Scripta Met., 20, 1986, 43.
128 Humphreys, F. J.; Proc. 9th Int. Riso Symp. on Met., Roskilde, 1988, 51.
129 Jarry, P., Loue, W. and Bouvaist, J.; Proc. 6th Int. Conf. on Composite Materials, London, 2, 1987, 350.
130 Rack, H. J.; Proc. 6th Int. Conf. on Composite Materials, London, 2, 1987, 382.
131 Arsenault, R. J.; Mat. Sc. & Engg., 64, 1984, 171.
132 Philips, W. L.; Proc. 2nd Int. Conf. on Composite Mats., Warrendale, 1978, 83.
133 Nair, S. V., Tien, J. K. and Bates, R. C.; Int. Met. Rev., 30, 1985, 275.
134 Mahoney, M. W., Ghosh, A. K. and Bampton, C. C.; Proc. 6th Int. Conf. on Composite Materials, London, 2, 1987, 372.
135 Rack, H. J. and Krenzer, R. W.; Met. Trans., 8A, 1977, 335.
136 Sherby, O. D. and Wadsworth, J.; Proc. ASM Seminar, Deformation Processing & Structure, ed. Krauss, 1982, 355.
137 Chokshi, A. H., Nieh, T. G., Wadsworth, J. and Mukherjee, A. K.; Proc. 8th Int. Conf. on Strength of Metals and Alloys, Tempere, 1988, 301.
138 Dunwoody, B. J., Moore, D. M. and Thomas, A. T.; J. Inst. of Met. 101, 1973, 172.
139 Hahn, G. T. and Rosenfield, A. R.; Met. Trans., 6A, 1975, 653.
140 LeRoy, G., Embury, J. D., Edwards, G. and Ashby M. F.; Acta Met., 29, 1981, 1509.
141 Gurland, J. and Plateau, J.; Trans ASM, 56, 1963, 442.
142 McDannel, D. L.; Met. Trans., 16A, 1985, 1105.
143 Roebuck, B.; J. Mat. Sc. (Letts.), 6, 1987, 1138.
144 Flom, Y. and Arsenault, R. J.; Mat. Sc. & Engg., 77, 1986, 189.
145 Nieh, T. G.; Met. Trans., 16A, 1985, 1105.
146 Flom, Y. and Arsenault, R. J.; Proc. 6th Int. Conf. on Composite Materials, London, 2, 1987, 189.
147 Crowe, C. R., Gray, A. R. and Hasson, D. F.; Proc. 5th Int. Conf. on Strength of Metals and Alloys, Aachen, 3, 1884, 834.
148 Nutt, S. R. and Carpenter, R. W.; Mat. Sc. & Engg., 75, 1985, 169.
149 You, C. P., Thompson, A. W. and Bernstein, I. M.; Scripta Met., 21, 1985, 181.

150 Zok, F., Embury, J. D., Ashby, M. F. and Richmond, O.; Proc. 9th Int. Riso Symp. on Met., Roskilde, 1988, 517.
151 Flom, Y. and Arsenault, R. J.; J. Met., 7, 1986, 31.
152 Nes, E.; Acta Met, 20, 1972, 499.
153 Makin, P. L. and Ralph, B.; J. Mat. Sc., 19, 1984, 3835.
154 Gardner, K. G. and Grimes, R.; Met. Sc., 13, 1979, 216.
155 Matsui, K., Uetani, Y., Yamada, M. and Marukami, Y.; Met. Sc., 10, 1976, 235.
156 Adenis, D. Moulins, L. P. and Guilhaudis, A.; Mem. Sc. Rev. Met., 66, 1969,135.
157 Izumi, O. and Oelschagel, D.; Z. Metalkde., 60, 1967, 845.
158 Ohashi, O. and Ichikawa, R.; Met. Trans., 3A, 1972, 2300.
159 Chaudhury, Z. A. and Suryanarayan, C.; Metallography, 17, 1974, 231.
160 Fink, W. L. and Willey, L. A.; Trans AIME, 133, 1939, 63.
161 McPherson, D. J. and Hansen, N.; Trans ASM, 46, 1954, 354.
162 Sahin, E. and Jones, H.; Proc. 3rd Int. Conf. on Rapidly Quenched Metals, London, 1978, 138.
163 Ichikawa, R. and Ohashi, T.; J. Jpn. Inst. Light Metals, 18, 1968, 314.
164 Hatch, J. E.; "Aluminium, Props. & Phy. Met.", ASM, Ohio, 1985.
165 Auren, L., Westengen, H. and Reiso, O.; Proc. 1st Int. Riso Symp. on Met., Roskilde, 1980, 275.
166 Ashby, M. F. and Brown, L. M.; Phil. Mag., 8, 1963, 1083 & 1649.
167 Frost, H. J. and Ashby, M. F.; "Deformation Mechanism Maps", Pergamon Press, 1982.
168 Arsenault, R. J. and Taya, M.; Acta Met., 35, 1987, 651.
169 Cottrell, A. H.; In "Dislocations and Plastic Flow in Crystals", Oxford Univ. Press, 1953.
170 Hirsch, P. B.; In "The Physics of Metals", The Cambridge Univ. Press, 2, 1975.
171 Taya, M. and Arsenault, R. J.; Scripta Met., 21, 1987, 349.
172 Derby, B. and Walker, J. R.; Scripta Met., 22, 1988, 529.
173 Armstrong, R. W., Codd, I., Douwaite, R.M. and Petch, N.J.; Phil. Mag. 7, 1962, 45.
174 Hansen, N.; In "Strength of Metals and Alloys", ed. Haasen, P., Pergamon Press, Oxford, 1979, 849.
175 McElroy, R. J. and Szkopiak, Z. C.; Int. Met. Rev., 17, 1972, 175.
176 Hansen, N. and Bronsted, P.; Res. Mechanica, 1, 1980, 197.
177 Hansen, N. and Ralph, B.; Acta Met, 34, 1986, 1955.
178 Christman, T. and Suresh, S.; Brown Univ. Report NSF-ENG-8451092/1/87.
179 Tanaka, K. and Mori, T.; Acta Met., 18, 1970, 931.

180 Ebeling, R. and Ashby, M. F.; Phil. Mag. 13, 1966, 805.

181 McNelly, T. R., Edwards, G. R. and Sherby, O. R.; Acta Met., 25, 1977, 117.
182 Gould, D. and Humphreys, F. J.; Proc. 3rd Int. Conf. on Strength of Metals and Alloys, Cambridge, 2, 1973, 301.
183 Lewis, M. H. and Martin, J. W.; Acta Met., 11, 1963, 1207.
184 Guyot, P. and Ruedl, E.; J. Mat. Sc., 2, 1967, 221.
185 Ansell, G. and Weertman, J.; Trans. AIME, 215, 1959, 838.
186 Misro, S. C. and Mukherjee, A. K.; In "Rate Processes in Plastic Deformation of Materials", ed. Li, J. C. M., ASM, Ohio, 4, 1975, 434.
187 Nieh, T. G., McNelly, C. M., Wadsworth, J., Yaney, D. L. and Gilman, P. S.; Proc. Conf. on Strength of Aluminium Alloys, Trans AIME, Pheonix, 1988.
188 Mori, T. and Tokushije, M.; Acta Met., 25, 1977, 635.
189 Wong, W. A., McQueen, H. J. and Jonas, J. J.; J. Inst. Met., 76, 1967, 237.
190 Perdrix, Ch., Perrin, M. Y. and Montheilet, F.; Mem. Sci. Rev. Met., 78, 1981, 309.
191 Humphreys, F. J.; Proc. 6th Int. Conf. on Strength of Metals and Alloys, Melbourne, 1, 1981, 625.
192 Drury, M. and Humphreys, F. J.; Acta Met., 34, 1986, 2259.
193 Humphreys, F. J.; 4th Int. Riso Symp. on Met., Roskilde, 1983, 41.
194 Keh, A. S. and Weissman, S.; "Electron Microscopy & Strength of Crystals", Interscience, New York, 1963, 231.
195 Hardwick, D. and McG.Tegart, W. J.; J. Inst. Met., 90, 1961-62, 17.
196 Li, J. C. M.; "Recrystallization, Texture and Grain Growth", ASM, Ohio, 1966, 45.
197 Sokolkov, E. N. and Sadovsky, V.; Phys. Metals Metallogr., 19 (2), 1965, 479.
198 Thomas, G. and Whelan, M. J.; Phil. Mag., 4, 1959, 511.
199 Hunt Jr., W. J., Richmond, O. and Young, R. D.; Proc. 6th Int. Conf. on Composite Materials, London, 2, 1987, 209.
200 Nieh, T. G., Henshall, C. A. and Wadsworth, J.; Scripta Met., 18, 1984, 1405.
201 Argon, A. S., Im, J. and Safojgu, R.; Met. Trans., 6A, 1975, 835.
202 Humphreys, F. J.; Proc. 1st Int. Riso Symp. on Met., Roskilde, 1980, 35.
203 Lytton, J. L., Shepard, L. A. and Dorn, J. E.; Trans AIME, 212, 1958, 45.

204 Baird, J. D.; Int. Met. Rev., 16, 1971, 1.
205 Sherby, O. D., Klundt, R. H. and Miller, A. K.; Met. Trans., 8, 1977, 843.
206 McQueen, H. J.; Met. Trans., 8A, 1977, 807.
207 Gardner, K. J., Griffin, P. and Grimes, R.; In " Recrystallization in the Control of Microstructure", The Iron & Steel Inst. / The Inst. of Met., London, 1973.
208 Burton, B.; In "Diffusional Creep of Polycrystalline Mats.", Trans Technical Publications, Ohio, 1977.

ACKNOWLEDGEMENT

I Wish to express my sincere thanks to my supervisor Prof. F. J. Humphreys for his excellent supervision and guidance throughout this study. I am very grateful to the Ministry of Science and Technology, Govt. of Pakistan for providing the scholarship.

I also acknowledge to Alcan International for providing materials for the research and thank to Prof. Pashley for providing the laboratory facility.

My thanks are also due to the technical staff G. W. Briers, N. H. Salpadru, C. Gleeson and J.Woodal for providing invaluable technical advice and help in using electron microscopes and other equipment in the department.

I also greatly acknowledge the assistance of my friends inside and outside the department who encouraged me and helped me directly or indirectly in this work.

Finally, I wish to express my appreciation to my mother and all my family for their unending support and encouragement throughout the duration of this study at Imperial College.